



**HAL**  
open science

# Diphoton lineshape of the BEH boson using the ATLAS detector at the LHC

Cyril Becot

► **To cite this version:**

Cyril Becot. Diphoton lineshape of the BEH boson using the ATLAS detector at the LHC: calibration, mass, width and interferences. High Energy Physics - Experiment [hep-ex]. Université Paris Diderot-Paris VII, 2015. English. NNT: . tel-01471210

**HAL Id: tel-01471210**

**<https://theses.hal.science/tel-01471210>**

Submitted on 23 Feb 2017

**HAL** is a multi-disciplinary open access archive for the deposit and dissemination of scientific research documents, whether they are published or not. The documents may come from teaching and research institutions in France or abroad, or from public or private research centers.

L'archive ouverte pluridisciplinaire **HAL**, est destinée au dépôt et à la diffusion de documents scientifiques de niveau recherche, publiés ou non, émanant des établissements d'enseignement et de recherche français ou étrangers, des laboratoires publics ou privés.

LAL 15-303  
SEPTEMBER 2015

UNIVERSITÉ SORBONNE PARIS CITÉ



Thèse préparée  
à l'UNIVERSITÉ PARIS DIDEROT  
École doctorale STEP'UP - ED N°560  
Laboratoire de l'Accélérateur Linéaire - UMR 8607

**Diphoton lineshape of the BEH boson using the ATLAS  
detector at the LHC :  
calibration, mass, width and interferences**

par

**Cyril Becot**

Soutenue le 24 septembre 2015  
devant un jury composé de:

<b>Maarten Boonekamp</b> (CEA Saclay - SPP)	Examineur
<b>Matteo Cacciari</b> (LPTHE - Université Paris-Diderot)	Examineur
<b>Louis Fayard</b> (LAL)	Directeur de thèse
<b>Kirill Melnikov</b> (Karlsruher Institut für Technologie)	Examineur
<b>Marco Pieri</b> (U.C. San Diego)	Rapporteur
<b>Pierre Savard</b> (University of Toronto)	Rapporteur
<b>Achille Stocchi</b> (LAL)	Président
<b>Guillaume Unal</b> (CERN)	Examineur

November 6, 2015



---

---

## Abstract

Since the data collected during the first run of the LHC by the ATLAS and CMS collaborations allowed for the discovery of the BEH boson, a huge effort has been done toward the detailed studies of its properties. This thesis is particularly oriented toward the understanding of the BEH boson lineshape in its diphoton decay channel, using the data collected by the ATLAS detector in 2011 and 2012. The electromagnetic calibration of the ATLAS detector is described in details, and the precise measurement of the BEH boson mass it allowed for, at  $m_h = 125.98 \pm 0.50$  GeV, is summarized. A first upper limit on the BEH boson decay width, that gave a limit at  $\Gamma_h < 5.3$  GeV at 95% C.L., is presented in details). The last part of this thesis presents a study of quantum interferences between signal and background processes in the  $gg \rightarrow \gamma\gamma$  channel, which are expected to distort the diphoton lineshape and create a shift of the measured BEH boson mass, that is estimated to be of 35 MeV, which is small but not negligible.

## Résumé

Depuis que les données collectées par les collaborations ATLAS et CMS au cours de la première période de fonctionnement du LHC ont permis la découverte du boson BEH, un effort important a été investi dans l'étude détaillée de ses propriétés. Cette thèse est orientée en particulier vers la compréhension de la distribution en masse du boson BEH dans son canal de désintégration en deux photons, en utilisant les données collectées par le détecteur ATLAS en 2011 et 2012. L'étalonnage en énergie des électrons et les photons est décrit en détail, et la mesure précise de la masse qu'il a permis, à  $m_h = 125.98 \pm 0.50$  GeV, est résumé. Une première limite sur la largeur de désintégration du boson BEH est aussi présentée en détail, et donne une limite à  $\Gamma_h < 5.3$  GeV à 95% C.L. . La dernière partie de cette thèse est dédiée à une étude de l'impact des interférences quantiques entre les processus de signal et de bruit de fond dans le canal  $gg \rightarrow \gamma\gamma$ , dont l'effet déforme le spectre en masse et crée un biais pour la mesure de masse dans ce canal, qui a été estimé à 35 MeV, ce qui est petit mais non-négligeable.



# Contents

<b>Introduction</b>	<b>11</b>
<b>1 Theory</b>	<b>13</b>
1.1 The Standard Model of particle physics . . . . .	14
1.1.1 Discovery of the neutrino and the Fermi theory . . . . .	14
1.1.2 Maximal parity violation and $V - A$ interactions . . . . .	15
1.1.3 The electro-weak symmetry group and prediction of $W$ and $Z$ bosons . . . . .	15
1.1.4 Development of the spontaneous symmetry breaking . . . . .	16
1.1.5 The electro-weak theory for quarks and leptons . . . . .	16
1.1.6 Hints of physics beyond the standard model . . . . .	17
1.2 Spontaneous Symmetry Breaking . . . . .	18
1.2.1 Breaking of global symmetries . . . . .	18
1.2.2 Spontaneous symmetry breaking of a $U(1)$ symmetry and the Goldstone theorem . . . . .	19
1.2.3 The Brout-Englert-Higgs mechanism and the associated scalar boson . . . . .	21
1.2.4 Application to the electro-weak symmetry group . . . . .	22
1.2.5 Elitzur's theorem . . . . .	23
1.3 Higgs boson production and decays . . . . .	24
1.3.1 Initial state and the parton distribution functions . . . . .	24
1.3.2 Standard Model Higgs boson production channels . . . . .	27
1.3.3 Standard Model Higgs boson decays . . . . .	30
1.4 Defining masses and widths . . . . .	33
1.4.1 General definition . . . . .	33
1.4.2 The Complex Pole Scheme . . . . .	35
1.4.3 The Breit-Wigner formula . . . . .	35
1.5 Interferences between signal and background processes in $gg \rightarrow h \rightarrow \gamma\gamma$ . . . . .	35
1.5.1 General description of the phenomenon . . . . .	35
1.5.2 State of the art computation for the gluon fusion . . . . .	38
1.5.3 State of the art computation for the other production mechanisms . . . . .	39
1.6 Overview of the methods setting limits on the Higgs boson width . . . . .	41
1.6.1 Width from off-shell events in $h \rightarrow ZZ^*$ and $h \rightarrow WW^*$ . . . . .	41
1.6.2 Width from Higgs boson couplings combination . . . . .	43
1.6.3 Higgs boson width at future colliders . . . . .	44
<b>2 Statistics for particle physics</b>	<b>45</b>
2.1 Fundamental building blocks . . . . .	45
2.1.1 Probability density function and likelihood . . . . .	46

2.1.2	Maximal likelihood estimation and inclusion of uncertainties . . . . .	47
2.2	Construction of confidence intervals . . . . .	49
2.2.1	Definition and choice of a test-statistics . . . . .	49
2.2.2	General definition of a confidence interval . . . . .	50
2.2.3	Particular cases used in particle physics . . . . .	51
2.3	Distribution of the test-statistics . . . . .	54
2.3.1	Distribution from pseudo-experiments . . . . .	54
2.3.2	Asymptotic formulae for the significance . . . . .	55
2.4	Expected results : the Asimov dataset . . . . .	56
<b>3</b>	<b>Description of the experimental setup</b>	<b>59</b>
3.1	The Large Hadron Collider . . . . .	60
3.1.1	Motivations for a $pp$ collider . . . . .	60
3.1.2	The CERN accelerator complex . . . . .	60
3.1.3	LHC magnets . . . . .	62
3.1.4	Bunch filling scheme for the LHC . . . . .	63
3.1.5	Experiments using LHC beams and collisions . . . . .	64
3.1.6	Luminosity . . . . .	64
3.1.7	LHC Performance . . . . .	65
3.2	Description of the ATLAS detector [1] . . . . .	68
3.2.1	Overall description of the ATLAS detector . . . . .	68
3.2.2	Coordinate system of the ATLAS detector . . . . .	68
3.2.3	Magnets of the ATLAS detector . . . . .	70
3.2.4	The inner tracker . . . . .	71
3.2.5	Hadronic and forward calorimeters . . . . .	73
3.2.6	The muon spectrometer . . . . .	74
3.2.7	Luminosity detectors . . . . .	74
3.3	Description of the ATLAS electromagnetic calorimeter . . . . .	76
3.3.1	Global description of the concept . . . . .	76
3.3.2	Interaction of electromagnetic particles with matter . . . . .	76
3.3.3	From electromagnetic shower to recorded signals . . . . .	80
3.3.4	Anatomy of the ATLAS EM calorimeter . . . . .	82
3.3.5	Energy reconstruction with the calorimeter signals . . . . .	89
3.4	Reconstruction of electrons and photons at ATLAS . . . . .	92
3.4.1	Reconstruction of electromagnetic clusters . . . . .	92
3.4.2	Offline identification of photons [2] . . . . .	93
3.4.3	Offline identification of electrons [3] . . . . .	96
3.5	Comparison with the CMS detector . . . . .	98
3.5.1	Overall description of the CMS detector . . . . .	98
3.5.2	Description of the electromagnetic calorimeter . . . . .	98
3.5.3	Reconstruction of electromagnetic particles in CMS . . . . .	100
<b>4</b>	<b>Electromagnetic calibration of the ATLAS detector</b>	<b>103</b>
4.1	Global overview of the calibration procedure . . . . .	104
4.2	Monte-Carlo based calibration . . . . .	105
4.2.1	Determination of the material in front of the calorimeter . . . . .	105

---

4.2.2	Multi-variate Calibration	108
4.3	Corrections to the energy response on data	111
4.3.1	Intermodule gaps	111
4.3.2	Pre-sampler high-voltage	111
4.3.3	High-voltage in the accordion	112
4.3.4	Inter-layer calibration	118
4.3.5	Presampler (PS) energy scale	119
4.4	Correction for an apparent non-linearity	122
4.4.1	Presentation of the problem	122
4.4.2	Extraction of the energy response difference	122
4.4.3	Cross-checks of potential explanations	126
4.4.4	Derivation of an ad-hoc correction	133
4.4.5	Correlation with the shower-shape mismodeling	136
4.5	Lateral energy leakage	137
4.5.1	Position of the problem	137
4.5.2	Overview of the method	139
4.5.3	Cross-checks of potential electron to photon differences	140
4.5.4	Final results	145
4.6	Determination of the energy scale of the calorimeter	146
4.6.1	Absolute energy scale	146
4.6.2	Stability, uniformity and linearity of the energy response	148
4.7	Extrapolation of the energy scale to photons	153
4.7.1	Mismodeling of the conversion reconstruction	153
4.7.2	Energy scales from photons	153
4.8	Electron and photon energy resolution	156
4.9	Comparison between 2011 and 2012 data-taking	157
4.9.1	Layer 1 Gain	157
4.9.2	Crack non-linearity	158
4.10	Possible improvements toward Run II	159
4.10.1	Inner detector rail mismodeling	159
4.10.2	Out of cluster leakage	160
4.11	Comparison with the CMS calibration	160
<b>5</b>	<b>Upper limit on the BEH decay width and measurement of its mass</b>	<b>167</b>
5.1	Overall description of the $H \rightarrow \gamma\gamma$ analyses	168
5.1.1	Selection of events for the $h \rightarrow \gamma\gamma$ analysis	168
5.1.2	Modelling of signal and background processes	171
5.1.3	Event categorization for the mass and width analysis	173
5.2	Measurement of the BEH boson mass	177
5.2.1	Measurement of $m_h$ in the $h \rightarrow \gamma\gamma$ channel	177
5.2.2	Impact of the systematic uncertainties on $m_h$	177
5.2.3	Consistency among classes of events	179
5.2.4	Combination with the $h \rightarrow ZZ^* \rightarrow 4l$ channel	182
5.2.5	Combination with CMS	183
5.3	Modelling of the width	185
5.3.1	Signal model as a function of the width	185

5.3.2	Comparison between different types of Breit-Wigner functions . . . .	185
5.4	Main results on the width . . . . .	188
5.4.1	Overall description of the statistical method and problems . . . . .	188
5.4.2	Upper limit on the Higgs boson decay width . . . . .	190
5.5	Checks on the observed non-asymptoticity . . . . .	198
5.5.1	Presentation of the problem on the full statistical model . . . . .	198
5.5.2	Impact of the various nuisance parameters . . . . .	199
5.5.3	Cross-check on a simplified model . . . . .	199
5.5.4	Comparison with the $h \rightarrow ZZ^* \rightarrow 4l$ channel . . . . .	201
5.5.5	Look-elsewhere effect and the Leadbetter formula . . . . .	202
5.6	Impact of the resolution and comparison with CMS . . . . .	203
5.6.1	Variation of the limit as a function of the resolution . . . . .	203
5.6.2	Upper limit on the width from the CMS collaboration . . . . .	204
<b>6</b>	<b>Interferences between <math>gg \rightarrow h \rightarrow \gamma\gamma</math> and <math>gg \rightarrow \gamma\gamma</math></b>	<b>207</b>
6.1	Monte-Carlo generation of interferences . . . . .	208
6.1.1	Precision of the Sherpa 2 computation . . . . .	208
6.1.2	Implemented Higgs boson propagator . . . . .	209
6.1.3	Cross-check of the output cross-sections . . . . .	209
6.1.4	Reweighting of the cross-section to the Standard Model . . . . .	211
6.2	Detector effect folding . . . . .	212
6.2.1	Simulation of photon conversions . . . . .	212
6.2.2	Identification and reconstruction efficiencies . . . . .	212
6.2.3	Implementation of the mass resolution . . . . .	213
6.3	Parton shower tuning . . . . .	215
6.3.1	Principle of the optimization . . . . .	215
6.3.2	State of the art description of the Higgs boson $p_T$ distribution . . . .	216
6.3.3	Results for the tuning . . . . .	216
6.4	Impact of interferences on the measurement of $m_h$ . . . . .	221
6.4.1	Generation of pseudo-Asimov datasets . . . . .	221
6.4.2	Main results on the mass shift . . . . .	221
6.4.3	Systematic effects affecting the mass shift . . . . .	224
6.4.4	Results by categories . . . . .	226
6.4.5	Conclusions . . . . .	228
	<b>Conclusion</b>	<b>229</b>
	<b>APPENDICES</b>	<b>230</b>
<b>A</b>	<b>Distribution of the reconstructed <math>Z^0</math> boson mass in <math>Z^0 \rightarrow ee</math> events profiled along <math>\phi</math> in narrow <math>\eta</math> bins</b>	<b>231</b>
<b>B</b>	<b>Calculation of the error on the mass and of the upper limit on the width as a function of the resolution</b>	<b>237</b>
	<b>Bibliography</b>	<b>239</b>

**Remerciements**

**263**



# Introduction

Within the last couple of years it became clear that the most important legacy of the Run I of the LHC was the discovery of a new scalar boson. This new particle constitutes the first - and so far only - observation of what appears to be a fundamental scalar particle, and finally completes the Standard Model of particle physics, whose only missing component was the exact mechanism for the electro-weak symmetry breaking. But as it is the newest sector of the theory, it is also vastly unexplored and its properties need to be determined with the best possible precision. Within the Standard Model all the properties of the BEH (or Higgs) boson are fixed once its mass is known, and this parameter  $m_h$  is the only free parameter of the theory. But in several scenarios beyond the standard model the existence of new particles can imply new decay channels for the Higgs boson, or different couplings due to the apparition of these particles in the loops, which may be detected by a broadening of the Higgs boson width. This thesis wants to understand the lineshape of the Higgs boson in its di-photon decay channel with the dataset that was collected in 2011 and 2012 by the ATLAS detector at the LHC. The measurement of the Higgs boson mass and an upper limit on its width are reported in this thesis, together with a description of the electro-magnetic calibration procedure for the ATLAS detector which is required to have a proper understanding of the mass distributions. Furthermore a preliminary study of the interferences between signal ( $gg \rightarrow h \rightarrow \gamma\gamma$ ) and background ( $gg \rightarrow \gamma\gamma$ ) processes is also reported as it is required to completely understand the Higgs boson line-shape in this particular channel, where the background is not negligible.

This document is organized as follows : the first three chapters are dedicated to a description of the scientific background surrounding this thesis and of the necessary tools that will be needed afterwards. The contents of the three following chapters are gradually converging towards the current understanding of the Higgs boson line-shape in its di-photon decay channel.

Chapter 1 begins with a brief historical summary of the development of the electro-weak theory before describing with more details the Brout-Englert-Higgs mechanism. Then the phenomenology of the Higgs boson productions and decays is outlined, while the last part of this chapter is dedicated to a brief review of the methods used to set limits on the Higgs boson width, and to the theoretical description of interferences between signal and background processes in the  $h \rightarrow \gamma\gamma$  channel.

Chapter 2 explains the statistical method that is used at the LHC and that is necessary to extract physical information which we are interested in from the data. It starts by the general outline of the statistical theory and ends by describing the standard statistical tests and tools used by ATLAS and CMS.

Chapter 3 describes the experimental setup without which this thesis could not have

been made. It starts with a description of the LHC collider and its performance, as well as the different pre-acceleration steps that are required for the beams before their injection into the LHC. Then the ATLAS detector is detailed, with a particular emphasis on the liquid Argon electro-magnetic calorimeter that plays a central role for the physics that is being studied in this thesis. At the end of this chapter the methods used to reconstruct electro-magnetic clusters and identify electrons and photons are described and its performance is given.

Chapter 4 details the full calibration procedure for the energy of electro-magnetic objects, starting from the material determination and Monte-Carlo calibration, going to the final cross-checks of the linearity of the response and of the electron to photon extrapolation of the energy scale. This includes the descriptions of the various pre-corrections and of the method used to set the in-situ energy scale. At the end of this chapter, the small differences that were observed between the 2011 and 2012 datasets are discussed.

Chapter 5 shows the results that were obtained for the Higgs boson mass and the Higgs boson width in the  $h \rightarrow \gamma\gamma$  channel. It starts with an overall description of the selection applied on the data, of its modelling and of the categories that are defined to improve the performance of the analysis. In this process the various uncertainties that have an impact on either the mass, the peak resolution or the signal strength are explained, together with the method used to extract it. Then the measurement of the Higgs boson mass is outlined, first in the  $h \rightarrow \gamma\gamma$  channel alone and then in its combination with the  $h \rightarrow ZZ^* \rightarrow 4l$  channel. Afterwards the upper limit on the width that has been set using a direct fit of the di-photon lineshape to a non-relativistic Breit-Wigner is detailed.

Finally, chapter 6 describes an on-going preliminary study of the impact of interferences between signal and background processes in the  $gg \rightarrow \gamma\gamma$  channel on the Higgs boson mass. First, the calculation implemented in the interference plug-in of Sherpa 2 is detailed and cross-checked, then the  $p_T$  spectrum generated by this plug-in is tuned to match the current best description of the Higgs boson  $p_T$  and a simple smeared detector simulation is described. The last part of this chapter gives the preliminary results of the mass shift that are obtained using the full statistical model used for the Higgs boson mass measurement.

Throughout this document comparisons between the analyses made by the ATLAS and CMS collaborations and its performance is outlined, whenever it is relevant. The comparison between the two detectors and their reconstruction methods for electro-magnetic particles has been made in chapter 3, while the comparison between the electro-magnetic calibrations procedures of the two detectors, as well as their impact on the BEH mass measurement, is done in chapter 4. The comparison between the categories that have been defined to measure the Higgs boson mass in ATLAS and CMS, as well as their impact on the width and on the statistical error on the Higgs mass, is done in chapter 5.

# Chapter 1

## Theory

### Contents

---

<b>1.1</b>	<b>The Standard Model of particle physics</b>	<b>14</b>
1.1.1	Discovery of the neutrino and the Fermi theory	14
1.1.2	Maximal parity violation and $V - A$ interactions	15
1.1.3	The electro-weak symmetry group and prediction of $W$ and $Z$ bosons	15
1.1.4	Development of the spontaneous symmetry breaking	16
1.1.5	The electro-weak theory for quarks and leptons	16
1.1.6	Hints of physics beyond the standard model	17
<b>1.2</b>	<b>Spontaneous Symmetry Breaking</b>	<b>18</b>
1.2.1	Breaking of global symmetries	18
1.2.2	Spontaneous symmetry breaking of a $U(1)$ symmetry and the Goldstone theorem	19
1.2.3	The Brout-Englert-Higgs mechanism and the associated scalar boson	21
1.2.4	Application to the electro-weak symmetry group	22
1.2.5	Elitzur's theorem	23
<b>1.3</b>	<b>Higgs boson production and decays</b>	<b>24</b>
1.3.1	Initial state and the parton distribution functions	24
1.3.2	Standard Model Higgs boson production channels	27
1.3.3	Standard Model Higgs boson decays	30
<b>1.4</b>	<b>Defining masses and widths</b>	<b>33</b>
1.4.1	General definition	33
1.4.2	The Complex Pole Scheme	35
1.4.3	The Breit-Wigner formula	35
<b>1.5</b>	<b>Interferences between signal and background processes in <math>gg \rightarrow h \rightarrow \gamma\gamma</math></b>	<b>35</b>

---

1.5.1	General description of the phenomenon . . . . .	35
1.5.2	State of the art computation for the gluon fusion . . . . .	38
1.5.3	State of the art computation for the other production mechanisms . . . . .	39
<b>1.6</b>	<b>Overview of the methods setting limits on the Higgs boson width . . . . .</b>	<b>41</b>
1.6.1	Width from off-shell events in $h \rightarrow ZZ^*$ and $h \rightarrow WW^*$ . . . . .	41
1.6.2	Width from Higgs boson couplings combination . . . . .	43
1.6.3	Higgs boson width at future colliders . . . . .	44

---

## 1.1 The Standard Model of particle physics

With time our understanding of the nature of fundamental particles and of the forces that rule their interactions has evolved, and this converged toward what is now known as being the Standard Model of particle physics. This model characterizes itself by the existence of three families of matter, each one being constituted by one neutrino, one charged lepton, two quarks, and their anti-particles. The forces are formed by two fundamental gauged symmetry groups,  $SU(3)_C$  that describes the strong interaction and generates its 8 gluons, and  $SU(2)_L \times U(1)_Y$  which describes the unified electro-weak interaction with its 4 vector boson. In addition to that, the model embeds a scalar field, the Brout-Englert-Higgs (BEH) field (sometimes called the Higgs field, both terms will be used in this thesis) that spontaneously breaks the  $SU(2)_L \times U(1)_Y$  symmetry down to  $U(1)_Q$  which describes the electro-magnetic interactions. Although this picture is now clear and complete both on the experimental and theoretical side, its full development took more than a century, starting from the discovery of the electron and the quantization of light at the end of the 19th century, ending with the experimental discovery of a scalar boson in 2012. In this chapter a very brief historical review of the construction of the electro-weak theory is sketched, but it will obviously not be complete. Further details may be found in [4–9], especially for the strong interaction and the quark sector that will not be reviewed here.

### 1.1.1 Discovery of the neutrino and the Fermi theory

In the early twentieth century the radioactivity coming from  $\beta$  decays had been discovered, and its properties were being studied [10]. In particular the energy spectrum of the outgoing electron was being studied by Lise Meitner and Otto Hahn and, following their studies and the definitive proof by Chadwick [11], displayed a continuous distribution while it was expected to be a discrete ray because of the energy-momentum conservation under the hypothesis of a two-body decay. It is only in 1930 that Pauli imagined the existence of a new weakly-interacting and light particle that would be involved within this process and carries out a part of the energy of the decay, the "neutrino", explaining the continuous spectrum that was observed. A theory of this interaction, based on contact-interaction, was published by Fermi in 1933 [12]. In 1936 this theory also proved useful in describing the decay of the newly discovered muon, whose decay was described as a four-fermion contact interaction, whose coupling constant  $G_F$  is called the Fermi constant. Although

this theory gives accurate predictions at low-energy, it predicts cross-sections that are diverging as  $E^2$  hence it is expected to be only an effective-theory to which massive vector bosons should be added to regularize the high-energy behaviour of the theory, which has been the first indirect hint of the existence of the W and Z bosons that will be presented later.

### 1.1.2 Maximal parity violation and $V - A$ interactions

At the middle of the twentieth century, parity was believed to be an exact symmetry of nature, which had been tested extensively in strong and electro-magnetic interactions, and it was believed to be valid in weak interactions too. It was noticed by Lee and Yang in [13] that there were no experimental data that could either rule out the parity conservation in weak interactions or confirm it, and they proposed experimental ideas to check for it. A year later a team lead C.S. Wu [14] did an experiment that showed that the weak-interactions were not respecting the parity-conservation (see also [15, 16]). Atoms of Cobalt-60 were subject to a magnetic field in which their spin would align, and they were cooled to a sufficiently low temperature so that the thermal fluctuations would not break this alignment. In the case of a parity-conserving interaction the electrons produced in the  $Co^{60}$   $\beta$ -decays were expected to be emitted symmetrically with respect to the magnetic field. It was seen that the decay electrons were predominantly emitted in the direction opposite to the magnetic field (i.e. opposite to the spin direction of the Cobalt atoms), in a fraction of 60%, which proved that the weak radioactive decays were not conserving the parity. In fact within the Standard-Model it is maximally violated in the sense that only left-handed particles and right-handed anti-particles are sensitive to the (charged) weak interaction, which implies that right-handed neutrinos would not interact, and within the SM they do not exist. This had strong implications on the weak interaction and on its Lagrangian, that was now expected to display a  $V - A$  structure which characterizes this maximal parity violation, which for instance transformed the Lagrangian for the  $\beta$ -decay  $n \rightarrow pe^- \bar{\nu}_e$  into :

$$\mathcal{L}_\beta = \frac{G_F}{\sqrt{2}} (\bar{p} \gamma_\mu (1 - \gamma_5) n) (\bar{e} \gamma_\mu (1 - \gamma_5) \nu) \quad (1.1)$$

where  $\frac{1-\gamma_5}{2} = P_L$  projects a spinor onto its left-handed component.

### 1.1.3 The electro-weak symmetry group and prediction of $W$ and $Z$ bosons

It was noticed by Schwinger [17] that there is a deep connection between weak and electro-magnetic interactions, in the sense that they are both mediated by spin-1 particles and that in both cases the gauge couplings does not depend on the particle that is considered. Schwinger only considered a simple triplet of vector fields, which already allowed him to connect the electric charge to the weak iso-spin and the hyper-charge, and the fourth vector boson was predicted by Glashow in [18]. These four bosons are the generators of the  $SU(2)_L \times U(1)_Y$  gauge group, where the  $SU(2)_L$  group only acts on left-handed fermion doublets, while the right-handed fermions are singlet of  $SU(2)_L$ , which creates the  $V - A$  structure of the interaction. This gauge group will later become widely accepted

as the basis of the unified electro-weak interactions. But at this point the theory was not renormalizable because there were no adequate mechanism to generate the mass of the gauge boson. This mass term had to be included "by hand", although a generic mass term was known to break the gauge invariance that is required to show that the theory is renormalizable. Still this paper predicted the existence of the  $Z^0$  boson that was indirectly confirmed first by the Gargamelle collaboration [19–21] that observed neutral currents interactions, that could only be mediated by a  $Z^0$  boson, then by the UA 1 and UA 2 collaborations at the  $S\bar{p}\bar{p}S$  that discovered the  $W^\pm$  [22, 23] and  $Z^0$  bosons [24, 25].

#### 1.1.4 Development of the spontaneous symmetry breaking

The details of the mechanism of spontaneous symmetry breaking and of its application to gauge symmetries will be given in the next section, and we shall here only give a few historical details. This mechanism originates from condensed matter physics, where it is at the heart of the description of the phenomenon of super-conductivity that was first formally developed in [26] and received a microscopical explanation with the BCS theory in [27]. This work was acknowledged and brought to particle physics by Nambu [28–31], whose aim was to understand the short-range of the strong interaction by generating a mass to its vector boson. This model required the existence of a mass-less boson, whose existence was afterwards proved to be a general property of the spontaneous breaking of global continuous symmetries by Goldstone [32, 33]. In the context of strong interaction this Nambu-Goldstone boson was believed to be the neutral pion ( $\pi^0$ ), that was not mass-less but its relatively small mass was believed to come from the fact that the symmetry was only approximate. The mechanism that extends the concept of symmetry breaking to local symmetries was first sketched in an article of Anderson [34] in the non-relativistic context of a Plasma and was separately brought into the context of particle physics by four independent articles by Brout and Englert [35], Higgs [36, 37] and Guralnik, Hagen and Kibble [38]. At this stage only Abelian symmetry groups had been considered and the extension to non-Abelian groups was done in [39]. Furthermore these studies were carried in the context of strong interaction, trying to explain the short range of this interaction by the generation of a mass to its vector boson. Its application to electro-weak interactions has been done by Weinberg [40] and Salam [41]. This mechanism predicts the existence of a new massive scalar boson, that has been discovered separately by the ATLAS [42] and CMS [43] experiments at the LHC on the 4th of July, 2012.

#### 1.1.5 The electro-weak theory for quarks and leptons

The electro-weak model based on the local  $SU(2)_L \times U(1)_Y$  symmetry group that is broken down to  $U(1)_Q$  with the BEH mechanism that is described in [40] has a very specific structure for the lepton sector, as the left-handed component for the charged lepton of a given family lies within a doublet with the corresponding neutrino, while the right-handed component lies within a singlet. The couplings of the  $W$ ,  $Z$  and  $\gamma$  photons to the different leptons are induced by the covariant derivative which gives a powerful predictive power to this theory, whose properties have now been precisely confirmed in a wide variety of experiments. In [40] the quark sector is not included, because the structure of the quark sector was not properly known at this time, as the existence of the charm quark was not

yet accepted. This completion of the theory, including the quark sector, only came with the GIM mechanism [44] that forbids the existence of flavour-changing neutral current (FCNC) at tree level. This suppression is necessary to explain the low branching ratio of  $K_L^0 \rightarrow \mu^+ \mu^-$  ( $BR \approx 10^{-9}$ ), that would be enormous if FCNCs were allowed, as it would imply interactions such as  $s\bar{d} \rightarrow Z \rightarrow \mu^+ \mu^-$ . But, even with this FCNC cancellation, the loop-induced process gave a branching ratio bigger than the one that is observed, hence the second part of this mechanism was the addition of a fourth quark, called the charm quark that would later be simultaneously observed by two independent collaborations [45, 46]. The quarks were expected to exist in left-handed doublets, such as the leptons, with one doublet by generation :  $(u; d)_L$  and  $(c; s)_L$ , and right-handed singlets  $u_R, d_R, c_R, s_R$ . At this stage the structure of the theory was completed, and only the last fermion family was missing, which would later be predicted [47] to allow the CP-violation that had been observed in the kaon sector [48].

### 1.1.6 Hints of physics beyond the standard model

Within our current knowledge there are only few well accepted experimental facts that do not fit within the framework of the standard model, and are explicitly calling for new physics phenomena. One fact comes from the galaxy rotation curve, which is the orbital velocity of a star in a galaxy as a function of the distance of this star to the center of this galaxy. This can be computed or simulated from the basic laws of gravity, and was seen that the measurement carried out on real galaxies were very different from the predictions [49]. One of the possible solutions to this problem would be to add an additional massive component, "the Dark Matter", that has not been discovered and that would contribute to a sizeable extent to the total mass of the galaxies, hence modifying their gravitational properties and the velocity curve. There are also some alternative hypothesis using, for instance, a modified version of the laws of gravity that may also solve this problem [50].

Another fact is the existence of a mass for the neutrinos, which is not possible in the Standard Model as there are no right-handed neutrinos. This mass was observed through the existence of oscillations between the different flavours of neutrinos [51], as these oscillations can only happen if there is a difference of mass between the different neutrino mass eigenstates. Several models exist to generate these masses [52], and predict the existence of new particles, potentially sterile neutrinos, that could have very high masses.

So far there is no evidence of new physics in the scalar sector. There are a few theoretical arguments that concern the consistency of the electro-weak theory, such as the naturalness of the Higgs boson mass [53] or the meta-stability of the electro-weak vacuum [54], but they do not imply a break-down of the physical laws of the SM and may well receive an answer within the current theoretical framework, without requiring any new physics phenomenon. But this sector is also the one that has been the most recently discovered and it is yet vastly unexplored, hence it may well bring some intriguing puzzles in the coming years and the study of its properties may unravel new physics.

## 1.2 Spontaneous Symmetry Breaking

The notion of symmetry has been of primary importance in the development of modern physics, and this has been reinforced by the Noether theorem [55] that allowed to link abstract symmetries to the conservation of physical quantities. Although the principle of symmetry had been used before, especially in the development of special and general relativity, it is with this theorem that it started to play a central role in the development of new fundamental theories. A short summary of the development of the concept of symmetries and of its impact on physics has been given in [56]. But this concept cannot explain everything as it was observed that depending on the energy or temperature scale at which a given system is studied, its behaviour may exhibit a different level of symmetry. In fact in this context the underlying physical laws, that may be explained with the Lagrangian, are still invariant under the fundamental symmetry of the nature but their specific solution are not invariant anymore, and this may be explained in the context of spontaneous symmetry breaking. There are several examples of this phenomenon in nature, and we will try to progressively develop them below, from the simple example up to the full construction that is needed to understand the BEH mechanism and the electro-weak symmetry breaking.

### 1.2.1 Breaking of global symmetries

The most simple illustrative example of spontaneous symmetry breaking that exists in nature corresponds to the bending of a rod [57], which is illustrated in fig. 1.1. In the absence of any force applied on the rod it will be a rigid straight line, and the whole physics of this problem is invariant under a rotation around the axis of this rod. This picture does not change if a small force is applied at both ends of this rod, but if this force becomes strong enough the rod will start to bend. At this point this system will not be invariant anymore under a rotation around the initial axis of the rod, as the system will collapse into a specific position. But the ensemble of the positions in which it may collapse is itself symmetrical under this rotation, as the different positions are not differentiable by their energy level or any conceivable selection rule. In this particular case the exact ground state the rod falls in is determined by small perturbations of the initial conditions of this problem. Any of the ground state is equivalent by rotational invariance, and every possible position is as likely as an other. This is a good illustration of the concept of symmetry breaking : in each case that will be discussed below the same phenomenon happen. The description of the system in term of its Lagrangian will always be invariant under a specific transformation, and the ensemble of solutions to the system will also be invariant under this transformation. The system will fall in a specific state of this ensemble, and in a given energy or temperature range this ensemble is reduced to one state, while outside of this range it will correspond to an infinite ensemble and the system will fall in a specific state. This ground state will not be invariant under the symmetry that rules the physical theory, but it belongs to a set of solutions that is itself invariant, and the underlying physics will still be invariant.

A similar phenomenon happens for ferro-magnetic materials [58]. In the absence of an external field the magnet has a  $O(3)$  rotational invariance, and we could expect the same property for the magnetic field generated by this ferro-magnetic material, which means that

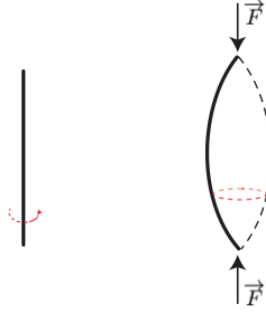


Figure 1.1: Bending of a rod under an external force parallel to its axis : the left case corresponds to the symmetric ground state when no external force is applied and the right one to the spontaneously broken ground state

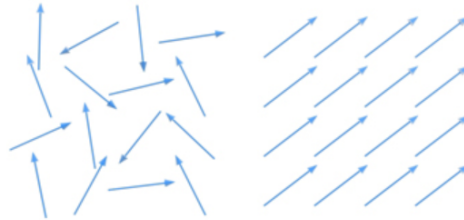


Figure 1.2: Direction of the spins in a ferromagnetic material : above  $T_c$  on the left and below on the right

it should be 0. It is not the case at low temperature where a non-negligible magnetization of the material appears, which is essentially due to the fact that the lowest energy level for this material is reached when the spins are aligned, otherwise the magnetic interaction between the spins increases the total energy of this system. As the temperature rises the kinematic energy available for thermal variations increases, and at a given critical temperature ( $T_c$ ) this counteracts the alignment from magnetic interactions and the material will not be magnetic anymore, in the absence of an external field. Below  $T_c$  the  $O(3)$  rotational invariance breaks down to  $O(2)$  which is a invariance by rotation around the magnetic field axis. The invariance by inversion of the system along this axis is broken.

But these two examples correspond to the breaking of global symmetries, which is not what we are interested in for the electro-weak symmetry breaking. For instance in ferro-magnetism materials, even in the phase where  $O(3)$  is not broken the spins are not rotated independently from each others : it is the complete system that is invariant under  $O(3)$ . For the electro-weak theory this invariance has to be local : every point in space may be subject to a different transformation of the symmetry group of the theory.

## 1.2.2 Spontaneous symmetry breaking of a $U(1)$ symmetry and the Goldstone theorem

Now we shall consider a simple toy model that describes a single complex scalar that is invariant under a global  $U(1)$  symmetry, i.e. for which  $\phi \rightarrow e^{i\alpha}\phi$  does not change the

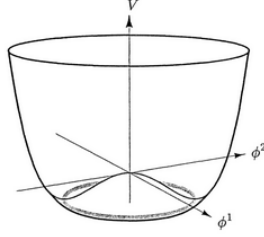


Figure 1.3: The so-called "Mexican Hat" potential driving the spontaneous symmetry breaking

Lagrangian. Its Lagrangian writes :

$$\mathcal{L} = \partial^\mu \phi^* \partial_\mu \phi - V(\phi^* \phi) \quad (1.2)$$

$$V(\phi^* \phi) = \mu^2 \phi^* \phi + \frac{\lambda}{2} (\phi^* \phi)^2 \quad (1.3)$$

where the potential  $V(\phi^* \phi)$  (the so-called "Mexican Hat" potential) describes the phenomenon that will spontaneously break the  $U(1)$  symmetry, and may be visualized in fig. 1.3. This potential was first used in particle physics in [33], and in order to induce the symmetry breaking one need to have  $\mu^2 < 0$  and  $\lambda > 0$ . It has a minimum at  $|\phi_0| = v = \sqrt{\frac{-\mu^2}{\lambda}}$  which is degenerate in the sense that any phase rotation will also give a minimum, i.e. the ensemble of minima is defined as  $\{ve^{i\alpha} \mid \alpha \in \mathbb{R}\}$ . As a complex field  $\phi$  actually embeds two degrees of freedom, which may be written as  $\phi = \phi_1 + i\phi_2$  and we chose that the true minimum of our theory corresponds to  $\phi_0 = v + i \times 0$ . Although choosing this particular projection of the field clearly is a convenient choice, it is equivalent to any other of the points of the minimum as they may be reached by a simple phase rotation, which is not observable. As  $v$  corresponds to the true minimum of the theory it is the point around which it should be developed, which we express through  $\phi = (v + \sigma(x)) + i\pi(x)$  and this gives the following Lagrangian :

$$\mathcal{L} = C + |\partial^\mu \pi(x)|^2 + |\partial^\mu \sigma(x)|^2 + 2\mu^2 \sigma^2 - \lambda(\pi^2 \sigma^2 + 2\pi^2 v \sigma) - \frac{\lambda}{2}(\sigma^4 + \pi^4 + 4v\sigma^3) \quad (1.4)$$

where  $C$  corresponds to a calculable constant that has no impact on physics. The first two derivatives are identified as the kinetic terms for the two degrees of freedoms, and the third term is the mass term for the  $\sigma$  (of mass  $\sqrt{-2\mu^2}$ ) but there is no mass term for the  $\pi$ . The following terms are corresponding in particular to interactions between the fields  $\pi$  and  $\sigma$ , and to self-interactions of  $\sigma$  with itself. With respect to the figure 1.3 the  $\sigma$  corresponds to lateral excitations of the field where it is actually  $|\phi|$  that is modified, and this requires energy to go against the rise of the potential. The massless  $\pi$  corresponds to a movement of the phase, that does not need energy as all the points at a given  $|\phi|$  but different phase are equivalent.

The existence of this massless "Goldstone" boson is completely general, and was first inferred in [33], following the work of Nambu [30, 31], although it was only rigorously demonstrated in [32]. For every spontaneously broken continuous symmetry there should be a massless scalar boson, but these bosons have never been observed. Here we have only considered global symmetries, and the Brout-Englert-Higgs mechanism [35–38] is a way to effectively evade this problem for gauge symmetries.

### 1.2.3 The Brout-Englert-Higgs mechanism and the associated scalar boson

Now we consider a local  $U(1)$  symmetry, where we need to add terms describing the gauge field into the Lagrangian, which is done as follows :

$$\mathcal{L} = -\frac{1}{4}(F_{\mu\nu})^2 + |D_\mu\phi|^2 - V(\phi) \quad (1.5)$$

where the first term correspond to the kinetic term for the gauge field, that will not be considered further below, the second term is the covariant derivative is  $D_\mu = \partial_\mu + ieA_\mu$  and the potential  $V(\phi)$  has the same functional form than in the previous subsection. The gauge field  $A_\mu$  is a real vector field while  $\phi$  still describes complex scalar field. This Lagrangian is invariant under the following transformation :

$$\phi(x) \rightarrow e^{i\alpha(x)}\phi(x) \text{ and } A_\mu(x) \rightarrow A_\mu(x) - \frac{1}{e}\partial_\mu\alpha(x) \quad (1.6)$$

If we define  $\phi = (v + \phi_1) + i\phi_2$ , the covariant derivative may be developed into :

$$|D_\mu\phi|^2 = |\partial_\mu\phi|^2 + e^2A_\mu A^\mu(v^2 + 2v\phi_1 + \phi_1^2 + \phi_2^2) - 2eA_\mu(-v + \phi_1)\partial^\mu\phi_2 + \phi_2\partial_\mu\phi_1 \quad (1.7)$$

and using the gauge transformation defined in eq. 1.6, we can chose a gauge where  $\phi$  is real hence  $\phi_2(x) = 0$  for every  $x$ , which gives :

$$|D_\mu\phi|^2 = |\partial_\mu\phi_1|^2 + e^2v^2A_\mu A^\mu + e^2A_\mu A^\mu(2v\phi_1 + \phi_1^2) \quad (1.8)$$

The second term correspond to a mass term for the gauge field  $A_\mu$  and the last term will give rise to interactions such as  $h \rightarrow AA$  and  $hh \rightarrow AA$ . The full Lagrangian is therefore written :

$$\mathcal{L} = -\frac{1}{4}(F_{\mu\nu})^2 + |\partial_\mu\phi_1|^2 + e^2v^2A_\mu A^\mu + e^2A_\mu A^\mu(2v\phi_1 + \phi_1^2) - 2\lambda v^2\phi_1^2 - \frac{\lambda}{2}(\phi_1^4 + 4v\phi_1^3) \quad (1.9)$$

and this includes kinetic and mass terms for both  $\phi_1$  and  $A_\mu$ , as well as interactions between these two fields. The masses of these two fields are determined by the vacuum expectation value  $v$  and the gauge coupling constant (for the mass of  $A$ ) or  $\lambda$  (for the mass of  $\phi_1$ ). The second part of the scalar field,  $\phi_2$ , has completely disappeared from the theory : there is not anymore a mass-less Goldstone boson. However the corresponding degree of freedom still exists. A mass-less vector boson only has transverse polarizations, because there is no rest frame for such a particle, while when it is massive it acquires a longitudinal polarization which is a third degree of freedom for this field. The mass-less Goldstone boson is "eaten" by the former mass-less gauge field which in turn acquires a third polarization component and its mass. In the high-energy regime, where the gauge symmetry is unbroken, the longitudinal component of the gauge boson behaves as the Goldstone boson it has absorbed [59, 60]. The remaining  $\phi_1$  corresponds to an actual massive particle that we call the BEH boson.

### 1.2.4 Application to the electro-weak symmetry group

Now we will consider the full electro-weak theory [40, 44, 61], which is described by the  $SU(2)_L \times U(1)_Y$  local symmetry [18, 41]. The Higgs field is now described by a complex vector field with two components, which is defined as follows :

$$\phi(x) = \frac{1}{\sqrt{2}} \begin{pmatrix} \phi^+ \\ \phi_0 \end{pmatrix} = \frac{1}{\sqrt{2}} \begin{pmatrix} \phi_1 + i\phi_2 \\ \phi_3 + i\phi_4 \end{pmatrix} = \begin{pmatrix} 0 \\ \frac{1}{\sqrt{2}}(v + \chi(x)) \end{pmatrix} \quad (1.10)$$

where the last equality comes from an adequate choice of gauge. The Lagrangian for the Higgs sector of the theory [62] is written

$$\mathcal{L} = |D_\mu \phi|^2 - \mu^2 \phi^\dagger \phi - \lambda (\phi^\dagger \phi)^2 \quad (1.11)$$

Here the covariant derivative corresponds to the  $SU(2)_L \times U(1)_Y$  part of the theory and is expressed as  $D_\mu \phi = (\partial_\mu - igW_\mu^a T^a - ig' \frac{Y}{2} B_\mu) \phi$ , where the  $T_i$  are linked to the Pauli matrices as  $T_i = \frac{1}{2} \sigma_i$ ,  $W_\mu^a$  corresponds to the triplet of gauge bosons associated to  $SU(2)_L$  and  $B_\mu$  the gauge boson associated to  $U(1)_Y$ .  $g$  and  $g'$  are the coupling constants of  $SU(2)_L$  and  $U(1)_Y$ , respectively. By construction  $\phi$  has an hyper-charge 1, and as we are interested at what happen in the vacuum we may take  $\phi = v$ . If we were to consider the full theory with the physical excitation  $\chi(x)$  too, we would describe the same mass term and mass generation mechanism, and would only add the interactions between the gauge and scalar bosons, which we are not interested in at this point. If we define  $W_\mu^\pm = \frac{W_\mu^1 \mp iW_\mu^2}{\sqrt{2}}$  this gives :

$$D_\mu \phi = -\frac{i}{2\sqrt{2}} \begin{pmatrix} g' B_\mu + gW_\mu^3 & \sqrt{2}gW_\mu^+ \\ \sqrt{2}gW_\mu^- & g' B_\mu - gW_\mu^3 \end{pmatrix} \times \begin{pmatrix} 0 \\ v \end{pmatrix} \quad (1.12)$$

which translates into :

$$|D_\mu \phi|^2 = \frac{v^2}{4} g^2 W_\mu^+ W_\mu^- + \frac{v^2}{8} (g' B_\mu - gW_\mu^3)^2 \quad (1.13)$$

The first term in the previous equation corresponds to the mass term for the  $W^\pm$  bosons and this indeed describes the physical  $W^\pm$  bosons, whose mass is  $m_W = \frac{vg}{2}$ . The last term is interpreted as giving the mass to the  $Z^0$  boson and can be written :

$$\frac{1}{2} \frac{v^2 (g^2 + g'^2)}{4} Z^\mu Z_\mu \text{ with } Z_\mu = \frac{g}{\sqrt{g'^2 + g^2}} W_\mu^3 - \frac{g'}{\sqrt{g'^2 + g^2}} B_\mu \quad (1.14)$$

where the physical particle corresponds to the  $Z^0$  mass eigenstate. The other eigenstate is the photon and has a zero mass. These two eigenvectors are orthogonal to each others and are aligned with  $\begin{pmatrix} g' \\ g \end{pmatrix}$  for the photon and  $\begin{pmatrix} g \\ -g' \end{pmatrix}$  for the Z boson. In eq. 1.13, developed in term of the physical eigenstates we can determine that the mass of the Z is of  $m_Z = \frac{1}{2} v \sqrt{g^2 + g'^2}$ . If we define the angle  $\theta_W$  as  $\cos\theta_W = \frac{g}{\sqrt{g^2 + g'^2}}$  and  $\sin\theta_W = \frac{g'}{\sqrt{g^2 + g'^2}}$ , the change of basis from  $(W_\mu^3, B_\mu)$  to  $(A_\mu, Z_\mu)$  is done with the following rotation :

$$\begin{pmatrix} Z_\mu \\ A_\mu \end{pmatrix} = \begin{pmatrix} \cos\theta_W & -\sin\theta_W \\ \sin\theta_W & \cos\theta_W \end{pmatrix} \times \begin{pmatrix} W_\mu^3 \\ B_\mu \end{pmatrix} \quad (1.15)$$

Furthermore the mass of the W and Z bosons are linked by the following relation :

$\rho = \frac{M_W^2}{M_Z^2 \cos^2 \theta_W} = 1$ . This comes from the "custodial" symmetry which is an approximate symmetry of the scalar sector of the theory in the limit where the hyper-charge coupling vanishes. In this case where  $g' \rightarrow 0$ , there is an approximate  $SU(2)_L \times SU(2)_R$  global symmetry in the scalar sector of theory, and  $M_W \rightarrow M_Z$  which is due to the fact  $Z_\mu = W_\mu^3$  i.e. there is no mixing with the  $U(1)_Y$  gauge field, and the three gauge fields of  $SU(2)_Y$  have the same properties. This approximate symmetry is broken both by the hyper-charge coupling and by the existence of a mass of the fermions, although it is only slightly broken and is valid at tree order. There are actual deviations of  $\rho$  that can happen at loop-order which were tested at LEP. The results have been proven to be close to the Standard Model expectation. More generally this means that deviations of the coupling of the Higgs boson to the Z boson should have equivalent deviations in its couplings to the W bosons.

We must also include a mechanism to generate the mass of the fermions, as the most naive mass term  $m\bar{\psi}\psi$  is not gauge invariant. We denote the left-handed doublets describing fermions fields  $L$  and the right-handed singlets  $R$ . The doublet may describe every quarks and leptons in there left-handed form, while the right-handed singlets do not include neutrinos. For a given generation this gives the following additional part of the Lagrangian :

$$\mathcal{L} = -\lambda_e(\bar{L}_{e,\nu_e}\phi R_e + \bar{R}_e\phi^\dagger L_{e,\nu_e}) - \lambda_u(\bar{L}_{u,d}\phi R_u) - \lambda_d(\bar{L}_{u,d}\phi R_d) \quad (1.16)$$

where the  $\lambda_i$  are called the Yukawa coupling. If we focus only on one particle, for instance the electron, and develop the Higgs potential around its minimum we find :

$$\mathcal{L} = -\lambda_e(\bar{L}_e R_e + \bar{R}_e L_e)\left(\frac{v + \chi}{\sqrt{2}}\right) = -\frac{v\lambda_e}{\sqrt{2}}\bar{e}e - \frac{\lambda_e\chi}{\sqrt{2}}\bar{e}e \quad (1.17)$$

where the first term is a mass term for the electron, that acquire a mass of  $\frac{\lambda_e v}{\sqrt{2}}$  and the second term describes the  $h \rightarrow ee$  interaction.

It should be noted that the mass generation mechanism is very different between vector bosons and fermions. For vector bosons it comes directly from the existence of the gauge field, through the covariant derivative, and the value of the vector boson mass and of its couplings to the Higgs boson is entirely defined in term of the vacuum expectation value and of the gauge coupling constant, which gives a strong predictive power to this mechanism. For the fermionic part of the theory, the Yukawa terms are not determined by any particular structure of the theory and are added by hand. In particular the Yukawa couplings  $\lambda_i$  are free parameters that may be adjusted to fit the observation, and they do not carry any predictive power on the mass of the particle.

### 1.2.5 Elitzur's theorem

It was shown in [63] that it is actually not possible to spontaneously break a local (or gauge) symmetry. Although this demonstration is explicitly done on a lattice and no equivalent demonstration exists for a theory in continuous space-time, it is believed that it also holds for this latter case. In fact, the BEH mechanism breaks a remnant global symmetry. The gauge symmetry itself needs to be broken in the Lagrangian to allow for the computation

of observables and to conduct the renormalization program. The action with which the observables are computed is  $\mathcal{S}_{eff} = \mathcal{S} + \mathcal{S}_{g.f.} + \mathcal{S}_{ghost}$  where  $\mathcal{S}_{g.f.}$  corresponds to terms that are fixing the gauge in which we want to do the computation, and  $\mathcal{S}_{ghost}$  to counter-terms that ensures that the result of the computation is the same in every gauge, but at this point the actual gauge is explicitly fixed, which is properly explained in [64]. In the toy example of an  $U(1)$  symmetry where we imposed the scalar field to be real, the gauge is completely fixed by the choice of the phase (equal at 0), and this is explicitly breaking the symmetry at the level of  $\mathcal{S}_{eff}$ . For a complete physical model, after gauge fixing there may still be a remaining global symmetry with respect to one or several parameters, but not anymore with respect to the infinite number of parameters required to describe the local gauge change. The BEH mechanism is actually breaking this remaining global symmetry, which is a subgroup of the original local symmetry.

## 1.3 Higgs boson production and decays

### 1.3.1 Initial state and the parton distribution functions

#### General concept of Parton Distribution Functions

A proton is made of three valence quarks (two ups and one down) that are sensitive to the strong interaction therefore it cannot be considered as a static object. The three valence quarks are exchanging gluons between each other, and the splitting of these gluons creates virtual pairs of a quark and its anti-quark. These virtual particles are called the sea quarks and are very important in the description of proton collisions, as for instance the processes that are mainly initiated by heavy quarks can only be initiated by the sea quarks and are very sensitive to their modelling. For a given collision energy  $Q^2$  we can compute the probability to find a given parton carrying a given fraction of the proton momentum, which is represented by the Parton Distribution Functions (PDFs)  $f(x, Q^2)$ . The PDFs allow to split the calculation of a cross-section into two parts : the evolution of the proton content before the collision, which is a complicated process that involves low energy and large distance interaction that are sensitive to non-perturbative effects, and the partonic cross-sections that involves a well defined family of partons and high-energies, which may be computed in perturbative QCD. The factorization theorem brings these two pieces together and allows to compute the cross-section for the production of given phenomena in the scattering of two hadrons. It is expressed as follows :

$$\sigma(P_1, P_2) = \sum_{i,j} \int dx_1 dx_2 f_{i/h_1}(x_1, \mu_F^2) f_{j/h_2}(x_2, \mu_F^2) \hat{\sigma}_{i,j}(x_1 P_1, x_2 P_2, Q^2, \mu_F^2) \quad (1.18)$$

where :

- $f_{i,h_n}$  corresponds to the PDF of the parton  $i$  in the initial hadron  $n$
- $\hat{\sigma}$  corresponds to the partonic cross-section
- The factorization scale  $\mu_F$  corresponds to the energy scale that distinguish long and short distance physical processes, i.e. below this scale the physics is described by the PDFs while above it comes from perturbative QCD

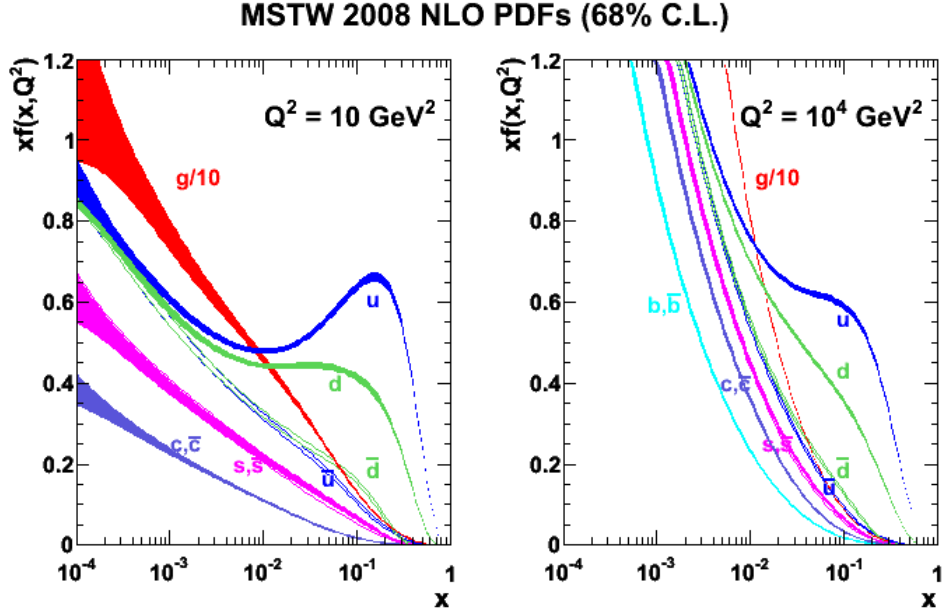


Figure 1.4: Parton distribution functions of the proton from the MSTW collaboration [70]

Furthermore this expression allows for the extraction of PDF sets from data, which is necessary as the non-perturbative component of the PDF cannot be evaluated from the theory, although we need a process that may be measured and for which the partonic cross-section is known at a sufficient order in perturbative QCD. The evolution of the PDF from the energy scale at which it is measured to the energy scale at which we need to evaluate it comes from the DGLAP equation [65–67] and requires the knowledge of functions that describe the splitting of incoming partons into several partons, in a regime where the outgoing partons are collinear to the incoming one. This has been derived up to NNLO in [68, 69], although the order at which the splitting are used in any computation need to match the order at which the partonic cross-section is used.

A typical result for the extraction of the PDFs is shown in fig. 1.4 and outlines some of the important features of PDFs. First the probability of finding a parton of a given family inside the proton diverges at low  $x$  as it corresponds to virtual partons with a low energy for which the splitting  $g \rightarrow q\bar{q}$  is more likely. The bulk of the momentum fraction of the proton is indeed carried by its valence quarks, and not by the sea. As the momentum transfer  $Q^2$  increases there are new quark families that have to be taken into account, as for instance the splitting  $g \rightarrow c\bar{c}$  is not allowed below  $Q = 2m_c$ . This effect is illustrated in fig. 1.4 by the absence of the bottom quark at low  $Q^2$  while it is not negligible at  $Q^2 = 10^4 \text{ GeV}^2$ .

### Most usual PDF sets

There are several collaborations that provide complete sets of PDFs, and they may differ by the methodology used to extract the PDF, the way the heavy quarks are handled within this extraction, the datasets they are considering and the way the uncertainties are handled. A proper review of all the existing PDF sets has been given in [71, 72] and in

the following only the few sets that are used the most in particle physics will be described. These PDFs are coming from the collaborations CTEQ [73, 74], MSTW [70] and NNPDF [75] and are now computed using NNLO fits. But these sets are under constant evolution and, in particular, have recently published updated versions of their results. These new versions will be used soon and include the additional informations provided by the LHC measurements.

These sets are determined by global analyses of the data provided by different experiments, coming either from the analysis of hadronic collisions or from deep-inelastic scattering. The different collaborations have chosen different sets of data, but they have also different prescriptions to extract information on the PDFs from the data. CTEQ and MSTW are using explicit parametrizations of the PDFs and the global fit extracts the free parameters that are involved in these parametrizations, and this is the most widespread method used by the different collaborations. NNPDF uses a method that is conceptually very different, as the parametrization of the PDFs actually comes from Neural Networks (NN) that are trained with the measurements provided by the experiments. This allows to have much more free parameters in the model, and not to be biased by the explicit choice of parametrization of the PDF. But this approach is still not completely unbiased as the NN that gives the best fit has to be determined, and this may create a dependency on the prescription used for this. All of these three PDF sets are using a different treatment of the heavy quark flavour, and also of whether  $\alpha_s$  is taken as an external parameter or is determined during the fit of the PDF.

### Combining PDF uncertainties : PDF4LHC and METAPDF

Each of the collaboration provides several PDF sets, a central one and several that are here to represent the various uncertainties on the PDF, which have to be propagated as an uncertainty on the cross-section of the processes we are interested in. Most collaborations determine this uncertainty from the variation of the  $\chi^2$  around the best-fit of the PDFs, but NNPDF uses an approach based on pseudo-datasets that are generated by randomly drawing each of the input variable within its error band, taking into account the correlation between the different variables in the randomization. As the central value and errors of the PDFs provided by the different collaborations do not necessarily agree, they have to be combined. During the Run 1 of the LHC this had been done using the PDF4LHC recommendation [76], which advocates the use of the envelope of the error bands defined by NNPDF2.0, CTEQ6.6 and MSTW2008. Unfortunately the agreement between these three PDF sets is poor, which is illustrated by fig. 1.5, and this is artificially increasing the impact of the PDFs on the uncertainty on cross-sections which is of the order of  $\approx 7\%$  for the production of  $gg \rightarrow H$ . These three collaborations have produced updated versions of their PDF sets that include LHC data and improvements regarding their methodology, and these improved PDF sets are expected to be used for the Run II of the LHC. The compatibility between the different sets improved a lot, as is illustrated in fig. 1.6, and the error it would imply on the cross-section is of the order of  $\approx 3\%$ . This is still not sufficient as it requires to produce a lot of different Monte-Carlo samples, and does not allow to implement the correlation of the PDF uncertainty with other effects in the statistical model. To solve this issue the META-PDF approach [77] has been developed and could be used for the Run II. All the PDF sets are estimated at a low energy scale  $Q_0$  at which they

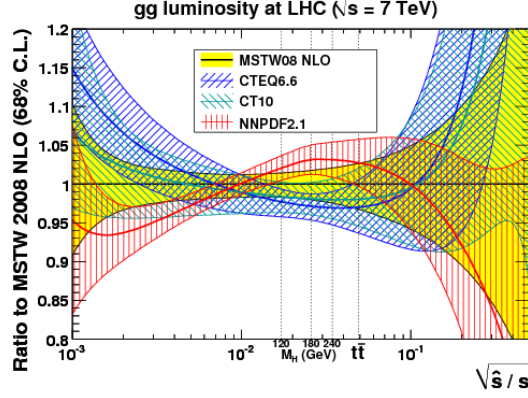


Figure 1.5: Ratio of gluon luminosity between the different PDF sets used during the Run 1 of the LHC and MSTW2008 [78]

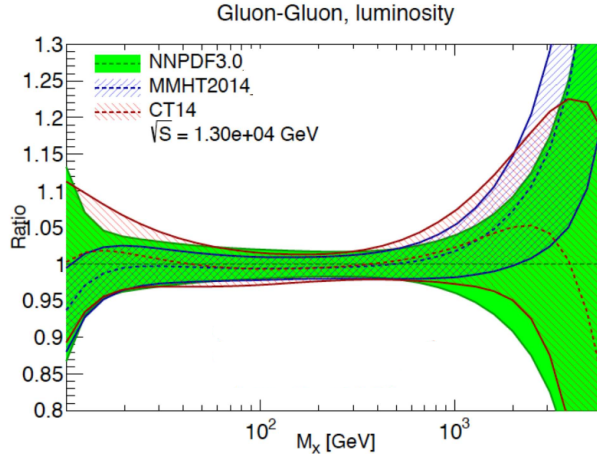


Figure 1.6: Ratio of gluon luminosity between the different PDF sets will be used in the Run 2 of the LHC and NNPDF3.0 [72, 79]

are combined, and the evolution of the PDFs to any other energy scale  $Q^2$  is determined by the DGLAP equations. At the same time the uncertainty on the combined PDF is determined, and as the different collaborations may have estimated the same uncertainties in a different way, this combination allows to sizeably reduce the number of PDF sets that have to be evaluated to determine the error bands.

### 1.3.2 Standard Model Higgs boson production channels

There are several processes that may produce a Higgs boson at the LHC, and their corresponding Feynman diagrams are all shown in fig. 1.7. All of these processes will be further described below. They have different initial states and may be used to probe different properties of the Higgs boson. The precision at which their cross-sections have been computed also differs from one process to another. The values of these cross-sections are shown in fig. 1.8 for several values of  $m_h$  in the region around the value of  $m_h$  at which the Higgs boson was found [42, 43].

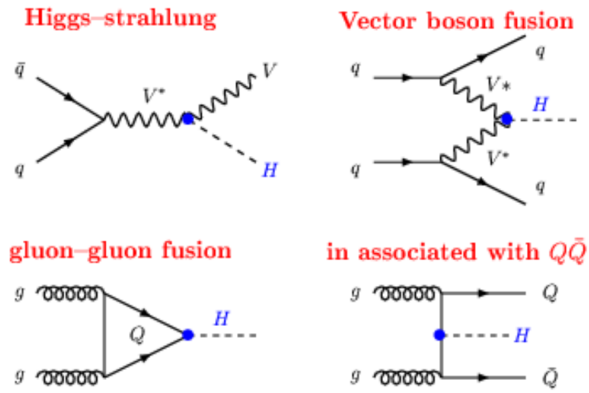


Figure 1.7: Most important diagrams for the production of a Higgs boson in proton collisions [80]

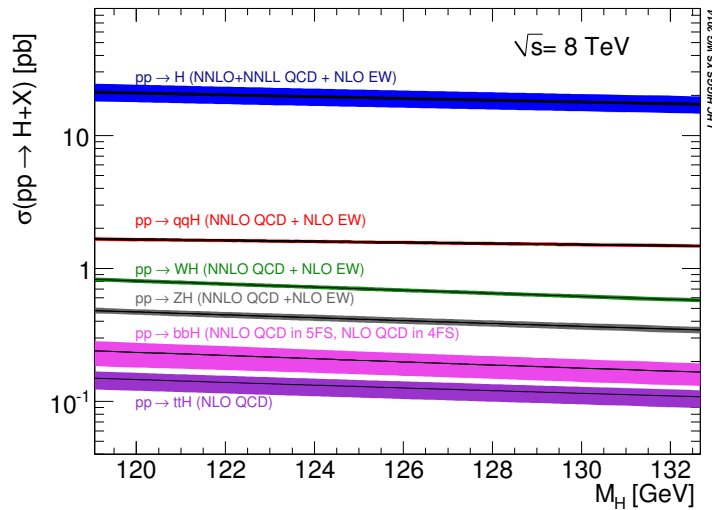


Figure 1.8: Cross-section of the most important production modes of the Higgs boson in  $p - p$  collisions [81]

## The gluon fusion process

The dominant production mode at the LHC corresponds to the gluon fusion process, whose leading order is already at one-loop and happens through a triangle of heavy quarks (mainly top quarks, but the bottom also contributes). The fact that it is not a tree order diagram is compensated by the very high gluon luminosity of the LHC, and this channel corresponds to  $\approx 86\%$  of the total Higgs boson production cross-section for  $m_H = 125$  GeV and  $\sqrt{s} = 8$  TeV, at which the official cross-section of the gluon fusion process, that is provided by the LHC Higgs cross-section working group [81], is of 19.27 pb. Computations for this process can use HRes 2 [82, 83] which gives the state-of-the-art computation of the Higgs boson transverse momentum. The LHC Higgs cross-section working group implements a calculation [84] that is exact at NNLO in  $\alpha_s$  and at NLO in  $m_{top}$  and  $m_b$ , with large logarithm resummation up to NNLL with exact finite quark mass dependence and electroweak corrections. The impact of higher order effects may be estimated by the variation of the QCD renormalization scale  $\mu_R$  between  $\frac{m_h}{2}$  and  $2 \times m_h$ , and within HRes 2 it gives an error of  $\pm 7\%$  for  $m_h = 125$  GeV. Recently first results of the computation of the  $gg \rightarrow H$  cross-section at  $N^3LO$  in  $\alpha_s$  have been published [85] for  $m_h = 125$  GeV, and a complete paper describing this result and including an evaluation of the electro-weak and finite mass effects is expected to be published soon. The central value of this  $N^3LO$  cross-section is 19.47 pb at  $\sqrt{s} = 8$  TeV and the uncertainty coming from QCD scale variation decreased to  $\pm 3\%$ . At 13 TeV this cross-section will be of  $44.31 \pm 2.64\%$ . As this channel offers the biggest statistics it will have the biggest weight in most precision measurements, and therefore it needs to be accurately described. During the Run 1 the Monte-Carlo that was used the most for  $gg \rightarrow H$  in ATLAS was PowHeg [86, 87], complemented by Pythia [88] for the parton shower, but this does not accurately describes the  $p_T$  spectrum of the produced Higgs boson, which may have an impact on some observables such as the signal strength. To improve this description a reweighting of the  $p_T$  spectrum was developed in [89]. Furthermore PowHeg only implements the  $gg \rightarrow H$  cross-section at NLO in  $\alpha_s$  which gives a cross-section that is lower, as there are less channels with additional partons produced in the loop than at NNLO or  $N^3LO$ , and a k-factor of  $\approx 1.45$  is applied as an additional weight to the PowHeg events to rescale its cross-section to the most up-to-date cross-section. Furthermore this channel provides so far the most powerful way to probe the coupling of the Higgs boson to the top quark, although it assumes that there is no new particle in the gluon fusion loop as they may also modify the cross-section or various distributions.

## Vector Boson Fusion and Higgstrahlung processes

The second most important production mode is the Vector Boson Fusion (VBF), that is initiated by two quarks that both emit either W or Z bosons that interact together to produce a Higgs boson. In this process the final state corresponds to a Higgs boson that is central and two outgoing quarks that are in the forward region. The study of this production channel allows for the determination of the couplings of the Higgs to the W and Z bosons, and the distribution of the two outgoing quarks may be sensitive to the determination of the CP-admixture of the Higgs boson. In importance the following production process is the Higgsstrahlung where an off-shell W or Z boson is produced in the s-channel and emits a Higgs boson. In principle all of these bosons could be off-shell

but at the LHC the dominant production comes from the case where the vector boson in the s-channel is off-shell and there is an on-shell Higgs boson and an on-shell vector boson in the final state. The best Monte-Carlo to compute both of these processes is HAWK [90] that includes the full NLO computation for both the QCD and electro-weak parts. For  $m_h = 125$  GeV and  $\sqrt{s} = 8$  TeV this gives a cross-section for the VBF process of 1.578 pb with an uncertainty of  $\pm 0.2\%$  from the QCD scale variation, while for Higgsstrahlung it is of 0.7046 pb  $\pm 1\%$  for WH and 0.4153 pb  $\pm 3\%$  for ZH. These errors are smaller than for the gluon fusion process because the leading order diagrams are at tree level and are quarks-induced, and also because this corresponds to electro-weak processes.

### Associated productions with quarks

The last production mode that has been considered at the LHC corresponds to the associated production with heavy quarks, where two initial gluons are both splitting into a  $q\bar{q}$  pair and among those four quarks two will interact to form a Higgs boson while the two other will be present in the final state and hadronize. If they are measured these associated productions will allow to directly measure the Yukawa coupling of the Higgs boson to a given family of quark, which is especially important for the top quark as there is no other way to directly probe its coupling to the Higgs boson, and given its mass it may probe physics at an higher energy scale. The best tool to study the  $t\bar{t}H$  production channel is PowHel [91] that implements the NLO matrix elements and is interfaced with a parton shower. At  $m_h = 125$  GeV and  $\sqrt{s} = 8$  TeV the  $t\bar{t}H$  cross-section is 0.1293 pb  $^{+3\%}_{-9\%}$  and the  $b\bar{b}H$  cross section is 0.2035 pb  $^{+10\%}_{-15\%}$ . Despite the small Yukawa coupling of the bottom with respect to the top, its PDF is much larger than the one of top which explains why its cross-section is still sizeable.

### 1.3.3 Standard Model Higgs boson decays

As the several decay channels of the Higgs boson progressively open when its mass increases, its total decay width increases too as this may be seen in fig. 1.9. Far from the threshold, for the bosonic channels the partial width evolves as  $\propto m_H^2$  while for fermionic channels it goes as  $m_H$ . In the standard model and in the low mass region where the Higgs boson has been discovered the total decay width of the Higgs boson is very small,  $\Gamma_h = 4.07 \pm 1.6$  MeV for  $m_h = 125$  GeV [92] and will be hard to measure unless it is sizeably broadened by new physics effects. We will discuss below the evolution of the branching ratios of the various channels, that are presented in fig. 1.10, as well as the main analyses that may be carried within these channel and their advantages and drawbacks, are presented. All the partial widths can be computed with the program HDECAY [93], which can be complemented by PROPHECY4F [94] for the specific case of  $h \rightarrow VV^* \rightarrow 4l$ , where  $V = W$  or  $Z$ .

#### Main decay channels

In the low mass region where the Higgs boson has been discovered, the main decay channel is by far the  $h \rightarrow b\bar{b}$  channel whose branching ratio is higher than 50%. This dominance comes from the fact that it is the heaviest particle whose decay channel is completely

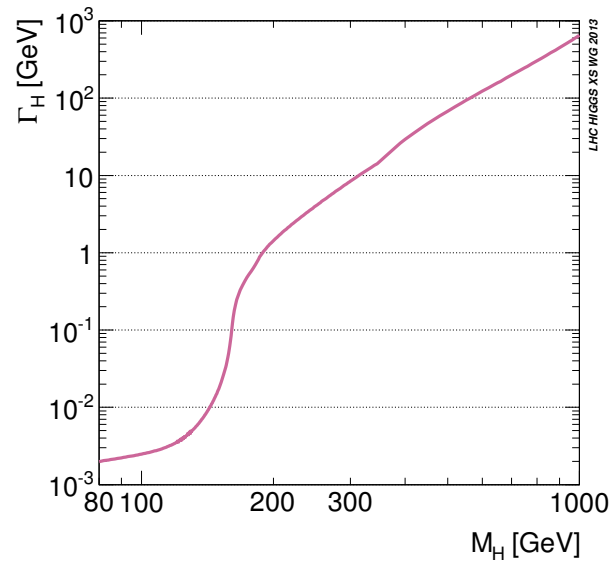


Figure 1.9: Total decay width of the Standard Model Higgs boson as a function of its mass [81]

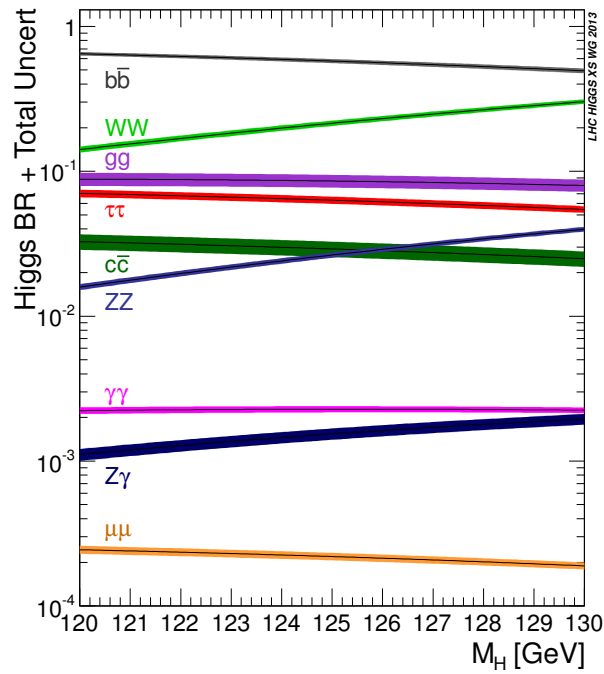


Figure 1.10: Branching ratio for the various Higgs boson decay channels as a function of the Higgs boson mass [81]

opened. It suffers from a high-level of background, and the fact that  $b$  quarks are hard to identify although specific algorithms exist to try to infer from the properties of a jet whether it has been initiated by a  $b$ -quark [95, 96]. Only the associated production channels may be studied, as requiring events where e.g. a  $Z$  boson or a  $t\bar{t}$  pair is observed allows to sizeably improve the signal-to-noise ratio, but it also implies a sizeable loss on signal statistics. Its observation is the most powerful way to measure the Yukawa coupling of the Higgs boson to the bottom quark.

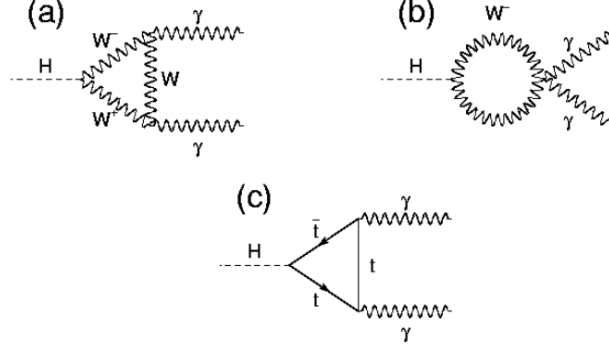
In this region the next decay channel in terms of branching ratio is the  $h \rightarrow W^{(*)}W^{(*)}$  channel that is steeply rising as it comes closer to its kinematical threshold ( $2m_W$ ). It is still below the  $b\bar{b}$  channel in terms of branching ratio, because one of the two vector bosons has to be off-shell which makes this decay less likely. Depending on the decays of the two  $W$  bosons this channel may be well identified, for instance if the two  $W$  decay into  $W \rightarrow l\nu$  where  $l = e, \mu$  it is possible to have a clean selection of  $h \rightarrow WW$  events. To this extent this channel is well suited to measure associated production modes or cross-sections as it has a reasonable statistics and background, but it is a very poor channel to study the lineshape of the resonance as all the decay channels involve either neutrinos or quarks, that have a poor energy resolution.

The  $h \rightarrow \tau\tau$  decay channel is so far the most promising channel to measure the Yukawa coupling of the Higgs boson to a lepton. The  $\tau$  energy resolution is poor as the decay of a  $\tau$  involves two neutrinos, and effectively this means that the  $Z \rightarrow \tau\tau$  decay is still a background at the measured value of  $m_h$ , which needs to be properly taken into account as it is the biggest background. It is not possible to precisely determine the properties of the lineshape of the Higgs boson in this decay channel, because of the poor energy resolution of the  $\tau$  leptons, but it is also possible to measure cross-sections and associated productions, as well as CP-admixture parameters.

The  $h \rightarrow gg$  and  $h \rightarrow c\bar{c}$  are not expected to be studied at the LHC. They suffer from the same issue of background than the  $h \rightarrow b\bar{b}$  channel but their statistics is much smaller and it is not yet possible to efficiently identify jets from gluon or charm quarks. However it was suggested that quarkonium interferometry [97] could constrain in a modest way the  $h \rightarrow c\bar{c}$  coupling using  $h \rightarrow J/\Psi\gamma$ , which has been done in [98].

## Precision channels

Most of the precision measurements, especially those related to the lineshape of the Higgs boson, are carried by two high-precision channels. The first one is the  $h \rightarrow ZZ^* \rightarrow 4l$  channel and the second the  $h \rightarrow \gamma\gamma$  channel, that will be further described below. There are several final topologies for the  $h \rightarrow ZZ^*$  decay channel but only the one with electrons and muons gives a reasonable precision, although this imply a loss in statistics as the branching ratio of both the  $Z$  bosons has to be taken into account. But the irreducible background for this process is also very low and its signal-to-noise ratio is higher than 2, with a very good resolution because electrons and muons are very well measured. It may be used to measure the lineshape parameter of the Higgs boson, differential cross-section, CP-admixture parameters, ect. But it is less promising than other decay channel for the measurement of associated production processes as it has a very low statistics hence require extensive datasets to do such studies, which are not yet available. As for the  $h \rightarrow WW^*$  channel the branching ratio of  $h \rightarrow ZZ^*$  rises steeply with  $m_h$ , for the same reason that


 Figure 1.11: Leading-order Feynman diagrams for the  $h \rightarrow \gamma\gamma$  decay [102]

it is getting closer to its kinematical threshold.

### The $H \rightarrow \gamma\gamma$ decay channel

The  $h \rightarrow \gamma\gamma$  decay channel is already loop-induced at leading order, because the photons are massless and therefore cannot directly couple to the Higgs boson, therefore it has a very small branching ratio, with  $BR(h \rightarrow \gamma\gamma) = 2.28 \cdot 10^{-3} \pm 4.9\%$  for  $m_h = 125$  GeV. There are three different diagrams contributing to this decay at leading-order, all of which are shown in 1.11, and the dominant contribution comes from the W loop. In terms of the couplings of the Higgs boson to the different particles (normalized to the SM couplings) the  $h \rightarrow \gamma\gamma$  branching ratio varies as [99]

$$BR(h \rightarrow \gamma\gamma) \propto 1.59\kappa_W^2 + 0.07\kappa_t^2 - 0.66\kappa_W\kappa_t \quad (1.19)$$

where the first two terms are coming from the W and top loops and the last from the interferences between the two, which are destructive and have a sizeable impact. Within the Standard Model and around the value of  $m_h$  where the Higgs boson has been discovered, this branching ratio is at its maximal value and is approximately constant. As it is a loop-induced process its branching ratio is very sensitive to new physics scenarios where heavy particles may appear in this loop. This channel was studied since the beginning of the prospects at LHC, on Monte-Carlo by C. Seez and J. Virdee [100], and then in ATLAS [101].

## 1.4 Defining masses and widths

### 1.4.1 General definition

The concept of the mass of a given particle is deeply connected to its propagation in the vacuum, as for instance a mass-less particle will never be at rest, independently of the frame in which it is studied. If we denote  $\phi(x)$  the operator that represent the state of a field at the space-time position  $x$ , the amplitude for this field to propagate from  $x$  to  $y$  is  $\langle 0|\phi(x)\phi(y)|0 \rangle$  where  $|0 \rangle$  corresponds to the vacuum, and its analytical formulation may be determined from the equation of motion. For a scalar field in a theory without interaction, the motion is described by the Klein-Gordon equation that is expressed as :

$$\partial_\mu\partial^\mu\phi + m^2\phi = 0 \quad (1.20)$$

where the operator  $\phi$  describing the field state and the wave function of a given particle of this field are mistaken for one another. The solution for this differential equation can be computed and is given by :

$$\langle 0 | [\phi(x)\phi(y)] | 0 \rangle \sim \int \frac{d^4 p}{(2\pi)^4} \frac{i}{p^2 - m^2} e^{-ip(x-y)} \quad (1.21)$$

In this expression, the term  $\frac{1}{p^2 - m^2}$  is called the propagator for the field  $\phi$  and represents the whole dynamic of its propagation in a free field theory. When we are interested in complete theory we need to consider the potential impact of virtual particles on the propagation of our initial particle. To do so the concept of one-particle irreducible diagrams is defined as the ensemble of the diagrams that can not be split in two by a removing a single line corresponding to the propagator, to which we associate the amplitude  $-iM^2(p^2)$ . Then the full propagation can be expressed in a diagrammatic way as is done in fig. 1.12. In terms of amplitudes, the first of these diagrams corresponds to the propagator of the free theory, while the other ones are corresponding to a factorization of the free theory and of  $-iM^2(p^2)$ . If we define  $m_0$  the mass we would have in the equivalent free theory, this corresponds to the following geometrical series [103] :

$$\frac{i}{p^2 - m_0^2} + \frac{i}{p^2 - m_0^2} (-iM^2) \frac{i}{p^2 - m_0^2} + \dots = \frac{i}{p^2 - m_0^2 - M^2(p^2)} \quad (1.22)$$

and the denominator may be expressed as  $p^2 - m_0^2 - Re(M^2) - iIm(M^2)$ , hence the pole of the propagator which defines the actual value of the mass is  $m^2 = m_0^2 + Re(M^2)$  and is slightly displaced with regard to the bare mass of a non-interacting theory. The last term  $Im(M^2(p^2)) = Im(M^2(p \rightarrow p)) = m\Gamma$  can be used to define the decay width of the particle, and can be expressed as the decay probability by the use of the Optical Theorem [103], which is done as follows :

$$Im(M^2(p^2)) \sim \frac{1}{2} \sum_f \int d\Pi_f |\mathcal{M}(p \rightarrow f)|^2 \quad (1.23)$$

where the sum runs over all possible final states for the decay of this particle. Hence the decay width is

$$\Gamma = \frac{1}{2m} \sum_f \int d\Pi_f |\mathcal{M}(p \rightarrow f)|^2 \quad (1.24)$$

If the different decay branching ratios are stable over the width of the resonance, the only possible variation of the width with respect to the collision energy  $\sqrt{s}$  comes from the evolution of the phase space over which the integral is done. This is typically the case for the W and Z bosons where the only variation with respect to a standard relativistic Breit-Wigner is the fact that the term involving the width is replaced by  $m\Gamma \rightarrow m\Gamma(s) = \Gamma_0 \times \frac{s}{m}$  [104] where  $\Gamma_0$  corresponds to the width at the pole. For a narrow resonance the phase space do not vary over the width of the resonance and the width may be taken as a constant. In the general case the full dependence of the decays on  $\sqrt{s}$  should be considered, which potentially includes opening of new decay channels, and it is a much harder task.

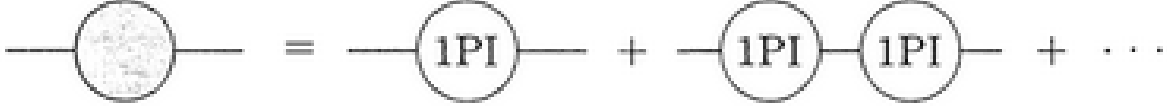


Figure 1.12: Sum of all possible amplitudes that correspond to the propagation of a given particle in a complete theory [103]

### 1.4.2 The Complex Pole Scheme

A possible prescription to define the propagator of the Higgs boson is the Complex-Pole scheme [105] which uses the full structure of the pole in the complex plane. This was developed for the search for a high-mass Higgs boson, and has since been used to develop the study of the off-shell event yield in the  $h \rightarrow ZZ^*$  and  $h \rightarrow WW^*$  decay channels in ATLAS [106] and CMS [107]. One of its main interest with respect to a Standard Breit-Wigner formula is that it does not factorize the production, propagation, and decay of the Higgs boson, as this factorization is not expected to hold in the off-shell regime. This prescription has the advantage of taking into account the variation of the position of the pole with respect to  $\sqrt{s}$  beyond leading-order, and does not assume that the width is constant at the on-shell width. This is needed as the mass goes higher as the opening of the decay into four fermions translates into a non-negligible three-loop component of the Higgs self-energy, that has to be taken into account.

### 1.4.3 The Breit-Wigner formula

Now we consider the case where the resonance is sufficiently narrow so that the decay branching ratios does not vary. We have seen before that the corresponding propagator writes  $\mathcal{M}(s|m, \Gamma) = \frac{i}{s - m^2 - im\Gamma}$  which translates into a probability distribution of :

$$f(s|m, \Gamma) = \frac{k}{(s - m^2)^2 + m^2\Gamma^2} \quad (1.25)$$

which is the relativistic Breit-Wigner function, where  $k$  is a normalization factor. In the low width regime this is equivalent to :

$$\frac{k}{((\sqrt{s} - m)(\sqrt{s} + m))^2 + m^2\Gamma^2} \approx \frac{k}{4m^2(\sqrt{s} - m)^2 + m^2\Gamma^2} = \frac{k'}{(\sqrt{s} - m)^2 + \frac{\Gamma^2}{4}} \quad (1.26)$$

which is the non-relativistic Breit-Wigner that was initially published in [108].

## 1.5 Interferences between signal and background processes in $gg \rightarrow h \rightarrow \gamma\gamma$

### 1.5.1 General description of the phenomenon

In quantum mechanics two processes that bring a given system from an identical initial state to another identical final state can interfere among each other, either destructively

or constructively. This needs to be taken into account properly, which is achieved by summing the amplitudes of the two processes. The case of the  $gg \rightarrow h \rightarrow \gamma\gamma$  channel is a perfect representation of this problem, as is outlined in fig. 1.13 where  $qg \rightarrow Hq$  is also included (the contribution of  $q\bar{q} \rightarrow Hg$  being neglected). There is a sub-part of the irreducible continuum background that is gluon-initiated and where the two photons are appearing through a box of light quarks. If we denote  $A_{gg \rightarrow h}$  and  $A_{h \rightarrow \gamma\gamma}$  the two vertices involved in the production and the decay in  $gg \rightarrow h \rightarrow \gamma\gamma$ ,  $A_{cont}$  the amplitude of the  $gg \rightarrow \gamma\gamma$  background and treat this resonance as a relativistic Breit-Wigner, the full amplitude for  $gg \rightarrow \gamma\gamma$  is written :

$$A_{gg \rightarrow \gamma\gamma} = A_{cont} - \frac{A_{h \rightarrow \gamma\gamma} A_{gg \rightarrow h}}{\hat{s} - m_h^2 + im_h \Gamma_h} \quad (1.27)$$

and the cross-section may be determined from  $|A_{gg \rightarrow \gamma\gamma}|^2$ . Most usually  $|A_{cont}|^2$  and  $|A_{signal}|^2$  are computed separately and the interference term neglected. It may be computed as :

$$\delta = \frac{A_{cont} A_{h \rightarrow \gamma\gamma}^* A_{gg \rightarrow h}^*}{\hat{s} - m_h^2 - im_h \Gamma_h} - \frac{A_{cont}^* A_{h \rightarrow \gamma\gamma} A_{gg \rightarrow h}}{\hat{s} - m_h^2 + im_h \Gamma_h} \quad (1.28)$$

and as the two terms in this equation are complex conjugate this may be simplified to

$$\delta = -\frac{2}{(\hat{s} - m_h^2)^2 + m_h^2 \Gamma_h^2} \text{Re}((\hat{s} - m_h^2 - im_h \Gamma_h) A_{cont}^* A_{h \rightarrow \gamma\gamma} A_{gg \rightarrow h}) \quad (1.29)$$

$$= -\frac{2}{(\hat{s} - m_h^2)^2 + m_h^2 \Gamma_h^2} ((\hat{s} - m_h^2) \text{Re}(A_{cont}^* A_{h \rightarrow \gamma\gamma} A_{gg \rightarrow h}) \quad (1.30)$$

$$+ m_h \Gamma_h \text{Im}(A_{cont}^* A_{h \rightarrow \gamma\gamma} A_{gg \rightarrow h})) \quad (1.31)$$

This is a partonic cross-section for a given value of the out-going  $m_{\gamma\gamma}$ , and if we want to have the impact of interferences on the total-cross section we need to compute the convolution with the PDFs and to integrate over the whole mass peak. Now if we are to consider the vicinity of the mass peak we can assume that the product of amplitudes  $A_{cont}^* A_{h \rightarrow \gamma\gamma} A_{gg \rightarrow h}$  is a constant, in which case the term that involves the real part (corresponding to eq. (1.30)) would cancel out in the total cross-section as it is odd around the pole, while the term involving the imaginary part (eq. (1.31)) would not, as it has the same  $\hat{s}$  dependence that the resonance itself. This term therefore gives an overall decrease of the  $gg \rightarrow \gamma\gamma$  cross-section if there is a relative phase between the signal and background amplitudes. The decrease of cross-section was first considered in [109] at LO where it was estimated to be negligible, but this was only due to an accidental cancellation of the effect at LO. It was first computed at NLO in [110], where a decrease of  $\approx 2\%$  on the  $gg \rightarrow H \rightarrow \gamma\gamma$  yield was computed. At this point the real part of the interference term had not been considered, because it does not have an impact on the cross-section, but its impact on the line-shape was not negligible and was first computed in [111] at LO. The NLO computation was provided later in [112] (following partial computations in [111, 113]), where a shift of  $\approx 70$  MeV was advertised (for the standard model), coming from the distortion of the line-shape that may be seen in fig. 1.14. Furthermore it was noticed in [112] that because of the different dependence of the interference term and of the signal on the width of the boson and on the couplings, this variation of the line shape may be used to constrain the Higgs boson width independently from the couplings, although ideally the two should be done in a global simultaneous fit.

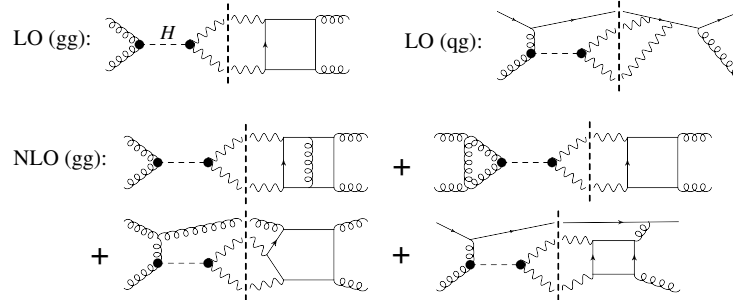


Figure 1.13: Representative diagrams for interference between the Higgs boson resonance and the continuum in the diphoton channel. They correspond to  $gg \rightarrow \gamma\gamma$  at NLO and  $qg \rightarrow \gamma\gamma q$ . The Higgs boson signal resonant amplitudes correspond to the diagrams on the left of the dashed vertical lines, and their time evolution goes from left to right, the background  $gg \rightarrow \gamma\gamma$  (or  $qg \rightarrow \gamma\gamma q$ ) amplitudes to the right diagrams, and their time evolution is inverted [112]

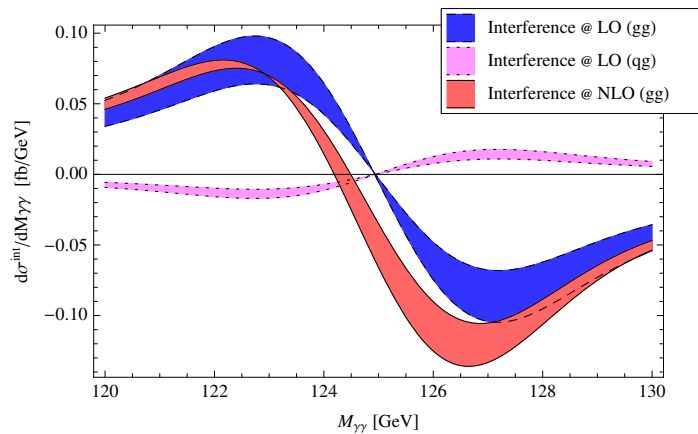


Figure 1.14: Di-photon invariant mass spectrum generated by the interference term between the Higgs boson signal and its background in the  $gg \rightarrow \gamma\gamma$  process (and  $qg \rightarrow \gamma\gamma q$  [112])

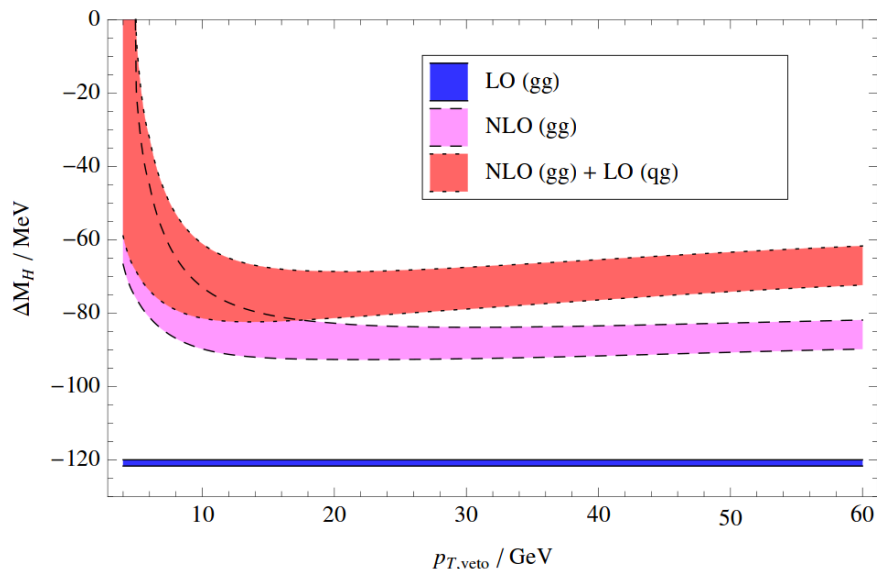


Figure 1.15: Higgs boson mass shift induced by the interferences between the  $gg \rightarrow H \rightarrow \gamma\gamma$  and its background  $gg \rightarrow \gamma\gamma$ , versus the jet-veto  $p_T$  cut [112]

## 1.5.2 State of the art computation for the gluon fusion

The most recent and complete computation of the interference term, for both the real and imaginary part, comes from [112]. The knowledge of the interference term at a given order in perturbation theory requires the knowledge of both the signal and interference amplitudes at the same order, which is limited by the background computation that exists only at NLO [114]. As may be seen in fig. 1.13 there are a few subtleties as, for instance, one can see that the tree Born graph corresponding to the background  $qg \rightarrow \gamma\gamma q$  can interfere with the signal  $qg \rightarrow qH$  (see top right graph of fig. 1.13) and is labelled "LO (qg)". The same signal graph  $qg \rightarrow qH$  can interfere (at higher  $\alpha_S$  order) with a background box diagram  $qg \rightarrow \gamma\gamma q$  (bottom right graph of fig. 1.13). This computation includes diagrams with a real emission of one additional gluon or quark, and had been carried out in the context of an Higgs effective-field theory where the top loop is not resolved. The result may be seen in fig. 1.14, where the term denoted "LO (qg)" corresponds to terms that are at tree-level and have a zero total cross-section. At leading order the phase between the signal and background amplitudes crosses 0 at the pole, as seen in the blue and pink curves of fig. 1.14, while at NLO this zero is slightly shifted. The inclusive mass shift was estimated to be of 70 MeV in [112] but it uses a simplified Gaussian signal model. At LO the mass shift was estimated to be of  $\approx 120$  MeV in [111]. In [112] a jet veto is simulated by throwing away events with  $p_{T,j} > p_{T,veto}$  and  $|\eta_j| < 3$ . The apparent Higgs boson mass shift is shown in fig. 1.15 versus the jet-veto  $p_T$  cut. One sees again that the mass shift for inclusive production (large  $p_{T,veto}$ ) is around 70 MeV at NLO (red curve), significantly smaller than the LO prediction of 120 MeV.

In fig. 1.16 the jet veto is removed and the mass shift is studied versus the lower cut on the Higgs boson transverse momentum,  $p_T > p_{T,H}$ . Since LO  $gg \rightarrow \gamma\gamma$  has zero  $p_T$ , it does not contribute to fig. 1.16, which only receives contribution from real radiation diagrams. The blue line receives contribution from the bottom left diagram of fig. 1.13.

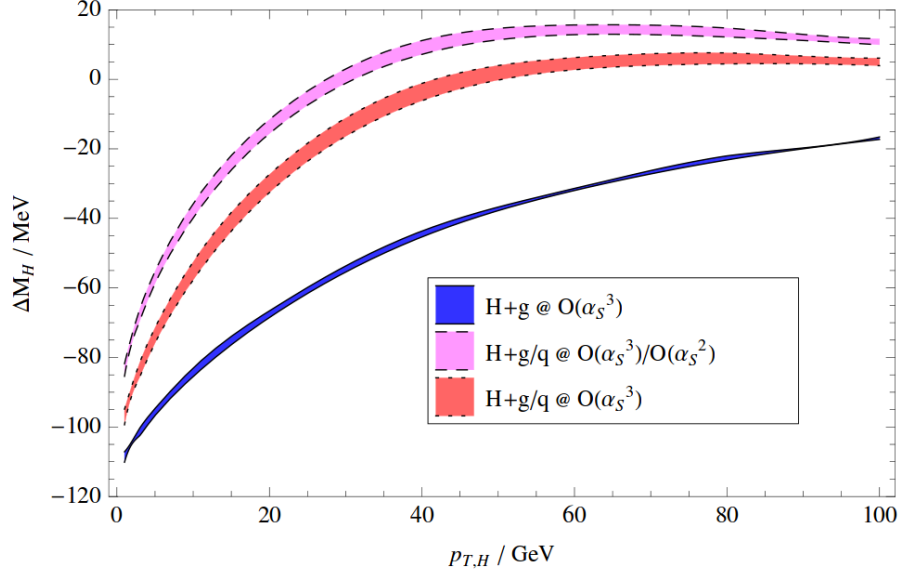


Figure 1.16: Higgs boson mass shift induced by the interferences between the  $gg \rightarrow H \rightarrow \gamma\gamma$  and its background  $gg \rightarrow \gamma\gamma$ , versus the lower cut on the di-photon  $p_T$

The top right diagram is then added in order to get the magenta line, and the final result (red line) is then obtained by summing the bottom right diagram.

Despite the improvement of the  $p_T$  spectrum brought by the inclusion of the one-parton emission in the matrix elements, the description of the  $p_T$  spectrum generated by the interference term is still poor and not well under control. This may be complemented by a Parton Shower, as will be seen later (in section 6.3), but this implies a sizeable uncertainty. An improved computation that includes soft-gluon resummation is currently being carried out and is expected to be published by the end of this year [115]. No computation of the interferences at an order higher than NLO is expected, because the  $gg \rightarrow \gamma\gamma$  box component of the background is not known to a better accuracy, and is not expected to be computed in the near future.

### 1.5.3 State of the art computation for the other production mechanisms

As the interference term is determined by the signal and irreducible background amplitudes we can naively think that the relative variation of the cross-section they are implying vary as the inverse of  $\frac{S}{B}$ . In this picture we expect the interference in the non gluon-fusion decay channel to be smaller, because the background is much smaller. Recently a first computation of the interference term at LO in  $h(\rightarrow \gamma\gamma) + 2$  jets has been published [116], which includes the interference between the VBF production channel and its background, but also the interference between gluon fusion plus two jets and its background, as well as the interference between the VBF and gluon-fusion plus two jets channels (this last graph corresponds to two gluons radiated by two initial quarks). This last part is expected to be very small [117–120]. A few examples of some of the representative Feynman diagrams for this interference term are shown in fig. 1.17. In [116] the computation of the interference

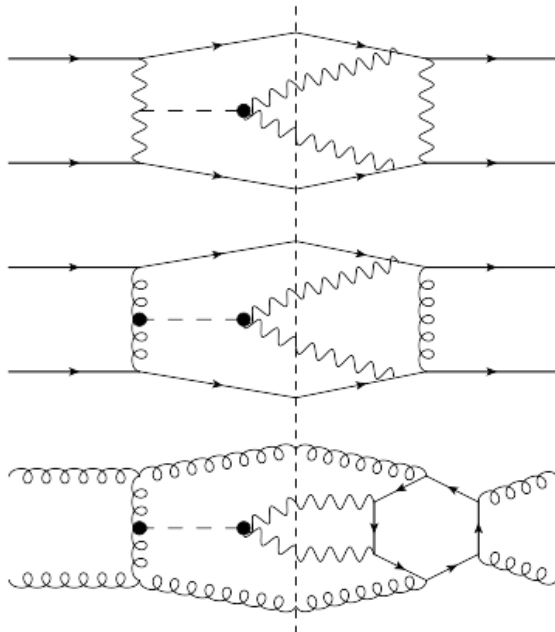


Figure 1.17: Some Feynman diagrams contributing to the interference term in the  $h+2j$ ets modes [116]

term in  $h(\rightarrow \gamma\gamma) + 2j$  is done only at LO, and only the real part of the interference has been considered (i.e. only the shift of the mass is studied, and not the impact on the cross-section). The mass shift from gluon-fusion plus two jets and the one from VBF have opposite signs, and with suitable selection cuts they largely cancel. For instance if the only cuts that defines the VBF category is on the dijet invariant mass, at  $M_{jj} > 400$  GeV, the two contributions are summing up to give a mass shift of  $\delta m_h = -6$  MeV. For the worst case studied in [116] the mass shift in  $h + 2j$  is as high as 20 MeV, which should be compared to the 70 MeV of [112] as it uses the same fit methodology. The work presented in [116] is very recent and has not been used in an experimental collaboration yet, as the Monte-Carlo tools that were used there are not yet public.

So far there is no computation of the interference for the other channels (e.g. VH). A new version of MadGraph5\_aMC@NLO [121] is currently under development and is expected to include the possibility to automatically generate NLO matrix elements to processes that are loop-induced at LO, and a module to separately generate signal, background and interferences [122]. This would allow to perform all the studies required to determine the interference terms in every production and decay channel, although still at NLO (potentially complemented by a parton shower program) therefore the issue of the control of the  $p_T$  spectrum description may still remain.

## 1.6 Overview of the methods setting limits on the Higgs boson width

An increase of the width of the BEH boson directly connects to new physics, as it can happen only through an enhancement of the Higgs couplings to one (or several) particle(s), which are very well defined in the SM once the quark masses are known, or by the existence of a new decay channel, or of new particle inside the loops that are involved in several decay channels. Therefore this would be a key parameter to measure, but it is also a measurement that is impossible to perform at the current colliders. Several methods have been developed to infer an upper limit on this parameter, and they all have advantages and drawbacks, as it is not possible to obtain soon a strong limit in a model-independent setting. This thesis will present a method to set a direct upper limit on the Higgs boson width, using a direct fit of the reconstructed di-photon lineshape in part 5. Some of the other methods that have been developed to determine upper limits on the Higgs boson width are explained below (a lower limit is given in [123]).

### 1.6.1 Width from off-shell events in $h \rightarrow ZZ^*$ and $h \rightarrow WW^*$

Due to the increase of the branching ratio of the  $h \rightarrow ZZ^*$  decay channel at  $m_h = 2 m_Z$  there is a sizeable contribution of the region at  $m_{4l} > 2 m_Z$  to the total Higgs signal cross-section, and this region actually amounts to  $\approx 15\%$  of the Higgs signal yield in the  $h \rightarrow 4l$  decay channel. This effect is illustrated by fig. 1.18. The cross-section in this off-shell region only depends on the Higgs boson couplings to the incoming and out-going particle as  $\sigma_{offshell} \propto (\kappa_{in}\kappa_{out})^2$  while, on-shell, the cross-section is a function of the width of the Higgs boson, as  $\sigma_{onshell} \propto \frac{(\kappa_{in}\kappa_{out})^2}{\Gamma_h}$ , hence from the ratio of these two cross-section it is possible to infer an upper-limit on the Higgs boson width, as long as the interferences between signal and background that are not negligible in the off-shell region are treated properly. This idea was initially developed in [124] (see also [123] where the analysis has been generalized to include anomalous couplings of the Higgs boson to two electroweak bosons), and has been used both in CMS [107] and ATLAS [106] where it has also been extended to the  $h \rightarrow WW^*$  decay channel. In ATLAS, after the combination of all the channels, the 95% C.L. observed limit on the width is at  $\Gamma_h = 22.7$  MeV assuming that the background k-factor is the same than the signal, and using the  $CL_s$  technique described below, while in CMS, that uses only  $h \rightarrow ZZ^* \rightarrow 4l$  and  $h \rightarrow ZZ^* \rightarrow 2l2\nu$  the 95% C.L. limit is at  $\Gamma_h = 22$  MeV using the test-statistics  $\tilde{q}_T$  that will be described below (see paragraph 2.2.3).

As it has been presented above (look at the width  $\Gamma_h$ ), this analysis assumes that the couplings in the off-shell region are the same than on the mass-shell, but the couplings are running parameters and this is where the model-dependence of this method appears. Within the standard-model this running of the couplings is small, about  $\approx 5\%$  between  $m_h = 125$  GeV and 300 GeV, and would have a negligible impact on the current upper limit on the width, that is at  $\approx 5\Gamma_{SM}$ . Within a given model the running can be computed and implemented in the analysis to give another estimate of the width, that would be specific to this model. The only quantities that may be interpreted in a model-independent approach are the on-shell and off-shell signal strength  $\mu_{off/on}$ , and a model dependency is injected

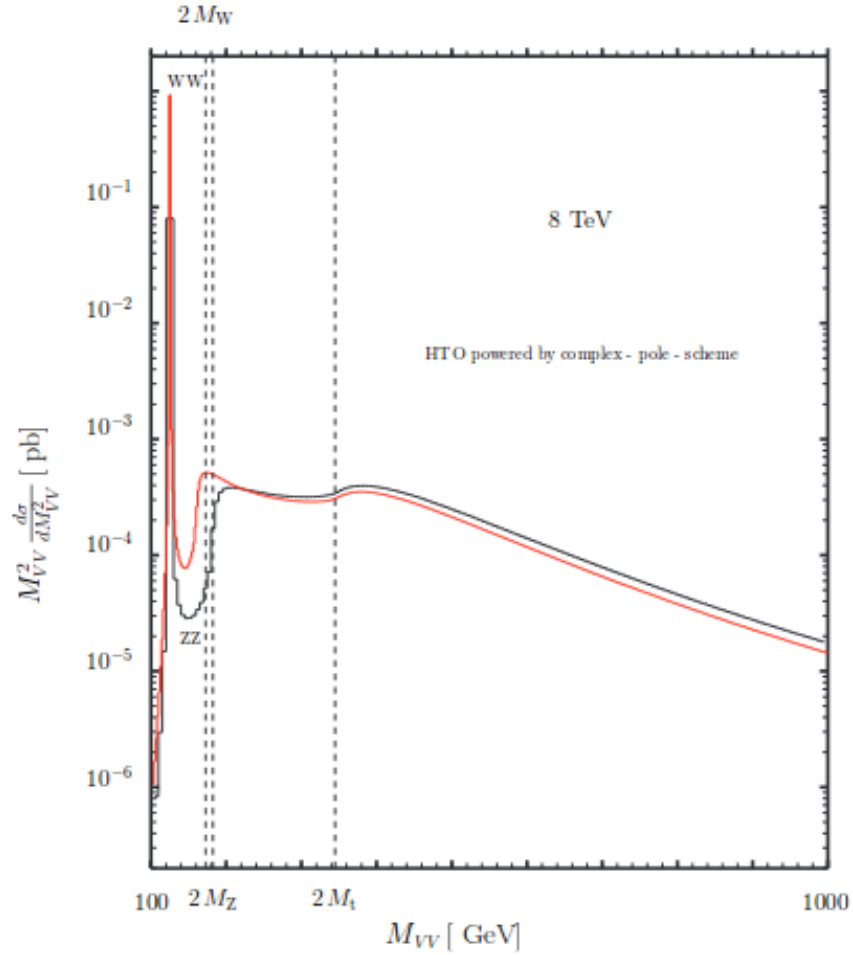


Figure 1.18: Invariant mass distribution generated by a Higgs boson in  $gg \rightarrow VV$ , with  $V = W$  (red curve) or  $Z$  (black curve) for  $m_h = 125 \text{ GeV}$  [125]

from the moment they are combined and interpreted as an information on the width. Therefore this upper-limit on the width should be seen more as a consistency check of the Standard-Model as it is not clear that a measurement by this method of a "width"  $\Gamma \neq \Gamma_{SM}$  would be connected to the width itself or to the couplings, although these two quantities are correlated. Such a scenario was developed in [126] where the addition of a light scalar in the gluon-fusion loop was able to sizeably modify the Higgs boson width without modifying  $\mu_{off/on}$ . Furthermore in the  $h \rightarrow ZZ^* \rightarrow 4l$  the off-shell region is defined up to  $m_{4l} = 1$  TeV and may receive contributions from a new physics sector at the TeV-scale that has not yet been discovered, which could also have a sizeable impact on this result. Examples are the presence of additional Higgs bosons [127] or anomalous  $h \rightarrow ZZ^*$  couplings [128].

## 1.6.2 Width from Higgs boson couplings combination

In the context of the Higgs combinations produced by ATLAS [99, 129] and CMS [130], whose initial aim is to determine the couplings of the Higgs boson to different particles, few scenarios (with some hypothesis) can be developed in order to set an upper limit on the Higgs boson width. It is impossible, without assumptions, to constrain the width as any increase of the width can be absorbed, keeping the rate constant, in an increase of the couplings. The rate  $i \rightarrow H \rightarrow j$  is given by, assuming all the coupling modification factors

have a common value  $\kappa$ ,  $rate_{i,j} = \frac{\kappa^4 \sigma_i^{SM} \Gamma_j^{SM}}{\kappa^2 \Gamma_{tot}^{SM} + \Gamma_{new}}$  and it is invariant if  $\kappa = \frac{1}{\sqrt{1-BR_{new}}}$  [127].

The most simple of these scenarios assumes that all the couplings to SM particles are at their SM value ( $\kappa_i = 1$ ), but that there is an additional decay channel to a state that is either invisible (in the sense that it does not interact with the detector) or undetected (in the sense that no specific analysis is searching for this final state). Within the combination all the probability amplitudes for a process that starts in a state  $i$  to end in a state  $f$  through a Higgs boson are proportional to  $\kappa_i \kappa_f$ , and the width may be expressed as

$\Gamma_h(\kappa_j, BR_{i,u}) = \frac{\kappa_h^2(\kappa_j)}{1 - BR_{i,u}} \Gamma_h^{SM}$ , where  $\kappa_h^2(\kappa_j)$  is equal to the sum of the scaled partial decay

widths to SM particles [131]. Once the  $\kappa_{i,j}$  are fixed to 1 (except for those corresponding to loops,  $\kappa_\gamma$ ,  $\kappa_{\gamma Z}$  and  $\kappa_g$ ) this benchmark model yields a measurement of the width of  $\frac{\Gamma_h}{\Gamma_h^{SM}} = 1.03_{-0.03}^{+0.13}$  in ATLAS, but it is also very model dependent as there is no modified couplings with respect to the Standard Model, except in the loops. For instance this implies that the minimal possible value of  $\Gamma_h$  is its SM value, when  $BR_{i,u} = 0$ .

A second method uses the unitarity constraint in vector-boson scattering to add the external constraint that  $\kappa_V < 1$ , which is valid in a wide class of models, in particular in all models with multiple Higgs doublets [70, 132–136], but is not valid in general as the unitarity conservation may come from a different mechanisms [137]. One then makes a fit with the ten free parameters  $\kappa_W$ ,  $\kappa_Z$ ,  $\kappa_t$ ,  $\kappa_b$ ,  $\kappa_{tau}$ ,  $\kappa_\mu$ ,  $\kappa_\gamma$ ,  $\kappa_g$ ,  $\kappa_{Z\gamma}$  and  $BR_{i,u}$ . Within

this framework a measurement of the Higgs boson width is obtained, at  $\frac{\Gamma_h}{\Gamma_{h,SM}} = 0.64_{-0.25}^{+0.40}$  for ATLAS.

The last benchmark model is similar except that  $BR_{i,u} = 0$ . This also allows to give

a more powerful measurement of the width, at  $\frac{\Gamma}{\Gamma_{SM}} = 0.64^{+0.31}_{-0.25}$  for ATLAS. Additional scenarios can be found in [129].

### 1.6.3 Higgs boson width at future colliders

At  $e^+e^-$  colliders the measurement of the beam energy allows for a measurement of the parameters of the line-shape of a resonance produced in the s-channel, that is much more precise than what would be obtained with an energy measurement provided by the detector itself, and for instance this is what allowed a precise measurement of the  $Z^0$  boson mass and width at LEP [138]. At LEP, this good measurement of the beam energy was achieved by resonant depolarization of the beam [139], but it was only possible up to a beam energy of  $E_{beam} = 60$  GeV due to the depolarization induced by synchrotron radiations, and for the FCC-ee electron-positron collider that is under study [140] it will only be possible up to  $E_{beam} = 80$  GeV. This is not sufficient for the Higgs boson which is anyway produced by Higgsstrahlung and other methods will be needed at FCC-ee and at the ILC [141]. A direct scan of the line-shape that allows to determine the Higgs boson width, which would only be possible at a muon collider [142, 143], where, for a luminosity of  $\approx 1 fb^{-1}$  a precision on the width of 0.15-0.45 MeV can be obtained. Therefore an indirect method has been developed and reported in [144], where the relatively pure sample of Higgs boson produced in  $e^+e^- \rightarrow Z^* \rightarrow ZH$  events are tagged by triggering on a clean  $Z^0$  decay channel (e.g.  $Z \rightarrow \mu\mu$ ) and checking that the mass of the object that recoils against the  $Z^0$ , which can be determined using the energy-momentum conservation (the so-called recoil-mass method), is compatible with a Higgs boson. This allows to measure the total Higgsstrahlung cross-section which is proportional to  $\Gamma(h \rightarrow ZZ)$ , and  $\Gamma_h$  is then determined by measuring the branching ratio of  $h \rightarrow ZZ^*$  within this pure Higgsstrahlung sample,  $BR(h \rightarrow ZZ^*)$ .  $\Gamma(h)$  is then obtained as  $\Gamma_h = \frac{\Gamma(h \rightarrow ZZ^*)}{BR(h \rightarrow ZZ^*)}$ . This method still implies some model-dependence as the Higgsstrahlung production is at an energy scale of  $\sqrt{s} = 250$  GeV while the  $h \rightarrow ZZ^*$  decay is at an energy scale of  $\sqrt{s} = m_h \approx 125$  GeV, but it is not as important as for the off-shell method used at the LHC as the energy scale that is being probed does not go up to the TeV scale. The FCC-ee [140] and ILC [145] (see also [141, 146]) collaboration are claiming to be able to reach with this method a statistical precision of 1 to 2% on the width with their full expected datasets. Similar results for CLIC may be found in [147].

# Chapter 2

## Statistics for particle physics

### Contents

---

<b>2.1</b>	<b>Fundamental building blocks</b>	<b>45</b>
2.1.1	Probability density function and likelihood	46
2.1.2	Maximal likelihood estimation and inclusion of uncertainties	47
<b>2.2</b>	<b>Construction of confidence intervals</b>	<b>49</b>
2.2.1	Definition and choice of a test-statistics	49
2.2.2	General definition of a confidence interval	50
2.2.3	Particular cases used in particle physics	51
<b>2.3</b>	<b>Distribution of the test-statistics</b>	<b>54</b>
2.3.1	Distribution from pseudo-experiments	54
2.3.2	Asymptotic formulae for the significance	55
<b>2.4</b>	<b>Expected results : the Asimov dataset</b>	<b>56</b>

---

### 2.1 Fundamental building blocks

The goal of any particle physics analysis is to make an inference on the fundamental properties of the nature, either by determining one or several parameters that are ruling the theory (the parameters of interest,  $\vec{\mu}$ ), or by trying to determine whether a new physics phenomenon exists or not. Our only input to do this is a set of observable quantities  $\vec{x}_e$  that have been measured separately on  $N$  events by a detector, and this defines the ensemble  $\{\vec{x}_e\}$  from which we may try to do the inference. If both the underlying theory and the detector response are perfectly known (in particular, if the parameters of interest are fixed), we can determine the probability of observing this ensemble,  $P(\{\vec{x}_e\}|\vec{\mu})$ . If the observables are properly chosen it will vary with respect to the parameter of interest, and this property will be used to produce our statistical inference on  $\vec{\mu}$ . Formally, in the frequentist point of view, we cannot know the probability for a given set  $\vec{\mu}$  to be the true one, but only what is the probability of observing  $\{\vec{x}_e\}$  under the hypothesis that  $\vec{\mu}$  are the underlying true parameters. The actual true value of these parameters are a fixed, but unknown, state of

nature and this is what we actually want to evaluate. In the Bayesian point of view one may determine the probability for a given hypothesis  $\vec{\mu}_{test}$  to be the true one, which has to be viewed as the degree of belief we may have in this hypothesis. The current chapter will try to describe the necessary methods and tools to build a measurement and the related confidence intervals in the frequentist point of view. The Bayesian point of view will not be described further as it is not actually used in this thesis, but a proper review of this method may be found in [52].

### 2.1.1 Probability density function and likelihood

In the frequentist point of view the probability for the outcome of an experiment is seen as the limit frequency of drawing this particular outcome when the experiment is repeated an infinite number of time, i.e.

$$P(A) = \lim_{N \rightarrow \infty} \frac{N(A)}{N} \quad (2.1)$$

This has clearly some limitation : for instance the experiment needs to be reproducible, which is not always the case as for instance the Higgs boson exists in nature or not, and it is not possible to redo this experiment. Still this definition is the most objective definition of probability that may have a practical use.

This definition may be directly applied to cases were  $A$  takes discrete values, but it is not always sufficient in particle physics. For instance in a counting experiment the different values that  $A$  may take are corresponding to a given integer number of events, and for each possible number of events there is a well defined probability of observing this number. But we are often interested in the value of continuous variables, for instance the invariant mass of the di-photon system in  $h \rightarrow \gamma\gamma$  events has a continuous distribution and the knowledge of the probability of observing a given event with a given  $m_{\gamma\gamma}$  is of little use as it will always be an infinitesimal number. For those cases we define the Probability Density Function (PDF) of  $x$ ,  $f(x)$ , from the probability of observing this variable within the interval  $[x, x + dx]$ , which is done as follows :

$$P(x \in [x, x + dx]) = f(x)dx \quad (2.2)$$

In practical particle physics cases there are various ways of determining the PDF of a given observable. It can either come from an analytic formula, or from Monte-Carlo simulations, or from several data-driven techniques. In general it is possible to combine the information of several observables (denoted  $\vec{x}_e$ ) in the PDF, although it requires the knowledge of the correlations between the various variables. For a set of  $N$  events this may be translated into  $f(\{\vec{x}_e\}) = \prod_{e=1}^N f(\vec{x}_e)$ , and if the observed number of events  $N$  is also a random number fluctuating around an expectation of  $N_{exp}$  events this formula may be extended by a Poisson term, and becomes  $f(\{\vec{x}_e\}) = \frac{1}{N!} e^{-N_{exp}} (N_{exp})^N \prod_{e=1}^N f(\vec{x}_e)$ . The observables that are considered are chosen in such a way that their distribution depends on the parameter of interests of our problem, or are different between the two physical models that we are testing against each others, which means that the total probability for the  $N$  observation will depend on the parameters  $\vec{\mu}$  :  $f(\{\vec{x}_e\}) = f(\{\vec{x}_e\}|\vec{\mu})$ . In particle physics the ensemble  $\{\vec{x}_e\}$  corresponds to the data given by the experiment and is fixed,

while  $\vec{\mu}$  will be varied to test different values : this is called the likelihood function and may be denoted  $\mathcal{L}(data|\vec{\mu})$ . If it is complemented by a Poisson term it will be called an extended likelihood.

If we take the example of a search for a narrow resonance with an unknown cross-section  $S$  over a background with a cross-section  $B$ , we may use the reconstructed invariant mass  $m$  of the potential decay products in selected events. Then the parameter of interest is  $S$  and the per-event PDF is  $f(m|S) = \frac{1}{S+B}(Sf_S(m) + Bf_B(m))$ , where  $f_S$  and  $f_B$  are the PDF for  $m$  corresponding to the signal and background processes, respectively, and may be constructed using the Monte-Carlo or other techniques, such as a side-band fit for the determination of  $f_B$ . Then if  $N$  events have been observed the likelihood of this analysis is

$$\mathcal{L}(data|S) = \frac{1}{N!}e^{-(S+B)}(S+B)^N \prod_{i=1}^N \frac{(Sf_S(m_i) + Bf_B(m_i))}{S+B} = \frac{e^{-(S+B)}}{N!} \prod_{i=1}^N (Sf_S(m_i) + Bf_B(m_i)) \quad (2.3)$$

and depending on the value of  $\mathcal{L}(data|S)$  for different values of  $S$  we may derive an exclusion limit on  $S$ , or claim a discovery, following the methods that will be further described below.

It is also possible to use histograms to conduct the statistical analysis, in which case the likelihood to be used will be a binned likelihood, that is defined as the product of the Poisson distribution of each bin :

$$\mathcal{L}_{binned} = \prod_{i=1}^{N_{bins}} \frac{n_{i,obs}^{n_{i,obs}}}{n_{i,obs}!} e^{-n_{i,exp}} \quad (2.4)$$

where  $n_{i,exp}$  depends on  $S$  and  $B$ . It may be shown that it is equivalent to the unbinned likelihood whenever the dataset is sufficiently large [148] although it is preferable to use an unbinned likelihood whenever possible as the binned likelihood implies a loss of information that could improve the performance of the statistical analysis.

### 2.1.2 Maximal likelihood estimation and inclusion of uncertainties

Since the work of Fisher, which is summarized in [149], the most widespread and general method for parameter estimation is based on the maximal likelihood estimator. This method assumes that an unbiased model of the data is known as a function of the parameter of interest, and the best estimate of this parameter is estimated as being the value that maximizes the likelihood function, which is demonstrated for instance in [150]. Furthermore it may be shown that in the large sample limit the maximal likelihood estimate reaches the smallest possible variance that an unbiased estimator may achieve [150]. In general the use of  $-2\ln\mathcal{L}$  is preferred first because it is usually computationally easier, as it transforms the products into sums and the exponential into their components, but also because for a binned likelihood where all the bins are sufficiently populated it is strictly equivalent to minimize  $-2\ln\mathcal{L}$  and to minimize a  $\chi^2$ .

But there is an additional complication as the parameters of interest are not always sufficient to completely describe a proper model of the data. For instance in  $h \rightarrow \gamma\gamma$  the background is determined by a analytical fit of this background, and there are no

prior knowledge or external constraints for the parameters of the background function. These additional parameters, that are needed for the completeness of the model but do not correspond to our primary physical interest, are called the nuisance parameters and will be denoted  $\vec{\theta}$ . They increase the degrees of freedom of the fit so that the model may adjust itself to the observed data, and in turn this increases the statistical uncertainty on the estimate of the parameter of interest.

These parameters may also be used to represent the systematic uncertainties that are involved in any physics analysis. In that case we most usually have an external knowledge on the systematic uncertainty, as it may be estimated from another analysis, which will be called the auxiliary measurement. The central value of this measurement is generally applied to correct the data, which is typically the case of the energy scale that corrects the energy measured on data, or on Monte-Carlo to correct the expectation, which is for instance the case of the number of events which is corrected for the mis-modeling of the identification efficiency, among other effects. These uncertainties are applied by a slight modification of the expression of the parameter of interest in the full statistical model, which is done as follows :  $m_H \rightarrow m'_H = m_H K(\theta)$ , where  $K(\theta)$  is linked to the constraint brought by the auxiliary measurement and will be further described below. These auxiliary measurements themselves involve a statistical modelling and the measured value of  $\theta$  will fluctuate around its true value  $\tilde{\theta}$ , where  $\tilde{\theta}$  is called the global observable, and this could be described by the implementing the full likelihood of the auxiliary measurement in the statistical model of our main measurement. As this would in general over-complicate the analysis, the likelihood of the auxiliary measurement is usually approximated by a Gaussian, whose central value corresponds to the global observable and is most usually set to 0, and whose standard deviation corresponds to the size of the systematic uncertainty ( $\delta$ ) that is considered. For instance in the case of the impact of the energy scale uncertainties on the Higgs boson mass, this translates into :

$$m_H \rightarrow m'_H = m_H(1 + \delta\theta) \tag{2.5}$$

$$L(m_H, \theta) \rightarrow L'(m'_H, \theta) = L(m'_H, \theta) \times G(\theta|\tilde{\theta} = 0, \sigma = 1) \tag{2.6}$$

where  $G(\theta|a, b)$  is a Gaussian of mean  $a$  and standard deviation  $b$ . It is not always possible to use a Gaussian constraint, because there may be some parameters in the model for which a negative value is meaningless. This is for instance the case of the resolution of the peak, which is uncertain but can only be positive. In that case a Log-Normal constraint is used, as it forbids negative values for the uncertain parameter, and it is defined by modifying the definition of the resolution through :

$$\sigma_{res} \rightarrow \sigma'_{res} = \sigma_{res} \times e^{\theta\sqrt{\log(1+\delta^2)}} \tag{2.7}$$

and the Gaussian term  $G(\theta|\tilde{\theta}, \sigma = 1)$  is kept in the definition of the full likelihood. As the exponential cannot become negative the parameter  $\sigma_{res}$  will not become negative either, whatever the value of the nuisance parameter  $\theta$ . This constraint is also used for instance for efficiencies. There is a last kind of constraint which is the flat constraint, where the nuisance parameter may take any value within the " $\pm 1\sigma$ " error band with an equal probability, but will never take a value that is outside of this error band. This is especially adequate for theory uncertainties that actually corresponds to missing terms in the theoretical computation. These terms will have a given value that is unknown and for

which we only have an upper limit, and this does not correspond to the measurement of a parameter that fluctuates around a true value.

Once the full model is constructed it will depend on a set of nuisance parameters  $\vec{\theta}$  that may be fairly large, and on a few parameters of interest  $\vec{\mu}$ . The best estimate of the parameters of interest is determined by the absolute maximum of the likelihood with respect to every parameter, and the value of the parameters corresponding to this minimum will be denoted  $\hat{\vec{\mu}}$  and  $\hat{\vec{\theta}}$ . In the following part we will also be interested in determining the compatibility of different hypothesis on  $\vec{\mu}$  with our data, which will require the value of the likelihood for each of these hypothesis. It is determined as the maximum value with respect to the nuisance parameters for fixed values of  $\vec{\mu}$ , and the values of the  $\vec{\theta}$  corresponding to this conditional minimum will be denoted  $\hat{\vec{\theta}}$ .

## 2.2 Construction of confidence intervals

Although we have described the statistical tools that are needed to give the best estimate of a parameter, we do not yet have the necessary tools to build a complete statistical analysis as we also need to compute error bands, or to determine whether one of the statistical hypotheses we are testing may be rejected or not. The proper way to construct these intervals and obtain these informations will be described below. More details can be found in [52, 151, 152].

### 2.2.1 Definition and choice of a test-statistics

It is usually not possible to use the full ensemble of measured values  $\{\vec{x}_e\}$  to conduct the statistical inference, as its information needs to be condensed before it can be used. This is done using a test-statistics, that we denote  $t(\{\vec{x}_e\})$ , and that may be any function that maps the ensemble  $\{\vec{x}_e\}$  to a real number.

First we consider the context of hypothesis testing, where two different statistical hypotheses are tested against each others. The first hypotheses  $H_0$  is the "null" or "background" hypothesis, which in particle physics most usually corresponds to the Standard Model, while the second one  $H_1$  characterize the existence of new physics. The value of  $t(\{\vec{x}_e\})$  will differ between the two hypotheses that are being tested, and we may define a threshold  $k$  below which the null hypothesis is accepted, and above which the alternative hypothesis is accepted as being the true one. In each of these cases the second proposition is rejected. The region defined by  $t < k$  is called the acceptance region (for the null hypothesis) and  $t > k$  the critical region. The first important property of a test-statistics is its size (or significance level)  $\alpha$ , which is the probability that a dataset generated under the background hypothesis falls outside of the acceptance region. We can also define the power of the test which is given by  $1 - \beta$  where  $\beta$  is the probability of accepting the null hypothesis when the data has been generated under the alternative one, i.e. the power is the probability of accepting the alternative hypothesis when it is true. Usually  $\alpha$  is chosen by the physicist depending on the analysis he is conducting, and the most powerful test-statistics is searched for (i.e. the one having the highest power for a given significance level). Although there is no general answer to this problem the Neyman-Pearson lemma

[153] states that for two simple hypotheses that do not depend on any parameter, the most powerful test is the ratio of the likelihood of the two hypotheses  $\lambda = \frac{L(\{\vec{x}_e\}|H_1)}{L(\{\vec{x}_e\}|H_0)}$ .

There is no equivalent principle for composite hypothesis that are depending on several parameters, but an intuitive generalization may be done by using the *ratio of profile likelihoods*, where the likelihood of the two hypotheses are maximized with respect to all the parameters of the model [154], except for the parameters of interest that are used to label the hypotheses.

## 2.2.2 General definition of a confidence interval

In the context of parameter estimation, the same profile likelihood ratio may be used, but we do not have anymore a background-only hypothesis. What is used instead is a series of test statistics where different points are tested for the parameter of interest. At each of these points the tested value of the parameter of interest is taken has being the null hypothesis while the alternative hypothesis corresponds to the overall best-fit of the data,

i.e. the test statistics is  $\lambda(\vec{\mu}_{test}) = \frac{L(\{\vec{x}_e\}|\vec{\mu}_{test}, \hat{\vec{\theta}})}{L(\{\vec{x}_e\}|\hat{\vec{\mu}}, \hat{\vec{\theta}})}$ . This is called the profile likelihood ratio

(between the likelihood of the tested parameter of interest and the value of the likelihood at its maximum). The confidence interval corresponds to the ensemble of points  $\vec{\mu}$  where the tested null hypothesis is accepted. The rejected interval may be written symbolically as  $I = \{\vec{\mu}|P(\lambda > k|\vec{\mu}) < \alpha\}$  [151], and this is called the Neyman construction [155]. In order to construct this interval the distribution of the test-statistics needs to be known, and the construction of this distribution will be explained below.

In practice this construction is simple in the case of a single observable  $x$ . For every value of the parameter of interest  $\mu$ , the distribution of the observable is constructed and the acceptance interval containing a fraction  $\alpha$  of the possible values for the observable is constructed for every value of  $\mu$ . Then the actual value of the observable  $x_0$  is measured on an experiment, and every value of  $\mu$  for which  $x_0$  falls into the acceptance interval is considered to be a part of the confidence interval for  $\mu$ . This construction is summarized in fig. 2.1, but it is harder to visualize it when there is a complete ensemble of observables and several parameters. It is still possible to do it using the complete test-statistics  $t$ , like above, where  $t$  is a profile likelihood ratio. This generalization is sketched in [151].

The problem of the Neyman construction is that it is too general : there are several possible definitions of an acceptance interval of size  $\alpha$ , depending on its center. As we will see below the different definitions may have different use in a physics analysis, the most important property that they should all share being the coverage. In the method described, as the data fluctuates, the confidence interval on  $\mu$  should also be seen as fluctuating, the true value of  $\mu$  being fixed. The coverage of a confidence interval is the probability that it contains the true value of the parameter, and it should correspond to the confidence level that we want to reach. The Neyman construction has perfect coverage by construction, and its coverage is directly determined by the size of the test-statistics, but there are other ways to construct a confidence interval in which the coverage is not perfect. It is acceptable to have a coverage higher than expected but a lower coverage should be avoided as it would give an overly aggressive interval.

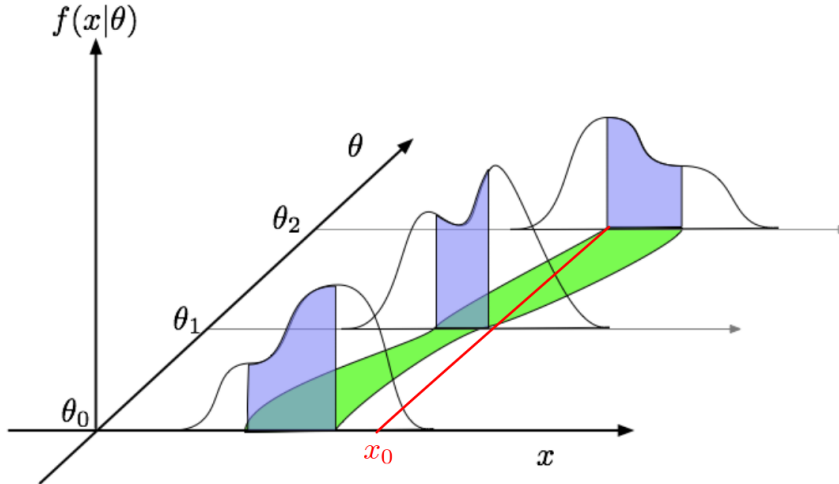


Figure 2.1: Schematic visualization of the Neyman construction, where  $\theta$  is the parameter of interest,  $x$  the observable and  $x_0$  its measured value [151]

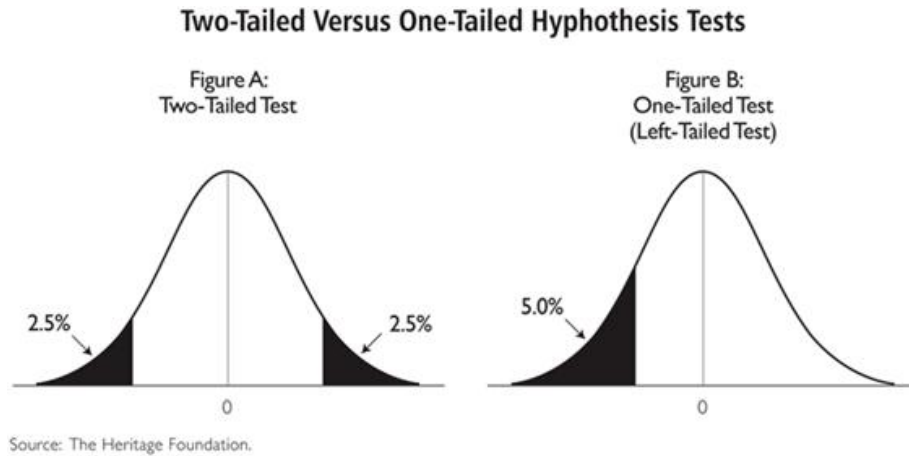


Figure 2.2: Schematics of the definition of a critical region of size  $\alpha = 5\%$  for a one-sided and a two-sided test-statistics

### 2.2.3 Particular cases used in particle physics

In this sub-part we will describe what are the most common ways to define confidence intervals in particle physics, and give the expression of the corresponding test-statistics to be used to conduct the statistical inference. We will see later that for most of these test-statistics an analytical formula may be approximated for their distributions, which allows to easily compute the probabilities that are needed for the construction of the confidence intervals that have been described above. Usually these probabilities are called the p-values of the tested hypotheses, and are computed as the integrals of the PDF of the test-statistics from its observed value up to  $+\infty$ . The coverage of the different methods used to set upper limits may be seen in fig. 2.3.

**Interval for measurements** In the case of a measurement we have a best estimate of the parameter of interest,  $\hat{\mu}$ , and we are interested in excluding values of  $\mu$  that are

incompatible with this estimate. There are two ways for specific values to be incompatible with the best-fit value : either because it is too low or because it is too high. In that case the critical region is chosen to be symmetric with regard to  $\hat{\mu}$  : if we were to generate data under the hypothesis that  $\mu$  is true, a fraction  $\frac{\alpha}{2}$  of the experiments should be rejected because they yield to a value of  $\hat{\mu}$  that is too low and another  $\frac{\alpha}{2}$  because they give a  $\hat{\mu}$  that is too high. This corresponds to the left case in fig. 2.2. In practice the following (two-sided) test-statistics is used [156] to do such an interval :  $t_\mu = -2 \ln \frac{L(\mu, \hat{\theta})}{L(\hat{\mu}, \hat{\theta})}$ , without any cut on  $\hat{\mu}$ .

**$CL_{s+b}$  interval for limits** Although the same reasoning may be conducted in the case of lower limits, we will only consider upper limits on a given parameter. For an upper limit the critical region should extend from the limit itself up to  $+\infty$ , and the acceptance region will always contain the lowest possible value for  $\mu$ . In this case, when we test an hypothesis  $\mu \neq 0$  the relevant alternative hypothesis is  $\mu = 0$ , and therefore the high value of  $\mu$  ( $\hat{\mu} > \mu_{test}$ ) should always be accepted. To do so the value of their test-statistics is set to 0, and this corresponds to the following (one-sided) test-statistics :  $q_\mu = -2 \ln \frac{L(\mu, \hat{\theta})}{L(\hat{\mu}, \hat{\theta})}$  if  $\hat{\mu} < \mu$  and  $q_\mu = 0$  otherwise. The confidence level constructed with this method is denoted  $CL_{s+b}$  and is equal to  $p_\mu = \int_{q_{obs}}^{+\infty} f(q_\mu|signal) dq_\mu$ , as in the case of a counting experiment what is actually observable is the number of signal plus background events, and it is on this total number of events that we actually set an upper limit. The limit on the signal comes after the background is taken into account and subtracted.

**The  $CL_s$  procedure** In this context, if there is a downward fluctuation of the number of background events an overly aggressive limit may be derived. In this case, given that both the signal and background only hypothesis are unlikely, it is not really meaningful to exclude the signal as there is no relevant alternative hypothesis that may explain the observation. This problem was treated in [157], where an alternative way of computing the confidence level for a given hypotheses has been advocated. The confidence level is not anymore the p-value of the hypotheses,  $p_\mu$ , but is actually penalized by the confidence level we have on the background hypotheses and is expressed as follows  $CL_s = \frac{CL_{s+b}}{CL_b} = \frac{p_\mu}{1 - p_b}$ .  $p_b$  is obtained on data generated under the background hypothesis but tested with the hypothesis  $\mu$ , and is computed as  $p_b = \int_{q_{obs}}^{+\infty} f(q_\mu|background) dq_\mu$ . Because of the  $CL_b$  penalty, the  $CL_s$  method is more conservative than the usual  $CL_{s+b}$  confidence level, and the confidence interval extracted in this way have a tendency to over-cover. This is done on purpose as an interesting feature of this method is to cancel any possibility of excluding a hypothesis to which we are not sensitive. This is particularly true for weak signals where the signal and background hypothesis are very close to each other and almost indistinguishable, where an exclusion is most likely coming from background fluctuations. But because of this property  $CL_s$  will never be able to exclude the background hypothesis in case there is for instance an actual deficit induced by new physics, and this is why it should be complemented by the  $p_0$  test (see [156] for a detailed description) whose only aim is to exclude the background [156].

**The Feldman-Cousins procedure** The Feldman-Cousins procedure has been described in [158], and is a way to produce an ideal frequentist interval without measuring a physical parameter in a region where it is meaningless, for instance it avoids the measurement of a negative mass. The boundaries of the confidence interval are defined by two hypothesis of equal likelihood, or by the physical boundaries of the problem. Effectively when we are far from the physical boundary this method will be equivalent to a measurement, while if we are at the boundary it will correspond to an upper limit. There is an intermediate range where not all the critical region will be on one side of the best estimate, as it should be in the case of an upper limit, but the two critical regions on each sides will not have the same size, as it should for a measurement. The transition between the two regimes is smooth and occurs without any loss of coverage, but an interval constructed under this prescription will correspond neither to an upper limit nor a measurement. Its main interest corresponds to cases that are at the border between these two regimes, where it is not possible to tell whether the sensitivity will be sufficient to do a measurement, but looking at the data before choosing whether a limit or a measurement will be done would create an under-coverage. In practice the Feldman-Cousins procedure corresponds to the following (two-sided) test-statistics : [156]

$$\begin{aligned} \tilde{t}_\mu &= -2 \ln \frac{L(\mu, \hat{\theta}(\mu))}{L(\hat{\mu}, \hat{\theta})} \text{ if } \hat{\mu} > 0 \\ &= -2 \ln \frac{L(\mu, \hat{\theta}(\mu))}{L(0, \hat{\theta}(0))} \text{ otherwise} \end{aligned}$$

It is possible to derive a similar type of interval for upper limits too, where the unphysical region is not considered, which is achieved using the following (one-sided) test-statistics :

$$\begin{aligned} \tilde{q}_\mu &= 0 \text{ if } \hat{\mu} > \mu \\ &= -2 \ln \frac{L(\mu, \hat{\theta}(\mu))}{L(\hat{\mu}, \hat{\theta})} \text{ if } \hat{\mu} > 0 \text{ and } \hat{\mu} < \mu \\ &= -2 \ln \frac{L(\mu, \hat{\theta}(\mu))}{L(0, \hat{\theta}(0))} \text{ otherwise} \end{aligned}$$

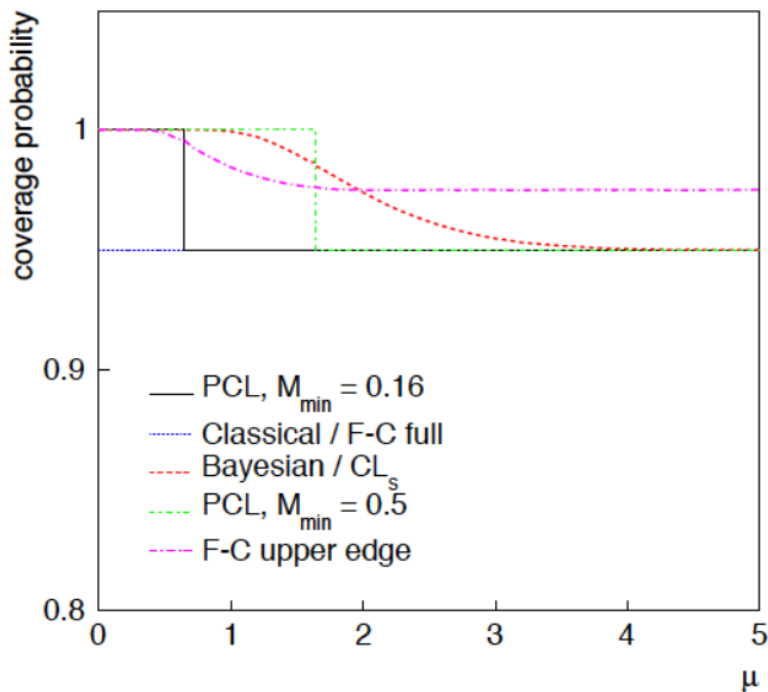


Figure 2.3: Coverage of upper limits obtained with several methods. The methods that are not defined in the text may be found in [159]. See also [160]

## 2.3 Distribution of the test-statistics

In the previous sections we had to assume that the distribution of the test-statistics was known to extract useful information. There are several ways to determine these distributions, and below the two methods that are used the most in particle physics will be described. The first one is the most general as it only requires a statistical model of the data, from which pseudo-experiments are generated to determine the distribution of the test-statistics. The second one is the most powerful as it provides an analytical formula for this distribution, but it cannot always be used as it makes few assumptions.

### 2.3.1 Distribution from pseudo-experiments

The first method generates pseudo-datasets at various values of the parameter of interest, and measures the test-statistics on each of these datasets. We then construct the distributions that interest us when the number of pseudo-experiments that is generated becomes sufficiently large.

In the case of a simple model with only one parameter this is simple, but there are few subtleties to take into account when nuisance parameters are involved in the modelling. First a specific value has to be chosen before the generation of the pseudo-datasets, and ideally it should be the true value for this parameter. As it is clearly not available it is estimated as being the best fit for this parameter under the hypothesis of the tested parameter of interest,  $\hat{\theta}(\mu)$ , which is the best estimate of the true parameter a physicist

may provide. During the generation of the pseudo-datasets, the nuisance parameters are set to these values in the statistical model, and therefore the difference between the pseudo-datasets that are generated for a given hypothesis only comes from statistical fluctuations and nothing else. But as the nuisance parameters are initially determined from an auxiliary measurement, which is itself described by a PDF, they should be varied. This is done at the time of the fit of the pseudo-dataset, where the global observable associated to a given nuisance parameter  $\tilde{\theta}$  is varied, randomly with a Gaussian distribution, which allows to randomize the outcome of the auxiliary measurement without varying the true hypothesis under which the pseudo-experiments are generated. This is called the "unconditional ensemble" [154, 161] (see also [162]). To determine the likelihood ratio two fits are done on each pseudo-dataset, the overall best fit and the best fit at the value that is being tested, and the nuisance parameters are left free in each of these fits.

As long as it is possible to provide a valid statistical model of the data, this method is completely general, but it has the drawback that depending on the p-value we want to reach it may require to generate an extensive number of pseudo-datasets, hence implying a very large number of fits too. Depending on the model this may be too time consuming and become impossible, in which case it may be sufficient to check that the asymptotic formulae that will be described below are valid on only one value of the parameter of interest, and use these formulae instead of the pseudo-experiments.

### 2.3.2 Asymptotic formulae for the significance

It was shown by Wilks and Wald [163, 164] that if the number of events in the observed dataset is sufficiently large, the maximum likelihood estimator of the parameter of interest follows a Gaussian distribution and the profile log-likelihood ratio can be developed as a parabola, i.e.  $-2 \ln \lambda(\mu) = \frac{(\mu - \hat{\mu})^2}{\sigma^2}$  where  $\sigma$  is the standard deviation of  $\hat{\mu}$ . A change of variable may be done to determine the distribution of  $-2 \ln \lambda$ , and this is precisely what is done in [156] for several test-statistics that are commonly used in particle physics. Given that the distributions are analytically known there is a direct connection between the value of the test-statistics measured on data for a given hypothesis, and the p-value of this hypothesis, hence it is sufficient to do the profile of the test-statistics as a function of  $\mu$  on data to determine the confidence interval on this parameter. The value of the test-statistics corresponding to the most usual confidence levels are given in table 2.1.

In the case of the two-sided test-statistics  $t_\mu$  the distribution  $f(t_\mu|\mu)$  is a simple  $\chi^2$  distribution, assuming that the hypothesis being tested by  $t_\mu$  is the same than the one used to generate the (pseudo-)data. It is possible to extend this formula to cases where these two parameters are different, which is done using a non-central  $\chi^2$  and is detailed in [156]. In the case of the one-sided test-statistics  $q_\mu$  half of the distribution of  $\hat{\mu}$  will have a test-statistics of 0, which will create a Dirac peak at  $q_\mu = 0$ . The other half creates a distribution of the test-statistics that follows  $\chi^2$  as it does not change with regard to  $t_\mu$ , hence the distribution will become  $f(q_\mu|\mu) = \frac{1}{2}\delta(q_\mu) + \frac{1}{2}\chi^2(q_\mu)$ . A nice point for both of these distributions is that they do not depend at all on the nuisance parameters, neither on their number nor on their values or the size of the systematic they represent. The only dependence in the nuisance parameter will be in the observed value of the test statistics,  $t_\mu^{obs}$ , as additional uncertainties will imply slower variation with respect to  $\mu$  and hence bigger uncertainties.

Confidence level	$q_\mu$	$t_\mu$
$1\sigma$		1
95%	2.71	3.84
99%	4.22	5.41
$5\sigma$		25

Table 2.1: Value of the test-statistics corresponding to a given confidence level, for the most commonly used test-statistics

This is not anymore the case for  $\tilde{q}_\mu$  and  $\tilde{t}_\mu$ , where the Gaussian distribution of  $\hat{\mu}$  is cut at 0 and depending the exact variance of  $\hat{\mu}$  and on its center the fraction of events falling in the region  $\hat{\mu} < 0$  may differ. It has been demonstrated in [156] that this may be well described by adding a Gaussian component to the distribution of  $t_\mu$  and  $q_\mu$ . More precisely for  $\tilde{t}_\mu < (\frac{\mu}{\sigma})^2$  the distribution of  $t_\mu$  and  $\tilde{t}_\mu$  are the same, but above this threshold the distribution of  $\tilde{t}_\mu$  is modified. This is well described by the following formula :

$$f(\tilde{t}_\mu|\mu) = \begin{cases} \frac{1}{\sqrt{2\pi}} \frac{1}{\sqrt{\tilde{t}_\mu}} e^{-\tilde{t}_\mu/2} & \text{if } \tilde{t}_\mu \leq \mu^2/\sigma^2, \\ \frac{1}{2} \frac{1}{\sqrt{2\pi}} \frac{1}{\sqrt{\tilde{t}_\mu}} e^{-\tilde{t}_\mu/2} + \frac{1}{\sqrt{2\pi}(2\mu/\sigma)} \exp\left[-\frac{1}{2} \frac{(\tilde{t}_\mu + \mu^2/\sigma^2)^2}{(2\mu/\sigma)^2}\right] & \text{if } \tilde{t}_\mu > \mu^2/\sigma^2 \end{cases} \quad (2.8)$$

It is important to note that the addition of a dependency on the variance of  $\hat{\mu}$  implies a dependency on the number of the nuisance parameter, and on the size of the associated Gaussian constraint in the case these nuisance parameters are associated to a systematic uncertainty.

In the case of  $\tilde{q}_\mu$  the solution is essentially the same, except that half of the potential outcomes of the experiment at high  $\hat{\mu}$  have a test-statistics set to 0, which requires the addition of the Dirac peak that we already had for  $f(q_\mu|\mu)$  but also implies that the  $\chi^2$  component that exists at high  $\hat{\mu}$  for  $\tilde{t}_\mu$  should not appear in the distribution of  $\tilde{q}_\mu$ . This gives the following formula :

$$f(\tilde{q}_\mu|\mu) = \frac{1}{2} \delta(\tilde{q}_\mu) + \begin{cases} \frac{1}{2} \frac{1}{\sqrt{2\pi}} \frac{1}{\sqrt{\tilde{q}_\mu}} e^{-\tilde{q}_\mu/2} & 0 < \tilde{q}_\mu \leq \mu^2/\sigma^2, \\ \frac{1}{\sqrt{2\pi}(2\mu/\sigma)} \exp\left[-\frac{1}{2} \frac{(\tilde{q}_\mu + \mu^2/\sigma^2)^2}{(2\mu/\sigma)^2}\right] & \tilde{q}_\mu > \mu^2/\sigma^2 \end{cases} \quad (2.9)$$

## 2.4 Expected results : the Asimov dataset

In particle physics we often want to estimate the expected sensitivity of an analysis before actually applying it on data. This is achieved using the so-called Asimov dataset whose construction and properties have been demonstrated in [156]. First a given hypothesis is chosen for the parameter of interest,  $\mu_A$ , and all the nuisance parameters are profiled on data at  $\mu_A$ , which completely determines the statistical model. If the model is a binned likelihood, an histogram that perfectly follows this model can be defined, where the content of each bin is defined as the median of the number of events in this bin ( $n_i^A = E[n_i](\mu_A, \hat{\theta}_A)$ ), without any statistical fluctuation. A typical example of such an Asimov dataset is shown in fig. 2.4. In the case of an unbinned likelihood it cannot be

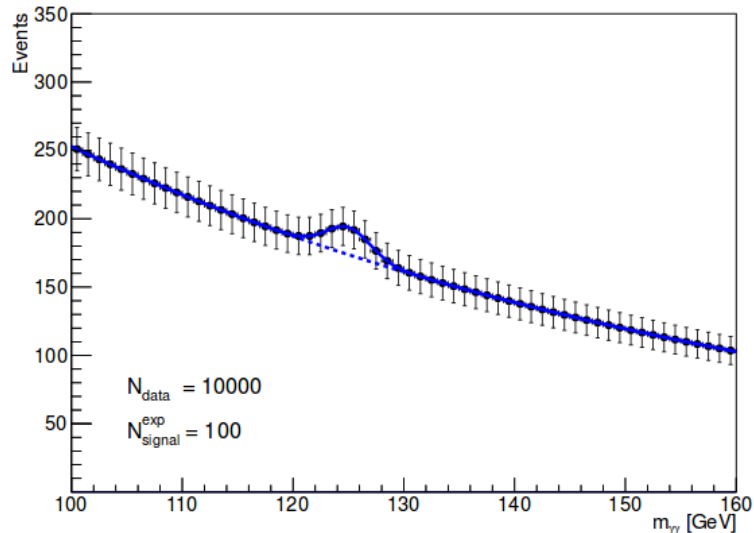


Figure 2.4: Typical example of an Asimov dataset corresponding to an example of the  $h \rightarrow \gamma\gamma$  analysis [89]

exactly defined and it is approximated as the limit of the equivalent binned likelihood in the limit where the width of the bins goes to 0. The test-statistics used in the analysis may then be evaluated on the Asimov dataset and it may be shown that if we were to generate pseudo-experiments under the hypothesis used to define the Asimov, the median of the test-statistics of the toys would be equal to the test-statistics measured on the Asimov dataset. In this sense the Asimov dataset corresponds to the most representative dataset that exists for a given hypothesis, and it allows to derive the expected uncertainty for a measured parameter or the expected exclusion limit for a given phenomenon.



# Chapter 3

## Description of the experimental setup

### Contents

---

<b>3.1</b>	<b>The Large Hadron Collider</b>	<b>60</b>
3.1.1	Motivations for a $pp$ collider	60
3.1.2	The CERN accelerator complex	60
3.1.3	LHC magnets	62
3.1.4	Bunch filling scheme for the LHC	63
3.1.5	Experiments using LHC beams and collisions	64
3.1.6	Luminosity	64
3.1.7	LHC Performance	65
<b>3.2</b>	<b>Description of the ATLAS detector [1]</b>	<b>68</b>
3.2.1	Overall description of the ATLAS detector	68
3.2.2	Coordinate system of the ATLAS dectector	68
3.2.3	Magnets of the ATLAS detector	70
3.2.4	The inner tracker	71
3.2.5	Hadronic and forward calorimeters	73
3.2.6	The muon spectrometer	74
3.2.7	Luminosity detectors	74
<b>3.3</b>	<b>Description of the ATLAS electromagnetic calorimeter</b>	<b>76</b>
3.3.1	Global description of the concept	76
3.3.2	Interaction of electromagnetic particles with matter	76
3.3.3	From electromagnetic shower to recorded signals	80
3.3.4	Anatomy of the ATLAS EM calorimeter	82
3.3.5	Energy reconstruction with the calorimeter signals	89
<b>3.4</b>	<b>Reconstruction of electrons and photons at ATLAS</b>	<b>92</b>

3.4.1	Reconstruction of electromagnetic clusters . . . . .	92
3.4.2	Offline identification of photons [2] . . . . .	93
3.4.3	Offline identification of electrons [3] . . . . .	96
<b>3.5</b>	<b>Comparison with the CMS detector . . . . .</b>	<b>98</b>
3.5.1	Overall description of the CMS detector . . . . .	98
3.5.2	Description of the electromagnetic calorimeter . . . . .	98
3.5.3	Reconstruction of electromagnetic particles in CMS . . . . .	100

---

## 3.1 The Large Hadron Collider

### 3.1.1 Motivations for a $pp$ collider

Improving the knowledge of physics at particle colliders can be schematically achieved in two ways : either increasing the particles energy or the number of recorded collisions. The first way allows the direct production of new, heavier, particles while the second gives sensitivity to smaller deviations from the prediction. Those approaches can be combined as some models may predict the existence of heavy particles, but with low production probabilities. To some extent this was the case in the design of the LHC, whose one of the design benchmarks was the search for the BEH boson : as its mass could have been as high as 1 TeV a high energy was needed to cover the whole range. This required the use of hadrons, as electrons would lose too much energy through synchrotron radiation, and as muons can not be yet accelerated in an efficient way.

The only stable hadrons are the protons and their anti-particles. Anti-protons have been used in the past at the  $Spp\bar{p}S$  where they helped discovering the W and Z bosons (as the initial state is  $q\bar{q}'$ ), and also at the TeVatron. However the  $\bar{p}$  production is complicated and not very efficient, and it considerably lowers the interaction rate of the collider. Given that the main production mode of the Standard Model BEH boson is already at one loop, its cross-section is fairly low, therefore a high interaction rate was a design requirement of the LHC and dictated the choice of protons for the two beams. The price of this choice is to have two beam pipes and two sets of magnets (in fact the magnets are "two in one" as will be explained below). Although only the case of the BEH boson is discussed here, the argument holds for many searches for particles predicted by beyond the standard model scenarios.

### 3.1.2 The CERN accelerator complex

The Large Hadron Collider (LHC) is a  $pp$  collider, and can also collide lead nuclei. It relies also on the pre-existing machines, since it is not possible to accelerate the beam from 0 to the desired energy (the nominal energy being 7 TeV) in one step. A sketch of the complete complex can be seen on fig. 3.1.

The first step is the creation of protons from an hydrogen bottle ( $H_2$ ) : these molecules are submitted to an intense electric field breaking them into protons and electrons. The protons are then accelerated in a linear accelerator (LINAC 2, used since 1978) where

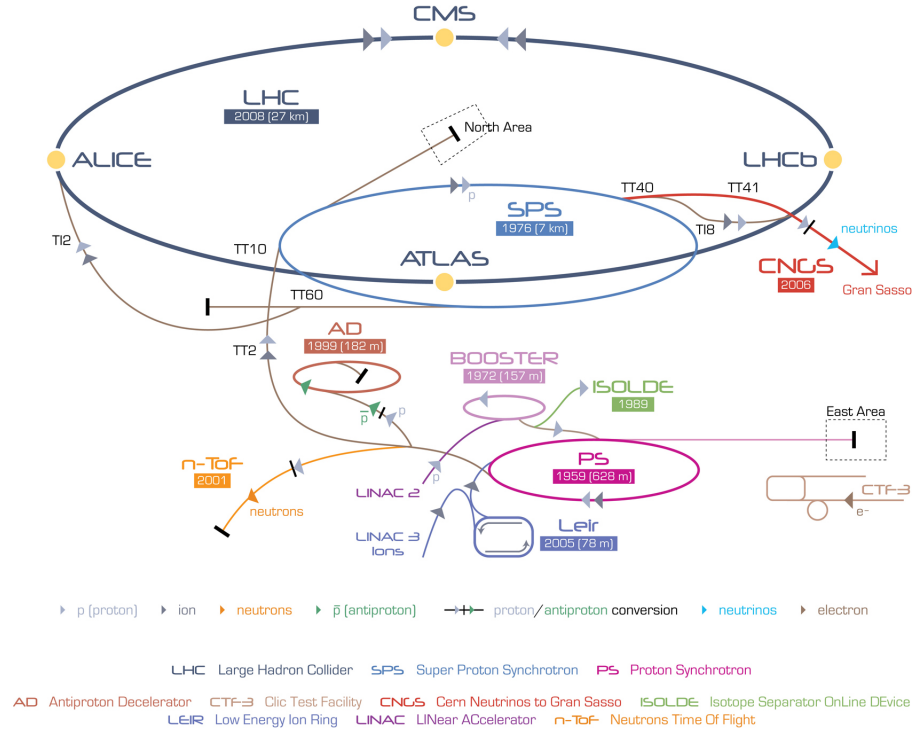


Figure 3.1: Schematics description of the CERN accelerator complex [166]

they reach a momentum of 50 MeV. It is also this accelerator that creates the bunch structure. They are then injected into the proton synchrotron booster (PSB) which consists of four circular accelerators, on top of each others. They are accelerated until they reach a momentum of 1.4 GeV/c [165] and are then injected into the Proton Synchrotron (PS), where they reach a momentum of 26 GeV/c. Until the early seventies, particles were directly injected in the PS. But given the destructive impact of coulomb forces on low energy beams it was not possible to increase the intensities, and this is why the PSB consists of four rings : each one has the same intensity limitations but they allow to simultaneously accelerate four beams that are merged afterwards.

When working with heavy ions the beginning of the chain is different. Lead ions, which come from vaporized lead, are stripped off of their electrons while being accelerated in the LINAC 3, and are then injected into the Low Energy Ion Ring (LEIR) where their momentum increases from 4.2 MeV/c to 72 MeV/c before they are injected in the PS. At this point the acceleration chain becomes the same as for protons.

After the PS, particles are injected in the 7km long Super Proton Synchrotron (SPS), which is one of the cornerstones of the CERN complex as it provides beams to a variety of experiments, including the LHC. Before the injection in the LHC, the protons are accelerated to 450 GeV and the remaining acceleration from the SPS to the multi-TeV energy is done in the LHC and takes roughly 20 minutes. At this point the beams can be put in collision, and can keep colliding for several hours.

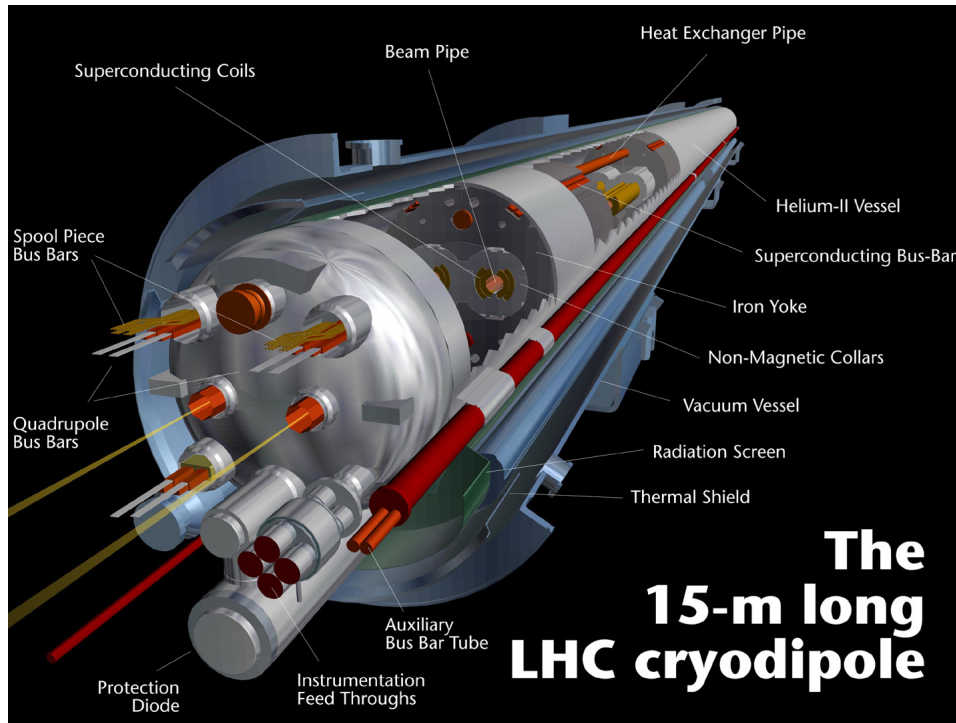


Figure 3.2: Description of a LHC dipole

### 3.1.3 LHC magnets

The LHC has been installed in the 27 km tunnel in circumference that was hosting the LEP collider and its experiments. The main difference between the two colliders is linked to the nature of the colliding particles, as electrons have to be continuously accelerated to compensate for synchrotron radiation losses while for protons the main challenge is to control the trajectory of high energy particles and keep them on the LHC circumference. Therefore the LHC is almost exclusively made of magnets while the LEP had a sizeable number of radio-frequency (RF) accelerating cavities.

The momentum of a particle in a magnetic field is given by  $p = 0.3Bq\rho$  where  $B$  is the strength of the magnetic field,  $q$  the charge of the particle and  $\rho$  the curvature radius of its trajectory (4.3 km is the radius of the tunnel). After several years of R&D, the magnets designed for the LHC were able to create a 8.3 T magnetic field, leading to a 10.7 TeV beam energy assuming that the curvature radius of the trajectory is the trajectory of the tunnel. The current nominal value is 7 TeV per beam as only the 1232 dipole magnets are used to bend the beams while the LHC also requires 392 quadrupoles to focus the beams, 688 sextupoles to decrease the proton energy spread and 16 superconducting RF cavities to accelerate the beam. And this only accounts for the main components, the full list of magnets can be found in [167]. Taking this into account the effective bending radius at the LHC is of 2.7 km, which gives in nominal conditions a center of mass energy of  $\sqrt{s} = 14$  TeV. It is realized by eight straight lines, connected by eight arcs.

The standard way of creating a magnetic field is to run an electric current into a coil and the field will be higher if the current gets higher. The same idea is used in LHC magnets. For the main dipoles, which can be seen on fig. 3.2, the required field is very

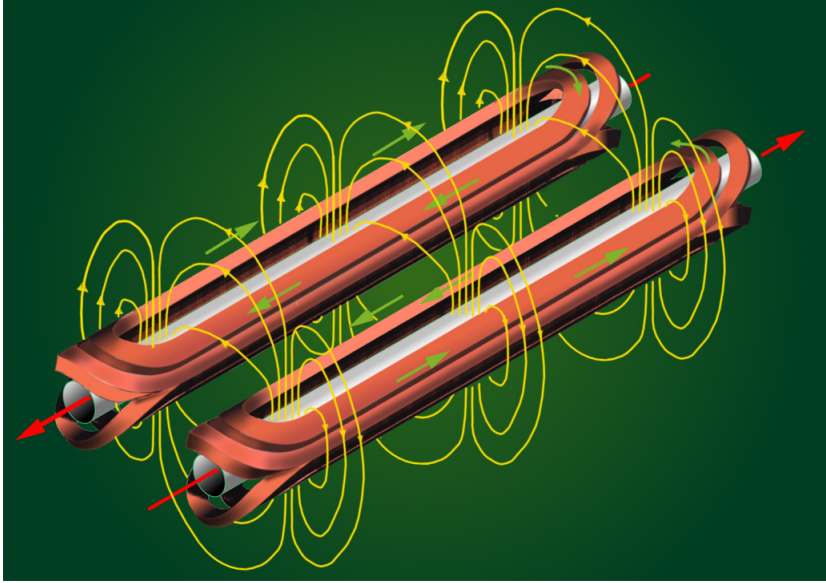


Figure 3.3: Current in the LHC dipoles (green) and resulting magnetic field (yellow)

high (8.3 T) and a sufficient current (11850 A) cannot be achieved with usual conductors. Super-conducting cables made out of Niobium-Titanium (NbTi) alloy have been used, and are cooled using super-fluid Helium 4. These filaments are embedded in a matrix of very pure Copper, that acts as an insulator in the superconducting phase while conducting the current and heat above the critical temperature for NbTi. The nominal operating temperature is 1.9 K. The particles in the two beams have the same charges and are accelerated in opposite directions, therefore the magnetic field in the two beam pipes need to be in opposite directions. This is achieved by setting a proper flow of the current in the two dipole coils, as pictured in fig. 3.3.

The radio-frequency cavities reuse the technology developed for LEP, and provide a voltage of 2 MV and an integrated accelerating field of 5 MV/m at a frequency of 400.8 MHz. As the two beams have to be controlled independently, the RF cavities operating on the two beam pipes are independent and each beam pipe has 8 RF cavities. These cavities also help in the conservation of the bunch structure as a proton that is delayed with regard to the rest of the bunch will be subjected to an higher accelerating field while one that is in advance will be decelerated. After the acceleration phase protons should not be affected by the RF field as they are synchronized with the center of the wave.

Powerful quadrupoles are placed on each side of the four experiments and produce low  $\beta^*$ . Their goal is to do a final transverse squeeze before the collision, during which the radius of the beam decrease from 1.6mm to about  $16\mu\text{m}$ .

### 3.1.4 Bunch filling scheme for the LHC

The design bunch spacing in the LHC is of 24.95 ns, which corresponds to  $\approx 7.49$  m and a collision rate of 40.08 MHz, where each collision can be identified by a single Bunch Crossing Identifier (BCID). This gives 3564 possible slots for proton bunches, but they cannot all be used and several filling schemes are described in [168]. They all have to respect certain constraints. First, a sufficient time is needed after the last bunch to dump

the beam before it accomplishes one turn of the LHC, which requires at least 119 empty bunches. Secondly several transfers from the SPS to the LHC are needed to completely fill the LHC, and between each batch 38 bunches have to be left free as this corresponds to the time needed for the kicker's magnetic field to rise. The same story repeats itself for the injection from the PS to the SPS : 8 bunches have to be left free between each transfer to the SPS. At the end, with its nominal parameters, the LHC is running with 39 batches of 72 bunches (2808 bunches), spaced with missing bunches to respect the aforementioned constraints, and each bunch contains  $\approx 1.15 \cdot 10^{11}$  protons. The scheme for heavy ions collision is different, and there are also different schemes developed for the low luminosity runs at the beginning of data taking.

Because of the 2008 LHC accident the running conditions for the Run 1 have changed. The bunch spacing is increased to 50 ns, and the beam energy decreased to 3.5 TeV (in 2011) then to 4 TeV (2012). A rough description of the bunch filling scheme may be found in [169], the most important thing being the decrease of the number of bunches to 1374 (sometimes 1380) and the increase of number of protons per bunch to  $\approx 1.7 \cdot 10^{11}$  (in 2012). Most of the batches contained 144 bunches.

### 3.1.5 Experiments using LHC beams and collisions

Seven experiments have been designed to analyze the LHC collisions data, among which four are bigger and have been constructed around the main interaction points. The two biggest detectors, ATLAS and CMS are general purpose detectors that will be described later. Their goal is to search for new physics in the broadest possible spectra, and to make precise measurements of standard model processes at the highest energies.

A third one, LHCb, is a forward spectrometer whose main research interest is the study of flavour physics and which is aiming at taking profit of the large number of  $b$  and  $c$  mesons that are produced in the forward direction. As it can not cope with more than a few pile-up events it is using a luminosity levelling, i.e. the collisions do not occur on the full area of the beam but only on a small subpart. During the run, the decrease of the beam intensity (and of the number of collisions per bunch crossing) is compensated by getting the beams closer to each other hence increasing the area of collision.

The last large experiment, ALICE, is specialized in heavy ion physics and aims to study the quark-gluon plasma.

Within the three smaller experiments, two are interested in low-angle scattering (LHCf and TOTEM), either to study the total cross-section or to test and develop models to be used in cosmic-rays physics. The last one, MoEDAL, has been made to search for magnetic monopoles.

### 3.1.6 Luminosity

The rate of a specific type of event can be linked to the accelerator's properties using :

$$\frac{dN_{event}}{dt} = L\sigma_{event} \quad (3.1)$$

where the cross-section  $\sigma_{event}$  depends on the physical process of interest and the luminosity is given by the machine operating parameters, using the following formula :

$$L = \frac{k n^2 \nu}{2\pi \sqrt{\sigma_{1x}^2 + \sigma_{2x}^2} \sqrt{\sigma_{1y}^2 + \sigma_{2y}^2}} F \quad (3.2)$$

where the various parameters are defined as follows :

- $k$  is the number of bunches in the machine
- $n$  is the number of protons per bunch
- $\nu$  is the revolution frequency of a particle in the machine ( $\approx 11245$  Hz)
- $\sigma_{i\ x,y}$  corresponds for each beam  $i$  to its size in each direction of the transverse plane at the collision point. Usually we define  $\sigma_{x,y\ eff} = \sqrt{\sigma_{1\ x,y}^2 + \sigma_{2\ x,y}^2}$
- $F$  is a geometrical reduction factor, due to the fact that the beams do not collide heads on but have a small crossing angle

The detectors are equipped with devices specialized in the measurement of the luminosity, whose main function is to detect the number of interactions for each bunch crossing. The luminosity is then

$$L = \frac{\mu_{vis} k f}{\sigma_{vis}} \quad (3.3)$$

where  $\mu_{vis}$  is the number of visible interactions per bunch crossing and  $\sigma_{vis} = \epsilon \sigma_{inelastic}$  the visible cross-section, and both these quantities already include detectors efficiency effects. These detectors need a specific calibration to determine  $\sigma_{vis}$ , that is related to the size and shape of the beams, which is achieved using Van Der Meer scans [170]. In these scans the beams are progressively separated from one another, while the rate of interaction is monitored by the luminosity detectors. This rate is a function of the beam separation and follows the beam shape (Gaussian at the LHC). From the RMS of this function it is possible to determine the transverse size of the beam and from its maximal value, the number of visible interactions in nominal running conditions.

The number of protons per bunch is given by the accelerators instrumentation and at the end the visible cross-section is given by :

$$\sigma_{vis} = \mu_{vis}^{max} \frac{2\pi \sigma_{x\ eff} \sigma_{y\ eff}}{n_{max}^2} \quad (3.4)$$

More details can be found in [171–174].

### 3.1.7 LHC Performance

At its nominal performance the LHC was expected to provide a luminosity of  $10^{34} \text{ cm}^{-2} \text{ s}^{-1}$  to ATLAS and CMS at a center of mass energy of  $\sqrt{s} = 14$  TeV. Assuming a 25 ns bunch spacing, this would have given, on average, about 23 simultaneous interactions by bunch-crossing (pile-up events). Given the decrease of energy and the change of bunch spacing in

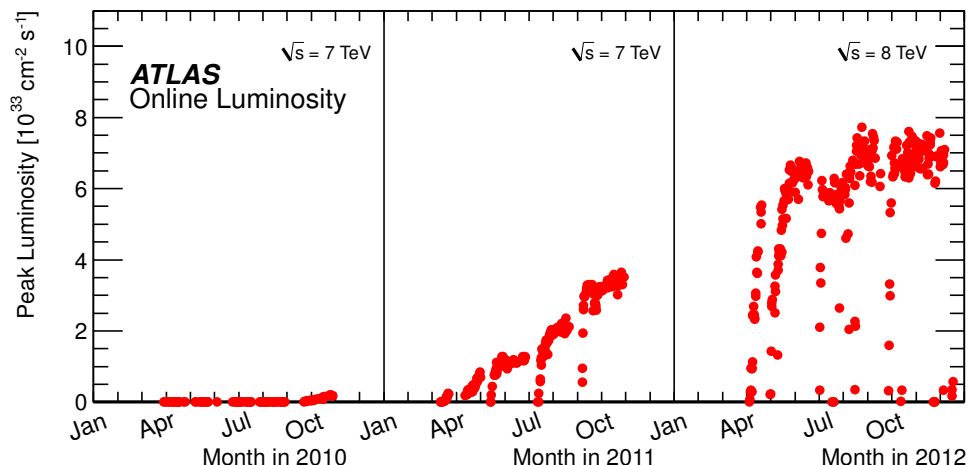


Figure 3.4: Peak luminosity delivered to ATLAS by the LHC between 2010 and 2012. This corresponds to the luminosity just after a fill.

the Run 1 (50 ns), a reasonable luminosity of  $7.5 \cdot 10^{33} \text{ cm}^{-2} \text{ s}^{-1}$  was achieved by increasing the number of protons per bunch. This gave an average number of pile-up events higher than anticipated, above 35 during the luminosity peaks. The instantaneous luminosity was not constant as a function of time during the years. This is shown in fig. 3.4 where one can see that the instantaneous luminosity kept rising during these three years, thanks to the hard work of machine experts.

The total integrated luminosity recorded by ATLAS and CMS is  $5 \text{ fb}^{-1}$  at  $\sqrt{s} = 7 \text{ TeV}$  and  $20 \text{ fb}^{-1}$  at 8 TeV. Collisions were also recorded in 2010 at  $\sqrt{s} = 7 \text{ TeV}$  but were not combined with the two other years, given the low integrated luminosity ( $40 \text{ pb}^{-1}$ ). It was still an important year, as the reduced interaction rate allowed to take data with loose online selection and reduced pile-up.

For the Run 2 the bunch spacing is expected to decrease to its nominal value, while the center of mass energy will increase to at least  $\sqrt{s} = 13 \text{ TeV}$ . The luminosity should reach  $1.6 \cdot 10^{34} \text{ cm}^{-2} \text{ s}^{-1}$  and the number of interactions by crossing could be as high as 45. We expect to have an integrated luminosity of 2-5  $\text{fb}^{-1}$  by the end of 2015 and 100  $\text{fb}^{-1}$  by the end of the run. Because of the energy increase, all cross-sections of interesting phenomena will increase as well, as can be seen in fig. 3.5. In some processes that involve a high mass scale the statistics will grow much faster at high energy : this is for instance the case of the BEH production in association with top quarks, where the production cross-section increases by a factor of four.

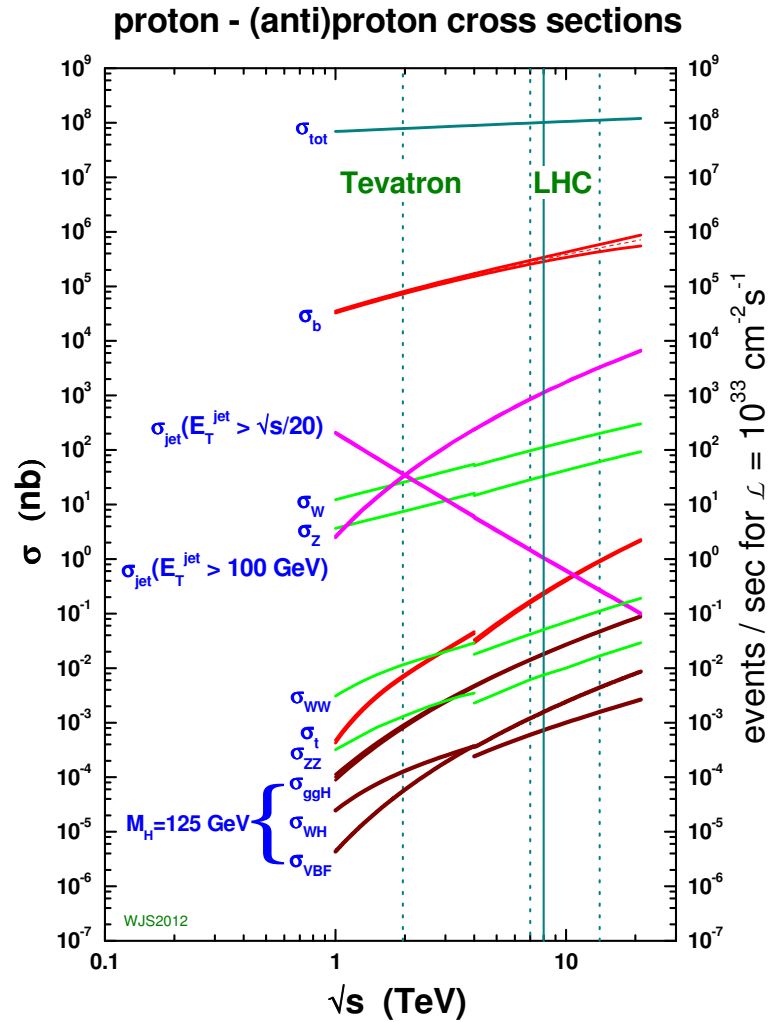


Figure 3.5: Evolution of the cross-sections for various processes as a function of the center-of-mass energy in hadron collisions. The break at 4 TeV corresponds to the switch between  $p\bar{p}$  and  $pp$  [175]

## 3.2 Description of the ATLAS detector [1]

### 3.2.1 Overall description of the ATLAS detector

The ATLAS detector is a general purpose detector, in the sense that its design has been done in particular to search for new particles and phenomena in the broadest possible range of signatures, although always targeting the high-energy signatures of the new physics, as well as to measure SM processes with  $W$  bosons,  $Z$  bosons or heavy quarks. To that end, it should be able to detect every particles that are long-lived enough to travel inside the detector. This includes electrons, photons, muons, hadrons and neutrinos. The detector should also offer reasonable particle-identification capabilities, in the central region that corresponds to the most usual production region of new heavy particles. This is achieved using a standard cylindrical geometry for the detector, where the axis of the cylinder corresponds to the beam axis and the center of the detector to the collision point. There are various sub-detectors that are built as several concentric layers, where each sub-detector has its own specific function, and will be further described in the following part. The detector also has a set of powerful magnets, that are including some of the sub-detectors in a magnetic field which allows a better reconstruction of charged particle.

The first detector is the inner tracker, which lies in a 2T solenoidal magnetic field and that is here to reconstruct the trajectory of every charged particle that is passing through it, hence allowing for a measurement of its momentum. It also needs to be sufficiently precise to be able to reconstruct displaced vertices, that are for instance a crucial input to identify jets coming from  $b$  quarks. The second layer consists of the two calorimeters, electro-magnetic and hadronic, in which incident particles will create a shower of secondary particles from which a measurable signal will be generated. The first one is the electro-magnetic calorimeter that measures the energy, position and direction of electrons and photons, while the second one, the hadronic calorimeter measures the energy and direction of jets by measuring the energy deposited by hadrons inside these objects. The final layer corresponds to the muon spectrometer, where the momentum of muons, which are the only charged particles that are expected to cross the previous layers, is measured, thanks to toroidal field of  $\approx 1T$  that curves their trajectories. At this point the only standard model particles that have not been detected are the neutrinos, that will cross the complete detector without any interaction. The only hint of their presence comes from the imbalance of the transverse momentum between what is measured in the detector and what is expected from the collision. Therefore the detector needs to be hermetic, which is accomplished by extending the detectors to a high rapidity, bringing them very close to the beam-pipe, with the forward calorimeters. Still given that the neutrinos are not actually detected, there may be new particles beyond the standard model that will have the same signature although they are different, which is typically the case of dark matter.

### 3.2.2 Coordinate system of the ATLAS dectector

The origin of the ATLAS coordinate system corresponds to the nominal crossing point of the two beams. The cartesian coordinate system  $(x; y; z)$  is defined as having the  $z$  axis following the beam axis, and the  $x$  axis is in the plane defined by the LHC ring, oriented from the detector center towards the the center of the LHC. Positive values of  $z$  correspond

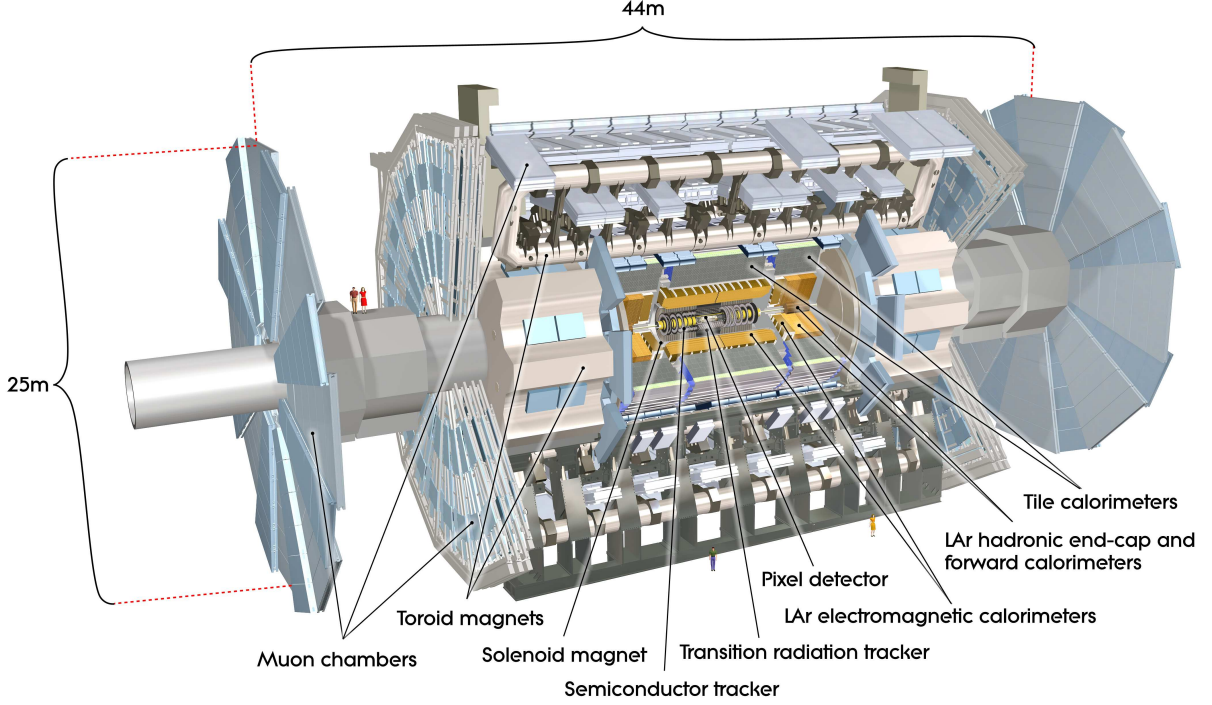


Figure 3.6: General schematics description of the ATLAS detector [1]

to the side oriented counter-clockwise with respect to the interaction point along the LHC ring. The cylindrical coordinates  $(\theta; \phi; z)$  is defined so that  $\theta = \frac{\pi}{2} \rightarrow 0$  corresponds to  $z > 0$  (also called "side A") and  $\theta = \pi \rightarrow \frac{\pi}{2}$  to  $z < 0$  ("side C"), where  $\theta = \frac{\pi}{2}$  corresponds to the direction perpendicular to the beam axis. The direction  $\phi = 0$  coincides with the  $x$  axis, and  $\phi > 0$  corresponds to the upper half of the detector. It is common in particle physics to use the pseudo-rapidity  $\eta = -\ln(\tan(\frac{\theta}{2}))$  instead of  $\theta$ , which is equivalent to the rapidity  $y = \frac{1}{2} \ln(\frac{E+p_z}{E-p_z})$  for ultra-relativistic particles.  $y$  has the nice property of being invariant under a boost along the beam axis ( $z$ ).

Then any observable may be projected on the transverse plane and the  $z$  axis using the following formulae :

$$P_T = \frac{P}{ch(\eta)}$$

$$P_z = P \tanh(\eta)$$

The distance between two objects in the detector may be determined using the variable  $\Delta R$ , which is computed as  $\Delta R^2 = \Delta\eta^2 + \Delta\phi^2$ , which is also invariant under a boost along the  $z$  axis.

This defines the general concepts used to determine the coordinates of every object in the ATLAS detector, but there are a few subtleties. For instance the actual interaction vertex from which an object of interest originates will not always be at  $z = 0$ , and we will see later that we have to take this shift into account using the pointing (the direction is measured using the first two longitudinal samplings of the calorimeter [176]). Also the end-cap of the calorimeters had to be slightly translated with respect to their nominal position, and this created a global shift of the coordinates in the end-caps. Then two

different coordinates are available : those that are seen from the calorimeter and the global ATLAS coordinates, which are translated by  $\delta\eta \approx 0.02$  (in the end-caps).

### 3.2.3 Magnets of the ATLAS detector

The ATLAS detector has two independent magnetic systems : the solenoidal magnet responsible for curving the charged particles trajectories in the inner tracker, and the toroidal magnet providing the field in the muon spectrometer. The generated magnetic fields are orthogonal to one another and they allow for independant measurements of the muon momentum in the innermost and outermost part of the ATLAS detector. Even if it is afterward possible to improve the momentum determination by combining both measurements, in itself this redundancy is a nice feature. For instance one could not use the inner detector information if the impact of pile-up on tracking becomes too high to deal with.

#### The solenoidal magnet

The solenoidal magnet, which is described in [177], is designed to provide a 2 Tesla magnetic field in the center of the detector. The magnet covers a region of 2.4m diameter and a length of 5.3m and it requires an electric current of 7600 A. This is achieved using a superconducting magnet, made out of a Niobium-Titanium alloy, and cooled by liquid Helium at 4.5 K. Filaments of this composite are embedded in a matrix of pure Aluminium, which allows to increase the critical current. It provides an alternative path for the current in case the magnet goes back to its normal conducting phase, which allows to use it at higher intensities without causing a quench. It is especially useful as this magnet has to be as thin as possible (5 cm thickness), since it lies upstream of the liquid Argon calorimeter and a high material budget would have worsen the calorimeter performance. In this configuration it contributes to  $0.66 X_0$  at  $|\eta| = 0$ . To further decrease the material, the magnet shares the same cryostat as the barrel liquid Argon calorimeter. An additional 2mm heat shield in aluminium lies between the magnet and the calorimeter. This is required to have both liquid argon and liquid helium, which have different temperatures, in the same cryostat.

The field return is done in the iron absorbers of the tile calorimeter. As it is far from the solenoid the magnetic field is not completely uniform in the tracking region and therefore has to be mapped precisely to get a sufficiently precise tracking. This was done only in the region of the inner tracker [178], using sensors based on Hall effect. The knowledge of the field beyond the tracking region, and especially of its return to the Tile calorimeter, comes from a model of the field.

#### The toroidal magnet

The toroidal magnets are here to provide the magnetic field necessary for the spectrometers to reconstruct the muons momentum, hence they are expected to cover a large volume and it would not be possible for it to generate a completely homogeneous field. The barrel system is constituted of 8 large barrel coils, that are arranged in a star configuration, and of two end-cap systems that are also made of 8 coils each, and that are following the same

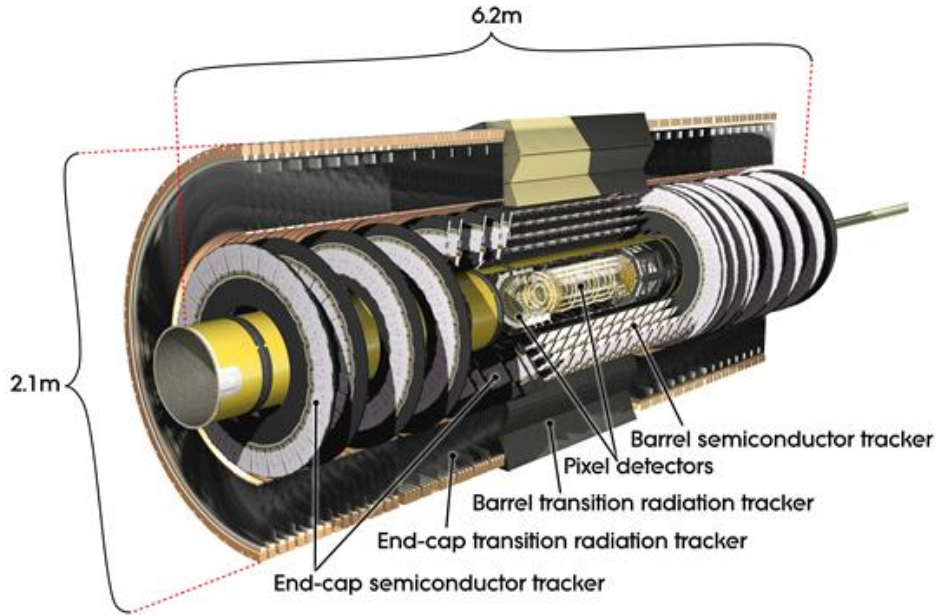


Figure 3.7: Schematics description of the inner tracker installation and of its various sub-components [1]

arrangement than in the barrel. The basic constituent of the magnets is the same than for the solenoid magnet, i.e. it uses liquid-helium cooled superconducting magnets based on an aluminium stabilized niobium-titanium alloy. The peak magnetic field provided by this magnet is of 4 Tesla, which requires a current of 20.5 kA, but it has sizeable variations inside its volume, especially close to the coils. A set of 1800 sensors based on Hall effect have been set up close to the coils and are used to measure the magnetic field where it varies the most. From this information it is possible to compute the magnetic field everywhere in the instrumented part of the muon spectrometer, with a precision of 1 mT. There are also two end-cap toroids [1], and together with the barrel toroid they produce a toroidal magnetic field of approximately 0.5 T and 1 T for the muon detector in the central and end-cap regions, respectively.

### 3.2.4 The inner tracker

The main role of the inner tracker is to provide a precise measurement of the parameters of the trajectory of charged particles, but it can also provide information to identify particles. In ATLAS the inner tracker is composed of three separate parts based on different technologies. The first two parts are based on sensors made of silicon semiconductors, while the last one uses the transition radiation technique, which allows to distinguish electrons from other particles, and is made out of straw tubes filled with Xenon. The closest layers to the beam-pipe are the more segmented. A global description of the installation and of the composition of the inner tracking may be seen in fig. 3.7. It is important to note that the tracking only extends up to  $|\eta| = 2.5$ .

### The pixel detector

The pixel detector corresponds to three most inner layers of the ATLAS tracker, which are those that allow for the most precise measurements of the tracks. In the barrel, the layers are arranged as three concentric cylinders while in the end-cap these are made of three disks perpendicular to the beam. Each of the pixel corresponds to a semi-conductor sensor made in silicon, that have a size of  $50\mu m$  in azimuth,  $400\mu m$  in  $z$  and a thickness of  $250\mu m$ . The complete pixel detector contains approximately 80 million read-out channels, each one corresponding to a pixel. The accuracy on the charged particle positions are of  $10\mu m$  in  $(R - \phi)$  and  $115\mu m$  in  $z$ . The first layer is called the b-layer and is of primary importance as it allows for a precise reconstruction of the tracks parameters, especially of its impact parameter with regard to the primary vertex, which is very sensitive for the reconstruction of b-jets where the B meson flies away from the interaction region before decaying. Furthermore it allows to discriminate between converted photons which (in general) are not expected to convert before reaching the b-layer, and electrons for which a hit should be recorded in the b-layer. For the Run 2 the current pixel detector will be complemented by an additional pixel layer, the IBL, that will be even closer to the beam pipe and is expected to improve the performance of the identification of jets that are initiated by b-quarks.

### The Semiconductor Tracker

The following part of the tracker is the Semiconductor Tracker (SCT) which is composed of four cylinders in the barrel and 9 disks in the end-cap, which allows for at least 4 additional hits everywhere in the detector. These detectors are made of silicon microstrips that are 12 cm long (in  $z$ ) and  $80\mu m$  wide (in  $(R - \phi)$ ). The smaller  $z$  coordinate accuracy comes from having two sensors per layer, with a slight angle (40 mrad, in the  $z - \phi$  direction) between each sensor. At the end the resolution in position from the SCT is of  $17\mu m$  in  $(R - \phi)$  and  $580\mu m$  in  $z$  (R) in the barrel (end-cap). There is a total number of approximately 6.3 million read-out channels in the SCT.

### The Transition Radiation Tracker

The Transition Radiation Tracker (TRT) is the last part of the ATLAS inner tracker, and is the further away from the beam. The most frequent signal creation mechanism is the ionization of the Xenon in the straw tube by a charged particle, which deposits a small signal, but the specificity of the TRT is the use of another physical process, the transition radiation, which is present only for electrons. Whenever a charged relativistic particle crosses the interface between two materials with different optical properties, it will emit a light radiation, "the transition radiation", which may be detected. This constitutes the basis of this sub-detector which is based on straw-tubes filled mainly with Xenon, and the transition radiation will be emitted at the boundary of the radiator material, which is made of polypropylene and polyethylene fibres. This radiation corresponds to X-rays photons with an energy of  $5 - 30$  keV, and is strictly proportional to the value of  $\frac{E}{m}$  for the incident particle, therefore for a given momentum it will be much higher for electrons than for pions and muons. These X-rays will be absorbed by the Xenon in the straw tubes, and increase the detected signal. Therefore there are two thresholds in the read-out

of the TRT : the first one specifies whether a given sensor was hit, while the second one (the "high-threshold hits") requires higher signal amplitude and is expected to be specific to electrons. The straw-tubes have a diameter of 4 mm, and contain a conductive wire (anode) in their center at which the signal electrons will be collected. In the barrel they are parallel to the beam axis while in the end-cap the straws are arranged radially in wheels, which allows to do measurement of the  $(R, \phi)$  coordinates with a precision per straw-tube of  $170\mu m$ . This is lower than the one from the SCT and the pixel, but this lack of precision is compensated by the higher number of hits in this sub-detector, as there are 73 parallel planes of straw-tubes in the barrel and 80 planes for each end-cap.

### 3.2.5 Hadronic and forward calorimeters

The measurement of the jet energy, as well as of the missing energy, requires an adequate measurement of the hadron energy that is inside the jet, and this requires specific calorimeters as the only interaction of neutral hadron will be the strong interaction, and the nuclear interaction length of the LAr EM calorimeter is too small to give sufficient performance for hadrons. Therefore different hadronic calorimeter have been included in ATLAS : one barrel Tile calorimeter up to  $|\eta| = 1$  and one extended barrel with the same technology up to  $|\eta| = 1.7$ , one LAr-copper calorimeter for the end-cap, and one forward calorimeter.

**The Tile Calorimeter** In the central part of the detector, the hadronic calorimeter consists in a sampling calorimeter made out of steel absorbers to create particle showers, and of plastic scintillator tiles as active medium to measure them. What is actually measured in this calorimeter is the ultraviolet scintillation light that is produced when a charged particle crosses the active medium. For each tile, this scintillation light is collected by a wavelength-shifting optical fibre, and is converted into visible light in this fibre. The output of the fibre is connected to a photo-multiplier where the signal is measured. It is segmented into three layers in depth, and the total depth of this system is of  $\approx 7\lambda$  (nuclear interaction length). This ensures a negligible amount of hadronic leakage to the muon spectrometer (punch-through), especially given that it should be added to the depth of the LAr calorimeter and of the services, giving a total of more than  $10\lambda$  in front of the muon spectrometer everywhere in the detector.

**End-cap Hadronic Calorimeter** The hadronic end-cap calorimeter (HEC) is also a sampling calorimeter based on a LAr technology, except that its absorbers are made of copper. It spans a region  $1.6 < |\eta| < 3.2$ , and is embedded in the same cryostat as the end-cap LAr EM calorimeter. Each HEC is built as two separate wheels, the first of which is composed of a series of 25 mm thick flat copper layer and 8.5 mm wide LAr gaps. In the second wheel the main change is the thickness of the copper layers, which is of 50 mm. The HEC is approximatively 10 interaction lengths deep.

**Forward Calorimeter** The measurement of the missing-energy and of forward jets requires a detector that is as hermetic as possible, which is achieved by extending the calorimeter system up to  $|\eta| = 4.9$  with the forward calorimeter (FCal), which is also a

sampling calorimeter based on a LAr technology. The detector is segmented in three layers in depth. The first layer uses absorbers in copper and is targeting the measurement of forward electromagnetic particles, while the two others, that are further downstream, are using tungsten absorbers. The size of the LAr gap varies between 0.27 mm in the first sampling to 0.51 mm in the third. The FCal is approximatively 10 interaction lengths deep.

### 3.2.6 The muon spectrometer

The muon spectrometer is composed of several chambers, whose technology varies as a function of their utility and of their position (in  $\eta$ ). Indeed it was not possible to achieve at the same time a precise measurement of the muon momentum and a response that is sufficiently fast for the trigger, therefore in a given region these two different kinds of chambers are installed. Furthermore given the variation of the muon-tracks density with respect to the pseudo-rapidity, the requirements were different between the inner-part of the detector and the outer one, hence the technology used slightly changes at  $|\eta| = 2$ . The complete layout of the muon system may be seen in fig. 3.8.

Up to  $|\eta| = 2$  the precision momentum measurement is done solely by monitored drift tubes (MDT) that are straw tubes in which a gas will be ionized, and the ionization electrons will be collected at a wire in the center of the tube. At every  $\phi$  there is at least 3 layers of chambers of this kind. At  $2.7 > |\eta| > 2$  the most inner layer changes and is using cathode strip chambers (CSC), which allow for a higher segmentation of the chamber. The CSC are essentially multi-wire proportional chambers, with the cathode segmented into strips, and where the direction of the strip is perpendicular to the one of the wires. This allows for two independent measurements of the muon : one for the ionization electrons that are collected at the wire, the other one from the induced signal collected at the strips. This also gives the two coordinates of the muon, which in the MDTs comes from the trigger chambers.

The trigger chambers extends up to  $|\eta| = 2.4$ . For  $|\eta| < 1.05$  the trigger is done by Resistive Plate Chambers (RPCs), in which two parallel plates are separated by a thin layer of gas than the crossing muon will ionize. This ionization signal will drift toward one of the two metallic plates at which it will be measured. Beyond  $|\eta| = 1.05$  the trigger uses thin gap chambers (TGCs), in which a layer of anode wires lies between two parallel plates that are at the ground. The whole system is inside a gas that the crossing muons will ionize, and the ionization electrons will be collected on the wires. An optimization of both the gas gap and of the high-voltage at which the system is operated allows to have a very fast response for both the RPCs and TGCs, which makes them well suited from triggering purposes.

It should be noted that in the very center of the detector ( $|\eta| < 0.1$ ) the muon chambers are not instrumented, and the LAr EM and Tile calorimeter are used to recover a sizeable part of the muons. For more details see [179, 180].

### 3.2.7 Luminosity detectors

Several techniques can be used to measure the luminosity delivered by the LHC to ATLAS, and some of them are using sub-detectors that have already been described before. For

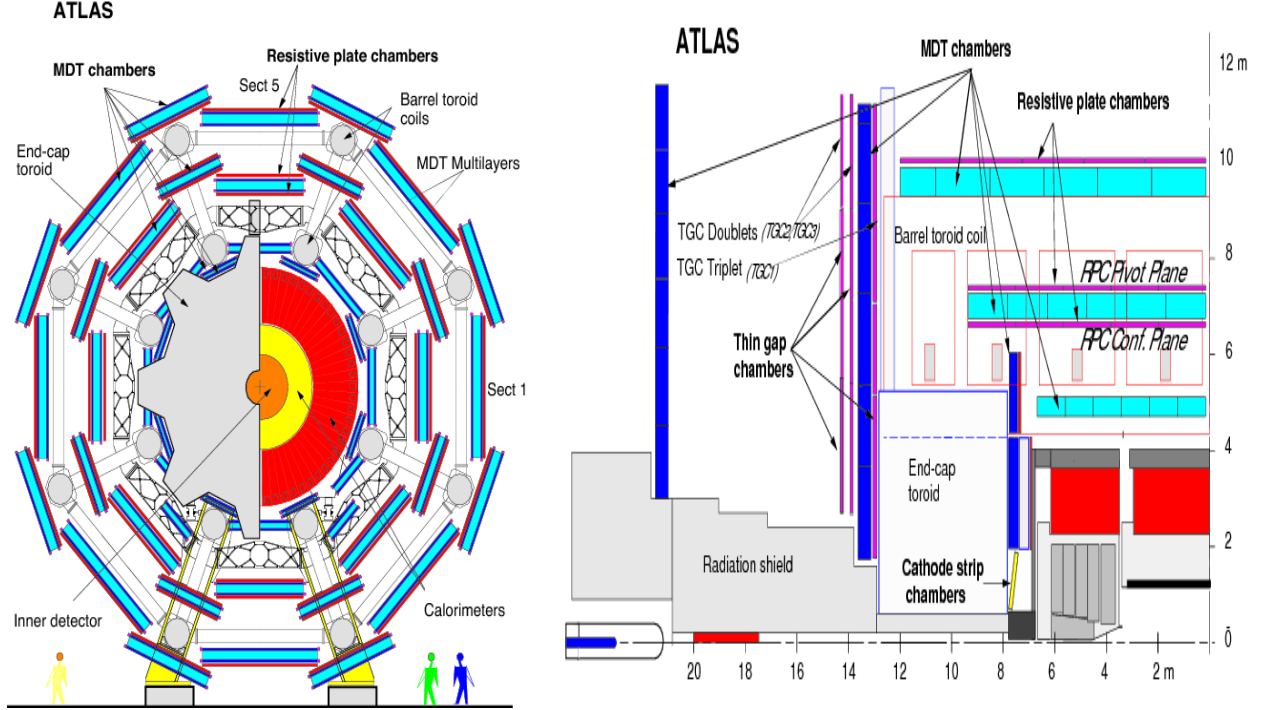


Figure 3.8: Schematic view of the muon spectrometer in the x-y (left) and z-y (right) projection. Inner, Middle and Outer chamber stations are denoted BI, BM, BO in the barrel and EI, EM, EO in the end-cap. [181]

instance the multiplicity of tracks in the inner detector, or the current measured at the output of the calorimeter are sensitive to the luminosity as is described in [174]. But there are also a few sub-detectors that have not been described before and which are essential in the luminosity determination. The two detectors below provide only a relative luminosity measurement and need to be calibrated using the Van Der Meer scans.

**Luminosity measurement using Cerenkov Integrating Detector (LUCID)** The LUCID detector is a Cerenkov detector, installed at 17 m from the interaction point ( $\eta \approx 6$ ). Effectively it gives a measurement of the multiplicity of charged particle in the forward direction, as all the Cerenkov signals will be integrated. This is connected to the rate of inelastic scattering at this angle, and from the measurement of this rate it is possible to determine the luminosity of the LHC.

**Beam Conditions Monitor (BCM)** The BCM, whose first use-case was to provide a beam diagnostic system in order to dump the beam in cases where it may damage the inner-tracker, can be used to measure the luminosity. It is made of four small diamond detectors that are set around the beam-pipe at  $\approx 2$  m ( $\eta = 4.2$ ) of the interaction point and estimates the level of background by giving a precise count of the number of crossing particles. There is one detector of this kind on each side of the interaction point.

## 3.3 Description of the ATLAS electromagnetic calorimeter

### 3.3.1 Global description of the concept

The electromagnetic (EM) calorimeter of the ATLAS detector is a sampling calorimeter, based on absorbers that are made of lead where most of the signal is actually created, and of liquid-argon gaps between the absorbers, that constitute the active material where the signal is actually measured. The details of the physical processes that are involved in the creation and measurement of this signal are described in the following part. This detector is of primary importance in ATLAS as it is the only detector that measures photons, and it is the most powerful for electrons (except at low-energy where the inner tracker is more precise), which are at the center of the Higgs physics program. Therefore it was thoroughly optimized to suit the needs of the  $h \rightarrow 4e$  and  $h \rightarrow \gamma\gamma$  channels, which requires a good energy resolution, good background rejection (especially against boosted  $\pi^0 \rightarrow \gamma\gamma$ ), and an efficient identification of electro-magnetic particles. Furthermore this calorimeter is segmented into three layers in depth, which allows to use the barycentre of the energy deposited in the first two layers to constrain the position of the primary vertex, which improves the mass resolution. With regard to previous noble-liquid calorimeters, the big break-through of the ATLAS EM calorimeter is the geometry of the absorbers and read-out electrodes, that is based on an accordion shape, following an idea of D. Fournier [182]. The details of this geometry and its advantages will be described below.

### 3.3.2 Interaction of electromagnetic particles with matter

A proper understanding of the electromagnetic showers development inside the EM calorimeter requires a knowledge of the interactions between electromagnetic particles and matter. This physics is diverse and depends a lot on the energies involved in the process, but we are here only interested in the physics of high-energy particles, whose interactions with matter are essentially ruled by bremsstrahlung for the electrons and conversion for the photons. The process of ionization also needs to be described as it is the source of the signals that are recorded by the EM calorimeter, and it has a fundamental role in the physics of electromagnetic showers. All other processes, such as Compton scattering, will not be described here but are explained in [52]. In ATLAS, all these processes are simulated using the Geant 4 framework [183, 184], which implements them with a description that is more complete than what will be described below. Also all the numerical values that will be quoted as example are corresponding to the ATLAS EM calorimeter, and are taken from [1], where the corresponding values for other materials may be found.

#### Ionization of a field by charged high-energy particles

In the low energy regime (from  $\beta\gamma = 0.1$  to  $\approx 20$ ) the main mechanism of energy loss for electrons and positrons is the ionisation of the surrounding medium. Effectively this corresponds to a scattering of the particle on the electrons of the atoms of the medium in which it moves, during which these electrons are also scattered out of their atoms. This can be treated as the scattering of the incoming particle on the atom itself, which is the

base of the Bethe formula [52] that gives the mean energy loss of the incident particle per unit length, and incidentally also the total energy that the electrons scattered in this interval will carry. This formula reads :

$$- \left\langle \frac{dE}{dx} \right\rangle = K z^2 \frac{Z}{A \beta^2} \left( \frac{1}{2} \ln \frac{2 m_e c^2 \beta^2 \gamma^2 T_{max}}{I^2} - \beta^2 \right) \quad (3.5)$$

and its effect is represented in fig. 3.5. The result is given in  $MeV g^{-1} cm^2$ , and the parameters are defined as follows :

- K is a constant
- Z is the charge of one nucleus in the target and A its atomic mass
- z the charge of the incident particle
- $\beta$  the velocity of the incident particle
- $T_{max}$  the maximal kinetic energy that may be transferred to the electron in a collision, which in a low-energy approximation can be expressed as  $2 m_e c^2 \beta^2 \gamma^2$
- $I \approx 10Z$  eV is the ionisation energy of the target atoms

Assuming this is the only source of loss, the energy loss of low energy particles is the most extreme, because they suffer from the field of the electron they are scattering on before escaping, and the energy loss decreases until  $\beta\gamma = 3 - 4$ , which correspond to what is usually called "minimum ionizing particles" (MIP). The value of the energy loss at the MIP can be fitted by a linear function of Z for sufficiently large Z ( $> 6$ ). Going at further higher energies, the loss will start to logarithmically grow, because of the increase of the transverse component of the electric field in the relativistic regime, which will make the incoming particle sensitive to electrons that are further away from its path. In the region where this formula is valid, and for a given target medium, the energy loss almost exclusively depends on the charge and the momentum of the incident particle, the dependence on its mass being fairly small. The dependency on the target density is recovered by converting  $\left\langle \frac{dE}{dx} \right\rangle$  to its equivalent in  $MeV cm^{-1}$ . It should be noted that for dense targets with incident particles in the relativistic regime an additional correction to the Bethe formula is required to take into account the fact that the increased electric field may polarize the target near its path.

### Bremsstrahlung

At higher energies the electrons will start to lose energy by emitting photons under the effect of the bremsstrahlung. It is a known fact that the trajectory of any charged particle in a magnetic field will bend, and that the momentum conservation requires the emission of an additional particle, which implies a decrease of the energy of the incident particle. In matter the magnetic field will be the electromagnetic field of the nuclei of the medium. It can be shown that the average energy loss can be simply parametrized as  $\frac{dE}{dx} = \frac{E}{X_0}$ ,  $X_0$  being the radiation length which grows linearly with the number of nucleons in the nuclei, and decreases with the number of protons, which is expected as the mean free path

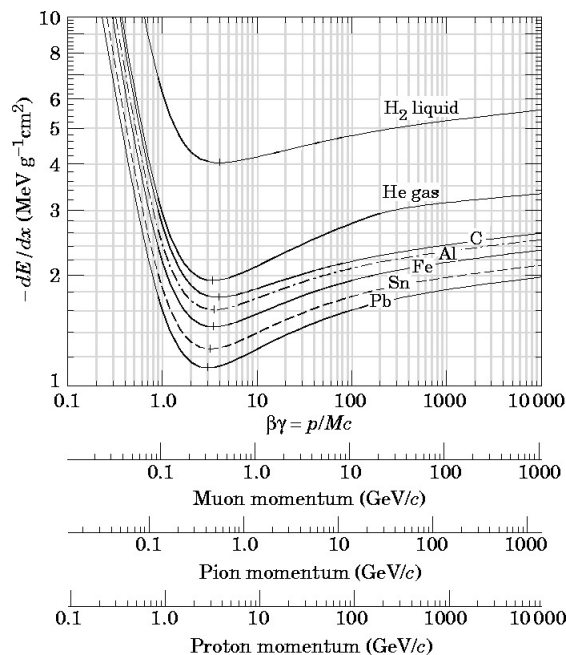


Figure 3.9: Mean energy loss for various type of particles and different mediums, as computed by the Bethe formula [52]

of a charged particle in a medium has to decrease when the density of charged particles increases. After one radiation length a given electron will only have in average a fraction  $\frac{1}{e}$  of its initial energy anymore. For the ATLAS EM calorimeter the main contribution to the radiation length comes from the lead, for which  $X_0 = 0.56$  cm.

### Photon conversions

Although the Compton scattering process has a non-negligible cross-section up to energies of a few GeVs, in this energy range the main mechanism for photon energy loss is the conversion of photons to  $e^+e^-$  pairs, which can only happen in a medium. In this process, after the  $\gamma ee$  vertex one of the two electrons will have to be off-shell because of energy-momentum conservation. This off-shell particle will then exchange another photon with one of the component of the medium - most probably a nucleus but it can also be an electron. This process is described in fig. 3.10. It may be shown that at high-energy ( $> 1$  GeV) the cross-section for photon conversion may be approximated as  $\sigma = \frac{7}{9} \frac{A}{X_0 N_A}$ , and therefore the dependence in the medium constituents is the qualitatively the same than for bremsstrahlung. It may also be used to show that the probability that a photon has not converted after  $\Delta x = \frac{9}{7} X_0$  is  $e^{-1}$ .

It should be noted that for very-high energies, both the bremsstrahlung and the photon conversion processes may be suppressed. As the electromagnetic interaction spreads over longer distances, the incident particle will start to become more sensitive to atoms further away from its path, and the scattering amplitudes over the multiple atoms will interfere, most usually destructively. This effect, which is called the "Landau-Pomeranchuk-Migdal" effect is further described in [52] and would start to have an importance for particles with energies of several TeVs in the ATLAS EM calorimeter.

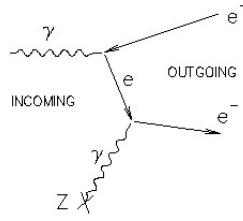


Figure 3.10: Feynman diagram for the photon conversion process

### Physics of electromagnetic showers

In a real detector, with an incident particle at sufficiently high energy, the processes of bremsstrahlung and photon conversion may happen in cascade, hence creating a shower of electromagnetic particles. It is the shower that is actually used to detect photons and electrons, and measures their energies in the EM calorimeters used at the LHC. Most of the physics of these showers may be described using two scales : a distance scale that is the radiation length  $X_0$ , and an energy scale  $E_c$  which is the critical energy.  $E_c$  corresponds to the energy at which the energy lost by an electron due to bremsstrahlung is equal to the energy lost by ionization, which is 7.4 MeV for electrons in the lead of the ATLAS EM calorimeter. This also corresponds to the energy scale at which an electromagnetic shower does not develop anymore : above  $E_c$  an electron will emit a photon through bremsstrahlung that may itself convert to an  $e^+e^-$  pair, but below  $E_c$  the electron will mainly ionize the medium and will not generate more electromagnetic particles, hence effectively stopping the shower development. It is possible to show that  $E_c = \frac{a}{Z+b}$  where a, b only depends on whether the target medium is a gas. Now we can introduce the two dimensionless variables  $y = \frac{E}{E_c}$  and  $t = \frac{x}{X_0}$ ,  $t$  being the depth in the shower, which can parametrize the shower.

It is possible to show that during the shower development the maximum of the energy deposited will occur at  $t_{max} = \frac{a-1}{b} = \ln y + C_j$  where a,b depend on the material and the incident particle energy and  $C_j = 0.5$  for photon,  $-0.5$  for electrons. Therefore the penetration power for the shower created by a given particle does not increase much with its energy, as it increases only by  $\approx 2 X_0$  when the energy is increased by a factor 10. It is also important to realize that the penetration power of electron showers is more important than the one of photons, by about  $1 X_0$ , which essentially comes from the fact that for photons the first interaction will have to be a conversion, which is less probable than the bremsstrahlung emission for an electron. Now it is also possible [185] to show that in a simplified shower model the maximal depth a particle may reach in the shower is proportional to  $X_0$  and to  $\frac{E_0}{E_c}$  where  $E_0$  is the initial energy of the incident particle, and 95% of the energy is contained in  $t_{95} = t_{max} + 0.08Z + 9.6$ . This explains why at higher energies there may be a sizeable energy leakage in the back of the ATLAS EM calorimeter or even beyond it. The full longitudinal shower profile can be described analytically and is represented in fig. 3.11 for a typical material. At the end, the total number of particles produced in the shower is proportional to  $\frac{E_0}{E_c}$  (that shows the need of having low  $E_c$ ), and this is what is used to determine the energy of the incident particle : each of the charged particle in the shower will create an ionization signal, and effectively the signal measured by the calorimeter correspond to a counting of these particles that is afterwards converted

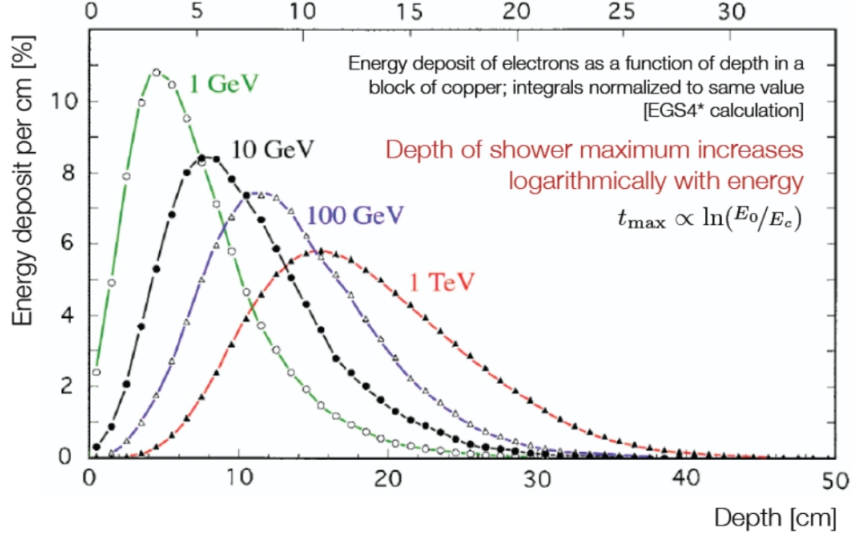


Figure 3.11: Electron shower profiles in copper for several energies of the incident electron, as a function of the depth in the material [185]

to an energy. This also explains the existence of the sampling term in the resolution parametrization, that corresponds to Poisson fluctuation on this count, which is measured in the ATLAS accordion sampling calorimeter.

Now we are not only interested in the depth of the shower, but also in its lateral extension. In the high-energy regime this is dominated by multiple-scattering effects, which generate a Gaussian distribution of the scattering angles in the collisions. The RMS of this distribution will correspond to the opening angle of the shower itself, and is given, for a shower that grows over a length  $x$ , by  $\langle \theta \rangle = \frac{E_s}{E_c} \sqrt{\frac{x}{X_0}}$  where  $E_s = m_e c^2 \sqrt{\frac{4\pi}{\alpha}} = 21.2$  MeV is the scale energy, related to the characteristic energy of fundamental processes in the multiple scattering. If we focus the development of a shower over  $1 X_0$ , this opening angle may be converted into a physical distance scale, which defines the Moliere radius  $R_M = \frac{X_0 E_s}{E_c}$ , which is a very powerful characterization of the showers that will develop in a given medium as 90% of the shower energy will be contained in  $1 R_M$ , 95% in  $2 R_M$ . In the ATLAS EM calorimeter  $R_M \approx 4.8$  cm [186]. The only dependence of the lateral shape of a shower on the material comes through a simple parametrization with regard to  $E_c$  and  $X_0$ , that is very accurate in the core of the shower. In the one or two first  $X_0$ , or far in the lateral tails (at several  $R_M$ ), this parametrization is not very accurate as other effects have a similar importance that the multiple interaction.

### 3.3.3 From electromagnetic shower to recorded signals

In the ATLAS EM calorimeter the showers are mainly generated in the lead, which is the denser material, and the LAr is primarily here as an active material in which the ionisation electrons can move and will drift toward an electrode where the signals they produce will be measured.

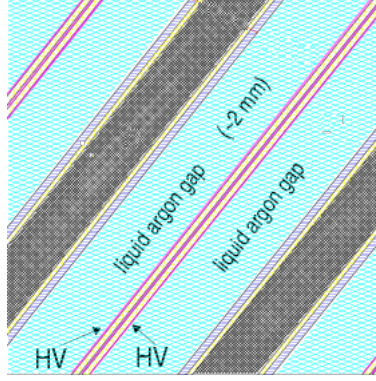


Figure 3.12: Description of the composition of the LAr EM calorimeter

### Drift of ionisation electrons toward electrodes

Between each lead absorber there is a LAr gap, in which an electric field is applied. In the middle of the gap lies an electrode at high voltage which will also collect the signal. This electrode corresponds to the red lines in fig. 3.12, but in fact it is itself divided in several parts : there are two outer electrodes on each side from which the electric field is imposed, and one inner electrode which is here to collect the signal. All of these electrodes are made out of copper, and between these lies a layer of Kapton (see for instance the original test-beam publication in 1991 [187]) which insulates the electrodes from each others. The two outer electrodes are connected to a different high-voltage (HV) power supply, which allows for redundancy and gives the possibility to preserve the energy response of the cells when one side of one cell does not hold the HV. The HV is uniform over the whole electrode since in general there is no current in the electrodes. The two sides of each gap are delimited by the lead absorbers, which are glued inside stainless steel, and are set at the ground of the system, which is required to set the gradient of potential in the proper direction to make the electrons drift toward the read-out electrode. To avoid short-circuits in this system, which would modify the field in the gap and decrease the calorimeter performance, and to stabilize the accordion shape of the electrodes, a honeycomb spacer lies in the LAr gaps. The honeycomb is the most optimized shape to conserve a mechanical stability without disturbing the electric field lines. In the barrel of the EM calorimeter, the full LAr gap width is 4.2 mm, the thickness of an absorber is 1.7 mm and the power supply gives a nominal HV of 2000 V, while in the end-cap it varies with  $\eta$  between 1000 and 2500 V [1]. In the barrel this corresponds to a drift time of  $T_{drift} \approx 450$  ns at  $T = 88.5$  K and the corresponding ionisation of a shower signal has a triangular shape before the electronic shaping, that lasts from 0 to  $T_{drift}$ , as may be seen in fig. 3.13. The drift velocity changes with the LAr temperature, which affects the energy response of the calorimeter as it changes the pulse length, hence it modifies the signal. The variation of the calorimeter response is of  $-2\%/K$  out of which the biggest part ( $-1.5\%$ ) comes from the change of the drift velocity ([188] paragraph 2.1.2.3), and the small remaining fraction comes from the variation of the LAr density. The presence of impurities in the LAr could also bias the energy response as the additional components may capture part of the ionisation electrons. It was shown that the level of impurities should stay below one part per million in order not to impact the response, and until now it stayed at the level of 0.1-0.3 per million,

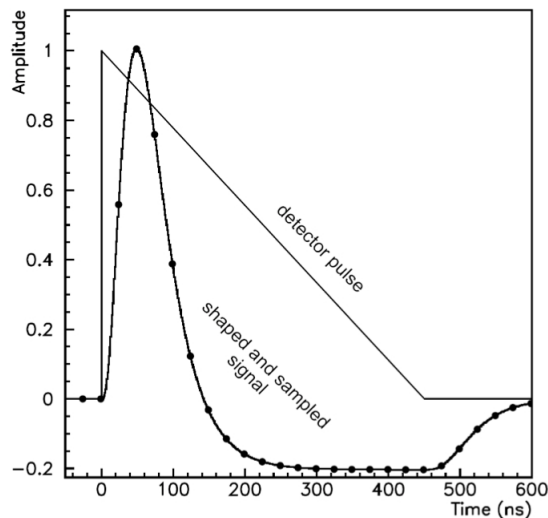


Figure 3.13: Ionisation signal from the ATLAS EM calorimeter, before (triangular) and after the electronic bipolar filtering. The dots correspond to the 25 samples that may be recorded for a given signal

depending on  $\eta$ .

### Impact of short-circuits and non-nominal HV

During the construction and the filling of the calorimeter few impurities have formed, and "connected" the electrodes at 2000 V to the lead which is at the ground. This creates a change in voltage distribution over the electrode, as it will be forced to be at 0 V at the point of the short and upstream, while it will vary from 0 to the power supply voltage beyond the short, and this effectively modifies the energy response of the cell in which the short happens. Moreover due to the effect of Ohm's law, the power supply that corresponds to the affected cell will start drawing current which means that every cell of the sector which is alimented by this power supply will be affected, and that the voltage measured at the power supply does not correspond to the one that exists at the level of the cells. Some attempts to burn these shorts by injecting a high current pulse were conducted [189], and were successful in several sectors, but not for all the observed shorts. When a short remains, it is sometimes possible to reduce the HV at a level where there is no leakage current, or even to set the HV at 0 V for the side where the short lies. In such cases a method to recover the energy response of the cell was described in [190] and essentially multiplies the measured cell energies by a power of the measured HV, where the exact exponent is fitted on a simulation. It was not possible to derive a correction for the case where there is a leakage current as it would require the knowledge of the position of the short-circuit.

### 3.3.4 Anatomy of the ATLAS EM calorimeter

There are actually three electromagnetic calorimeters in ATLAS, each in its own cryostat : one barrel calorimeter and two end-caps, as may be seen in fig. 3.14. In the end-caps, beyond the electromagnetic calorimeter one finds the end-cap hadronic calorimeter, and

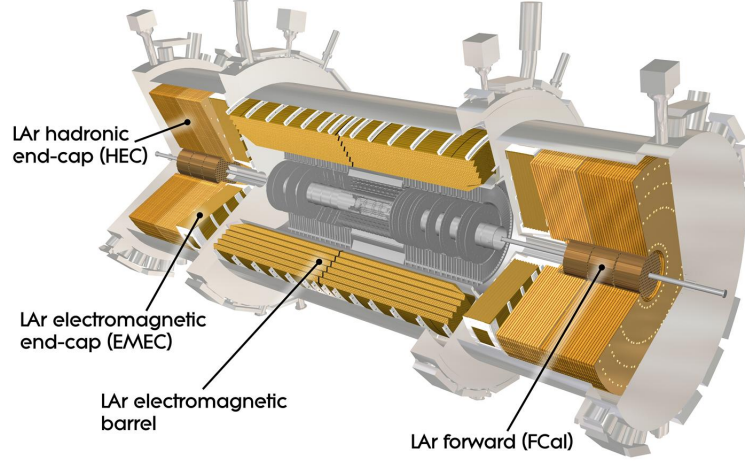


Figure 3.14: Overall schematic description of the liquid argon calorimeters [191]

in the most inner part of the end-caps cryostats are the forward calorimeters. While both of them are also based on a liquid-argon technology, they are described in subsection 3.2.5 and will not be detailed here as their geometry, absorbers and services are fairly different. The barrel of the calorimeter was also constructed as two separate yet identical parts, one for  $\eta < 0$  (side C) and one for  $\eta > 0$  (side A) that were assembled and installed in the same cryostat afterwards. As a consequence there is a small gap of  $\Delta\eta = 2 * 0.025/8$  (around  $2 \times 5$  mm) at  $\eta = 0$  which is not instrumented.

### Anatomy of an accordion cell

One of the big breakthrough of the ATLAS EM calorimeter is the geometry of its electrodes, which follows an accordion shape in  $\phi$ , where the LAr gaps, electrodes and absorbers are interleaved and projective with respect to the interaction point. The previous LAr calorimeters were made in a sequence absorbers, gaps and electrodes that were placed at given radii, and the readout was done on the side of the electrodes which required holes in the calorimeter at specific  $(\eta, \phi)$  coordinates. In ATLAS the readout is done either on the front of the cells for the first layer of the calorimeter or on there back for the others, which allows for a more hermetic and uniform detector. It also allows for a faster read out as the connections are shorter [192]. In the barrel a constant width was required for the LAr gap, which was achieved by changing the angle at each fold of the accordion, decreasing it at increasing radius. This was not possible in the end-cap, but it is compensated by varying the HV as a function of  $\eta$  too.

The calorimeter is read-out in three different samplings in depth, and the cells of the three samplings have different properties, that are displayed in fig. 3.15 for  $\eta = 0$ , hence they can serve different purposes in physics analyses. The first sampling (strips) has a very fine segmentation in  $\eta$  which allows to differentiate between a genuine photon and an energy deposit coming from a  $\pi^0 \rightarrow \gamma\gamma$  decay which may happen inside a jet, and where the  $\pi^0$  is boosted hence the opening angle of the diphoton pair is small, but can

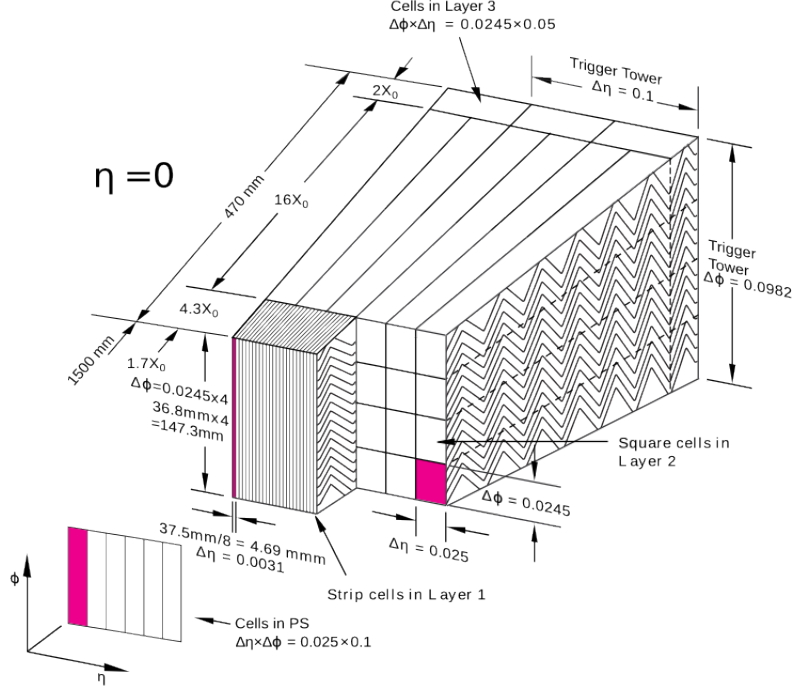


Figure 3.15: Sketch of a typical barrel module of the liquid argon EM calorimeter [1]

still be resolved in the strips. The second sampling (middle) carries most of the energy measured and is the deepest, while the third one is thinner and is mainly here to estimate the amount of energy leaking beyond the LAr. The exact segmentations of the cells of the three layers as a function of  $\eta$  are given in table 3.16, and there are 256 cells in  $\phi$  for the second layer. Due to the accordion geometry of the electrodes, a given electrode usually spreads over the size of two cells (in  $\phi$ ) in the middle, although it is read-out in only one of them. In the barrel there are 1024 accordion-shaped absorbers (see fig. 3.15) while in the outer wheel of the end-cap ( $|\eta| < 2.5$ ) there are 768 absorbers, and 256 in the inner wheel.

As stated before, each electrode needs to be connected to two HV power supplies, but these supplies will be the same for several cells. In the barrel all the HV sectors have a segmentation of  $\Delta\eta \times \Delta\phi = 0.2 \times 0.2$  ( $= 8 \times 8$  middle cells), as is the case for most of the end-cap sectors except for a few cases where the sector is smaller in  $\eta$ . These smaller sectors are defined as follow :  $|\eta| \in [1.375 - 1.5]$ ,  $[1.5 - 1.6]$ ,  $[2.0 - 2.1]$ . The same power supply is feeding the three samplings, which requires the existence of electrical connexions between the electrodes, and this is achieved using a resistive ink that connects the layers. This can be seen in fig. 7 of [193].

### The Front End Boards

The signals from the read-out electrodes are collected from the back of the calorimeter (for the middle and back layer), or from its front (for the strips), and are then sent to the Front-End Crates (FECs) next to the feed through of the calorimeter, and are described in fig. 3.17. For the EM calorimeter, there is no cold electronics inside the LAr cryostat. The electronic amplification and shaping of the signal, as well as its digitization, is done

	Barrel		End-cap	
<b>EM calorimeter</b>				
Number of layers and $ \eta $ coverage				
Presampler	1	$ \eta  < 1.52$	1	$1.5 <  \eta  < 1.8$
Calorimeter	3	$ \eta  < 1.35$	2	$1.375 <  \eta  < 1.5$
	2	$1.35 <  \eta  < 1.475$	3	$1.5 <  \eta  < 2.5$
			2	$2.5 <  \eta  < 3.2$
Granularity $\Delta\eta \times \Delta\phi$ versus $ \eta $				
Presampler	$0.025 \times 0.1$	$ \eta  < 1.52$	$0.025 \times 0.1$	$1.5 <  \eta  < 1.8$
Calorimeter 1st layer	$0.025/8 \times 0.1$ $0.025 \times 0.025$	$ \eta  < 1.40$ $1.40 <  \eta  < 1.475$	$0.050 \times 0.1$	$1.375 <  \eta  < 1.425$
			$0.025 \times 0.1$	$1.425 <  \eta  < 1.5$
			$0.025/8 \times 0.1$	$1.5 <  \eta  < 1.8$
			$0.025/6 \times 0.1$	$1.8 <  \eta  < 2.0$
			$0.025/4 \times 0.1$	$2.0 <  \eta  < 2.4$
			$0.025 \times 0.1$ $0.1 \times 0.1$	$2.4 <  \eta  < 2.5$ $2.5 <  \eta  < 3.2$
Calorimeter 2nd layer	$0.025 \times 0.025$ $0.075 \times 0.025$	$ \eta  < 1.40$ $1.40 <  \eta  < 1.475$	$0.050 \times 0.025$	$1.375 <  \eta  < 1.425$
			$0.025 \times 0.025$ $0.1 \times 0.1$	$1.425 <  \eta  < 2.5$ $2.5 <  \eta  < 3.2$
Calorimeter 3rd layer	$0.050 \times 0.025$	$ \eta  < 1.35$	$0.050 \times 0.025$	$1.5 <  \eta  < 2.5$
Number of readout channels				
Presampler	7808		1536 (both sides)	
Calorimeter	101760		62208 (both sides)	
<b>LAr hadronic end-cap</b>				
$ \eta $ coverage			$1.5 <  \eta  < 3.2$	
Number of layers			4	
Granularity $\Delta\eta \times \Delta\phi$			$0.1 \times 0.1$	$1.5 <  \eta  < 2.5$
			$0.2 \times 0.2$	$2.5 <  \eta  < 3.2$
Readout channels			5632 (both sides)	
<b>LAr forward calorimeter</b>				
$ \eta $ coverage			$3.1 <  \eta  < 4.9$	
Number of layers			3	
Granularity $\Delta x \times \Delta y$ (cm)			FCal1: $3.0 \times 2.6$	$3.15 <  \eta  < 4.30$
			FCal1: $\sim$ four times finer	$3.10 <  \eta  < 3.15,$ $4.30 <  \eta  < 4.83$
			FCal2: $3.3 \times 4.2$	$3.24 <  \eta  < 4.50$
			FCal2: $\sim$ four times finer	$3.20 <  \eta  < 3.24,$ $4.50 <  \eta  < 4.81$
			FCal3: $5.4 \times 4.7$	$3.32 <  \eta  < 4.60$
			FCal3: $\sim$ four times finer	$3.29 <  \eta  < 3.32,$ $4.60 <  \eta  < 4.75$
Readout channels			3524 (both sides)	
<b>Scintillator tile calorimeter</b>				
	Barrel		Extended barrel	
$ \eta $ coverage	$ \eta  < 1.0$		$0.8 <  \eta  < 1.7$	
Number of layers	3		3	
Granularity $\Delta\eta \times \Delta\phi$	$0.1 \times 0.1$		$0.1 \times 0.1$	
	Last layer $0.2 \times 0.1$		$0.2 \times 0.1$	
Readout channels	5760		4092 (both sides)	

Figure 3.16: Summary of the main parameters of the ATLAS calorimeters [1]

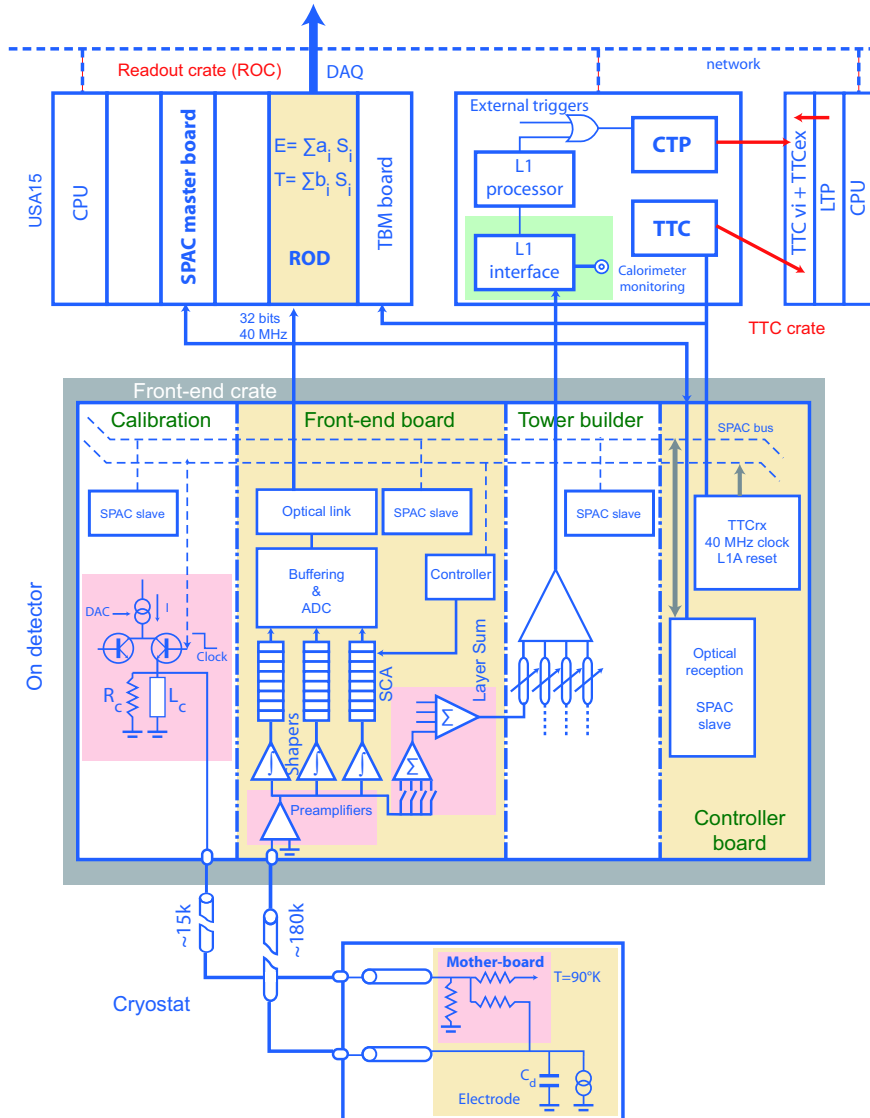


Figure 3.17: Block diagram depicting the EM calorimeter front-end crates components [1]

on the Front-End Board (FEB) [194, 195], which we will focus on in this sub-part. The trigger and calibration boards will be described later. The main role of the FEB is to amplify and shape the signal from the electrodes, then to send it to the read-out back-end if the event from which the signal originates passes the trigger.

First, a pre-amplifier multiplies the signal to a level which is above the noise of the full electronic chain that comes downstream. The gain of the pre-amplifier, as well as the detector sampling fraction, are roughly constant over the detector and changes only at  $|\eta| = 0.8$ , where the thickness of the lead absorber is modified, which is compensated by changing the gain of the pre-amplifier between the region  $|\eta| < 0.8$  and  $|\eta| > 0.8$ . The output of the pre-amplifier is sent to the shaper, which is one of the key elements of the calorimeters electronics. It uses a bipolar CR-RC<sup>2</sup> electronic filter, whose main property is to give an output signal with a null integral, as may be seen in fig. 3.13. This has the advantage that it suppresses the pile-up noise on average, and afterwards the only impact of the pile-up will be a degradation of the resolution due to the Poisson fluctuations of the

number of pile-up interactions. Simultaneously to this shaping an additional amplification of the signal is done, and there are in fact three outputs from the electronic shaping chip, each one corresponding to a different gain : high, medium and low (HG/MG/LG), where the ratio of these three gains is 93/9/1. The output of this chip is sampled every 25 ns and stored in Switched Capacitor Arrays (SCA), with one SCA by gain. These SCAs can register up to 144 samples which give sufficient time to wait for the trigger decision before further processing. If the event is saved, the corresponding samples are digitized using a commercial 12 bits Analog to Digital Converter (ADC). Together with the three gains, the 12 bits ADC gives the required dynamic range of 16 bits. In order to choose which gain will be used for a given event, the sample corresponding to the expected maximum of the ionization peak (the third sample recorded in the event) is digitized in MG, and depending on the value of the ADC counts for this sample, the gain in which the cell will be read is chosen. All the samples corresponding to the same pulse will be digitized in the same gain for a given cell. Basically a cell of the middle layer will be read-out in HG until its transverse energy reaches 30 GeV, then in MG up to 400 GeV, then in LG and the ADC will saturate at a transverse energy of roughly 3 TeV. It is not necessary to have the whole pulse (25 samples) to reconstruct the energy of a particle, and for the Run 1 it was decided to save only the first five contiguous samples. The digitized samples are then sent to the read-out crates which are in the service cavern where there is no radiation. The read-out crates will not be detailed here but are documented in [196].

### Trigger cards

During their processing in the FEBs, right after the shaper, the calorimeter signals are sent to the Tower Builder electronics card [194], which is the only component of the trigger that lies in the FECs. The tower builder receives the signal of several cells and sums them to build a trigger tower which is the basic ingredient for the calorimeter trigger. The region covered by a given tower is of  $\Delta\eta \times \Delta\phi = 0.1 \times 0.1$  which corresponds to  $4 \times 4$  middle cells in most of the detector. The signal of the trigger tower is digitized in the cavern by steps of 1 GeV, and with a saturation of the trigger ADC at 256 GeV, but this is sufficient for a trigger. This digital signal is obtained from an analog signal obtained in the Tower Builder sent to the service cavern, where the trigger informations from all the calorimeter and the other sub-detectors are gathered and processed, which corresponds to the level 1 trigger (L1). Several algorithms may create a L1 trigger signal, which is then sent back to the controller board of the FEC. After a trigger signal, the whole detector is sent to the read-out back-end and stored in the read-out buffers, and it is the controller board that will initiate the digitization and read-out of the SCAs on the FEBs. The latency of the L1 trigger system is of  $2.5 \mu s$ , and it has a rate of  $\approx 75 kHz$ .

Afterwards there are two other levels of trigger. The layer 2 (L2) has access only to the region of interests (RoI), that are cones around the regions from which a trigger signal originated, but it has access to all the sub-detectors in this region, including all the cells of the calorimeter in the RoI, which allows to run more complex algorithms and to decrease the trigger rate by a factor  $\approx 100$ . The last level is the "Event Filter" which is a high-level trigger in which the full event can be reconstructed and processed, using a reconstruction program that is very close to the offline reconstruction. At the end the trigger rate is of  $\approx 100 Hz$ . A visual description of the full chain of triggers may be found

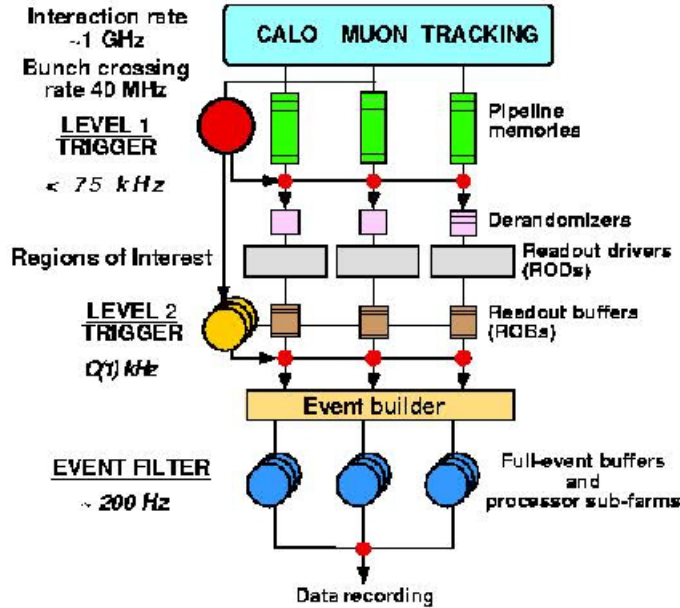


Figure 3.18: Sketch of the ATLAS trigger systems [197]

in fig. 3.18.

### The presampler

Although it is also based on a LAr technology, the pre-sampler (PS) of the ATLAS EM calorimeter is very different from the accordion calorimeter. First, the pre-sampler does not contain any absorber material, but only the electrodes and the LAr, and it also does not cover the entire calorimeter, as it stops at  $|\eta| = 1.8$  in the end-cap. The geometries for the barrel ( $|\eta| = 0 - 1.52$ ) and end-cap ( $1.5-1.8$ ) pre-samplers are different, but are relying on the same concept of having a thin layer of LAr ( $\approx 1$  cm in the barrel) in which electrodes are interleaved. In such a scheme the main energy loss will be by ionization of the LAr, which allows to recover part of the energy for a particle that would have started showering before reaching the PS.

The barrel pre-sampler modules are made of interleaved cathode and anode electrodes, and have a spacing of 2 mm between each others. The anode electrodes are made of three layers, like the electrodes of the accordion calorimeter, with the two outer layers being connected to a +2 kV HV and the inner layer being here for the read-out. The three layers are separated by a glass-fibre composite. The cathodes consist of two layers that are connected to the ground. In the end-cap the electrodes are perpendicular to the beam-axis and thus parallel to the cryostat wall [188]. There are three electrodes : two external electrodes are fixed to the inner and outer walls of the end-cap PS and are connected to a negative HV, while the third one, where the signal will be read, is connected at a ground. The spacing between the external and the read-out electrodes is still of 2 mm in the end-cap.

### 3.3.5 Energy reconstruction with the calorimeter signals

#### Reconstruction of the calorimeter pulses

The only outputs that are measured for a given cell in a given event (and saved for the cells that are above a given threshold), are the 5 digitized samples of the ionization pulse, which are evaluated in number of ADC counts. These are the values from which the energy and timing of the signal in this cell will be reconstructed. Every other informations that are needed to reconstruct the cells energies come from either test-beam studies or the detector simulation, or calibration runs. The calibration runs rely on a specific electronic card that injects a signal in the calorimeter, and that will be described below. The complete formula used to reconstruct the energy is [198] :

$$E_{cell} = F_{\mu A \rightarrow MeV} F_{DAC \rightarrow \mu A} \frac{1}{\frac{M_{phys}}{M_{cal}}} G \sum^{Samples} a_j (s_j - p) \quad (3.6)$$

where the parameters are defined as follows :

- $s_j$  correspond to the measured digital samples, in ADC counts
- $p$  corresponds to the electronic pedestal, which is measured in specific calibration runs
- $F_{\mu A \rightarrow MeV}$  corresponds to the conversion factor between the ionisation current generated in a cell and the total energy deposited in this cell in MeV, which has been measured in a test-beam [199]
- $F_{DAC \rightarrow \mu A}$  makes the conversion between the digital signal sent to the calibration card and its output which is an analogical current. This allows to convert back the samples  $s_j$  to the original current, and it is known from the calibration cards construction
- $G$  is the gain of the cell, measured during the calibration runs (expressed in ADC  $\rightarrow$  DAC)
- $\frac{1}{\frac{M_{phys}}{M_{cal}}}$  is a factor that corrects the gain to take into account the fact that the injected calibration signal is exponential while the physics signal is triangular, and have therefore slightly different maximal amplitudes after the bipolar shaping. It can be obtained from delayed calibration runs, as is described in [200]
- $a_j$  corresponds to a part of the Optimal Filtering Coefficients (OFC) that are at the heart of the calorimeter signal reconstruction, and are determined using the expected shape of the signal [4, 201]

There are in fact two sets of OFCs,  $a_i$  and  $b_i$ , which are linked to the amplitude and the timing of the signal. We define the following two values  $U = \sum^{samples} a_i (s_i - p)$  and  $V = \sum^{samples} b_i (s_i - p)$ , and the OFCs are defined as the values of the  $(a_i, b_i)$  for which  $\langle U \rangle$  corresponds to the amplitude of the signal A, and  $\langle V \rangle = A\tau$  where  $\tau$  is the

timing of the signal, and for which the variance of  $U$  and  $V$  are minimal. Therefore this gives by construction the most powerful determination of the amplitude and of the timing of the pulse. This minimization requires the knowledge of the expected shape of the signal, as well as of the expected noise as it modifies the variance of  $U$  and  $V$ . During the 2011 data-taking this optimization was done only considering the electronic noise, and the pile-up noise was added only for the 2012 run but was assuming 20 simultaneous interactions and a bunch-crossing period of 50 ns.

### Electronics calibration

As can be seen on fig. 3.17 a specific electronics card [202], the Calibration Board, is embedded in the FEB crate. Its main role is the injection of a signal of known amplitude and timing to the cells. The calibration pulse originates from a known digital signal which is converted to an analog current in the calibration board. This current flows in an inductance  $L_C$ , and once  $L_C$  is loaded the current is switched off and the magnetic energy is released and creates a voltage which is transmitted to the read-out electrode by a resistance that is in the LAr cryostat. Given that the central process here is the decay of the charge of an inductance it can only give an exponential signal, which is an approximation of the triangular shape of the physics signal. A given calibration board serves several calorimeter cells in  $\phi$ , but always only one in  $\eta$  which allows to study to cross-talk between cells in calibration runs. Indeed, due to the structure of the absorbers that are following the accordion in  $\phi$ , there is no cross-talk in  $\phi$  in the LAr itself. A cross-talk could still exist in the electronic read-out but it is expected to be much smaller than the one in the LAr, which is in  $\eta$  only. The exact repartition of the calibration lines to the EM calorimeter cells may be seen in fig. 3.19. Typical peak-peak cross-talk values for neighbouring cells are  $\approx 7\%$  for the strips and  $\approx 1\%$  for the middle layer [203].

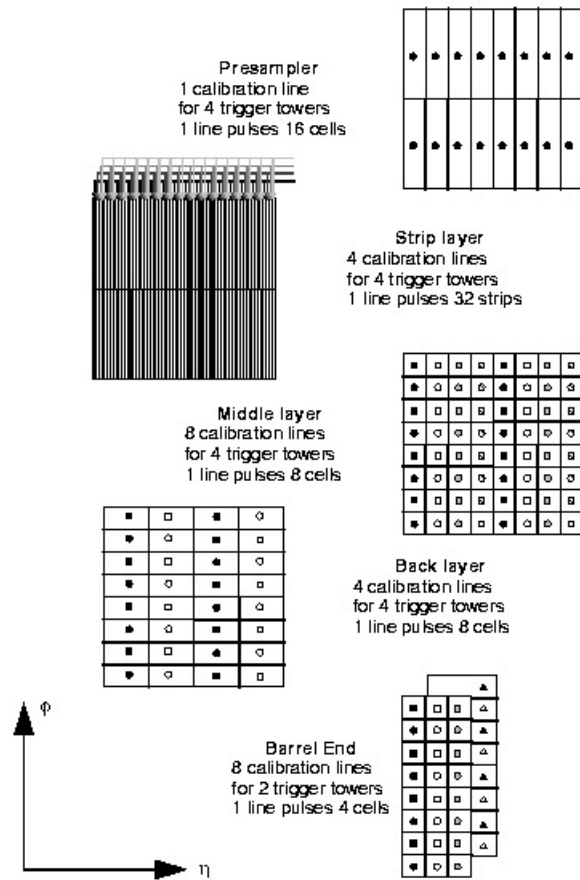


Figure 3.19: Schematic description of the repartition of the electronic calibration lines to the LAr cells, in the barrel of the EM calorimeter [188]

## 3.4 Reconstruction of electrons and photons at ATLAS

### 3.4.1 Reconstruction of electromagnetic clusters

#### The sliding window cluster seeding

The algorithm used to find clusters in the electromagnetic calorimeter is based on a sliding window technique, which has been described in [204], as well as the full logic on which the cluster construction is based. This constructs pre-clusters of  $3 \times 5$  middle cells (in  $\eta \times \phi$ ), and sums all the cells in the 4 longitudinal samplings that are facing these 15 cells (including the pre-sampler). If one of these pre-clusters has a transverse energy above 2.5 GeV an actual cluster is seeded. After having found these  $3 \times 5$  cells pre-clusters, one will produce the final clusters, whose exact size will depend on the nature of the particle and of the detector (barrel or end-cap). For an electron or a converted photon in the barrel, the size of the cluster is of  $3 \times 7$  cells which allows to recover part of the energy lost by bremsstrahlung, that is expected to be found in  $\phi$  given the direction of the inner tracker magnetic field, along the beam axis. For unconverted photons, that are not sensitive to this effect, the cluster is of  $3 \times 5$  which allows to slightly decrease the impact of the noise. In the end-cap every electromagnetic object has a cluster of  $5 \times 5$  cells. The size of these clusters was optimized before the data-taking, and they were chosen to improve the energy resolution of the electromagnetic objects. These cluster sizes are likely to be changed for the Run 2.

#### Differentiation between electrons, unconverted and converted photons

In ATLAS the differentiation between electrons, converted photons and unconverted photons relies solely on the inner tracker. Tracks matching the cluster (in  $\eta$  and  $\phi$ ) are searched for, and if two matching tracks are found an attempt to fit a conversion vertex is carried out. To be valid this conversion vertex has to satisfy a few conditions, for instance on the invariant mass of the two-tracks system that needs to be close to 0 ( $= m_\gamma$ ). In some cases there may be converted photons for which only one track is reconstructed, for instance if the two tracks are too collimated to be separately reconstructed or if the conversion is very asymmetric and one of the tracks is not energetic enough to be detected. In such cases it is not possible to build a conversion vertex, but there is a track matching the cluster that may be reconstructed, and it is still possible to flag the photon as converted. Strong requirements are enforced on this track parameters, such as requirements on the position of the first hit in the track which can not be on the b-layer as we consider only photons that convert in the tracker, or on the fraction of high-threshold hits in the TRT which discriminates between conversion electrons and pions. The full logic of conversion reconstruction has been described in [205–208]. The clusters that are not flagged as coming from converted photons and in front of which there is no matching tracks are considered as coming from unconverted photons, while those for which there is a track are flagged as electrons. Although there might be some ambiguities between converted photons and electrons, a tool was developed to resolve them and is also described in [208]. For the final results of the Run 1 an additional constraint on the conversion radius was enforced

( $R_{conv} < 80$  cm) in order to remove conversions in the outer part of the inner detector where the conversion reconstruction is expected to be inefficient, and where most of the converted photons are coming from fake conversions. In two-tracks conversion  $R_{conv}$  is the radius of the conversion vertex while in one-track conversion it is the radius of the first hit of the track.

### 3.4.2 Offline identification of photons [2]

#### The identification menus

The identification of photons in ATLAS is based on a sequence of rectangular cuts that are applied on several variables that characterize the shape of the corresponding electromagnetic showers [209]. Another discriminating variable is the amount of energy that leaks beyond the EM calorimeter as charged hadrons are expected to deposit a sizeable part of their energy in the hadronic calorimeter too. For the photons two identification criteria are provided, loose and tight, the first one giving the highest efficiency to select photons, but also the largest background contamination. The second one, which is used for the  $h \rightarrow \gamma\gamma$  analysis, decreases the signal efficiency but improves the purity of the sample. The variables used for the identification are independent of whether the photons are flagged as converted, although the precise values of the cuts may vary. The loose selection only looks at energy leaking in the hadronic calorimeter and at the shape of the shower as seen in the middle sampling, which is expected to give a coarser description of the shower as it is less granular than the strips. This menu uses the same cuts for converted and unconverted photons, and gives a photon efficiency higher than 99% at  $E_T^\gamma > 40$  GeV. The tight menu includes the cuts from the loose criteria, and adds cuts on the shape of the shower as it is seen in the strips, which is a more powerful layer to reject the background from jets in which light hadrons (such as  $\pi^0$ ,  $\eta$ ) may decay to two collimated photons. Using the fine segmentation of the strips it is possible to build variables that are sensitive to the difference between such a decay and a prompt photon, as can clearly be seen on fig. 3.20 where for the  $\pi^0 \rightarrow \gamma\gamma$  decay there are two distinguished energy maxima in the strips that are not resolved in the middle. This gives a photon efficiency of  $\approx 85\%$  and a very good rejection of the jet background of  $R = \frac{N_{jet}}{N_{fake \gamma}} = 5000$ . The optimization of the tight menu is done separately for the converted and unconverted photons. The exact variables that are considered during the optimization of the tight and loose menus are shown in table 3.1. Another approach based on a neural network was developed for photons in the 2011 data [89, 210]. The input variables to the neural network algorithm are the same as for the cut-based approach, with the addition of the photon pseudo-rapidity.

#### Fudge-Factors for shower shape variables

As will be described later in this thesis, the lateral shape of the electromagnetic showers is imperfectly described by the ATLAS detector simulation [211, 212], and the source of this mismodelling has not been understood yet. As these variables are at the heart of the photon identification strategy, a method to overcome this discrepancy was needed and this corresponds to the "Fudge Factors" that are documented in [4]. The mismodelling is approximated by a shift of the mean of the shower shape variable and can be effectively

Category	Description	Name	Loose	Tight
Acceptance	$ \eta  < 2.37$ , with $1.37 <  \eta  < 1.52$ excluded	–	X	X
Hadronic leakage	Ratio of $E_T$ in the first sampling of the hadronic calorimeter to $E_T$ of the EM cluster (used over the range $ \eta  < 0.8$ or $ \eta  > 1.37$ )	$R_{had_1}$	X	X
	Ratio of $E_T$ in the hadronic calorimeter to $E_T$ of the EM cluster (used over the range $0.8 <  \eta  < 1.37$ )	$R_{had}$	X	X
EM Middle layer	Ratio of energies in $3 \times 7 \eta \times \phi$ cells over $7 \times 7$ cells	$R_\eta$	X	X
	Lateral width of the shower	$w_{\eta_2}$	X	X
EM Strip layer	Ratio of energies in $3 \times 3$ cells over $3 \times 7$ cells	$R_\phi$		X
	Shower width calculated from three strips around the strip with maximum energy deposit	$w_{s_3}$		X
	Total lateral shower width	$w_{s\text{tot}}$		X
	Energy outside the core of the three central strips but within seven strips divided by energy within the three central strips	$F_{\text{side}}$		X
	Difference between the energy associated with the second maximum in the strip layer and the energy reconstructed in the strip with the minimal value found between the first and second maxima	$\Delta E$		X
	Ratio of the energy difference associated with the largest and second largest energy deposits over the sum of these energies	$E_{\text{ratio}}$		X

Table 3.1: Variables used for loose and tight photon identification. The X corresponds to the variables that are included in a given menu [2]

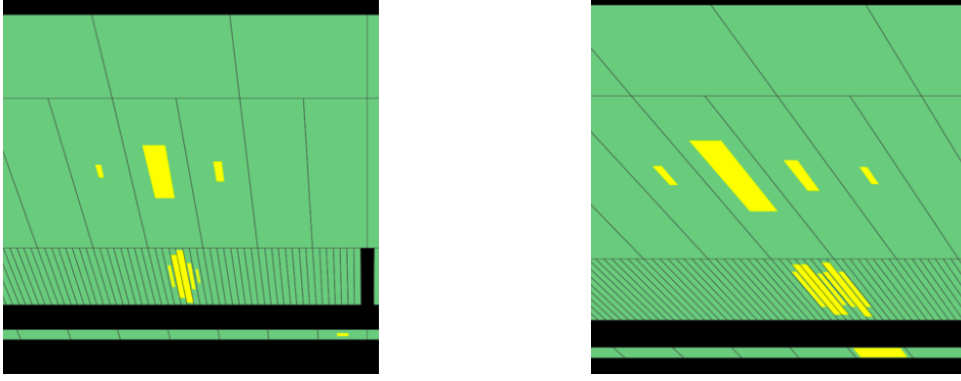


Figure 3.20: Zoom of two events displays on the EM calorimeter, showing the energy deposited by a prompt photon (left) and the shower created by a  $\pi^0 \rightarrow \gamma\gamma$  (right)

corrected on the MC, by adding a constant value to the simulated shower shape of each photon. These fudge-factors are estimated in single-photon samples, and are taken as the data to MC difference of the average of the shower-shape that is being considered, and are afterwards applied on the MC to correct it. The corrected MC is then used to optimize the cuts and evaluate the photon efficiency and the background rejection.

### Estimation of the efficiency

Three different methods have been developed to estimate the photon efficiency, and are afterwards combined together, which improves the result especially given that they cover different energy ranges. Preliminary results for the Run 1 photon efficiency can be found in [213] and the final results are expected to be published later [2].

The first method, which is particularly optimized for the low-energy regime, is based on a tag-and-probe technique that uses radiative  $Z \rightarrow ll\gamma$  decays. The main cut that impacts the photon is a cut on  $m_{ll\gamma}$ , every other cut being done on the quality of the lepton reconstruction and on their energies, and this is sufficient to give a pure photon sample. The photon identification can then be studied and the efficiency to select photons using the tight menu is estimated as  $\epsilon_\gamma = \frac{N_{tight \gamma}}{N_{Z \rightarrow ll\gamma \text{ events}}}$ . The main source of systematic uncertainty in this study is the uncertainty on the background normalization, whose impact is estimated by subtracting it from the  $m_{ll\gamma}$  fit. This method has the drawback that the energy of the photon in radiative Z events is fairly low, and this analysis stops at  $p_T = 80$  GeV and is precise only up to  $p_T = 40$  GeV.

The second method makes an extrapolation from the shower shape variables of the electrons in  $Z \rightarrow ee$  events to estimate photon shower shapes. For each of the shower shape variables a Smirnov transform [214] is built on MC to transform the distribution for electrons into the photon distributions. This transform is then applied to the shower shape variable observed for  $Z \rightarrow ee$  electrons on data, which is a very pure sample of electrons, and the distributions for the transformed electrons correspond to what is expected for photons. The photon identification criteria are applied on the transformed electrons, which allows to derive the photon efficiency. The main systematic for this method is the material budget in front of the calorimeter, which modifies the transform built on the MC as the shower shapes are changing with the material. As this method is using the  $Z \rightarrow ee$

peak it can only probe the transverse energy range 30-100 GeV, but has a decent precision over this whole range.

The last method, the "matrix method" [215, 216], uses a dataset of single-photons that are passing the loose identification criteria, and gets the level of background by splitting the dataset in two with regard to a variable that can isolate the background, and the background is then extrapolated to the region where the signal is. Applying the same method to a dataset where the tight identification criteria is enforced allows to derive the photon efficiency of the tight identification menu. In this case the variable that is used to extract the background is the track isolation, as the prompt photon are expected not to be surrounded by tracks while the photons from the jet backgrounds will be. The dominant systematic comes from the difference between the true track isolation and the observed one, which changes the selection efficiency when applying this isolation. The big advantage of this method is its ability to cover a wide energy range (20-1500 GeV) as it uses single photons, for which it is easy to get a large statistics.

These three methods are then combined to give the best possible determination of the efficiency. The photon efficiency, which is displayed in fig. 3.21 is everywhere above 90% for  $E_T^\gamma > 40$  GeV, while its uncertainty is everywhere below 2% and even falls below 1% for  $E_T^\gamma > 40$  GeV. These efficiencies are increasing with  $E_T^\gamma$ .

### 3.4.3 Offline identification of electrons [3]

The procedure for the electron identification in ATLAS, as well as its performance, is fully documented in [3]. It provides more identification menus than for the photon identification, as it can cut not only on the shower shape variables but also on the quality of the tracks, the number of hits in the different layers of the tracker, and the high-threshold hits information from the TRT. Four menus based on rectangular cuts on these variables are provided. Loose, medium, tight are single-electron identification criteria but there is also one menu, the MultiLepton, that was optimized for the  $h \rightarrow ZZ^* \rightarrow 4l$  channel where there are low  $p_T$  electrons. The information from the TRT, especially the fraction of hits in the reconstructed track that are passing the high-threshold criteria, is not included in the loose selection but is considered in all the others. It is similar for the b-layer hit information. In addition to these cut-based menus three menus based on a likelihood-ratio have been developed : loose, medium and very-tight. The final  $h \rightarrow ZZ^* \rightarrow 4l$  analysis of the Run 1 used the likelihood-based loose identification criteria, which was optimized for this particular signature and gave the same signal efficiency than the cut-based multi-lepton menu, but improved the background rejection by a factor of  $\approx 2$ . The efficiency is estimated on data using a tag-and-probe method based on  $Z \rightarrow ee$  and  $J/\Psi \rightarrow ee$  decays, where strong requirements are set on one of the two electrons (the tag electron), and the only requirement on the second electron (the probe electron) is on the di-electron invariant mass and on the track quality. Then the number of probe electrons that pass a given identification gives the electron efficiency of this specific identification criteria. The main uncertainty on this method comes from the background modelling, which is evaluated from control regions where the isolation and identification cuts of the tag electrons are inverted. The results from Z and  $J/\Psi$  decays are afterwards combined together. The electron identification efficiency is above 95% for  $E_T$  above 15 GeV and its uncertainty varies from 1.5% at low  $E_T$  to 0.5% for  $E_T > 25$  GeV.

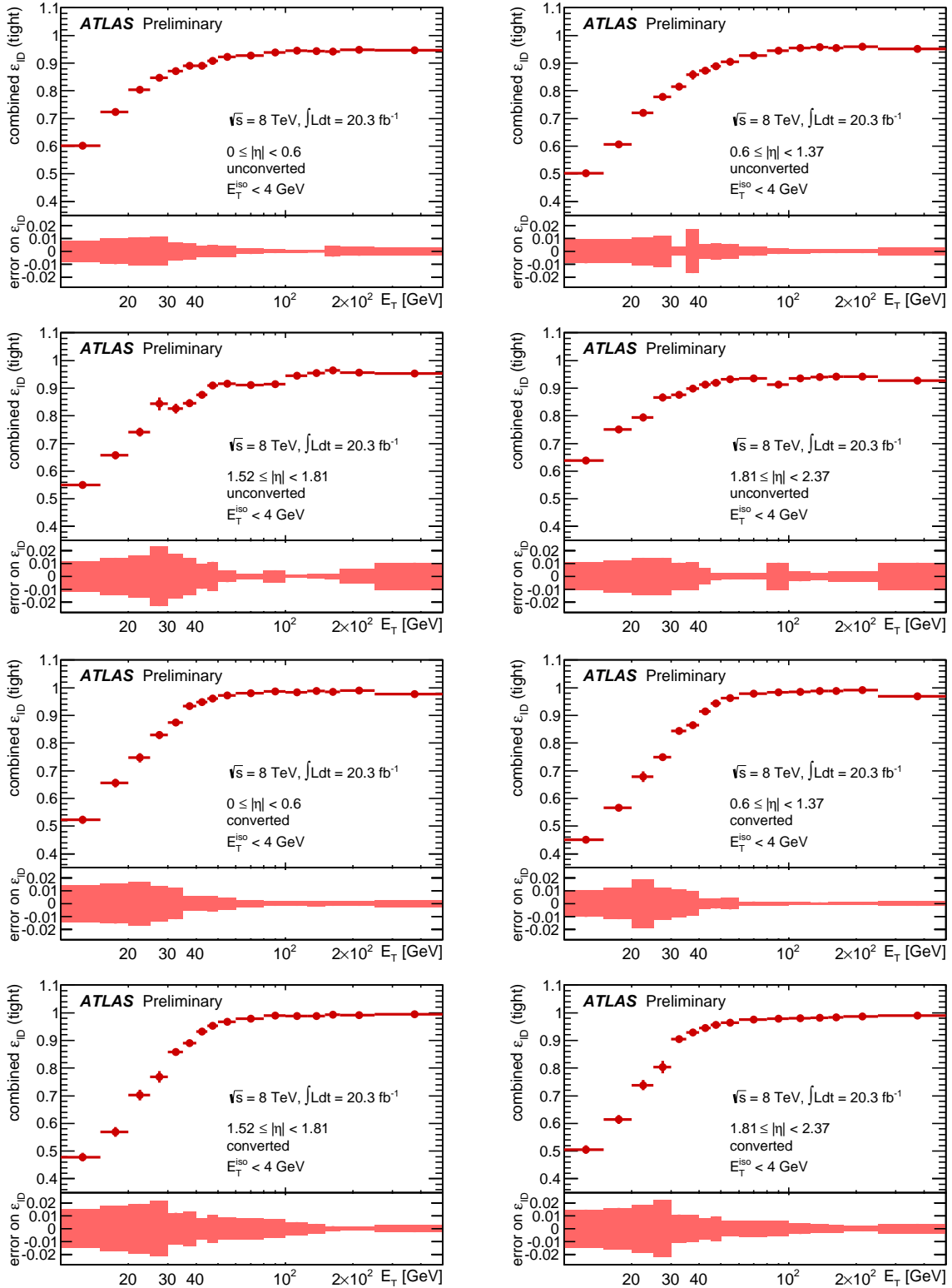


Figure 3.21: Photon efficiency of the tight photon selection criteria, for converted (bottom) and unconverted (top) photons, as a function of their transverse energy and pseudo-rapidity [213]

## 3.5 Comparison with the CMS detector

### 3.5.1 Overall description of the CMS detector

The CMS detector [217] was conceived to address the same physics program as ATLAS, and follows a similar building architecture, but the conception of the sub-detectors and of the reconstruction algorithms is different. Its overall design architecture may be seen in fig. 3.22. A detailed comparison of the design of the two detectors can be found in [218]. First, its inner tracker is entirely done with technologies based on Silicon, and the magnetic field in the region of the tracker is much stronger than in ATLAS, reaching 4 T. Both the electromagnetic and hadronic calorimeter are within the solenoid magnet, which gives additional constraints to the detector electronics. The hadronic calorimeter is a sampling calorimeter, made of brass absorbers and of plastic scintillators as active material. There are also one or two thin layers of scintillator outside of the magnet coil at low  $\eta$  in order to detect late showers and suppress noise in the muon chambers. The electromagnetic calorimeter will be described below. The magnetic field return is done with a steel yoke, within which the muon chambers are embedded. The muon chambers are made of RPCs for the trigger and either drift tube chambers (in the barrel) or CSCs in the end-cap. The detector is made hermetic by adding a forward calorimeter made of steel absorbers and quartz fibres to collect the signal. The overall design of the CMS detector (and the fact that the CMS hadronic calorimeter has a worse resolution than the one from ATLAS) implies that its event reconstruction relies more on the tracker than ATLAS does, which is for instance illustrated by the use of the particle flow [219] or the fact that given the high material budget in the return yoke, the resolution of the muon momentum would be worse without the tracker.

### 3.5.2 Description of the electromagnetic calorimeter

The CMS electromagnetic calorimeter is a homogeneous calorimeter made of lead tungstate ( $\text{PbWO}_4$ ) crystals. An overall scheme of its design may be seen in fig. 3.23. The complete shower of the incident particle is measured and not only its energy deposits in the active material samplings, which means that it is less sensitive to statistical fluctuations on an event-by-event basis, and the stochastic resolution term becomes smaller by construction. As the  $\text{PbWO}_4$  crystals have a high density, short radiation length and a small Moliere radius of 2.3 cm [221] they allow for a compact calorimeter with reasonably fine granularity (a crystal has a segmentation of  $\Delta\eta \times \Delta\phi = 0.0174 \times 0.0174$  in the barrel). The scintillation light is collected in the rear of the crystals where its yield is measured by photo-detectors, whose exact technology varies between barrel (avalanche photo-diode) and end-caps (vacuum photo-triode). A laser system has been designed [222] to monitor the response of the crystal and compensate for temporary radiation induced losses of the crystal transparency. The CMS EM calorimeter is built as one barrel calorimeter and two end-caps, where the separation between the two detectors is done at  $|\eta| = 1.5$ , while the full calorimeter covers the region up to  $|\eta| = 3$ . It is not segmented in depth and cannot be used to reconstruct the direction of incident particles, which means that the reconstruction of the primary vertex only relies on the tracking detector. To improve the  $\pi^0$  rejection capabilities in the end-cap a pre-shower detector is added in front of the calorimeter, and

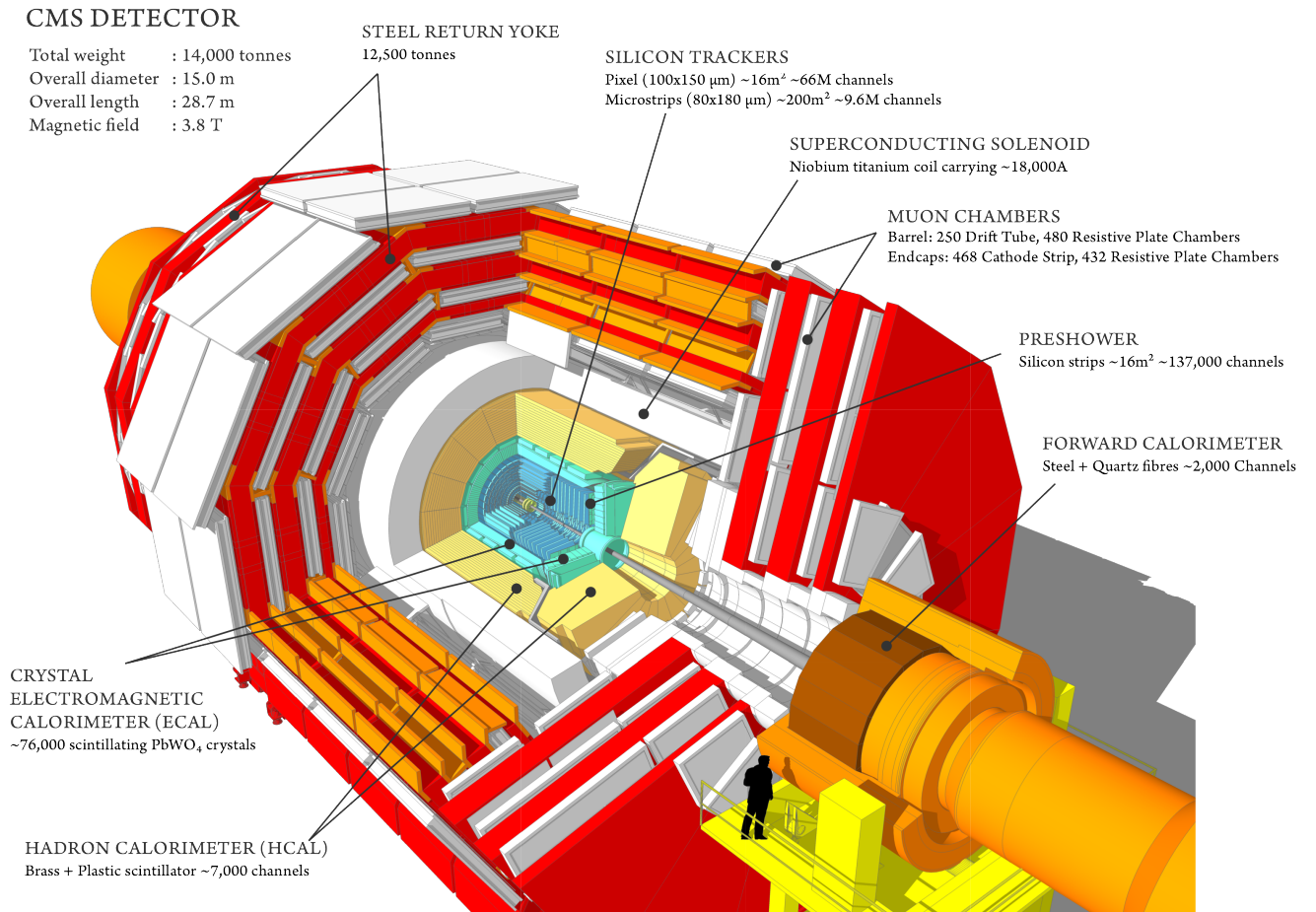


Figure 3.22: Overall layout of the CMS detector [220]

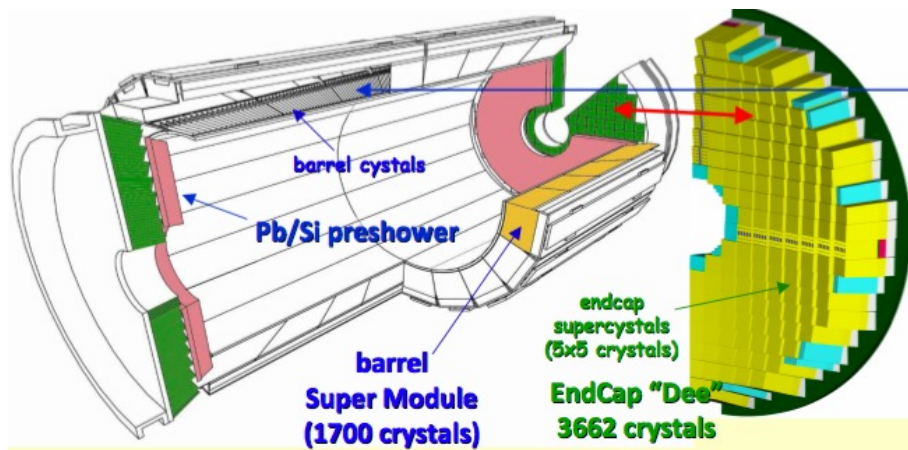


Figure 3.23: Schematic description of the CMS electromagnetic calorimeter [223]

it is made of two planar silicon detectors that are placed after lead absorbers.

### 3.5.3 Reconstruction of electromagnetic particles in CMS

The reconstruction of electromagnetic particles in CMS is based on the super-cluster algorithm and is fairly different than in ATLAS. This starts by finding a seeding crystal, whose energy should pass a given threshold, and from this seed the super-cluster is expanded dynamically. Lines of  $5 \times 1$  crystals (in  $\eta \times \phi$ ) that are contiguous to the super-cluster are looked at in both  $\phi$  directions, and if they pass some energy threshold they are added to the super-cluster, although no more than 17 lines may be added. The variable  $R_9 = \frac{E_{3 \times 3}}{E_{SuperCluster}}$  is defined, and if the  $R_9 > 0.94$  (in the barrel, 0.95 in the end-cap) the super-cluster is narrowed to its  $5 \times 5$  inner crystals, otherwise the full super-cluster is kept to estimate the particle energy. At this point no difference have been made between electrons, converted and unconverted photons. Given the high magnetic field and high material budget in the CMS tracking region, in addition to the fact that there is no additional material between the tracker and the calorimeter, the shower shapes are more sensitive to the type of incident particle in CMS than in ATLAS : for instance the electrons are expected to radiate more, and the angular opening (at the level of the calorimeter) of the conversion pairs will be larger. Both of these effects happen in  $\phi$ . This means that, from the calorimeter point of view, the  $R_9$  variable drives the discrimination between the different particle hypotheses, as may be seen in fig. 3.24 for the discrimination between the different conversion status. The discrimination between the photon and electron hypothesis comes from the tracker and is described in [224]. As the cluster reconstruction does not depend on whether the incident particle converted, the photon energy calibration may be done in the same way, which implies that the systematic uncertainties related to the conversion reconstruction mis-modelling are considered as not relevant.

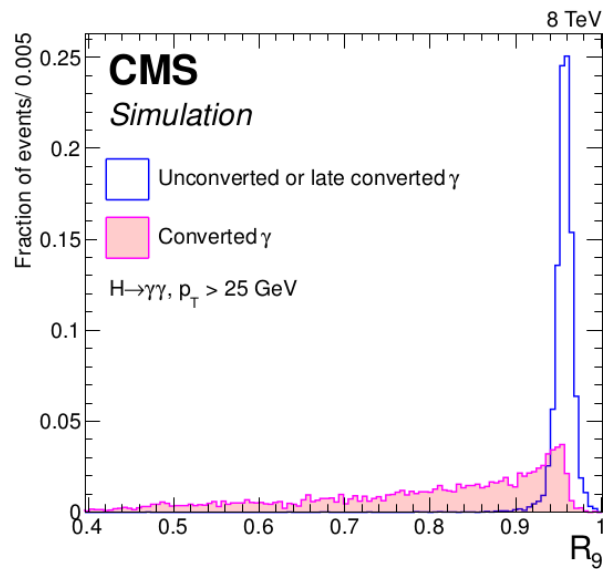


Figure 3.24: Distribution of  $R_9 = \frac{E_{3 \times 3}}{E_{SuperCluster}}$  for converted (with a radius of conversion lower than 85 cm) or unconverted photons (or late-converted) in CMS [221]



# Chapter 4

## Electromagnetic calibration of the ATLAS detector

### Contents

---

<b>4.1</b>	<b>Global overview of the calibration procedure</b>	<b>104</b>
<b>4.2</b>	<b>Monte-Carlo based calibration</b>	<b>105</b>
4.2.1	Determination of the material in front of the calorimeter	105
4.2.2	Multi-variate Calibration	108
<b>4.3</b>	<b>Corrections to the energy response on data</b>	<b>111</b>
4.3.1	Intermodule gaps	111
4.3.2	Pre-sampler high-voltage	111
4.3.3	High-voltage in the accordion	112
4.3.4	Inter-layer calibration	118
4.3.5	Presampler (PS) energy scale	119
<b>4.4</b>	<b>Correction for an apparent non-linearity</b>	<b>122</b>
4.4.1	Presentation of the problem	122
4.4.2	Extraction of the energy response difference	122
4.4.3	Cross-checks of potential explanations	126
4.4.4	Derivation of an ad-hoc correction	133
4.4.5	Correlation with the shower-shape mismodeling	136
<b>4.5</b>	<b>Lateral energy leakage</b>	<b>137</b>
4.5.1	Position of the problem	137
4.5.2	Overview of the method	139
4.5.3	Cross-checks of potential electron to photon differences	140
4.5.4	Final results	145
<b>4.6</b>	<b>Determination of the energy scale of the calorimeter</b>	<b>146</b>
4.6.1	Absolute energy scale	146
4.6.2	Stability, uniformity and linearity of the energy response	148

---

<b>4.7</b>	<b>Extrapolation of the energy scale to photons</b>	<b>153</b>
4.7.1	Mismodeling of the conversion reconstruction	153
4.7.2	Energy scales from photons	153
<b>4.8</b>	<b>Electron and photon energy resolution</b>	<b>156</b>
<b>4.9</b>	<b>Comparison between 2011 and 2012 data-taking</b>	<b>157</b>
4.9.1	Layer 1 Gain	157
4.9.2	Crack non-linearity	158
<b>4.10</b>	<b>Possible improvements toward Run II</b>	<b>159</b>
4.10.1	Inner detector rail mismodeling	159
4.10.2	Out of cluster leakage	160
<b>4.11</b>	<b>Comparison with the CMS calibration</b>	<b>160</b>

---

## 4.1 Global overview of the calibration procedure

The energy calibration for electrons and photons in the ATLAS detector is an involved process, that will be described below. It required several studies to optimize the energy reconstruction, develop all the pre-corrections to be applied on data to correct for biases in the energy response, extract the systematic effects that would create uncertainties, determine the absolute energy scale of the calorimeter, and cross-check these results on other processes. The sequence of all these steps is described on fig. 4.1, and will be detailed in this part. It starts with the determination of the material budget in front of the calorimeter. This is a study that requires a proper inter-calibration of the first two layers of the EM calorimeter, derived using the signal from muons crossing the detector. Once the material budget is known, a multi-variate algorithm (MVA) is trained on Monte-Carlo samples to reconstruct the particles energy from different variables that can be measured in the calorimeters. On data there are several effects that may create localized or time-dependent biases of the energy response, which require the determination of a set of pre-corrections that are applied to data after the MVA energy reconstruction. At this point the absolute energy scale of the EM calorimeter, as well as its energy resolution, can be determined by a fit of the  $Z \rightarrow ee$  mass peak, whose shape is well known from the LEP measurements [52, 138]. These measurements are applied to every electro-magnetic particle that is reconstructed inside the ATLAS detector, and effectively this is what constitutes the energy calibration of electro-magnetic particles. The last step corresponds to a cross-check of the validity of this calibration in a different energy range, and of the validity of the extrapolation to photons of the in-situ energy-scale extracted with electrons. This last step insures that neither energy-dependent effects biasing the energy response, nor effects that could have a different impact on electrons and photons have been missed, hence guaranteeing that the full calibration chain is robust.

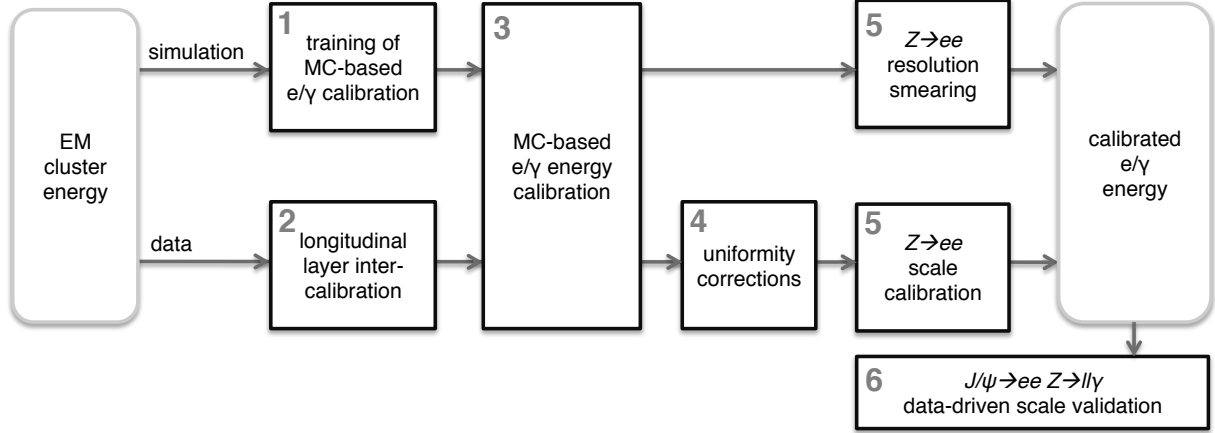


Figure 4.1: Flowchart of the electro-magnetic calibration procedure for the ATLAS detector [198]

## 4.2 Monte-Carlo based calibration

The ATLAS electromagnetic calorimeter does not measure the total energy of an incoming particle as there are energy losses before the calorimeter, in the lead absorbers, ... that will not be measured because they will not translate into ionization electrons in the argon, hence measuring the particles energy requires to find a way to recover for these effects. In the past ATLAS had been using the so-called "Calibration hits" method [225] where all the energy deposits, including in dead material and before the EM calorimeter, are stored in the Monte-Carlo datasets and explicit parametrizations of these losses as a function of measurable quantities are derived. These parametrizations are used to correct for the measured clusters energies and give the measurement of the initial energy of the incident particle. This method has not been used for the last Run 1 results, except for the region of the crack ( $1.37 < |\eta| < 1.52$ ) which is not used in the  $h \rightarrow \gamma\gamma$  analyses, and will therefore not be described further in this thesis. A multi-variate (MVA) calibration [226] was implemented and is doing an equivalent job, except that explicit analytic formulae for the losses are not needed as the MVA is expected to find them on its own. Therefore it is more powerful than the calibration hits as it can use weak dependences of given effects on a variable that would not be implemented in the calibration hits, or complicated correlations that were needed to be known analytically before. But a proper training of this MVA requires an accurate description of the detector response and of the material budget in front of the EM calorimeter, as it would give a perfect estimation of the energy only if it had been trained with a perfect simulation of the detector. This required a sizeable amount of work [198] both for the determination of the material budget in ATLAS and for its implementation inside the Geant 4 detector simulation.

### 4.2.1 Determination of the material in front of the calorimeter

**Inner detector material budget** For the Run 1 analyses, the material budget of the inner tracker, as well as its uncertainty, has been estimated using prior knowledge coming from its construction, especially the weights of its components [1]. This gave a relative uncertainty on the ID material of  $\pm 5\%$ , and although a few methods had been developed

(see [227, 228]) to give an in-situ estimate of the ID material, looking at the tracks either in photon conversions [207, 229], or in secondary hadronic interactions [230], none have been able to give a competitive uncertainty, as they suffer from systematic effects regarding the track efficiencies that are hard to control. They have not given any hint of deviation in the material description that would not be covered by the 5% uncertainty. In the following the ID material is assumed to be perfectly known and well implemented in the ATLAS detector simulation, and the uncertainty on the ID will be propagated.

**Material budget upstream of the calorimeter** Before the data-taking different methods had been developed to estimate the amount of matter upstream of the calorimeter that are summarized in [231]. They all relied on the variation of the electromagnetic particles shower shapes as a function of the material budget. However, as will be explained in section 4.5, it was realized that the lateral shower shapes were not accurately described by our Geant 4 simulation [211, 212] and it has not been possible to use them. Still an equivalent solution had been implemented, using a longitudinal shower shape namely  $\frac{E_1}{E_2}$ , which is the ratio of the energies in the first two layers of the calorimeter, as more material in front of the EM calorimeter will imply an earlier shower and therefore an increased amount of energy in the first layer with regard to the second. It is in fact the ratio of the averages of  $E_1$  and  $E_2$  that is used and for simplicity it will be denoted  $E_{1/2}$ .

The first step of this method [232] is the estimation of the sensitivity of the chosen shower shape to the material in front of the accordion, which is represented by a single factor given by

$$\frac{\partial X/X_0}{\partial E_{1/2}} \quad (4.1)$$

that is displayed in fig. 4.2. It is evaluated by studying the variation of  $E_{1/2}$  under material changes in the Geant 4 simulation, and estimated from a linear interpolation of  $E_{1/2} = f(X_0^{Injected})$  where  $X_0^{Injected}$  is the amount of material that is added in the modified detector simulation. Several modifications of the material budget have been tried and all yield a similar sensitivity factor, therefore only one was kept. This method is only sensitive to the integral of the material budget in front of the calorimeter, and can not actually resolve detailed radial variations, but it is possible to study both electrons and unconverted photons to create a mild sensitivity and split the material between what lies between the PS and the first layer, and what is in front of the PS. To make sure these photons are actually unconverted and did not convert toward the end of the tracker where we cannot reconstruct the conversion pair, a veto on the presampler activity is enforced ( $E_0 < 500$  MeV), and the unconverted photon samples is really only sensitive to the amount of material between the PS and the accordion.

Once these factors are known the amount of material in data can be estimated by simply scaling eq. 4.1 by  $E_{1/2}^{Data}/E_{1/2}^{MC}$ , assuming the relative calibration of  $E_1$  vs  $E_2$  in data is correct, as will be explained later. This study has been carried along  $\eta$ , and has been used to give hints of where the material budget in the simulation should be modified. Every modification that had been implemented was qualitatively supported by studies of either the detector building plans or by pictures of the detector construction. The evolution of the material budget between the final Run 1 detector simulation and the one that was used before is described on fig. 4.3. The most striking improvement is the suppression of

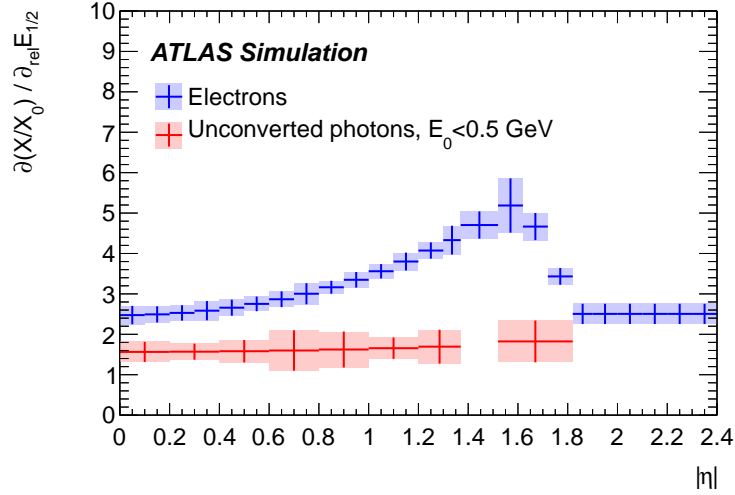


Figure 4.2: Sensitivity of the shower shape variable  $E_{1/2}$  to the amount of material in front of the EM calorimeter accordion [198]

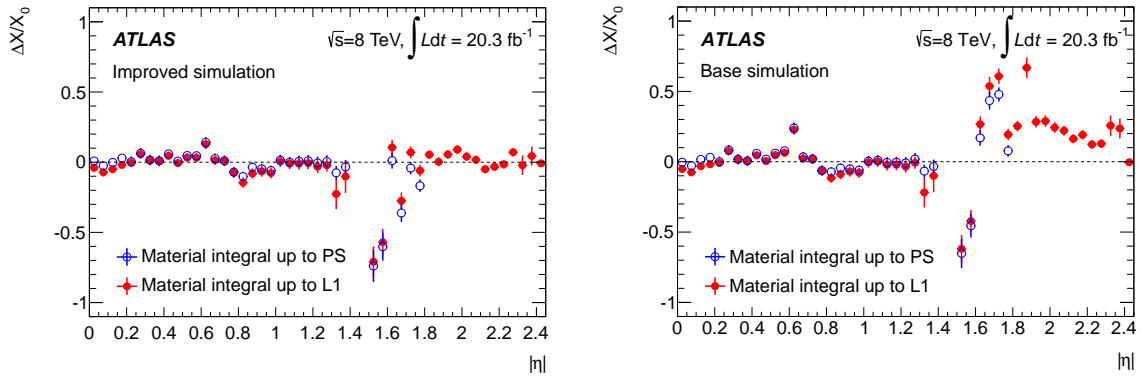


Figure 4.3: Difference in material budget in front of the EM calorimeter accordion between data and simulation, as seen with the final Run 1 detector simulation (left) or the previous version (right).  $\Delta X < 0$  translates into an excess of material in the simulation with regard to the data [198]

the big discrepancy at  $|\eta| = 1.9$ , which was coming from a mismodelling of the SCT heater tubes. There are still a few discrepancies between the final detector simulation and the real detector, especially at the beginning of the end-cap ( $|\eta| = 1.4 - 1.5$ ) where there is a sizeable excess of material in the simulation that has not been understood. The transition inside the inner detector at  $|\eta| \approx 0.8$  also suffers from a budget deficit in the simulation.

The uncertainty on this measurements comes from the statistical uncertainty on the sensitivity factor that is extracted from finite MC samples, variations of the Geant 4 physical processes descriptions, and from the inter-calibration of the two first layers of the calorimeter that will be described in subsection 4.3.4. Whenever the remaining discrepancy between data and MC is higher than this estimated uncertainty, the full difference is taken as the uncertainty. The total uncertainty on the material budget is shown in fig. 4.4.

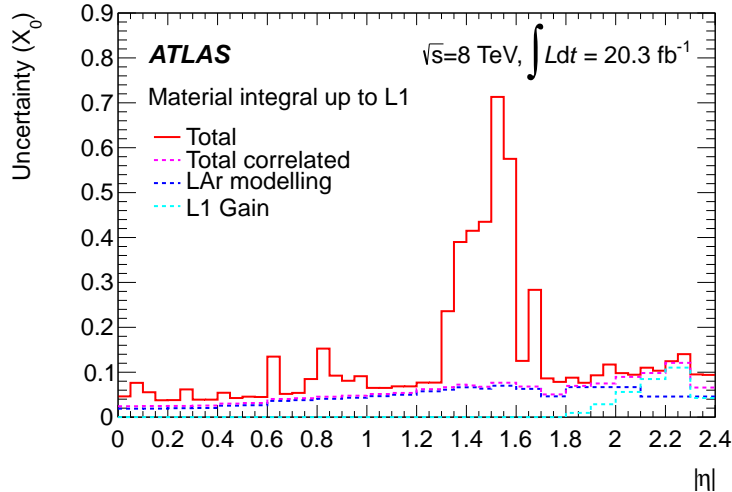


Figure 4.4: Uncertainty on the total material budget in front of the first sampling of the EM accordion calorimeter [198]

## 4.2.2 Multi-variate Calibration

The multi-variate calibration [226] used for electrons and photons is done using a boosted regression tree (BRT) implemented in the TMVA package [233]. There are in fact several BRTs, which correspond to different type of particles and different parts of the phase space. Three different BRTs have to be trained for electrons, converted and unconverted photons as they may be sensitive to different effects, e.g. the material in front of the electromagnetic calorimeter will not have the same impact on unconverted photons than it has on electrons. The conversion status of a given photon is defined by its conversion radius : converted photons have  $0 < R_{conv} < 800$  mm while unconverted either have a "negative" radius or one higher than 800 mm, which corresponds to the limit beyond which the conversion reconstruction is not reliable anymore. It was also decided to have several BRTs as a function of the pseudo-rapidity of the cluster and of the transverse energy in the LAr accordion, as it was observed that it was giving a better resolution in specific corners of the phase space. This is because TMVA had more freedom to independently optimize its response in specific problematic regions of the detector. This binning in  $\eta_{cluster}$  closely follows known detector features and response variations.

The BRTs are trained to give a multiplicative correction factor to the energy measured in the accordion, i.e. the target variable is  $\frac{E_{true}}{E_{accordion}}$  where  $E_{accordion}$  is the sum of the measured energies in the three samplings of the calorimeter while  $E_{true}$  is the incident particle energy given by the simulation. Using this ratio narrows the range in which the target variable varies, hence improving the performance of the BRT. All the particles use the same measurable input variables, except for the converted photons for which additional informations are used. These variables are listed below :

- $E_{accordion}$  which is the sum of energies in the three accordion layers
- $E_{PS}$  the energy measured in the presampler, that recovers part of the energy lost by the particle before the EM calorimeter

- $X$  which is the shower depth ( $= \frac{\sum X_i E_i}{\sum E_i}$ , where  $E_i$  is the amount of energy measured in layer  $i$  and  $X_i$  the amount of matter in the same layer or before at this position)
- The cluster barycentre where both  $\eta$  in the ATLAS frame and in the calorimeter frame (including also the position with respect to the cell edge in this calorimeter frame) are looked at while  $\phi$  is taken only in the calorimeter frame. The position in the calorimeter frame allows to take into account variations of the energy depending on the position of the particle with regard to the lead absorber, which may increase the amount of energy loss in inactive material, and with regard to the cell edge, as a particle hitting the calorimeter closer to a cell edge has a tendency to have more energy leaking outside the cluster. Having also the position in the ATLAS frame allows to have more sensitivity to the material budget in front of the calorimeter

For the converted photons  $R_{conv}$  is also used, but only if the sum of the  $p_T$  of the two tracks is above 3 GeV. If both of the conversion tracks are reconstructed and have hits in either the pixel or silicium detectors, the following variables are also considered :

- $p_T^{conv}$  which is the sum of the conversion track transverse momenta
- $\frac{p_T^{max}}{p_T^{conv}}$  the ratio of the highest momentum between the two conversion tracks to the transverse momentum of the vectorial sum of the two tracks

One important thing to note is the absence of variables related to the shape of the shower. Although promising on Monte Carlo they are not accurately modelled by our current detector simulation, as will be seen later, and it was therefore decided not to use them in the calibration.

When compared to the previous calibration based on the calibration hits method, the use of BRTs has improved the performance of the calibration for simulated  $h \rightarrow \gamma\gamma$  events, illustrated by fig. 4.5 left. Improvements were observed both on the linearity of the energy response, which is illustrated by the better compatibility between the input mass and the maximum of the invariant mass peak in fig. 4.5, and on the energy resolution. The linearity is estimated as the variation of the position of  $\frac{E_{MVA}}{E_{true}}$  with respect to the true energy, and has been estimated to be below 0.3% for every electromagnetic particle above  $E_T^{true} = 10$  GeV. The values of the energy resolution for various  $\eta$  and  $p_T$  bins are shown in fig. 4.6. With regard to the previous calibration, the most striking improvement was seen on converted photons whose resolution improved by typically 20% (mainly because the conversion tracks momentum is used) while the energy resolution of unconverted photons improved by  $\approx 10 - 15\%$  in the endcap and only 3 – 10% in the barrel. In most of the detector electrons have seen only a modest improvement of a few percents. For low energy electrons coming from  $J/\Psi \rightarrow ee$  (fig. 4.5 right), where the energy resolution is the worst, one does not even see an improvement.

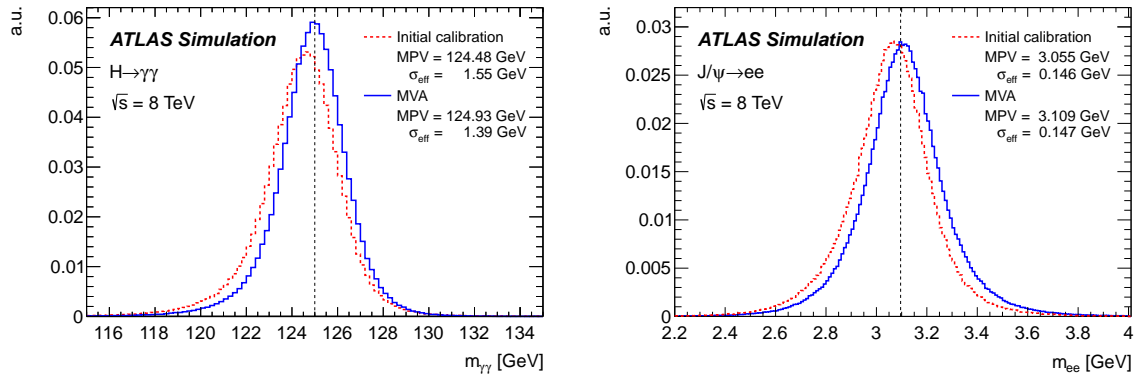


Figure 4.5: Invariant mass distributions for simulated  $h \rightarrow \gamma\gamma$  and  $J/\psi \rightarrow ee$  decays reconstructed either with the calibration hits method (“Initial calibration”) or the final Run 1 calibration based on BRTs. The vertical dashed lines corresponds to the input mass [198]

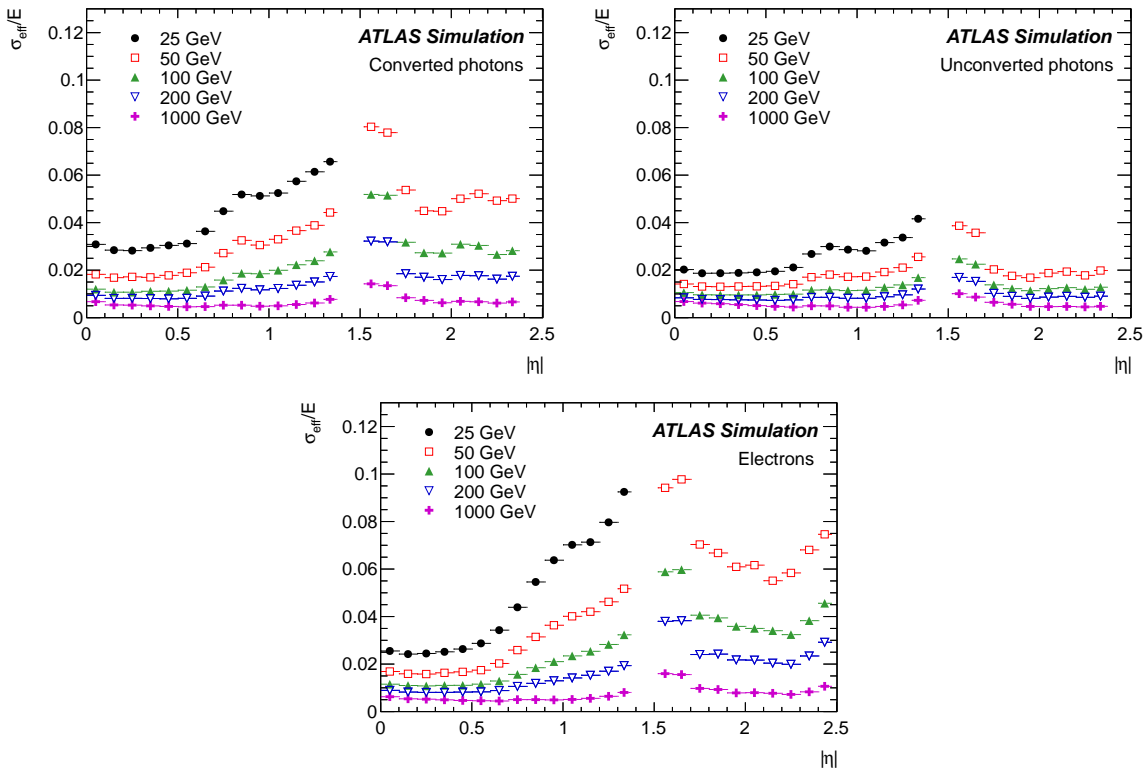


Figure 4.6: Relative energy resolution for the various type of particles as a function of  $|\eta|$  and  $E$ , using the MVA calibration. The points with  $E = 25$  GeV are not shown in the endcap and they correspond to very low  $E_T$  ( $< 10$  GeV) [198]

## 4.3 Corrections to the energy response on data

### 4.3.1 Intermodule gaps

The EM calorimeter is built as 16 modules in  $\phi$ , and at the separation between two modules there is an inter-module widening (IMW) of the LAr gap. This implies a decrease of the energy response in these small regions as a subpart of the shower will ionize the LAr with a lower electric field, and therefore a lower energy response. Effectively this translates in a downward variation of the particles energies with a  $\phi$ -periodicity of  $\frac{\pi}{8}$ , that can be observed in fig. 4.7. Furthermore the effect is bigger at  $\phi > 0$  than on the other side, which has been interpreted as a gravity-induced modification of the gaps between the modules. On the top of the detector the modules started to spread apart under the effect of their weights, giving a decrease of  $\approx 2\%$  of the energy response, while on the bottom they were getting compressed, yielding to a decrease of only  $\approx 1\%$ . This structure was only observed in the barrel, which could be explained by the mechanical differences in the construction of the endcap : barrel modules are well tightened from the inner and outer sides of the calorimeter, while the edges of the endcap modules have freedom to distort themselves and adapt to the gaps. A correction was derived to recover for this effect, and is based on a fit of the energy response (estimated by  $\frac{E}{p}$  of electrons coming from  $W \rightarrow e\nu$  events) in a given module to a double Fermi-Dirac function [227, 234], where the ratio between the flat top of the energy response and the rest of the module is used to determine the correction. Although the impact of this effect was already taken partially into account by setting the absolute energy scale of the calorimeter with  $Z \rightarrow ee$  events, it had an impact on the energy resolution and the correction improved slightly the constant term.

### 4.3.2 Pre-sampler high-voltage

In nominal conditions the barrel PS of the EM calorimeter is operated at the same voltage than the accordion, i.e. 2000 V. But this subpart of the calorimeter suffered from a sporadic noise that appeared in 2010 and became more and more frequent as the instantaneous luminosity was increasing, and whose source was not clearly identified. To mitigate this effect it was decided to decrease the PS HV, to 1600 V for the 2011 run and the first part of the 2012 run. Then it was further reduced to 1200 V in September 2012 with some channels operating at 800 V. In the endcap PS the effect has not been observed, which may be explained by a different layout of the detector or the fact that the nominal HV is lower, and no action had to be taken to preserve its performance. Although a recipe to correct the energy response for a non-nominal HV exists, using the expected HV dependence of the PS response [198, 235], it is only perfect when the OFCs and electronic calibration constants have been recomputed using the actual HV value. This was not done until September, and the period where the PS HV was at 1600 V has been processed with the OFCs computed for the nominal HV, hence leaving a  $\approx 1\%$  bias in the energy response that is absorbed in the absolute energy scale measured in-situ using the Z peak. After this procedure the stability of the PS response has been checked, and a difference between the two periods was observed (fig. 4.8). To make the response stable with regard to time a correction was derived, comparing the PS response between the two periods in  $Z \rightarrow ee$  events, and it was decided to apply it to the period after September 2012. The remaining

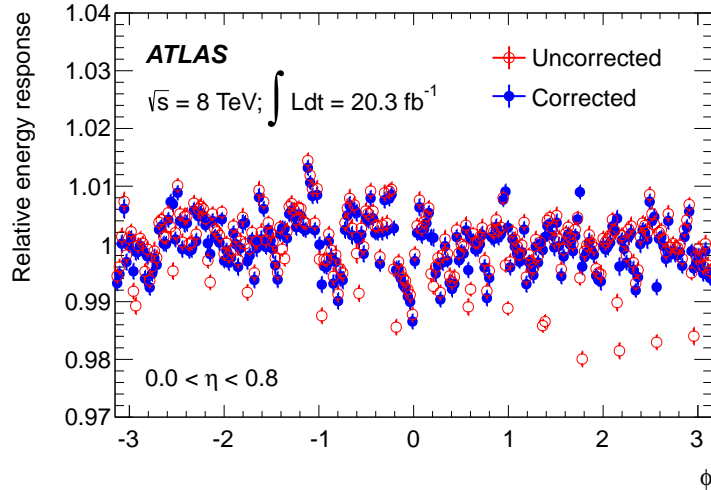


Figure 4.7: Energy response estimated from  $\frac{E}{p}$  of electrons from  $W \rightarrow e\nu$  candidates where the electron falls in  $0 < \eta < 0.8$ , as a function of  $\phi$  of the electrons, before and after the inter-module correction [198]

possible bias is still taken into account by the in-situ energy scale, and effectively this improvement of the detector stability improves the energy resolution.

### 4.3.3 High-voltage in the accordion

While doing detailed studies of the reconstructed invariant mass distributions of  $Z \rightarrow ee$  candidates, sizeable and localized deviations of the energy response were observed, and are described below [234]. They are always affecting one accordion HV sector, and most of them have been understood and corrected for.

**Short-circuits in the accordion** Most of these defaults are linked to short-circuits in the LAr accordion gaps, which are generated by impurities in the liquid argon accordion that connect the electrodes to the lead absorbers, which are themselves connected to the ground. This creates a potential difference between the power supply and the location of the short-circuits, and also an electric current because of Ohm's law. In such cases the voltage generated by the power supply decreases, but the correction computed using the expected HV dependence of the response does not apply as it assumes that the current is negligible (a few  $\mu A$ ) while it can become higher than 1 mA in case of a short-circuit. The main problem to derive a correction for this effect is then the loss of homogeneity of the voltage on the electrode : it is 0 V between the most inner part of the calorimeter and the short-circuit (if there is a "complete" short-circuit) and upstream it increases from 0 to the power supply voltage value, in proportion of the resistors that are crossed. A proper correction would need the knowledge of the position of the short-circuit.

The average reconstructed di-electron mass in  $\phi$  bins for a  $\eta$  range (0.4 - 0.6) with HV sectors suffering from this effect is displayed in fig. 4.9, while the maps of the current for the full detector are shown in fig. 4.10 and HV in fig. 4.11. The deviations of the energy response can clearly be seen by the localized drop of almost 2 GeV of the reconstructed  $Z^0$  mass at  $\phi \approx 0$  and  $\approx -1$ . It can be seen from the current map for the second half-gap

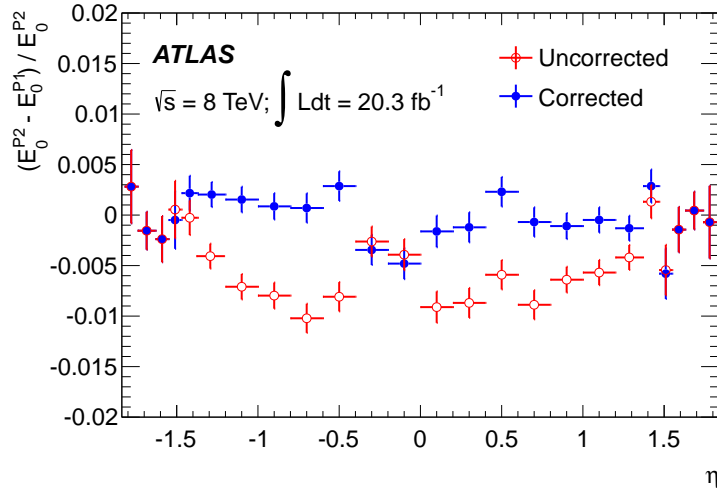


Figure 4.8: Difference of presampler energy response between the period before September 2012 (P1) and after (P2), measured using  $Z \rightarrow ee$  events [198]

that the power supply of this sector leaks a current of more than 1 mA, while a normal sector is close to 0 A, hence confirming the effect indeed comes from short-circuits. The HV maps in fig. 4.11 shows that these sectors are operated at a lower voltage (less than 500 V).

The variation of electrical potential over the electrode will only happen on one of the electrodes of the sector, and for all the others the potential will still be uniform over the electrode, but it will not be at its nominal value neither at the value that is measured at the power supply, which explain the partial loss of energy response over the whole HV sector. Some of the cables that are needed to insure the power supply are shared between all the electrodes of a given sector, and they are obviously carrying a resistance. In case of short-circuit the power supply will leak a non-negligible current and due to the effect of Ohm's law, a tension will be created across these connections, which means that the potential at the beginning of the electrode will not be the same than the one that is measured, which is the one at the power supply. Therefore the impact of the short-circuit will propagate and modify the energy response in the whole HV sector, and depending on how deep the short is in the calorimeter it may affect several of its layers. It is not possible to derive an exact correction which would require the knowledge of the position of the short, however an empirical correction is derived based on profiles such as the one shown in fig. 4.9, where the effect of this correction is also shown. The full set of plots of the  $Z^0$  mass profiles may be seen in appendix A.

**Wrongly corrected half-module** Some HV sectors have been splitted in two, with the two halves operated separately and potentially at a different voltage. This is usually not a problem but we found one case where the HV correction was not applied to the proper half, but to the one that was at nominal voltage. The corresponding di-electron mass distribution is displayed in fig. 4.12, where on the side that should be corrected the energy response has decreased below its nominal value while on the other side the energy is over-evaluated. The correction to the cells energies, as registered in the database, is of

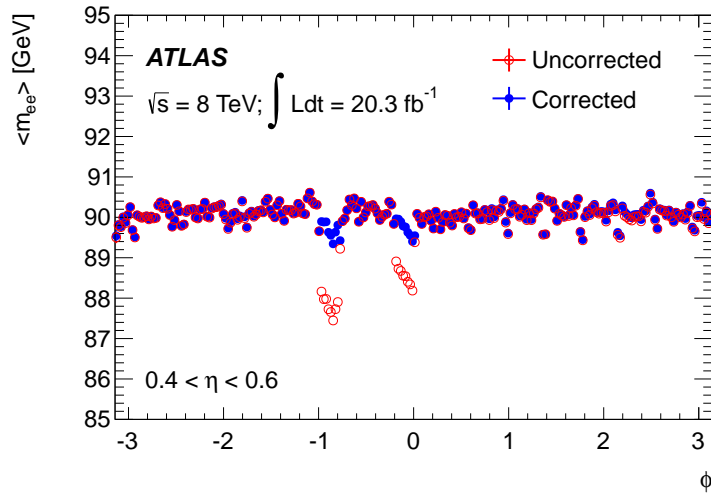


Figure 4.9: Reconstructed invariant mass of  $Z^0 \rightarrow ee$  candidates with electrons falling in  $0.4 < \eta < 0.6$ , as a function of  $\phi$  of one of their electrons, before and after the HV correction [198]

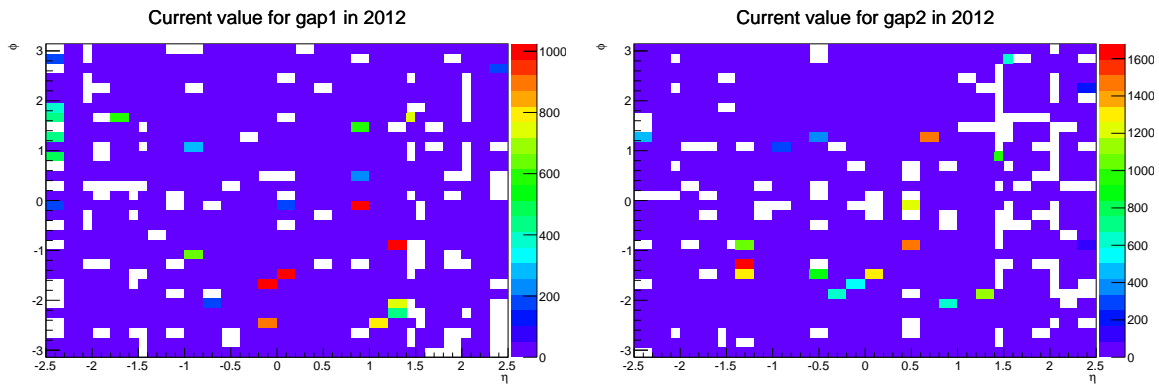


Figure 4.10: Mapping of the current (in  $\mu A$ ) generated by the HV power supply for the two half-gaps. The blank bins are associated to sectors that have a current of exactly 0 A registered in the database

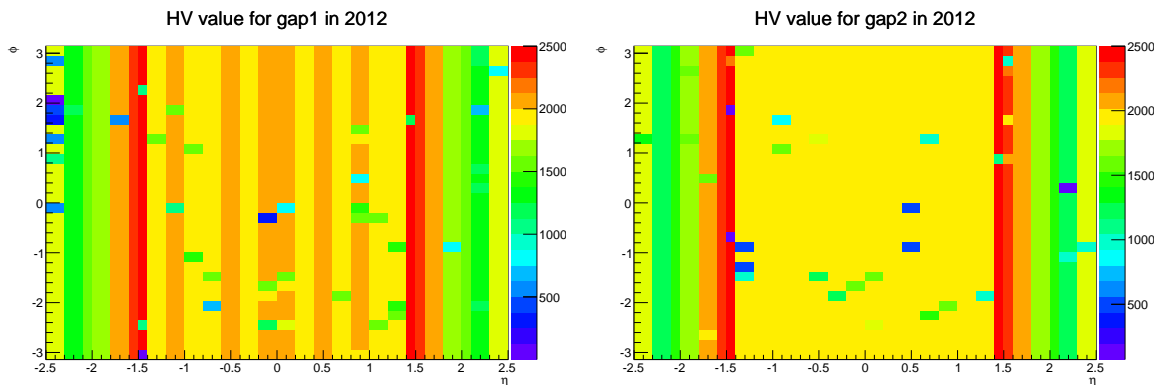


Figure 4.11: Mapping of the tension generated by the HV power supply (in Volts) for the two half-gaps

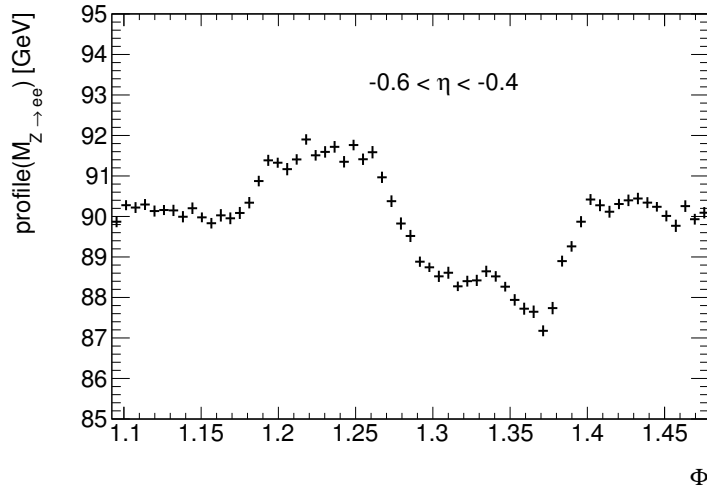


Figure 4.12: Variation along  $\phi$  of the reconstructed di-electron invariant mass in  $Z^0 \rightarrow ee$  events for a specific HV sector where the two halves are at a different voltage, but the wrong one received a correction

3% which is compatible with the 1.5% variation of the di-electron mass that is observed on both sides of this sector.

Further checks were done to find the origin of this inversion, which turned out to be a mistake in the original mapping of the cables to the power supply, that had already been seen in signal injection tests. Although a few other sectors are operated in two halves, they are most usually not operated at two different HV, and no equivalent effects had been seen in signal injection tests. The mapping in the ATLAS database was updated for future runs to use the correct one.

**Description of the correction** Using the expected invariance of the reconstructed mass of  $Z \rightarrow ee$  events around the beam axis, it was possible to derive an offline correction for this effect, using profiles such as the one shown in fig. 4.9. Using the fact that for a perfect detector the di-electron mass should not depend on  $\phi$ , we can assume that the average reconstructed  $Z \rightarrow ee$  mass in a faulty HV sector should be the same than for other sectors at the same  $\eta$  and correct the energy of particles falling in this sector. This correction is a multiplicative factor directly applied to the energy of electromagnetic particles that are falling within problematic sectors, and has been derived to equalize the energy response, estimated by the reconstructed  $Z \rightarrow ee$  mass, of a faulty sector to the one of the other sectors at same  $\eta$ . The value of all the correction factors and the location of the corresponding sectors can be found in table 4.1. Although this correction is derived using the  $Z^0$  peak it is done to correct the response of the cells and therefore one will apply it to other energy range and particles too. The main effect of this correction is to improve the energy resolution of the calorimeter. Its impact on the energy scale was already recovered on average by the use of the absolute energy scale extracted from  $Z \rightarrow ee$  events. The same correction was applied on 2012 and 2011 data, as only one sector had a change of energy response between the two years.

$\eta$ range $\times$ $\phi$ range	Correction factor
$[-0.6, -0.4] \times [\frac{13\pi}{32}, \frac{14\pi}{32}]$	1.035
$[-0.6, -0.4] \times [\frac{12\pi}{32}, \frac{13\pi}{32}]$	0.965
$[0.4, 0.6] \times [\frac{-2\pi}{32}, 0]$	1.028
$[0.4, 0.6] \times [\frac{-10\pi}{32}, \frac{-8\pi}{32}]$	1.044
$[0.6, 0.8] \times [\frac{12\pi}{32}, \frac{14\pi}{32}]$	1.022
$[1.2, 1.4] \times [\frac{-24\pi}{32}, \frac{-22\pi}{32}]$	1.038
$[1.9, 2.0] \times [\frac{18\pi}{32}, \frac{20\pi}{32}]$	1.029
$[-1.4, -1.2] \times [\frac{-10\pi}{32}, \frac{-8\pi}{32}]$	1.048
$[-1.4, -1.2] \times [\frac{-14\pi}{32}, \frac{-12\pi}{32}]$	1.048
$[-1.8, -1.6] \times [\frac{18\pi}{32}, \frac{16\pi}{32}]$	1.024
$[-2.5, -2.3] \times [\frac{-18\pi}{32}, \frac{-16\pi}{32}]$	1.037
$[-2.5, -2.3] \times [\frac{8\pi}{32}, \frac{10\pi}{32}]$	1.031
$[-2.5, -2.3] \times [\frac{16\pi}{32}, \frac{18\pi}{32}]$	1.040
$[-2.5, -2.3] \times [\frac{18\pi}{32}, \frac{20\pi}{32}]$	1.030
$[-2.5, -2.3] \times [\frac{20\pi}{32}, \frac{22\pi}{32}]$	1.020

Table 4.1: Correction factors applied to the particles' energies to flatten the reconstructed invariant mass of  $Z \rightarrow ee$  candidates, correcting for incorrect HV behaviours in specific sectors

**Improperly averaged corrections** Although we derived a correction only for the two aforementioned HV problems, we found out a few others that are related, although in these cases they are not impacting a full HV sector but only one layer 1 or one layer 2 cell. The first one corresponds to the case where the HV on one half LAr gap is put at 0, leaving the other half gaps of the Voltage power supply to its nominal value. The online correction is computed separately for each of the three samplings of the calorimeter, but is always averaged over one cell. Given that the three samplings have different granularities this can give residual deviations : if a problem occurs in a gap corresponding to a given cell of the middle sampling, all the strips facing the faulty gap will receive a correction. Given that strips cells are 4 times bigger in  $\Delta\phi$  than middle cells, the correction gets propagated to particles falling close to the 3 other middle cells facing this layer 1 cell, although it should not have been corrected. Effectively this means that the energy for particles hitting the middle cells having the faulty gap will be under-evaluated, while elsewhere it will be over-evaluated, as can be seen in fig. 4.13. Properly correcting this effect would require sizeable changes to the reconstruction program. Only 3 sectors displaying this effect have been found.

**Remaining effects** A final effect was observed, but not understood. We found 5 HV modules with drops of the energy response that seemed to affect a region of only one cell in  $\phi$  but the full sector in  $\eta$ . A typical case is displayed in fig. 4.14. As the origin of this effect has not been found we decided not to correct for it.

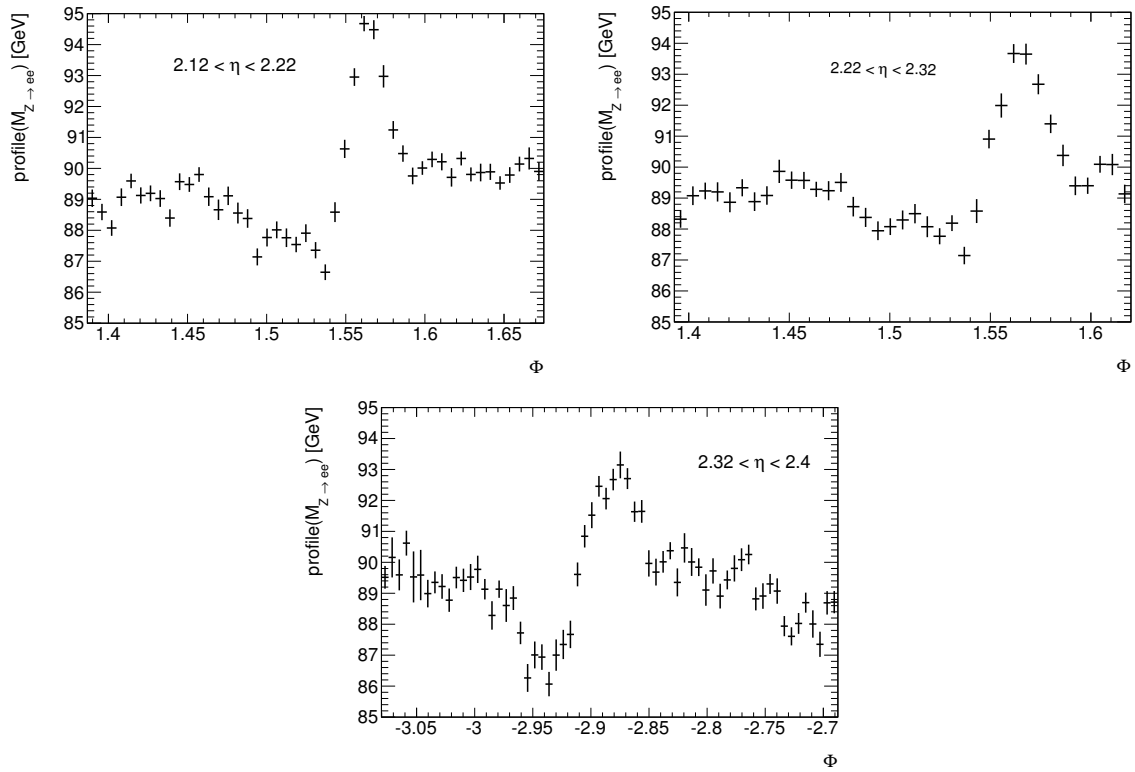


Figure 4.13: Mass distribution in sectors where a HV correction is averaged over a whole strip cell while only one middle cell has a problem. The two top sector are more complicated as several electrodes are operated at different voltages in the middle sampling

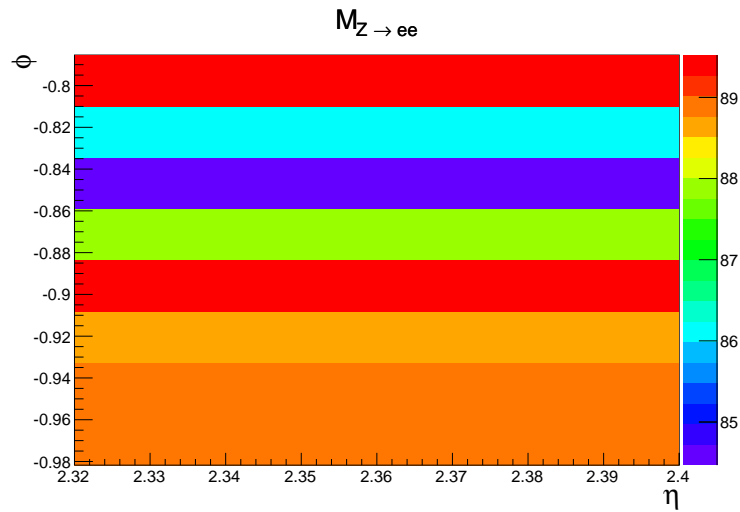


Figure 4.14: 2D distribution of the reconstructed  $Z \rightarrow ee$  mass (in GeV) in a specific sector with a drop of the energy response over the whole sector in  $\eta$  but only one cell in  $\phi$

### 4.3.4 Inter-layer calibration

After the electronic calibration described in [202, 236, 237], there may be residual effects that have not been accounted for and need to be corrected before the in-situ energy scales are computed, as they only allow to derive one scale factor by  $\eta$  bin. It was observed, already at the time of the ATLAS test-beam (see fig. 20 of [238]), that there is a difference of  $\approx 3\%$  of the energy response of the first layer of the EM calorimeter with regard to the second one, on average. As the fraction  $\frac{E_1}{E_2}$  varies with the energy this relative mis-calibration would create a non-linearity, and would also bias the material determination whose current method relies on this fraction. Therefore it was decided to derive an inter-calibration correction factor  $\alpha_{1/2}$  whose goal is to equalize the energy response between the two first samplings before any other correction, especially before the overall in-situ energy scale. It should be noted that although the third sampling of the calorimeter may in principle suffer from similar effects, it was not studied as it starts to have a weight in the energy measurements at a few hundred GeV which is beyond the energy range we were interested in Run 1, especially for the Higgs boson measurements in the diphoton channel where the mean  $p_T$  is  $\approx 60$  GeV.

In order to have a measurement of  $\alpha_{1/2}$  that does not depend on the amount of material in front of the calorimeter, whose determination already requires corrected  $E_1$  and  $E_2$ , it was decided [235] to study the energies deposited by muons in the EM calorimeter, that are almost insensitive to matter : the energy they deposit in a layer is only proportional to the depth of active material crossed. They are selected in  $Z \rightarrow \mu\mu$  events where it is required that  $p_T^\mu > 25$  GeV, which gives a very pure sample. Their trajectory is measured in the inner tracker and extrapolated to the calorimeter to determine cells that have been crossed by the particle. Because of the accordion geometry, an electrode of the EM calorimeter usually spreads over two cells in the middle sampling, and it is therefore necessary to sum several cells to estimate the muons energies. It was chosen to use the most energetic cell around the extrapolated track, and its most energetic neighbour in  $\phi$ , as the magnetic field tends to bend the tracks in  $\phi$ . In the strips the cells are bigger in  $\phi$  but have a sizeable level of cross-talk between adjacent cells in  $\eta$ , that is not well modelled in the simulation, and to mitigate this effect it was decided to sum three contiguous strip cells in  $\eta$ . The energy deposited by the muons is small ( $\approx 200$  MeV in the middle layer) therefore the measurement suffers from an important electronic noise, that is at the level of 40 to 50 MeV in the middle layer. Therefore the distribution of the energies in each sampling is described by the convolution of a Landau distribution, that describes the energy deposition of the muon, and a Gaussian, that describes the electronic noise. Two methods have been developed to extract the Most Probable Value (MPV) of the deposited energy. The first one uses a full fit of the energy distribution while the second one is using a truncated mean, as the Landau distribution as a large tail toward high energies. Denoting  $\langle E_{1/2} \rangle$  the ratio of the MPVs in the first and second layer, the inter-layer calibration factor is then simply the ratio of  $\alpha_{1/2} = \langle E_{1/2} \rangle^{data} / \langle E_{1/2} \rangle^{MC}$ , and can be seen in fig. 4.15. The difference between the two methods is taken as an uncertainty, while the statistical uncertainty on  $\alpha_{1/2}$  is completely negligible. In principle this factor can be applied to either of the two samplings, and after the overall in-situ energy scales this choice will not make any difference, but as it was noticed that the spike at  $\eta \approx 1.5$  is carried by the middle sampling, it was decided that it is its energy that should be modified.

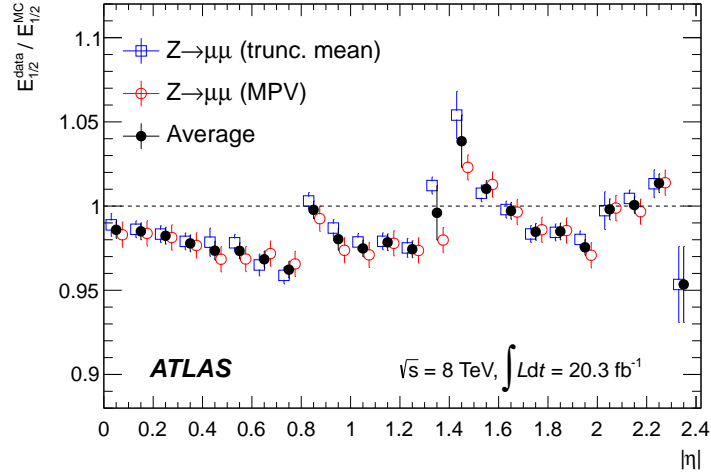


Figure 4.15: Inter-layer calibration correction factor  $\alpha_{1/2} = \langle E_{1/2} \rangle_{Data} / \langle E_{1/2} \rangle_{MC}$  as measured with muons, where  $\langle E_{1/2} \rangle$  corresponds either to this fraction most probable value obtained from a fit, or to its average value in a window [198]

Although this inter-calibration factor is extracted with muons, it is directly applied to electrons and photons, and this extrapolation implies a systematic uncertainty on  $\alpha_{1/2}$  due to the improper modelling of the details of the EM calorimeter in Geant 4. The following uncertainties were studied, and they all were evaluated by implementing related variations at the Geant 4 level of the simulation of signal particles samples :

- Uncertainties on the cross-talk between the LAr cells, either in a given sampling or between the first two layers, which affects the muon energy measurement
- Uncertainties on the size of the inactive material area in the electrode between the first and the second layer but also on its exact position, which changes the area of transition within which the electric field is decreased
- Uncertainty on the variation of the response of a cell due to the variation of the electric field along an electrode due to their accordion geometry

The total uncertainty on  $\alpha_{1/2}$  varies between 1% and 1.5% as a function of  $\eta$ , and translates into a non-linearity of the energy response as it is taken into account by the overall energy scales set using the  $Z \rightarrow ee$  mass peak, meaning that the uncertainty on the particles energy is 0 for 40 GeV electrons, but rises to 0.1% of the energy for unconverted photons from  $h \rightarrow \gamma\gamma$  decays. This uncertainty on  $\alpha_{1/2}$  has also been propagated to the uncertainty on the material determination described in [232]. For this study another uncertainty coming from the mis-modelling of the lateral shower shape, that has a bigger impact on the second layer than the first, has been taken into account and was evaluated as the full Data/MC discrepancy.

### 4.3.5 Presampler (PS) energy scale

Being an independent detector with a different design from the one of the LAr accordion calorimeter, the PS has its own energy scale that also needs to be computed. It could

simply be estimated as  $\alpha_{PS} = \frac{E_0^{data}}{E_0^{MC}}$  where  $E_0$  corresponds to the PS energy, measured with electrons coming either from W or Z bosons [235]. However this ratio is plagued by potential biases from material mis-modeling in front of the PS, that have to be taken into account before this ratio can be interpreted as being the PS energy scale. As an increased material budget before the PS creates earlier and broader showers, it is expected to increase the fraction of energy in the pre-sampler and in the strips. It can be observed on fig. 4.16 that the impact of material upstream of the PS on both  $E_0$  and  $E_{1/2}$  can be described by a linear parametrization, while the impact of material between the PS and the first sampling is only shifting this parametrization with regard to  $E_{1/2}$ . Therefore, under any material variation the PS energy response can be described using the following formula :

$$\frac{E_0^{var}}{E_0^{MC}}(\eta) = 1 + A(\eta)\left(\frac{E_{1/2}^{var}}{E_{1/2}^{MC}b_{1/2}}(\eta) - 1\right) \quad (4.2)$$

In this formula variations of  $A(\eta)$  are describing the impact of the (ID) material budget upstream of the PS (i.e. the slope of fig. 4.16) while  $b_{1/2}$  describes any other bias that affects  $E_{1/2}$ , such as the mis-modeling of the material budget between the PS and the accordion or the relative calibration of the first two layers, and needs to be measured. This is done using unconverted photons, that are insensitive to the material in front of the PS, and for which a veto on the PS activity is required ( $E_0 < 500$  MeV) to ensure that the photons have not converted beyond the region where the tracker may reconstruct conversions. Therefore they only measure effects that may bias  $E_{1/2}$ , and  $b_{1/2}$  is then taken as  $\langle E_{1/2}^{Data} \rangle / \langle E_{1/2}^{MC} \rangle$ . Once  $b_{1/2}$  is known eq. 4.2 can be used to estimate a corrected PS energy  $E_0^{corr}$ , which corresponds to what would be the result of the simulation if the amount of material in front of PS was correct, by replacing  $E_{1/2}^{var}$  by  $E_{1/2}^{Data}$  in the right hand of eq. 4.2. The pre-sampler energy scale, which may be found in fig. 4.17, is then simply computed with electrons from W and Z decays using the following formula :

$$\alpha_{PS} = \frac{E_0^{Data}}{E_0^{Corr}} \quad (4.3)$$

The PS energy scale that is applied on data corresponds to the average of  $\alpha_{PS}$  over one PS module, and the variation of  $\alpha_{PS}$  over one module is taken as an uncertainty on this measurement. The uncertainty on  $\alpha_{PS}$  varies between 2-3% depending on  $\eta$ .

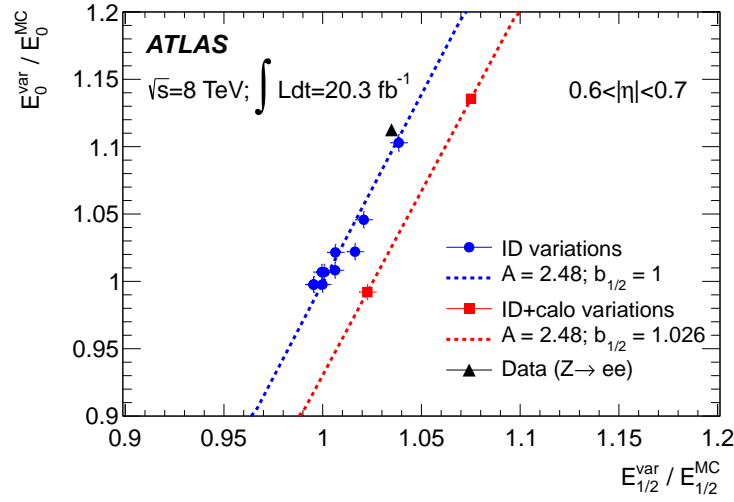


Figure 4.16: Variation of the PS energy and of  $E_{1/2}$  in  $Z \rightarrow ee$  events with regard to material distortion [198]. Calorimeter material variations correspond to an addition of  $5\%X_0$  between the PS and the first layer, while ID variations refers to additions of up to  $15\%X_0$  in the inner detector volume, depending on  $\eta$

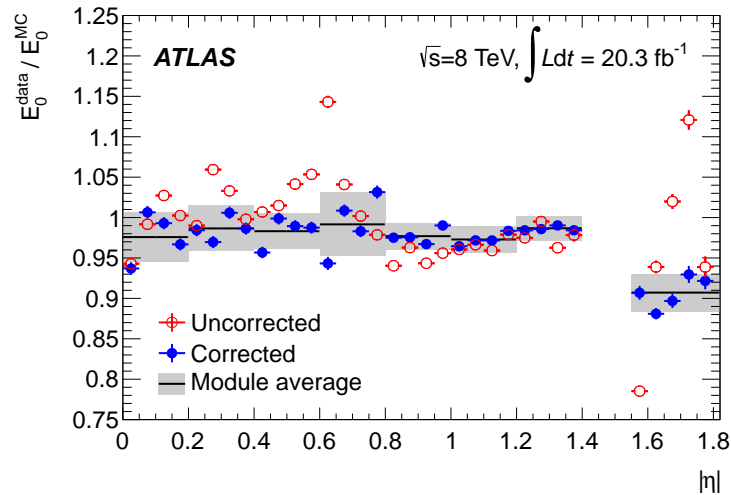


Figure 4.17: Value of the pre-sampler energy scale. The uncorrected value corresponds to  $\frac{E_0^{Data}}{E_0^{MC}}$  while the corrected one are computed using eq. 4.2 and is the PS energy scale applied on data [198]

## 4.4 Correction for an apparent non-linearity

### 4.4.1 Presentation of the problem

As was mentioned in subsection 3.3.4, the electronics of the detector has three different gains, that are effectively covering different transverse energy ranges. As the in-situ energy scales are determined using  $Z \rightarrow ee$  events they assume a given mixture of the various gains, and if the inter-calibration of the three gains is imperfect these energy scales may not be valid at a different energy where the fraction of cells read-out in each gain is different than the one observed at the  $Z$ , and this would create a non-linearity of the energy response. This is especially a problem for  $h \rightarrow \gamma\gamma$  as in the middle layer the turn-on of the Medium Gain (MG) is essentially between the average energy of  $Z \rightarrow ee$  events and the one of  $h \rightarrow \gamma\gamma$  events. Typically in the barrel only a few percents of  $Z \rightarrow ee$  events have one of their electrons whose cluster has a cell read-out in medium-gain, while for  $h \rightarrow \gamma\gamma$  it is already almost two third of the events. In the following section we will be interested only in the gain of the middle layer cells. At the  $Z \rightarrow ee$  peak all the events will have some of the cells of the strips read-out in MG for every electron cluster, but the energy in the strips is small. For the energies we were interested in for the run 1 the back layer only has a mild impact on the energy measurement. In the following the events will be labelled as MG as long as one of the electromagnetic clusters in the event has at least one cell of the middle sampling that is read-out in MG, and HG (High Gain) if all the cells are read-out in high-gain. A similar denomination is used for electrons and photons. The case of the low-gain will not be discussed as there is no pure source of electrons or photons with a sufficiently high yield to study it, and it is not relevant for  $h \rightarrow \gamma\gamma$ .

The relative calibration of high and medium gain can be studied using the di-electron invariant mass in  $Z \rightarrow ee$  events, that has a sizeable number of events in both MG and HG. It was first observed at the end of 2012 [239] that the mass distribution of the events registered in HG or MG are shifted with regard to each other, in a way that can not be reproduced by the MC, as may be seen for the barrel events in fig. 4.18. At this time only three broad bins were done, splitting between events where the two electrons are falling in the barrel, the end-cap or when there is one electron in each of these sub-parts. Most of the shift of the reconstructed  $Z$  mass between HG and MG comes from a kinematic effect, that will be explained below, and which is well simulated by the MC. But there is also a remaining  $\approx 200$  MeV shift that is different between data and MC, which gives an apparent non-linearity of the energy response. In the note [239] this was only treated as a systematic uncertainty and it was estimated to give a systematic uncertainty of 0.15% on the Higgs boson mass measured in the  $h \rightarrow \gamma\gamma$  channel. This number was derived taking into account the distribution of  $m_{ee}$  observed in the three bins for the two gains, and the different fraction of events in each gain for  $Z \rightarrow ee$  and  $h \rightarrow \gamma\gamma$ .

### 4.4.2 Extraction of the energy response difference

This study was conducted by splitting the datasets in two separate categories : the events where one middle cell (i.e. one cell in the middle longitudinal sampling) was read-out in MG, and those where all the middle cells are read-out in HG. But selecting a specific electronic gain biases the energy distribution of the selected sample, and this in turn has

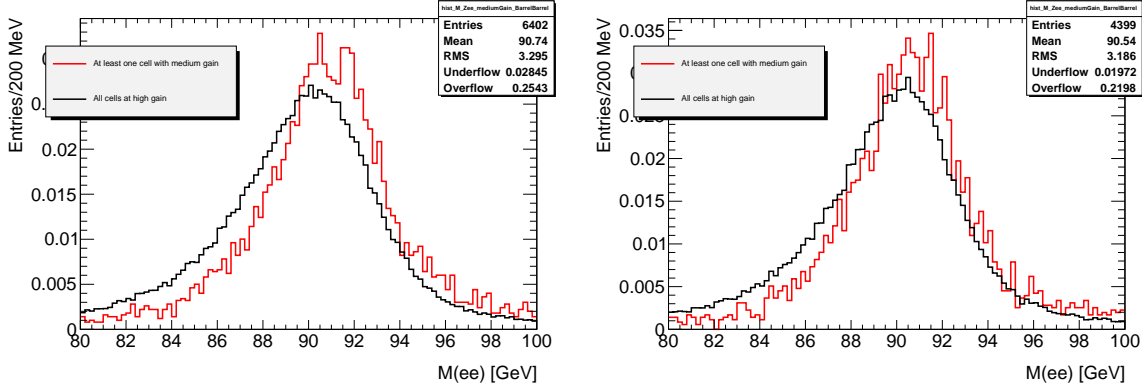


Figure 4.18: Di-electron invariant mass distribution of  $Z \rightarrow ee$  events where the two electrons are falling in the barrel. The left plot corresponds to the data and the right to the MC, HG events are in black and MG in red

an impact on the distribution of the di-electron invariant mass. Indeed the MG electrons will be at higher energies than the HG ones, and on average this means that they will come from  $Z \rightarrow ee$  events that are in the high-mass tail of the Z Breit-Wigner. Therefore the reconstructed di-electron invariant mass distribution for MG events is expected to be biased toward higher masses, and the one from HG events toward lower masses. But this effect is purely kinematical hence it is well modelled by the MC, if the gain-switching threshold is properly modelled in the MC. In order to remove this effect, it was decided to study the difference of the reconstructed  $m_{Z \rightarrow ee}$  mass between MC and data, which allows to subtract the kinematical effect hence cancelling it. But the gain-switching thresholds are not perfectly implemented in the MC, and depending on the cell it may differ by up to 5% with regard to the thresholds of the real detector. This is usually not a problem as no other analysis may be sensitive to this exact threshold. Furthermore on the MC the selected read-out gain is only a relabelling of the energy range : the detector simulation gives the energy of the cell in MeV and the corresponding number of ADCs is determined using the conversion factor measured on the detector. The chosen gain is defined by sharp cuts on the value of the number of ADC counts, and the read-out electronic is perfectly calibrated and linear. To get rid of the threshold mis-modelling it was decided to do this analysis in small bins of  $E_T$ , of typically 5-10 GeV. Then the energy and mass distributions in each bin are well under control, as we are selecting precisely the energy of the electrons falling in each bin. Technically this is achieved by studying the profiles of the reconstructed di-electron invariant mass  $m_{ee}$  along the transverse energy of one of the electrons  $E_T$ , which gives the average and statistical uncertainty of  $m_{Z \rightarrow ee}$  by transverse energy bin. The second electron in the event is averaged over, and as its energy is corrected by the in-situ energy scale any observed mis-modelling of the reconstructed Z mass will only be connected to a mis-modelling of the energy response of the first bin, which may be defined with the formula  $\frac{\Delta E}{E} = 2 \frac{\Delta M}{M}$  (see demonstration in subsection 3.3.4).

For the final Run 1 measurement, the study [240] was carried out in fine  $\eta$  bins, and almost everywhere in the detector the difference of the reconstructed Z mass between the two gains is not zero, but it is usually quite small, at the level of 100-200 MeV, which would translate into a 0.2-0.4% difference of energy response between the two electronic gains. But there are a few bins at the beginning of the end-cap where the

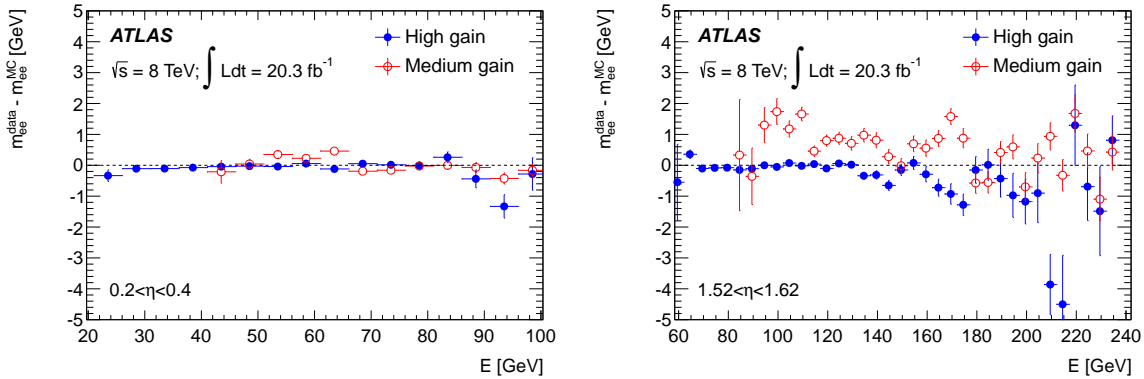


Figure 4.19: Profile of the reconstructed Z mass for two specific  $\eta$  bins where the apparent difference between the two chains is the biggest (right) and the smallest (left)

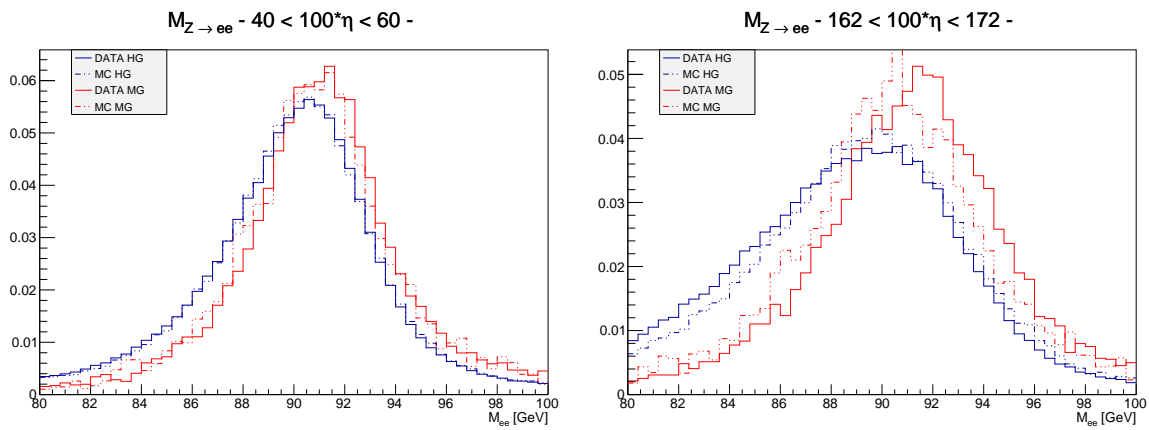


Figure 4.20: Distribution of the di-electron invariant mass in HG and MG, for data and MC, in the bins where the difference is the biggest for the barrel ( $0.6 < \eta < 0.8$ ) and the end-cap ( $1.62 < \eta < 1.72$ )

difference in the reconstructed Z mass is much bigger, reaching 1 GeV which, interpreted as a difference of energy response between the two electronic chains, would correspond to a 1% difference. Two of the most extreme bins are displayed in fig. 4.19. Assuming that the difference between data and MC does not depend on the energy of the electron, which seems acceptable with the current statistics, we can derive a single number that characterizes the energy response deviation, by averaging all the  $E_T$  bins. This number is given in table 4.2 for all the  $\eta$  bins that have been considered. As this study used profiles of the reconstructed Z mass and not fits of these distributions, there may be a bias in the estimated mass, which is expected to cancel out in the data to MC difference. To confirm this cancellation, the di-electron invariant mass distribution is displayed in fig. 4.20, for the bins where the effect is the most striking in the barrel and in the end-cap, and it is clear that the data to MC difference is bigger for the MG than the HG, hence driving the energy response difference. Furthermore in the end-cap the data-MC shift is in a different direction for the two gains.

$\eta$	(Data-MC) $M_Z^{HG}$ [MeV]	(Data-MC) $M_Z^{MG}$ [MeV]	Absolute difference (MeV)
[-2.4, -2.32]	-411	52	463
[-2.32, -2.22]	83	121	38
[-2.22, -2.12]	-219	-40	179
[-2.12, -2.02]	-140	-43	97
[-2.02, -1.92]	-102	-48	54
[-1.92, -1.82]	-198	49	247
[-1.82, -1.72]	-145	213	358
[-1.72, -1.62]	-388	539	927
[-1.62, -1.52]	-41	685	726
[-1.37, -1.20]	-72	95	167
[-1.20, -0.80]	-25	-50	25
[-0.80, -0.60]	-37	161	198
[-0.60, -0.40]	-53	43	96
[-0.40, -0.20]	-16	175	191
[-0.20, 0]	-32	130	162
[0, 0.20]	-49	107	156
[0.20, 0.40]	-55	40	95
[0.40, 0.60]	-61	145	206
[0.60, 0.80]	-30	148	178
[0.80, 1.20]	-30	103	133
[1.20, 1.37]	-65	177	242
[1.52, 1.62]	-82	712	794
[1.62, 1.72]	-415	657	1072
[1.72, 1.82]	19	235	216
[1.82, 1.92]	-186	33	219
[1.92, 2.02]	-125	26	151
[2.02, 2.12]	-156	-45	111
[2.12, 2.22]	-174	-37	137
[2.22, 2.32]	-92	104	193
[2.32, 2.40]	-184	74	258

Table 4.2: Apparent energy response difference between HG and MG, as measured by the reconstructed Z mass, as a function of  $\eta$  of the electron. The uncertainty on these numbers is small (typically  $< 30$  MeV)

### 4.4.3 Cross-checks of potential explanations

At this point the energy response difference between the two gains is only an apparent energy response difference : it appears when we split the dataset between the two gains, but this does not imply that it is a problem of inter-calibration of the two gains as we may also split the dataset with regard to another effect that is correlated with the gain, and it may well be that it is this unknown effect that is not properly modelled in the simulation. Several cross-checks of effects that could generate this bias have been conducted, and are described below.

#### Mapping of HG and MG clusters in the detector

In some cases there could be hot-spots of HG or MG clusters in the detector, either because the gain-switching threshold is lower in the region of the hot-spot, or for another reason that might be connected to the bias we observe. Therefore the first thing that was done was a mapping of the HG and MG clusters in the detector, compared between data and MC, as even a hot-spot would not have an impact on the performance if it was properly modelled. This comparison can be seen in fig. 4.21, where the region at  $|\eta| < 0.05$  and near the crack is removed by the program that builds the clusters on final analysis datasets format, which does not handle the changes of segmentation or alignment that are occurring in these regions. The overall agreement between the data and MC maps is very good, and there are only a few discrepancies that are localized at the end of the end-cap ( $|\eta| > 2$ ), therefore they cannot explain the discrepancy that we observed between the two gains. In the barrel there are a few cold-spots for the HG, that are corresponding to dead cells, and that are all reproduced in the MC.

#### Effect of material budget in front of the EM calorimeter

Another possible explanation of this effect was a mis-modelling of the material budget in front of the EM calorimeter. In such a scenario, a particle of a given energy will start to shower earlier in the detector when the amount of material upstream of the calorimeter is increased, which will imply broader electro-magnetic showers in the calorimeter. In this case the amount of energy in the most central cell of this particle cluster will be reduced as the energy will be more spread in the cluster, and as it is usually this cell that is read-out in MG, the cluster will be less likely to be flagged as MG, which in turn biases the di-electron mass distribution for each of the two gains. An important reason to investigate this is the fact that the worst difference between the two gains lies at the low  $\eta$  edge of the end-cap, where the knowledge of the material budget is also the worst. This was checked using simulations of  $Z \rightarrow ee$  events, with one sample that used the nominal detector description for the simulation, and one that used a simulation where additional material was added upstream of the calorimeter. The amount of additional material was the maximal amount allowed by the material studies based on  $\frac{E_1}{E_2}$ . As usual the profile of the reconstructed  $Z$  mass along the energy of the electron is computed, and the difference of this profile between the nominal MC and the one with an increased material budget may be found in fig. 4.22. As expected the additional material modifies the energy response of the detector, in a way that is not constant with regard to the energy of the incident particle, which is represented by the slopes observed on this figure. But the most important point is that the additional

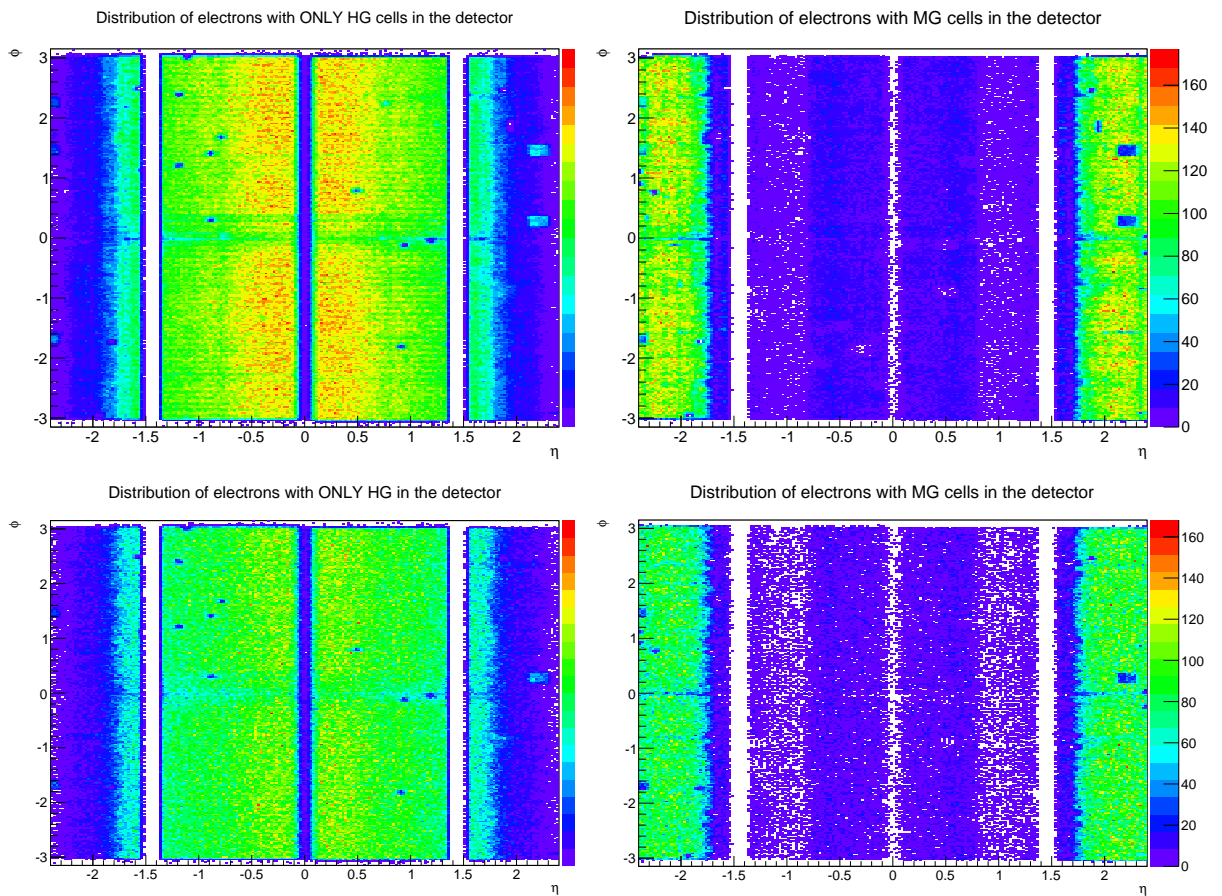


Figure 4.21: Distribution of HG (left) and MG (right) electrons in data (top) and in MC (bottom), for electrons from  $Z \rightarrow ee$  events

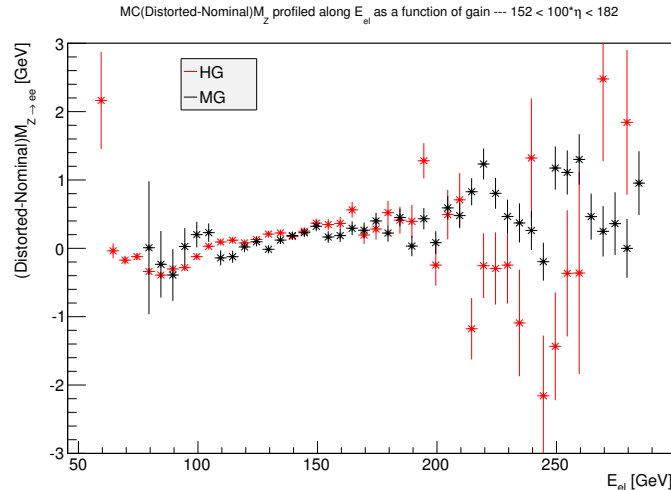


Figure 4.22: Difference, between the nominal  $Z \rightarrow ee$  Monte-Carlo and one with the maximal possible addition of material upstream of the calorimeter, of the reconstructed  $Z$  mass profiled along the energy of one of its electrons, for the electrons in HG and in MG. Only the region at the beginning of the end-cap is displayed

material biases the energy response of the two gains in the same way. Therefore a mis-modelling of the material budget upstream of the calorimeter cannot explain the observed response discrepancy between the two gains : the data to MC difference in reconstructed  $Z$  mass will change with regard to the material, but not the HG to MG difference of this variable.

### Timing of the cells in each gain

Computing the OFCs require a proper prediction of the ionization pulse from the physical signal, and in particular if the timing of the pulse is too delayed with respect to the prediction its amplitude will not be properly reconstructed. At its maximum the physics pulse is essentially flat for a few nano-seconds, which means that the maximal acceptable delay before the reconstructed cell energy starts to be biased is of 3-4 ns (in addition the OFCs minimize the sensitivity to timing). Given that the output of the shaper of the three gains is different they can in principle have a different timing, and if their relative timing is too different this aforementioned bias will translate in an apparent gain inter-calibration issue. In order to check for this issue, the timing of the most energetic cell in electron clusters coming from  $Z \rightarrow ee$  events has been studied, and averaged separately for the high and medium gain in narrow bins of  $\eta$ , which may be seen in fig. 4.23. The calibration of the pulse timing is done on MC, and  $t = 0$  correspond to the timing of the ionization pulses of particles that are coming from  $z = 0$  and are travelling at the speed of light. Therefore the small trend that is seen on MC only represents the fact that the collisions are in average slightly displaced with respect to  $z = 0$  and the related pulses will come in earlier on one side of the detector than the other. The variations observed on data are only representative of the imperfections of the electronics of the detector, which do not exist on MC. Effectively, in each electronic shaper chip the three gains are corresponding to three electronic circuits, as is described in [241], and each of these circuits has its own time constant, which implies that the three circuits will have different timings as they

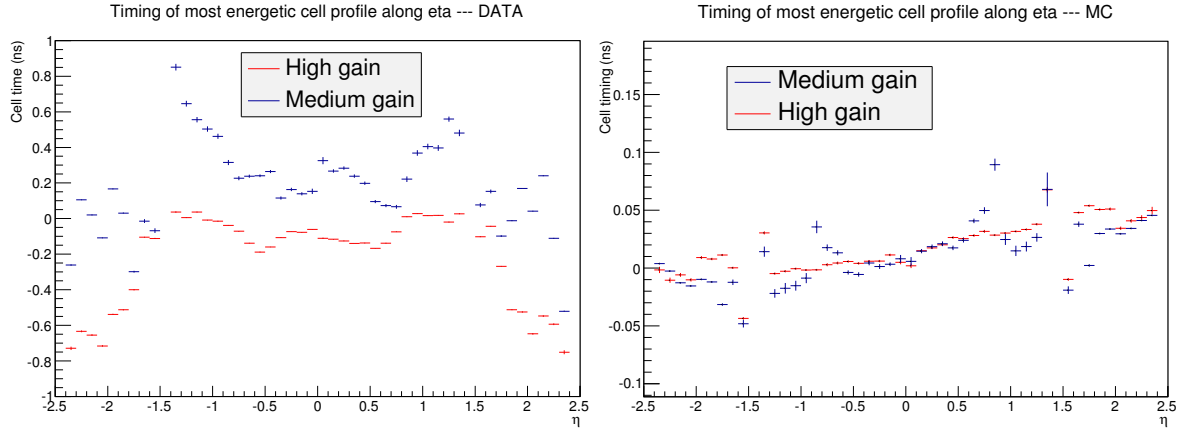


Figure 4.23: Average timing of the most energetic cell in electron clusters coming from  $Z \rightarrow ee$  events, separately for the two gains

are not calibrated independently for each gain. This feature is clearly seen in fig. 4.23 where the HG and MG have a fairly different timing, but the timing shift between the two gains is of less than 0.8 ns everywhere in the detector hence cannot be the source of the difference between the two gains.

### Inter-layer calibration

As this study was developed before the final Run 1 calibration was frozen, some of the pre-corrections that have been described above were not applied and could have a link with the observed difference between the two gains. This was the case of the inter-layer calibration, as in some cases an incoming electro-magnetic particle may deposit more energy in the strips than in the middle, which means that its cluster is less likely to contain a middle cell read-out in MG, although the total energy in the complete cluster is the same. If the strips are not properly calibrated with regard to the middle, an apparent bias between the responses of the two gains may appear, although it is in fact a bias in the strips calibration. This was checked on data by comparing the reconstructed  $Z$  mass before and after the application of the layer inter-calibration, and can be seen in fig. 4.24 for the region at the beginning of the end-cap, where the magnitude of both the layer inter-calibration scale and of the difference between the responses of the two gains is the largest. From this figure, it is clear that the inter-layer calibration does not create a difference between HG and MG and can not be at the source of the effect we observe.

### Electronics non-linearities

Several checks of the behaviour of the electronics have been derived, which are mostly based on the electronic calibration runs and on the expected shape of the ionization pulses, but none of them displayed an unexpected effect or generated a better understanding of this problem. The first check has been a comparison of the factors  $\frac{M_{phys}}{M_{cal}}$  (see eq. 3.6), which are used to equalize the amplitude of the exponential pulse of calibration runs to the triangular shape of physics run, between the two electronic gains, and this may be seen

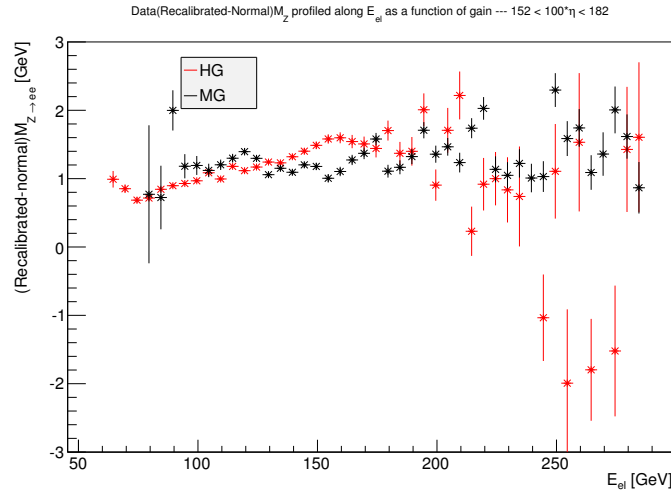


Figure 4.24: Difference of the reconstructed  $Z$  mass profiled along the energy of one of its electrons, between the data with and without the layer inter-calibration used with its nominal tune, for the electrons in HG and in MG. Only the region at the beginning of the end-cap is displayed

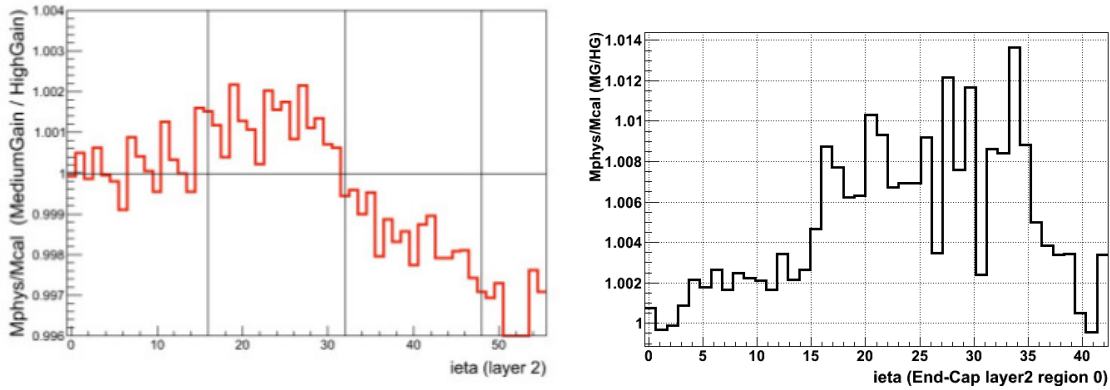


Figure 4.25: Ratio of  $\frac{M_{phys}}{M_{cal}}$  between high-gain and medium-gain in the barrel (left) and in the end-cap (right) [240]

in fig. 4.25. At  $|\eta| = 1.8$  ( $ieta = 16$ ), there is a clear structure where  $\frac{M_{phys}}{M_{cal}}$  varies from a baseline of 1.002 at  $|\eta| < 1.8$  to 1.006 at  $|\eta| > 1.8$ , but there is no similar structure in the barrel ( $|\eta| = 0.4 - 0.6$  corresponds to  $ieta = 16 - 24$ ), and the effect on  $\frac{M_{phys}}{M_{cal}}$  is still present toward the end of the end-cap where nothing is seen with  $M_Z$ . Therefore it seems that this structure is not correlated to the apparent difference between the two gains.

The second check was an estimation of the impact of using wrong OFCs on the estimation of the amplitude of the ionization pulse. The OFCs obtained from the high-gain were used to reconstruct the amplitude and timing of pulses recorded in MG. Although this variation of OFCs is extreme and not supported by any observation, it also allows to use OFCs that are expected to hold in an actual physical case, although it is for a different energy range. This check may be seen in fig. 4.26, and there are no clear structures that may be connected to what had been seen with the  $Z^0$  boson mass. The structure seen at

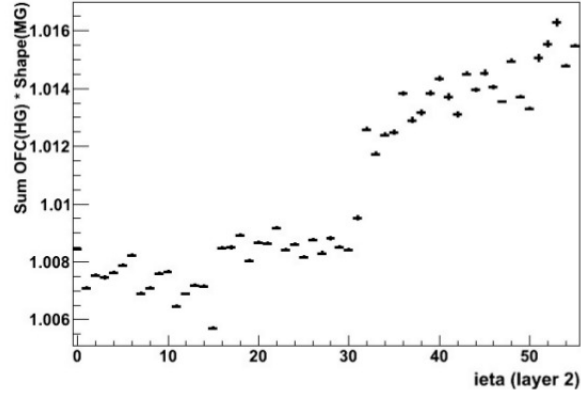


Figure 4.26: Effect of applying the wrong OFCs (computed for HG) on a pulse shape (coming from MG) [240]

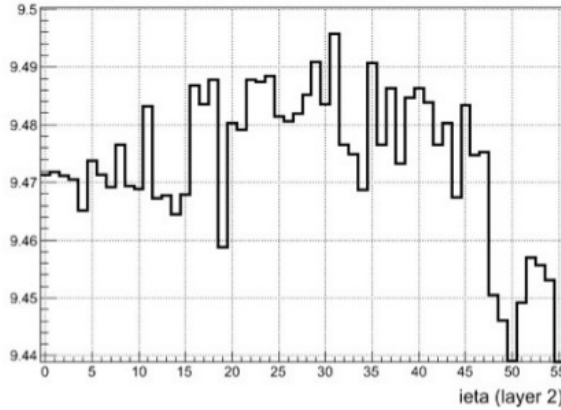


Figure 4.27: Ratio of the gain ramps between HG and MG (in the barrel) [240]

$ieta = 32$  ( $|\eta| = 0.8$ ) likely corresponds to the variation of the lead absorbers that changes the ionization signal, and it is not connected to any structure seen with the  $Z^0$  mass.

The ratio of the gain ramps between HG and MG may be seen in fig. 4.27 for the barrel, and there are also no clear structures that may be connected to what is seen with the  $Z^0$  boson.

The last check concerns the intercept with 0 of the MG calibration run, in terms of injected DAC counts. During the calibration runs for the medium gain the response is not probed down to an injected signal of 0 DAC counts, as the medium gain is not expected to be used for such a low signal. Effectively this implies that the value of injected DAC counts for which the fit of the response (in terms ADC counts) is 0 will not be 0, but this intercept will have a non-zero value. The value of this intercept as a function of  $|\eta|$  is displayed in fig. 4.28 for the barrel, and there are no strong variation in the barrel, up to  $|\eta| = 1$ , while the biggest effect in the barrel is observed at  $|\eta| \approx 0.6$ .

### Extracting the response difference from $\frac{E}{p}$

In  $Z \rightarrow ee$  events the Z boson is most usually produced with a small transverse momentum, and the two electrons are therefore roughly back-to-back. Previously we profiled the Z

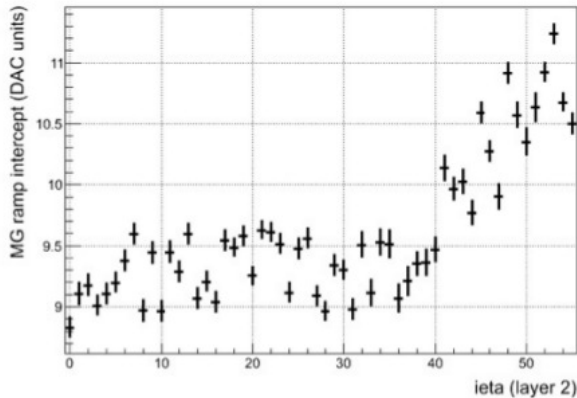


Figure 4.28: Intercept of the calibration ramp for the medium gain with the axis corresponding to a signal of 0 reconstructed amplitude (i.e. fitted number of injected DAC count in the calibration run for an output of 0 ADC counts) [240]

mass along the energy and pseudo-rapidity of one of its electrons, and assumed that any mis-modelling seen in the  $Z$  mass was originating from a mis-modelling of the energy response of this electron, as the second one is averaged out and the in-situ energy scale are correcting its response on average. But given this correlation of the direction of the two electron direction, the mis-modelling may still be on the second electron, and therefore could appear on the first one only through the correlation. This explanation can be ruled out by looking at the energy to momentum ratio for each of these electrons ( $\frac{E}{p}$ ), as with this variable there is no remaining dependency on the second electron. The momentum is estimated using the tracker information, where it is expected to be precisely calibrated, while the energy is still estimated with the EM calorimeter. In some regions with high-material budget, for instance at the beginning of the end-cap, the performance of the track momentum measurement may be worse but the effect observed using the reconstructed  $Z$  mass is expected to be sufficiently big to be seen with  $\frac{E}{p}$  too. The profiles of  $\frac{E}{p}$  along the energy of the electron are displayed in fig. 4.29 for the two bins where the effect observed with the reconstructed  $Z$  mass was the biggest in the barrel and in the end-cap, and it is clear from these plots that the effect is also observed with  $\frac{E}{p}$ . It is possible to convert the difference observed in  $\frac{E}{p}$  into an equivalent in reconstructed  $Z$  mass difference by using the formula  $\frac{\Delta M}{M} = 2\frac{\Delta E}{E}$ , and we observed an overall qualitative compatibility between the two methods, for instance  $\frac{E}{p}$  gives a mass difference of  $1160 \pm 130$  MeV in the bin  $1.62 < \eta < 1.72$  instead of the 1072 MeV that were observed with the di-electron mass, and  $316 \pm 71$  MeV instead of 178 MeV in  $0.6 < \eta < 0.8$ . The fact that the compatibility is only qualitative is expected as we only use profile of  $\frac{E}{p}$ , which is a variable with long tails toward higher values, that are not necessarily well modelled, and also because of the impact of additional material budget on this variable.

### FEBS with lower MG threshold in 2011

The previous study was performed on the 2012 dataset only, and qualitatively cross-checked with the 2011 dataset, as the available statistics is not sufficient to derive the correction that will be described below separately for the two years. But in 2011 there was

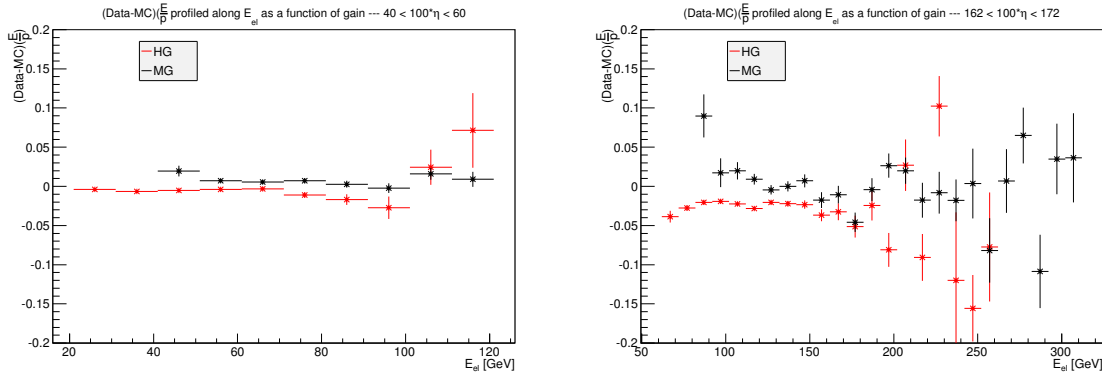


Figure 4.29: Profile of  $\frac{E}{p}$  for electrons from  $Z \rightarrow ee$  events that have either  $0.4 < \eta < 0.6$  (left) or  $1.62 < \eta < 1.72$  (right)

an additional detector feature that can be exploited, as for 17 of the FEBs the threshold at which the cells were read-out in MG was lower (11 FEBs in the barrel and 6 in the end-cap). Studying the mass distribution separately for these FEBs and the other, as is done in fig. 4.30, could help separate an effect coming from the gain only from other effects, especially kinematics effect as for these FEBs the implicit kinematic cut that exists when requiring MG electrons will be removed. This cross-check has some limitations, first it is statistically limited because these FEBs are only representing a small fraction of the 2011 dataset, but also because the energy reconstruction for the FEBs with low thresholds uses the calibration coefficients and OFCs that are computed for the MG electronic chain, and are not optimized for the low-energy range. If we forget about this last point, and that the inter-calibration of the gains is good, we would expect the mass distribution for the low-threshold FEBs to be close to the mass distribution of all the events, but we observe in fig. 4.30 some difference. Although this should be considered with caution, because of the aforementioned limitations of this argument, it may be a additional hint of improper gain inter-calibration.

#### 4.4.4 Derivation of an ad-hoc correction

No clear origin of this mis-modelling has been identified so far, therefore it was decided to derive an ad-hoc correction on this effect, whose role is to correct for the difference of energy response between the two gains on average, assuming that it is a difference of electronic calibration between the two electronic chain.

First, for a given cluster the bias of energy response may be broken into two-components (one for each gain) :  $\delta E = (1 - TO_{Es2}^{MG})\delta E_{HG} + TO_{Es2}^{MG}\delta E_{MG}$ , where  $TO_{Es2}^{MG}$  corresponds to the turn-on of the MG read-out as a function of the energy of the cluster in the middle sampling and  $\delta E_{HG, MG}$  corresponds to the bias of the particles energies in a given gain induced by a problem in the MG response. The turn-on is fitted on MC by Fermi-Dirac functions, with a different function for different bins in  $\eta$ , and there is a single function for electrons, converted and unconverted photons, since we parametrize the TO as a function of the energy in the middle sampling. The typical turn-on for  $h \rightarrow \gamma\gamma$  events may be seen in fig. 4.31. In the following we assume that the HG electronics is properly calibrated, and only the MG is biased, which implies that the only issue for the low-energy clusters

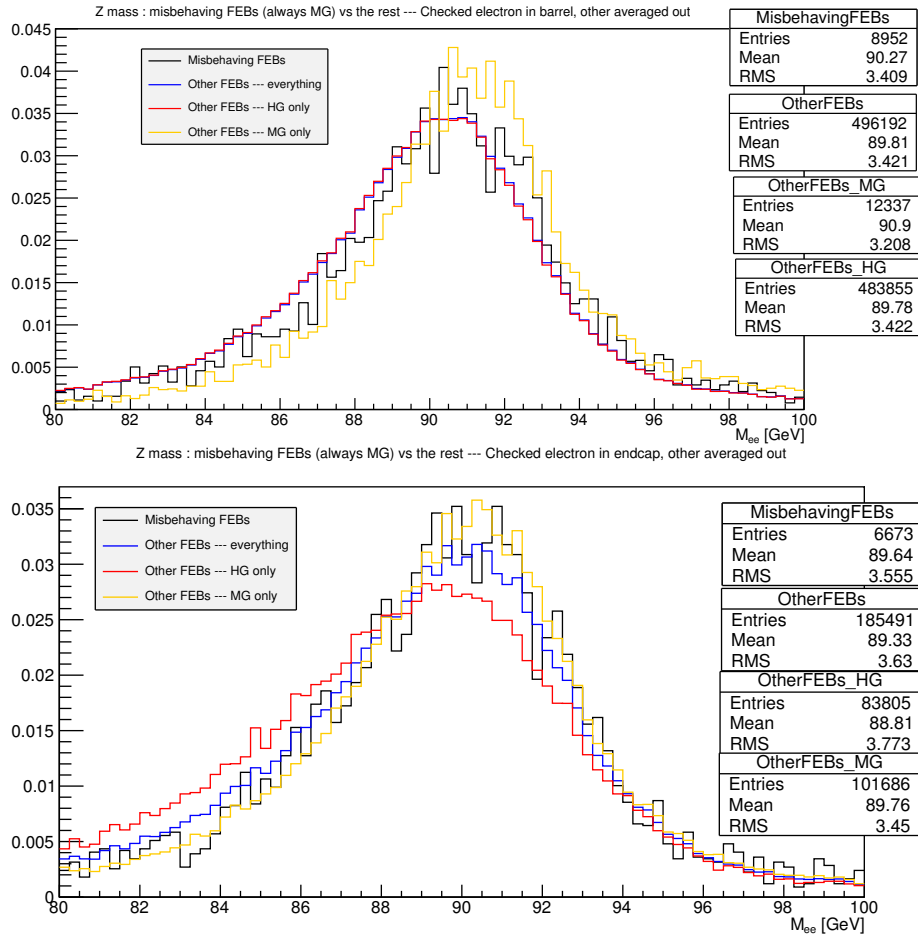


Figure 4.30: Di-electron mass distributions for  $Z \rightarrow ee$  events, separated between the FEBS where the gain switch is at a lower threshold, and separating the other events between those that are read-out in HG and those that are read-out in MG. The top plot corresponds to the barrel and the bottom to the end-cap

comes through the energy scales, that are computed on a dataset that has a non-negligible fraction of MG clusters. Furthermore we have only one measurement of the potential bias of the two gains, which comes from  $Z \rightarrow ee$  events, but the impact of a bias in the MG energy response will not be the same for clusters of different energies. If a cluster of low energy is flagged in MG, the fraction of energy in this MG cell is more important than it would be for a MG cluster of higher energy, which means that the bias of low-energy MG clusters will be more important than at the Z peak. But for even higher energies, there will be several cells read-out in MG, which will also increase the importance of this bias on high-energy clusters. The very high-energy clusters will also have some cells read-out in low-gain, but in the following we consider that MG and LG are biased in the same way, and can be considered altogether. This means that the values  $\delta E_{MG}$  need to be scaled as a function of the cluster energy, and this evolution of the bias on the clusters' energies is estimated from MC, by injecting a 1% bias to the cells that are read-out in MG and measuring the bias this creates on the cluster's energy itself. This function, that we will denote  $var_{MG}E(E, \eta)$  is fitted separately in several bins of  $\eta$  by polynomial functions. If we denote  $\Delta E_{HG, MG}^0$  the bias that is measured with  $Z \rightarrow ee$  events we get the following parametrization for the bias in energy response :

$$\delta E = (1 - TO_{Es2}(E, \eta)) \Delta E_{HG}^0(\eta) + TO_{Es2}(E, \eta) \Delta E_{MG}^0(\eta) var_{MG}E(E, \eta) \quad (4.4)$$

The last piece we need to derive the correction is a way to convert the bias in the Z mass that is observed into its equivalent in term of energy. To do so we start with the basic formulae  $m^2 = 2E_1E_2(1 - \cos\theta)$  that is valid as long as there are two particles with negligible masses in the final state. It is easy to show that an infinitesimal variation of the energy gives the following variation of mass :  $2m dm = m^2(\frac{dE_1}{E_1} + \frac{dE_2}{E_2})$  but the in-situ energy scales are applied on both electrons, and the second electron is averaged over. By construction the energy scale are made to take into account any potential discrepancy between data and MC on average, which implies that  $dE_2 = 0$ , and hence gives  $\frac{dm}{m} = \frac{1}{2} \frac{dE_1}{E_1}$ . If we inject this into eq. 4.4 we get the final value of the bias :

$$\delta E = \frac{2E}{M_Z} (\Delta M_{MG}^0 var_{MG}E(E, \eta) TO_{Es2}(E, \eta)) + \Delta M_{HG}^0 (1 - TO_{Es2}(E, \eta)) \quad (4.5)$$

where  $\Delta M_{HG, MG}^0$  corresponds to the mass bias that is measured with the  $Z \rightarrow ee$  mass peak. Effectively eq. 4.5 gives a proper way to extrapolate the bias on the reconstructed Z mass that we observe by splitting the  $Z \rightarrow ee$  dataset into the two gains to any other energy range, assuming that it is really an improper calibration of the electronic gain. The  $\delta E$  can then be subtracted to the energies measured on data to correct for this effect. As it is not clear that this corresponds to the actual origin of the effect, which has not been found, it was decided to associate a conservative uncertainty to this correction, and the value of this uncertainty has the same value than the correction itself.

The impact of this correction on  $h \rightarrow \gamma\gamma$  events may be seen in fig. 4.32, where it is estimated in a  $h \rightarrow \gamma\gamma$  simulation, on an event-by-event basis by computing the difference of the di-photon invariant mass before and after the application of this correction. The average of this distribution, which also corresponds to the expected decrease of  $m_H$  measured in the  $h \rightarrow \gamma\gamma$  channel, is of 115 MeV, although it has an important tail toward higher values that directly connects to the variations along  $\eta$  observed with the  $Z \rightarrow ee$

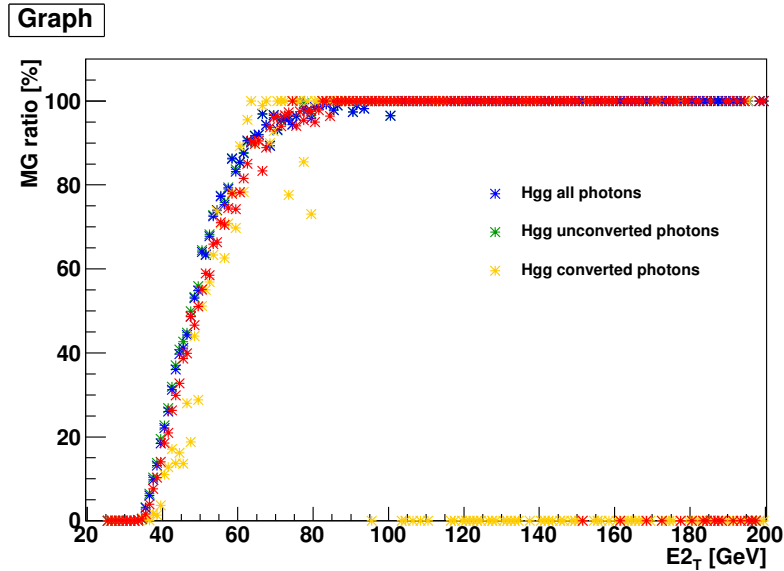


Figure 4.31: Turn-on of the middle layer MG as a function of the transverse energy measured in the middle, for typical simulated  $h \rightarrow \gamma\gamma$  events [240]

peak. For instance the events that have a correction as high as one GeV are those that have one leg falling at the beginning of the end-cap. These 115 MeV also roughly correspond to the value of the uncertainty on the Higgs boson mass that is induced by this issue, although the exact value depends on the way the categories that are used in the analysis are defined.

#### 4.4.5 Correlation with the shower-shape mismodeling

For the final Run 1 measurements the study that was presented above, and the correction that comes with it, were used although there were no clear hint of the origin of this effect as specific structure that could be correlated to this effect had neither been found on calibration runs nor on the detailed study of the  $Z \rightarrow ee$  peak presented above. This study was resumed later, as a part of the preparation for Run 2, by another group [242] that observed a correlation between the discrepancy of the response between the two gains and the mis-modelling of shower shapes, in particular for the variable  $w_{s,tot}$  (see table 3.1) that has a much higher value in data than in the MC in the region around  $\eta \approx 1.65$ , which explains part of the effect for the bin at the beginning of the end-cap where the effect is the worst. But this study is still under development, and this correlation with shower-shape mis-modelling may not explain the full effect that had been observed. In addition it does not explain the smaller effect that had been observed elsewhere in the detector. It is also not yet clear how the impact of shower-shape could be effectively corrected nor how to derive an uncertainty from this mis-modelling. All the conclusion of the analysis described above were confirmed in this new study, especially the fact that although the effect is correlated with shower shapes, it does not seem to be explained by a material budget mis-modelling as it was observed on a distorted MC sample that the shower shape and response variation created by additional material are cancelling out in the difference between HG and MG. More work is needed to understand the correlation with the mis-

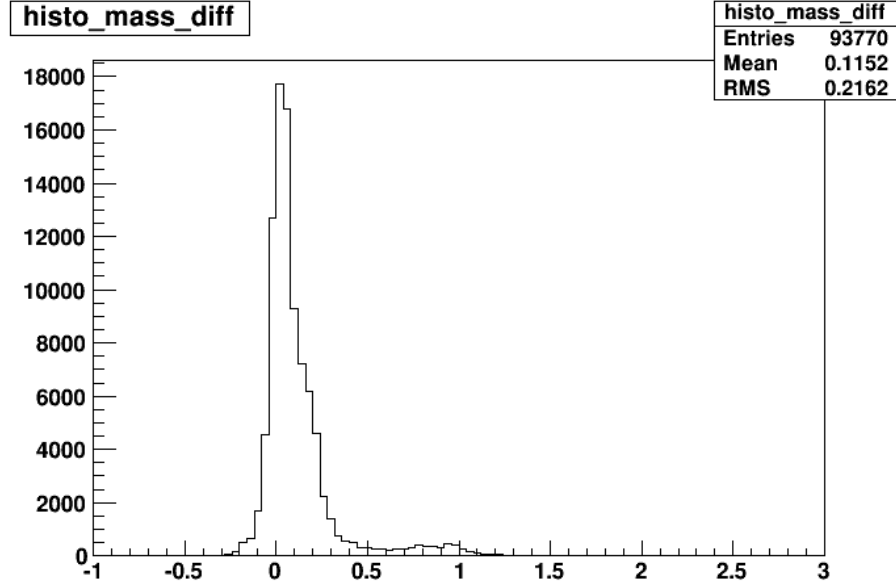


Figure 4.32: Distribution of the difference of reconstructed di-photon mass in simulated  $h \rightarrow \gamma\gamma$  events before and after the effective correction described by eq. 4.5, in GeV [240]

modelling of  $w_{s,tot}$  since it has a higher value in data than in MC, which also seems in contradiction with the estimation of material budget upstream of the EM calorimeter (see fig. 4.3 which seems to indicate that there is an excess of material in the simulation).

## 4.5 Lateral energy leakage

### 4.5.1 Position of the problem

#### Shower-shape mis-modelling

During the first year of the Run 1 data-taking it was realized that the lateral shape of electro-magnetic showers was poorly modelled by the Geant 4 detector simulation implemented in ATLAS : as may be seen in fig. 4.33 the showers are wider in data. A lot of studies were carried out to understand this effect but it was never completely understood or fixed. An improved description of the calorimeter absorbers, where they are not described as a mixture of materials but split into their actual components, have been implemented in the detector description and decreased this mis-modelling by a factor  $\approx 2$ . But the remaining half of the effect is still an open point, and was found out to be incompatible with missing material in the detector simulation. If this mis-modelling is not universal it can bias the energy estimation provided by the MVA, as it is possible that the average amount of energy leaking outside of an electro-magnetic cluster varies with respect to  $p_T$  or is different between electrons and photons. For electrons at  $E_T \approx E_T^{Z \rightarrow ee}(e)$  this loss of energy is corrected for by the in-situ energy scales, but this will not work in an other energy range or for photons if the leakage is not universal.

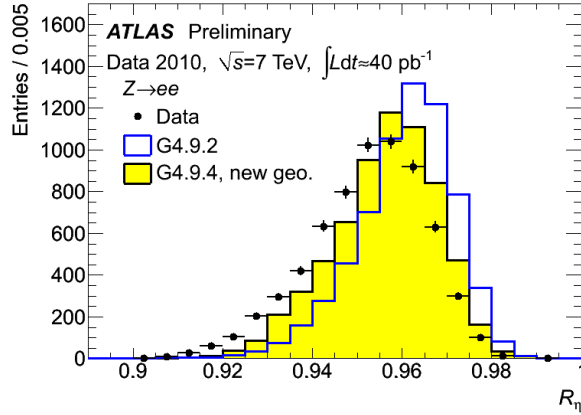


Figure 4.33: Distribution of  $R_\eta = \frac{E_{3 \times 7}}{E_{7 \times 7}}$  measured on  $Z \rightarrow ee$  events either on the 2010 dataset, and on two versions of the Monte-Carlo that implements a different description of the absorbers. "new geo" corresponds to the last version of the absorbers that is now used in the simulation [243]

	$ \eta  < 0.8$	$0.8 <  \eta  < 1.475$	$1.475 <  \eta $
$3 \times 5$ cells	0.3%	1.1%	1.6%
$3 \times 7$ cells	0.3%	1.0%	1.5%
$5 \times 5$ cells	0.1%	0.2%	0.6%

Table 4.3: Differential fraction (data minus Monte-Carlo) of energy leaking outside of electromagnetic clusters, as measured using  $W \rightarrow e\nu$  events on the 2010 data and Monte-Carlo, in three broad  $\eta$  bins and for several cluster sizes, computed with respect to the number of cells in the second layer (in  $\eta \times \phi$ ) [244, 245]

### Correction extracted from the 2010 Monte-Carlo

The first study of this effect has been done using the 2010 Monte-Carlo, and used  $W \rightarrow e\nu$  events as the statistics of  $Z \rightarrow ee$  events available in this year was not sufficient. The fraction of energy leaking outside of the electromagnetic clusters was derived in three broad  $\eta$  bins and for several cluster sizes, and the results concerning the difference of leakage between data and Monte-Carlo are summarized in table 4.3. The energy leakage was evaluated in  $19 \times 19$  middle cells which allowed to compute the integral of the shower. It is the only time this could be done as it requires low-level datasets that are heavy and cannot be used when the number of events becomes big. From this study we know that the energy leaking outside of a cluster of  $7 \times 11$  cells, which will be used later, is negligible.

When the Monte-Carlo calibration was based on the calibration hits method these numbers were applied as a correction to the cluster energy, both for electrons and photons clusters and independently of the particle energy. This is not anymore the case with the calibration based on a MVA technique, but the MVA itself learns the leakage and is able to recover for it, although this is based on the leakage as it is seen on the detector simulation. In both cases the mis-modelling of the energy leakage is taken into account by the in-situ energy scale and therefore does not have an important impact on the estimation of the particles energy for electrons around  $\approx 40$  GeV. It is more important in the extrapolation of electrons to photons. In 2010 there were no clean photon probes to estimate the leakage

from photons. It was also difficult to estimate the  $p_T$  variation due to the fact that showers could become broader at increasing energy, because of a lack of statistics.

## 4.5.2 Overview of the method

As we are looking for a possible difference between electrons and photons in the mis-modelling of the lateral energy leakage, we would like to have pure sources for both of these particles, which is possible with  $Z$  decay, either  $Z \rightarrow ee$  or radiative  $Z \rightarrow ll\gamma$  decays. The  $Z \rightarrow ll\gamma$  events constitute the only pure source of photons that is available at a hadron collider, but they have the drawback that they are fairly rare. There is not yet a large dataset from these decays and the  $p_T$  spectrum of the photons is softer than the one of the electrons.

For all the electromagnetic particles passing a few weak criteria ( $p_T > 15$  GeV, loose identification) several informations about all the cells within a cone of  $\Delta R = 0.4$  around the particle have been saved on the final analysis datasets, together with a link between the particle and the cells that are in this cone. Within these cells,  $7 \times 11$  (in  $\eta \times \phi$ , in the middle sampling) correspond to the initial particle, while others are sporadically present either because there are two clusters that overlap, or for other reasons that have not been understood. A dedicated logic has been developed and is actually doing an iterative search for this array of  $7 \times 11$  cells, which allows to build back  $\approx 90\%$  of the electromagnetic clusters. Within the other 10% a first half are lost because they are too close to an alignment or segmentation change (at  $\eta = 0$  and in the crack), where this logic is expected not to work, while the last 5% are lost either because one or several cells are missing. The clusters are only built in the middle sampling, as there are too many segmentation changes in the strips to implement this logic properly.

Once this  $7 \times 11$  cells cluster and its center have been found it is possible to build clusters of arbitrary sizes, as long as they are smaller. The fraction of energy leaking outside a given cluster is estimated as  $\frac{E_{s2}(7 \times 11) - E_{s2}(cluster)}{E_{s2}(cluster)}$  where the size of  $E_{s2}(cluster)$  depends on the type of particle we are looking at and its position in the detector. As will be shown below, the mis-modelling of  $\frac{E_{s2}(7 \times 11) - E_{s2}(cluster)}{E_{s2}(cluster)}$  is different between electrons and photons, and several tentative scenarios have been checked to determine whether we understand the source of this difference. They will be described below too.

Because of the difference of cluster size between electrons and unconverted photons a slight dependence with respect to the pile-up could have been expected. This is corrected by the bipolar shaping of the calorimeter electronics, which is perfect only for infinite bunch train. The variation of the cell energy that is observed as a function of the position of the bunch crossing inside the bunch train, is sizeable mainly at the beginning of the bunch train where it is not possible to average the in-time and the out-of-time pile-up, and has been corrected for [246]. This correction requires the knowledge of the luminosity with respect to the BCID and of the energy deposited in a cell per collision as a normalization (in addition to the luminosity). This may be extracted from special runs where there is only one bunch. The remaining dependencies are cancelling in the data-MC difference and in the electron to photon difference.

### 4.5.3 Cross-checks of potential electron to photon differences

#### Difference between electron-like and photon-like clusters

There are two main reasons that may give a different mis-modelling for the lateral energy leakage between electrons and photons, the first one being the different nature of the two particles and the second the difference of the size of the clusters that are used to reconstruct these particles. Two ways of measuring this effect are possible : the leakage can either be measured with clusters of different sizes for electrons and photons, using the nominal size of these clusters, or for clusters of a given size that is the same for electrons and photons (e.g.  $3 \times 7$  cells) and complemented by a measurement of the difference of leakage between clusters of different size, using only one kind of particle. We decided to use the first method but have still measured for each type of particles the difference between clusters used in the barrel for electrons ( $3 \times 7$  cells) and unconverted photons ( $3 \times 5$  cells).

**Difference between clusters of different size** To study the impact of different cluster sizes the mis-modelling of the energy leaking outside of a  $3 \times 5$  cells cluster into a  $3 \times 7$  cells cluster has been studied, and may be seen in fig. 4.34. If we take  $\frac{E(3 \times 7) - E(3 \times 5)}{E(3 \times 5)}$  as an estimation of the width of the electromagnetic shower, the showers would be narrower on data than in the MC which is in contradiction with what had been observed with the studies of the shower shape variables (e.g.  $w_{s,tot}$ ) or what is observed when the full energy leakage is studied. It is not clear what is the exact origin of this negative baseline. It may originate from a uniform material mis-modelling, for instance at the level of the beam-pipe, but there is no supporting evidence for this to happen. The closest distorted material geometry available corresponds to a scaling of the inner detector material budget by +5% (conf A) and does not mimic this effect. The big variation that exists just before the crack ( $1.3 < |\eta| < 1.37$ ) can be explained by a material mis-modelling, which is supported by the studies of the Z boson lineshape that is not properly modelled in this region, but not by the material studies based on  $\frac{E_1}{E_2}$ . Still it was decided to cut this part of the detector in the extraction of the leakage, as well as the part at the end of the crack which is too close to the various changes of segmentation that are happening in the crack, and therefore the part  $1.3 < |\eta| < 1.6$  will not be further considered in the following section.

**Impact of the pedestal shift** As electrons and unconverted photons clusters have different sizes, the data to MC shift of electronic pedestal that is described in subsection 4.6.2 can have a different impact between these two types of particles, although it is expected to be fairly small, as this shift gives an impact that is less than one MeV per cell. The difference of mis-modelling between different types of particles may be seen in table 4.4, and taking into account the pedestal shift slightly improves this difference, although not by much. As the  $Z \rightarrow ee$  electrons and  $Z \rightarrow ll\gamma$  photons have a different  $p_T$  spectrum this would be the case even if they all had the same cluster sizes, which can be seen in the end-cap. The pedestal shift will therefore be applied.

**Impact of the Geant 4 physics list** Within the Geant 4 tool-kit several different models can be used to generate different types of physical processes that impact the

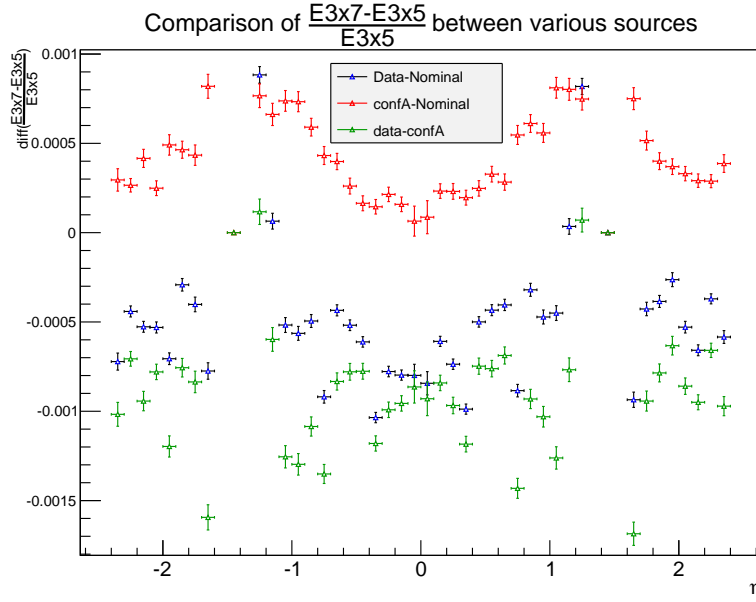


Figure 4.34: Relative energy response mis-modelling difference between clusters of different sizes, using electrons from  $Z \rightarrow ee$  events. "Nominal" corresponds to the nominal MC and "confA" to a distorted geometry with an increased inner material budget

Particle type	$ \eta  < 0.8$	$0.8 <  \eta  < 1.3$	$1.6 <  \eta  < 2.37$
Before pedestal subtraction			
El - Unconv	$-0.00052 \pm 0.00040$	$-0.00113 \pm 0.00060$	$-0.00056 \pm 0.00040$
El - Conv	$-0.00152 \pm 0.00108$	$-0.00369 \pm 0.00101$	$-0.00148 \pm 0.00107$
After pedestal subtraction			
El - Unconv	$-0.00030 \pm 0.00040$	$-0.00093 \pm 0.00060$	$-0.00054 \pm 0.00040$
El - Conv	$-0.00123 \pm 0.00107$	$-0.00338 \pm 0.00101$	$-0.00140 \pm 0.00107$

Table 4.4: Difference of energy leakage mis-modelling between different types of particles, before and after the subtraction of pedestal shift. The numbers taken for the photons corresponds to a combination of the  $Z \rightarrow ee\gamma$  and  $Z \rightarrow \mu\mu\gamma$  numbers. Differences as  $\frac{E_{3 \times 7} - E_{3 \times 5}}{E_{3 \times 5}}$  shown in fig. 4.34.

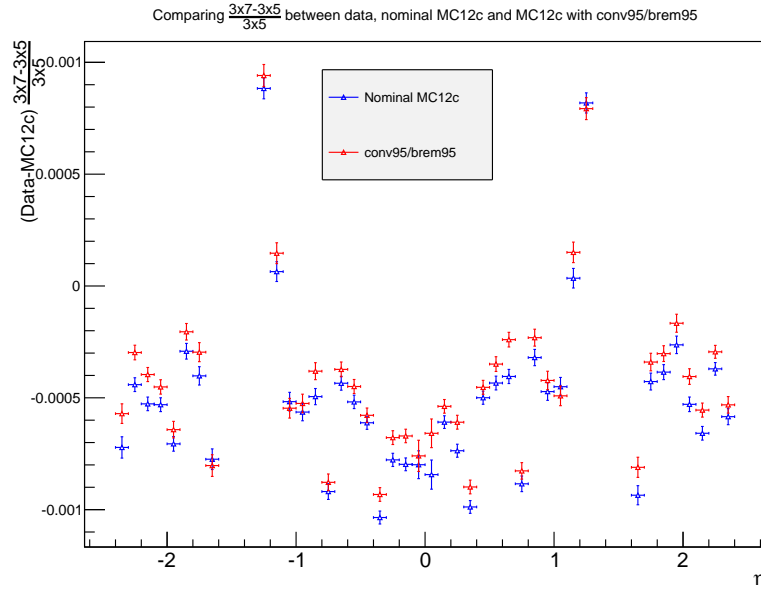


Figure 4.35: Mis-modelling of the lateral energy leakage for electrons for two versions of the description of conversion and bremsstrahlung processes, the most recent being conv95/brem95

development of a shower, such as the bremsstrahlung or the photon conversion. A complete model for all these processes is called a physics list, and as the state-of-the-art computation evolves, the physics list may change. During the production of the last Monte-Carlo samples for ATLAS (MC12C) the physics list had not been updated and was using an older description of the conversion and bremsstrahlung processes. With respect to this older physics list the newer one was expected to generate broader showers, which could have explained the mis-modelling of  $\frac{E(3 \times 7) - E(3 \times 5)}{E(3 \times 5)}$ . To study this, a sample of  $Z \rightarrow ee$  events was passed through the two versions of the full detector simulation, and the mis-modelling of the electron energy leakage was computed for both, which may be seen in fig. 4.35. Although the mis-modelling of  $\frac{E(3 \times 7) - E(3 \times 5)}{E(3 \times 5)}$  slightly improves with the new implementation, this is only by a negligible amount and the local features are still present.

### Impact of additional material in front of the calorimeter

An increased amount of material budget in front of the electromagnetic calorimeter is expected to broaden the showers measured in the calorimeter, as they would start to shower earlier, and this may have a different impact if the photons are converted or not. In this context the sub-detector that is expected to have the largest impact is the inner tracker hence it was decided to use the distorted geometry where its material is scaled by +5% to do this test, whose results are displayed in fig. 4.36. In this test the difference between converted photons and electrons is smaller than the difference between unconverted photons and electrons, which goes in the opposite direction than what is observed in data (see subsection 4.5.4), therefore we believe that additional material cannot explain the difference between converted photons and electrons.

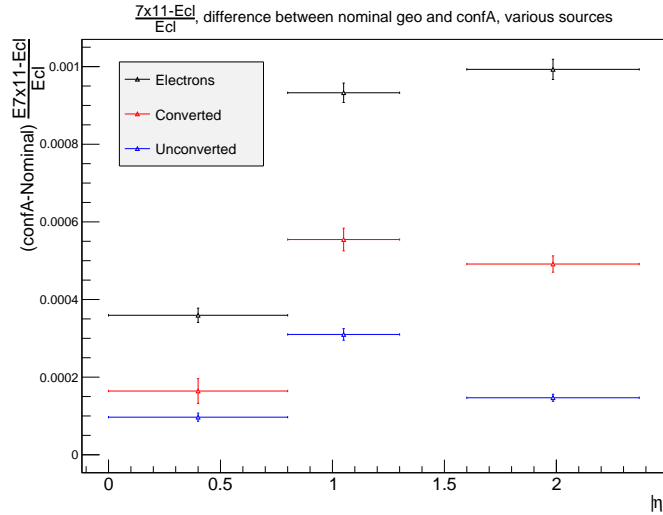


Figure 4.36: Difference of lateral energy leakage between the detector simulation with an increased tracker material and the nominal simulation, for different types of particles

### Impact of conversion reconstruction mis-modelling

As this analysis makes a classification with respect to whether the photon is converted, the impact of the mis-modelling of photon conversion reconstruction that is described in subsection 4.7.1 needs to be taken into account. This is done on Monte-Carlo by reweighting the photon population that has a true conversion status different than the reconstructed one, so that the fraction of events whose conversion status are mis-reconstructed match the one that is measured on data. As the total number of true converted and true unconverted photons in a MC sample only depends on the number of events generated it should not be impacted by the conversion reconstruction mis-modelling, and therefore an additional reweighting is derived for those photons where the true converted status is the same than the reconstructed. The difference of lateral energy leakage between these reweighted samples and the nominal ones may be taken as an uncertainty, and is seen in table 4.5, where it is clear that this effect is not negligible. The size of the inner cluster used to compute the leakage is chosen from the reconstructed conversion status of the photon, and this difference of cluster size between converted and unconverted photons has a big impact and is driving the uncertainty that is induced by this reweighting. If we consider that the weights are giving the most accurate description of the detector the electron to photon difference of leakage mis-modelling decreases for unconverted photons while it sizeably increases for converted photons.

### Lateral leakage in the strips

Up to now, the leakage has been computed only in the middle layer, and naively we can expect that this is a conservative estimation of the effect. At the energies we are interested for  $h \rightarrow \gamma\gamma$  the back layer has a negligible weight in the energy measurement, and we expect the shower to be narrower in the strips hence the leakage should be better modelled as it is expected not to exist. In this sense if we apply the energy loss fraction that is measured in the middle to the full cluster energy we may over-estimate the uncertainty that will be

	Unconverted	Converted
$Z \rightarrow ee\gamma$		
$0 <  \eta  < 0.8$	$0.00031 \pm 0.00026$	$-0.00039 \pm 0.00075$
$0.8 <  \eta  < 1.3$	$0.00051 \pm 0.00048$	$-0.00127 \pm 0.00074$
$1.6 <  \eta  < 2.37$	$0.00049 \pm 0.00041$	$-0.00059 \pm 0.00079$
$Z \rightarrow \mu\mu\gamma$		
$0 <  \eta  < 0.8$	$0.00028 \pm 0.00031$	$-0.00025 \pm 0.00090$
$0.8 <  \eta  < 1.3$	$0.00048 \pm 0.00041$	$-0.00120 \pm 0.00079$
$1.6 <  \eta  < 2.37$	$0.00035 \pm 0.00029$	$-0.00031 \pm 0.00079$

Table 4.5: Difference of the lateral energy leakage between samples with or without the reweighting of the conversion reconstruction mismodelling

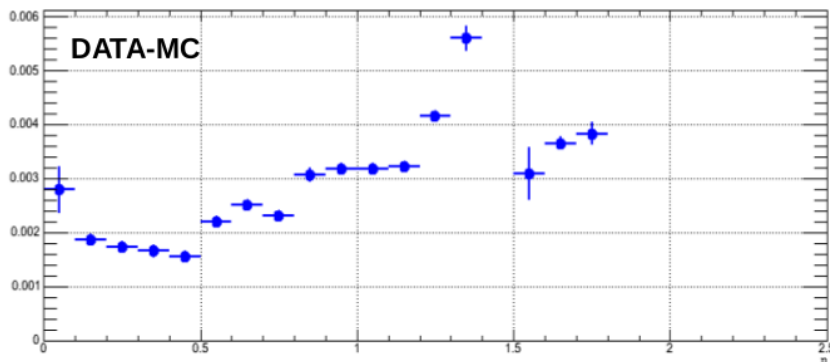


Figure 4.37: Mis-modelling of the lateral energy leakage in the strips (in %), computed as  $\frac{E(56 \times 2) - E(24 \times 2)}{E(24 \times 2)}$  where  $E(N \times M)$  corresponds to the energy in  $N \times M$  cells (in  $\eta \times \phi$ ) around the particle in the strips [247]

applied, while if we are able to probe that the leakage in the strips is well modelled or does not exist, this fraction can be scaled by the fraction of energy in the middle sampling. This check can be seen on fig. 4.37 where the mis-modelling of the leakage in the strips is displayed, and is computed with electrons coming from  $Z \rightarrow ee$  events. It is of the order of 2-3% hence cannot be neglected, and the full effect of the leakage measured in the middle layer is still used to estimate the uncertainty.

### Lateral leakage for lower $p_T$ photons

A first cross-check of the potential non-linearity induced by the leakage had been conducted on  $Z \rightarrow ee$  events, with electrons that have a  $p_T$  higher than 25 GeV, and no source of non-linearity had been observed. To further develop this cross-check we decided to do it on photons too, and given the selection criteria for  $Z \rightarrow ll\gamma$  events it is possible to go to lower  $p_T$ , down to 15 GeV. Below this energy the information from the cells were not available anymore. Two  $p_T$  bins were studied, the first between 15 and 25 GeV and the second one above 25 GeV, and they are summarized in table 4.6, where the electrons are always asked to have  $p_T > 25$  GeV (and the effects of conversion mis-modelling and pedestal shift are taken into account). There is no obvious variation of the leakage with respect to the

Particle type	$ \eta  < 0.8$	$0.8 <  \eta  < 1.3$	$1.6 <  \eta  < 2.37$
$15 < p_T^\gamma < 25 \text{ GeV}$			
El - Unconv	$0.00022 \pm 0.00036$	$-0.00082 \pm 0.00052$	$-0.00128 \pm 0.00038$
El - Conv	$-0.00162 \pm 0.00139$	$-0.00394 \pm 0.00112$	$-0.00357 \pm 0.00105$
$p_T^\gamma > 25 \text{ GeV}$			
El - Unconv	$-0.00002 \pm 0.00040$	$-0.00056 \pm 0.00060$	$-0.00014 \pm 0.00040$
El - Conv	$-0.00162 \pm 0.00109$	$-0.00458 \pm 0.00102$	$-0.00185 \pm 0.00108$

Table 4.6: Difference of mis-modelling of the lateral energy leakage between electrons and photons for different kinematic ranges for the photon from  $Z \rightarrow l\bar{l}\gamma$

	$0 <  \eta  < 0.8$	$0.8 <  \eta  < 1.3$	$1.6 <  \eta  < 2.37$
Unconverted photons	0.04%	0.1%	0.05%
Converted photons	0.16%	0.46%	0.19%

Table 4.7: Magnitude of the uncertainty related to the difference of the mis-modelling of lateral leakage between photons and electrons

energy, although this is limited by the statistical uncertainty on the photons. A similar study was conducted, using a reweighting of the photon  $p_T$  spectrum to the electron  $p_T$  spectrum which allows to suppress the kinematic dependence of this effect, and it gave the same conclusion. In the following we decided to keep only the photons above  $p_T > 25$  GeV in order not to suffer from potential non-linearities that we could have missed during this cross-check.

#### 4.5.4 Final results

A conservative uncertainty has been associated to the electron to photon difference of lateral energy leakage mis-modelling, and is taken directly as the double difference  $(Data - MC)(e - \gamma) \frac{E(7 \times 11) - E_{cluster}}{E_{cluster}}$ . This double difference is evaluated for each  $|\eta|$  bin with and without the conversion mis-modelling and the most conservative values are taken [234, 248]. At the end, in a given bin, if the statistical uncertainty on this effect is bigger than the effect itself, we take the statistical uncertainty to represent this systematic uncertainty, and not the magnitude of the effect itself, as it is not clear whether there is no effect at all or whether we are just not sensitive to it, and the value of these uncertainties are given in table 4.7. For unconverted photons the uncertainty for the low and large  $|\eta|$  bins corresponds to a statistical uncertainty, while for converted photons the effects in all bins are coming from the central value of the effect itself. Moreover after the reweighting that is used to model the impact of conversion reconstruction mis-modelling there is a very small leakage mis-modelling at all between unconverted photons and electrons while the effect is fairly big between converted photons and electrons, which is a hint that there is an effect that is fairly different between converted and unconverted photons. Therefore we decided to de-correlate the systematic uncertainties used for converted and unconverted photons.

## 4.6 Determination of the energy scale of the calorimeter

### 4.6.1 Absolute energy scale

Even after the initial electronic calibration, the MC-based calibration and all the pre-corrections applied on data, there may be some remaining discrepancies between the detector simulation and the actual detector. These discrepancies may affect both the central value of the energy response and the energy resolution, and this needs to be taken into account. The potential difference in the central values may come from effects such as a different LAr temperature between the data and the simulation and needs to be effectively recovered in the data, and this is done by extracting the in-situ energy scales  $\alpha$  using the  $Z \rightarrow ee$  peak as a standard candle. They will act as multiplicative factors to the particles energies. The potential difference in the resolution comes from effects such as an improper description of the spread of the material or of the temperature gradients, which are parameters that are intrinsic to the detector and need to be effectively corrected in the simulation. This is done by deriving an effective constant term, at the same time as the in-situ energy scales, that is applied on simulation as a Gaussian smearing to the particles energies. The whole extraction of the in-situ scales and of the resolution is done by ensuring that the di-electron invariant mass distribution in the corrected data and the smeared MC match, which relies on a few formulae [249, 250].

Denoting two particular  $\eta$  bins (i, j), the di-electron invariant mass for  $Z \rightarrow ee$  events with one of the electrons falling in i and the other in j is given by  $m_{ee}^2 = 2E_i E_j (1 - \cos\theta_{ee})$  where  $\theta_{ee}$  corresponds to the opening angle between the two electrons (the impact of the uncertainty on the angle  $\theta_{ee}$  on the mass  $m_{ee}$  is neglected). If the energy scale is not perfectly estimated the energies  $E_i, E_j$  are not the true energies but may be replaced by  $E_i = (1 + \alpha_i) E_i^{MC}$ , because the Monte-Carlo is assumed to be perfectly calibrated. This can be translated on the di-electron invariant mass as  $m_{ee} = m_{ee}^{MC} \sqrt{1 + \alpha_i + \alpha_j + \alpha_i \alpha_j}$ , and keeping only the first order in  $\alpha_i, \alpha_j$  this gives  $m_{ee} \approx m_{ee}^{MC} (1 + \frac{\alpha_i + \alpha_j}{2}) \equiv m_{ee}^{MC} (1 + \alpha_{i,j})$ . In a similar way the variation of the resolution can be derived. It can be shown that  $(\frac{\sigma_m}{m})^2 = \frac{1}{4} ((\frac{\sigma_{E_i}}{E_i})^2 + (\frac{\sigma_{E_j}}{E_j})^2)$  and an additional resolution constant term  $c_i$  term may be included into the resolution as  $(\sigma_{E_i}^{Data})^2 = (\sigma_{E_i}^{MC})^2 + c_i^2 E_i^2$ . This gives

$$((\frac{\sigma_m}{m})^{Data})^2 = ((\frac{\sigma_m}{m})^{MC})^2 + \frac{c_i^2 + c_j^2}{4} \equiv ((\frac{\sigma_m}{m})^{MC})^2 + c_{i,j}^2 \quad (4.6)$$

In practice, the distributions of  $m_{ee}$  are studied separately in each of the (i,j) configurations, and a fit is performed where  $\alpha_{i,j}$  and  $c_{i,j}$  are the parameters of interest. This gives two matrices that are inverted to determine the values of the energy scales and of the effective constant term for each of the individual  $\eta$  bins ( $\alpha_i, c_i$ ).

Two different methods have been developed to fit the  $\alpha_{i,j}$  and  $c_{i,j}$ , and the difference between the two results has been taken as an additional uncertainty. The first method, whose result is taken as the central value, is based on a template fit method, where histograms are created in each (i,j) configuration and for a two-dimensional grid of  $\alpha_{i,j}$  and  $c_{i,j}$ , by shifting and smearing a Monte-Carlo sample. These histograms are then compared to the data, using a  $\chi^2$  test, and the best values of  $\alpha_{i,j}, c_{i,j}$  correspond to the template

that gives the minimal  $\chi^2$ . The second method is based on an unbinned likelihood fit. In order to obtain the  $\alpha_{i,j}$  one uses a likelihood based on parametrized functions close to Breit-Wigner distributions which are displaced by  $M_Z \rightarrow \frac{M_Z}{1+\alpha_{i,j}}$ . In order to get the  $c_{i,j}$  one uses a convolution of a Breit-Wigner and a Crystal-Ball, and  $c_{i,j}$  comes from a comparison of the resolution fitted in data and on the MC. The final values of the energy scales are given in fig. 4.38, and the resolution in fig. 4.39. As the two sides of the detector are identical, we expect the energy scales to be symmetric with regard to  $\eta = 0$ , which is the case except in the end-caps where there is a shift between the two due to a different LAr temperatures. Once the  $\alpha_i$  correction is applied on data and the Monte-Carlo is smeared by the  $c_i$  they are in good agreement, as is illustrated by fig. 4.40.

Several source of uncertainties have been considered, in addition to the comparison between the two methods, and are explained below. The value of the uncertainty on the energy scale can be seen in fig. 4.38, and is much better than  $2 \cdot 10^{-3}$  everywhere except at  $\eta = 1.5$  which is removed in the  $h \rightarrow \gamma\gamma$  analysis. The uncertainty on the resolution will be discussed in section 4.8.

- Uncertainties regarding the event selection, which come from the potential bias that is introduced by the electron identification requirements or by the chosen trigger. The energy scales are extracted a second time with tightened identification criteria, and the difference between the two sets of scales is taken as an uncertainty. For the trigger, the efficiencies scale factors that are applied on MC to reproduce the data efficiencies are varied within  $\pm 1\sigma$ , and the values of the scales that are extracted after this variation define the uncertainty from the trigger requirement. The  $m_{ee}$  range that defines the  $Z \rightarrow ee$  peak region in which the fit of the energy scales is done is also varied (by 2.5 GeV) to extract an uncertainty.
- Impact of the bremsstrahlung, as ideally the energy scales should only correct the EM calorimeter energy response, but there may be a substantial energy loss by the electrons before the EM calorimeter because of the impact of the magnetic field. As the tracking algorithm is able to estimate the ratio  $\frac{q}{p}$  ( $q$  being the charge of the particle and  $p$  its momentum) at both the interaction point and at the end of the tracker, it has been possible to build a variable that estimates the fraction of energy lost by the electron,  $f_{brem} = 1 - (\frac{q}{p})^{IP} / (\frac{q}{p})^{out}$ . The energy scales are re-extracted using a sample where a cut on this variable is required, and the variation with regard to the nominal sample is taken as an uncertainty.
- Uncertainty on the modelling of the pile-up, which is evaluated by varying how the pile-up distribution in MC is reweighted to match the one of the data
- Uncertainty on the modelling of the background, which are fairly small but could still bias the fit. The impact of electro-weak backgrounds ( $Z \rightarrow \tau\tau$ ,  $t\bar{t}$  and di-boson) is tested by removing them from the templates. The normalization of the QCD background (multi-jet) is determined with a data-driven technique that uses a control region where the electron identification criterion is reverted. Once the normalization is determined, it is subtracted from data and the energy scales are re-evaluated, the difference between the nominal scales and those extracted from the background subtracted data being taken as an uncertainty.

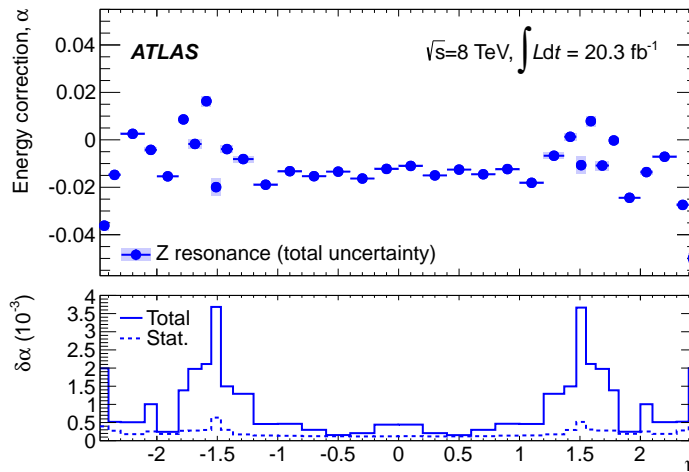


Figure 4.38: Value of the energy scales  $\alpha$  that are applied to correct the energy response on data, and of its uncertainty (bottom). It should be noted that the values of the energy scales that were extracted after the first year of data-taking (2010 [251]) are already applied on the cells energies [198]

Once the energy scales are determined and applied on data, the energy response of electrons with  $E_T = \langle E_T^{Z \rightarrow ee}(e) \rangle = 40$  GeV is perfectly determined up to the accuracy of the scale extraction method, which is of  $5 \cdot 10^{-4}$  in most of the detector. Most of the bins where the accuracy is worse are not considered in the  $h \rightarrow \gamma\gamma$  analysis. The other uncertainties on the electromagnetic energy response are either coming from non-linearities of the energy response, or from the extrapolation of the energy scale going from electrons to photons.

#### 4.6.2 Stability, uniformity and linearity of the energy response

**Stability of the energy response with regard to time** Because of the radiation hardness of the LAr EM calorimeter, its energy response is expected not to vary with respect to time, and the only effect that is expected to create an evolution in time of the EM particles energy response is the variation of the PS HV, that is corrected for. Still this stability needs to be checked for, which can be done by splitting the 2012 data taking in several periods of time and measuring separately the energy response in each of these periods, either using  $m_{ee}$  in  $Z \rightarrow ee$  events or  $\frac{E}{p}$  for electrons from  $W \rightarrow e\nu$  events, as can be seen in fig. 4.41. After the pre-corrections the stability of the response was better than 0.05% during the 2012 data-taking.

**Stability of the energy response with regard to the pile-up** The same kind of cross-check can be done with respect to the number of pile-up events in a given bunch crossing, which is expected not to bias the energy response on average, thanks to the electronic bipolar shaping that is included in the calorimeter read-out electronics. As can be seen in fig. 4.42, this stability is also better than 0.05%. It should be noted that when studied as a function of the number of reconstructed vertices the energy response is not stable anymore, as choosing a given value for  $N_{vertex}$  biases the number of in-time pile-up

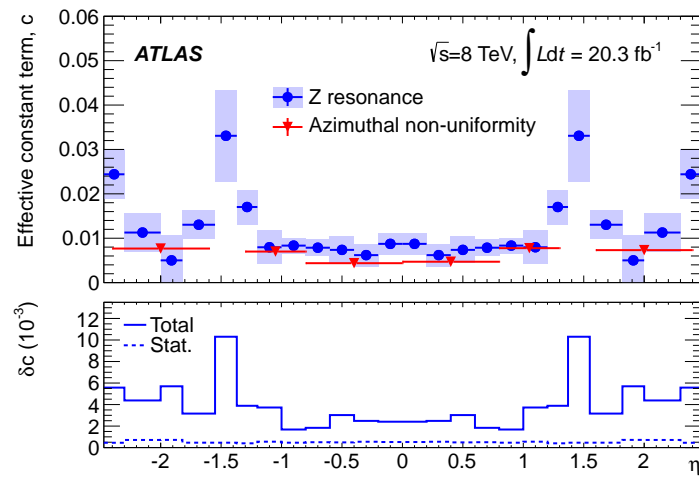


Figure 4.39: Value of the effective constant term used to smear the Monte-Carlo hence adding resolution effects not implemented in the MC simulation, and its uncertainty (bottom) [198]

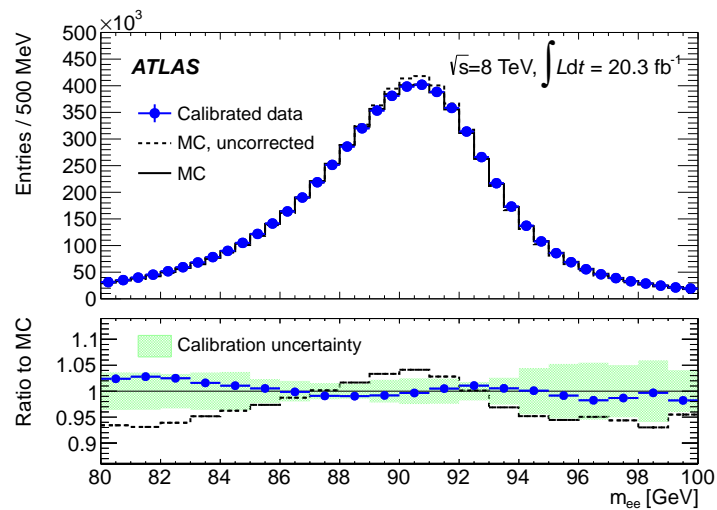


Figure 4.40: Comparison of the distribution of the di-electron mass in  $Z \rightarrow ee$  events between data and MC [198]

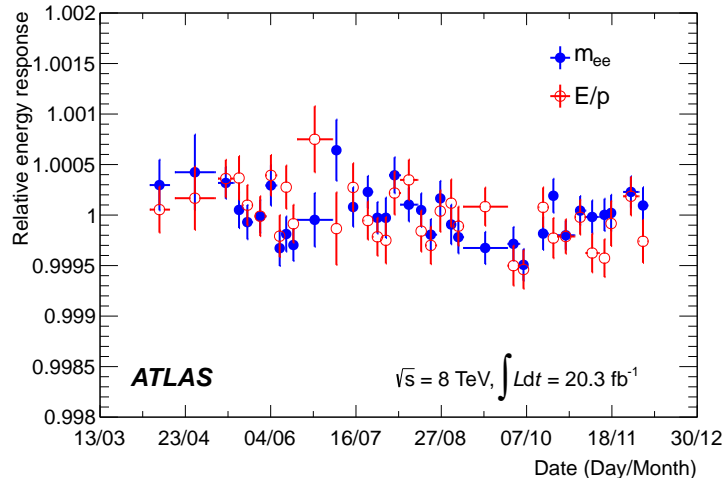


Figure 4.41: Energy response as a function of time, measured either using  $m_{ee}$  in  $Z$  events or  $\frac{E}{p}$  for electrons from  $W$ s, normalized to its average. Each point corresponds to  $\int Ldt = 100 \text{ pb}^{-1}$  [198]

events with respect to the average and therefore the bipolar shaping does not compensate completely the in-time pile-up, but then this trend is well reproduced by the simulation.

**Non-uniformity of the energy response in  $\phi$**  The remaining non-uniformity after the pre-corrections and in-situ energy scales could in principle be looked at in two different directions,  $\eta$  and  $\phi$ , but as the non-uniformity in  $\eta$  is already corrected for by the in-situ energy scales, it was not studied and only the remaining non-uniformity in  $\phi$  is computed in [234]. It is estimated in 6 broad  $\eta$  bins, using the reconstructed di-electron mass in  $Z \rightarrow ee$  events. First the most-probable value of  $M_{Z \rightarrow ee}$  is determined in fine  $\phi$  bins that correspond to one cell in  $\phi$  ( $\Delta\phi = 0.025$ ). From this an expected statistical error on the estimated  $M_{Z \rightarrow ee}$  after integration over all the bins in  $\phi$  is estimated as  $\sigma_{stat}^2 = \frac{1}{N_{bin}} \sum_{i=1}^{N_{bin}} \sigma_{(i),stat}^2$  where  $\sigma_{(i),stat}^2$  is the measured statistical error on  $M_{Z \rightarrow ee}$  in a given  $\phi$  bin. If there was no additional source of non-uniformity, this would on average correspond to the rms (= standard deviation) along  $\phi$  of the estimated  $M_{Z \rightarrow ee}$  therefore the remaining non-uniformity is estimated as  $\sigma_{unif} = \sqrt{RMS^2 - \sigma_{stat}^2}$  where  $RMS$  is the measured standard deviation, and directly translates into a contribution to the resolution constant term. The result is shown in fig. 4.43 and also in fig. 4.39. In the most central part of the detector this non-uniformity, which contributes to the constant-term, is at the level of 0.45%, and it increases to 0.75% in the endcap, which should be compared to the design value of the constant term that was of 0.7% [252], which nicely agrees, although it does not take into account the short-range non-uniformities in  $\eta$ , that are also impacting the constant-term.

**Cross-check of the linearity of the energy response and pedestal shift** Two ways have been used to cross-check the linearity of the response, and make sure that no effect impacting the linearity have been forgotten. The result of both methods is shown in fig. 4.44 for the most central bin of the detector, where  $\Delta\alpha = \alpha - \alpha_{Z \rightarrow ee}$  is a direct comparison of the energy scales measured in the cross-check and the nominal ones.

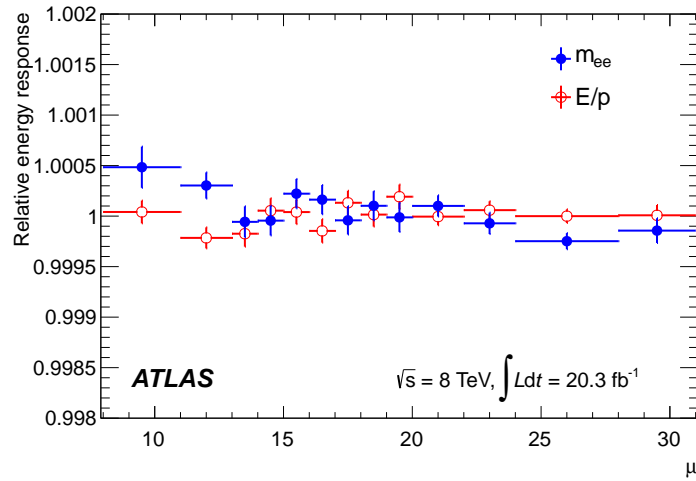


Figure 4.42: Energy response as a function of the average number of pile-up events ( $\mu$ ), measured either using  $m_{ee}$  in  $Z$  events or  $\frac{E}{p}$  for electrons from  $W$  bosons, normalized to its average [198]

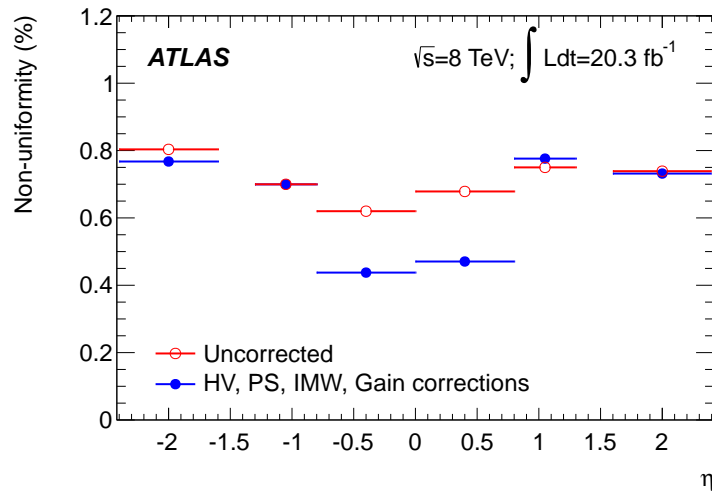


Figure 4.43: Uniformity of the energy response along  $\phi$  in broad  $\eta$  bins, as measured from the RMS of the reconstructed  $Z \rightarrow ee$  invariant mass after subtraction of the expected statistical fluctuations [198]

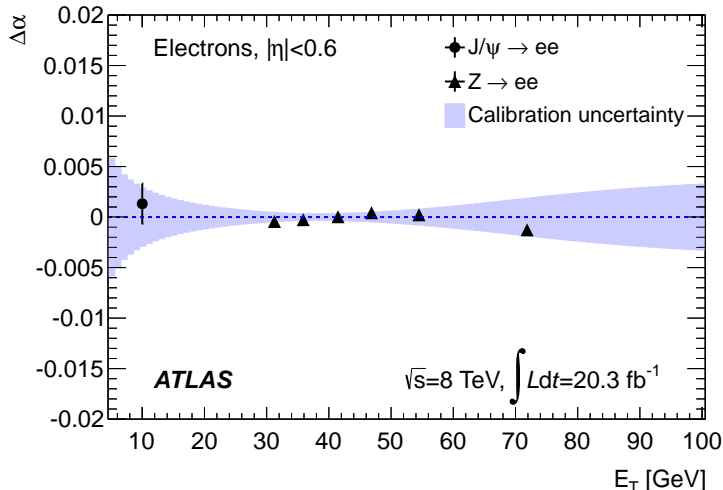


Figure 4.44: Linearity of the energy response, measured using the variation of the reconstructed  $M_{Z \rightarrow ee}$  as a function of the transverse energy of one of the electrons, the second one being averaged out, and with the reconstructed  $M_{J/\Psi \rightarrow ee}$  for the point at lowest  $E_T$  [198]

The first method [250] re-uses the method used to determine the energy scale of the EM calorimeter that has been explained above, but determines the energy scale in bins of  $E_T^e$ . When filling this histogram, the two electrons from  $Z \rightarrow ee$  decay are considered, which means that for each electron going in this histogram the second one is averaged out and is unbiased because its response is corrected on average by the in-situ energy scales. Therefore any non-linearity that appears in this method would directly be linked to a non-linearity at a given energy. No unexpected non-linearity have been observed using this method, with the caveat of the region of the crack in 2011, that will be discussed in subsection 4.9.2.

The second method is setting the in-situ energy scale with the  $J/\Psi$  resonance in its di-electron decay channel [250]. This overall method is similar to the one used to set the scales with the  $Z$  peak, but the background is higher and the available statistics is smaller because the  $J/\Psi$  has to be boosted to pass the selection and prescaled trigger criteria. The scales extracted from this resonance and from the  $Z$  peak are in fairly good agreement, but the results from the  $J/\Psi$  have a tendency to be higher than those from the  $Z$  by  $\approx 1\sigma$ . It was observed that the correction of a difference of electronic pedestal between data and simulation could improve the compatibility between the  $J/\Psi$  and  $Z$  results. This difference was first observed during the resolution systematic studies [253, 254], and it was found out that it was caused by a different electronics setting during the pedestal calibration runs and the physics runs: in the first case the link to the trigger card was switched off, in order to be able to do the pedestal calibration separately for the trigger and normal read-out, but additional signal reflections slightly shifted the pedestal. Although very small (0.25-0.45 MeV by cell depending on  $\eta$ ) this effect is not negligible at the level of the  $J/\Psi$  as it is giving a few MeV shift per cluster hence a few 0.1% shift in the energy scale extracted from the  $J/\Psi$ , but only a few 0.01% at the  $Z$  peak.

Uncertainty	$ \eta  < 0.6$	$0.6 \leq  \eta  < 1.37$	$1.52 \leq  \eta  < 1.81$	$1.81 \leq  \eta  < 2.37$
Inefficiency	0.02	0.03	0.10	0.02
Fake Rate	0.01	0.06	0.06	0.03

Table 4.8: Uncertainty on the photon energy scale coming from the fake rate and inefficiency mismodelling, in % [198]

## 4.7 Extrapolation of the energy scale to photons

### 4.7.1 Mismodeling of the conversion reconstruction

As the MVA used for the calibration of converted or unconverted photons has been trained separately for each case, if a photon is flagged with the wrong conversion status, its calibration will be improperly estimated, increasing the energy for true unconverted photons and decreasing it in the reverse case, by  $\approx 2\%$ . This can easily happen for converted photons where the conversion tracks are not reconstructed, especially if the conversion occurs at high radius. But it can also happen in the case of unconverted photons, where pile-up events are creating many tracks that may be reconstructed as conversion tracks, hence faking a converted photon. This is not a problem if the conversion reconstruction efficiencies and the fake rates are properly modelled by the detector simulation, but it was found not to be completely the case. Therefore an evaluation of the amount of true converted and true unconverted photons [255] is done using the fraction  $E_{1/2}$  of the photons. The basic idea is that a converted photon will have a high  $E_{1/2}$ , mainly because it starts to shower earlier. Template histograms are built from the MC, separately for photons that are reconstructed as converted or unconverted, and the relative amount of true converted and true unconverted photons is varied between the different templates. These templates are compared to the data, and the one which gives the best agreement gives the fake rates and the inefficiencies.

The dataset on which this study is conducted is the same than the one used in the  $h \rightarrow \gamma\gamma$  analysis, but only the leading photon is looked at as it allows to mitigate the impact of jet background. The background is extrapolated from control regions that are defined by reverting the identification or isolation cuts, and is then subtracted from the data. This procedure is done separately in each of the  $E_{1/2}$  bins that are considered in the templates. All the uncertainties on  $E_{1/2}$ , as well as the uncertainty on the inner tracker material, are propagated to this analysis. At the end the fake rates and inefficiencies were found to be higher in data than in the MC, by up to a few percent. This is propagated as an uncertainty on the photon energy scale by reweighting the amount of fakes and the inefficiencies in the MC, and the final impact on the energy scale has been found out to be between 0.01% and 0.1% depending on  $|\eta|$ , and is displayed in tab. 4.8.

### 4.7.2 Energy scales from photons

We assume that the in-situ energy scales extracted from the  $Z \rightarrow ee$  decays are effectively correcting the EM calorimeter energy response, and therefore that they can be used for the photons too. This is true if all the effects that are different between electrons and photons are well under control and taken into account. We need to cross-check that no

effect impacting this extrapolation have been forgotten [256]. This is done using radiative  $Z \rightarrow ll\gamma$  events, where  $l$  may be an electron or a muon, and studying the double ratio  $R = \frac{\langle m(ll\gamma)_{Data} \rangle / \langle m(ll)_{Data} \rangle}{\langle m(ll\gamma)_{MC} \rangle / \langle m(ll)_{MC} \rangle}$ , where  $\langle m \rangle$  corresponds to the most probable value of the two or three-body invariant mass and is estimated using a fit of this distribution. The big advantage of this double ratio is that it mitigates the effect of the lepton energy scales uncertainties by a factor of  $\approx 3$ .

Indeed it is possible to show that, if we parametrize the impact of a lepton energy scale uncertainty as  $E'_l = (1 + \Delta)E_l$ , the square of the three-body invariant mass becomes  $m_{ll\gamma}^{\prime 2} = m_{ll\gamma}^2 + \Delta m_{ll}^2 + \Delta m_{ll\gamma}^2 + \Delta^2 m_{ll\gamma}^2$  and the two-body invariant mass  $m_{ll}' = (1 + \Delta)m_{ll}$ . Keeping only the first order in  $\Delta$  this gives the three-body invariant mass  $m_{ll\gamma}' \approx m_{ll\gamma}(1 + \frac{\Delta}{2}(1 + (\frac{m_{ll}}{m_{ll\gamma}})^2))$  while the ratio becomes  $\frac{m_{ll\gamma}'}{m_{ll}'} \approx \frac{m_{ll\gamma}}{m_{ll}}(1 - \frac{\Delta}{2}(1 - (\frac{m_{ll\gamma}}{m_{ll}})^2))$ . Now the photon energy scale may be implemented as  $E'' = (1 + \alpha)E$  and then the square of the three-body invariant mass becomes  $m_{ll\gamma}''^2 = m_{ll\gamma}^2 + \alpha(m_{ll\gamma}^2 - m_{ll}^2)$  while the two-body invariant mass is not modified. At first order this gives  $m_{ll\gamma}'' = m_{ll\gamma}(1 - \frac{\alpha}{2}(1 + (\frac{m_{ll}}{m_{ll\gamma}})^2))$  and the ratio is obvious. Now when determining the impact of the lepton energy scale on the extracted photon energy scale, we usually inject a variation of  $\Delta$  to the lepton energy, that has the size of the uncertainty, and determine by how much the photon energy scale should be modified to recover from this variation. The deviation between this value of the energy scale and the nominal value gives the uncertainty  $\delta\alpha$ . It is clear that using only  $m_{ll\gamma}$  would give  $\delta\alpha = \Delta \times (1 + (\frac{m_{ll}}{m_{ll\gamma}})^2)(1 - (\frac{m_{ll}}{m_{ll\gamma}})^2)^{-1}$ , while if we use the ratio we get  $\delta\alpha = \Delta$ . In radiative decays the photon is usually the least energetic particle, and the ratio  $\frac{m_{ll}}{m_{ll\gamma}}$  is 0.7 on average, therefore the ratio allows to recover a factor of 3. Doing the double-ratio with the Monte-Carlo allows to cancel the kinematic differences between  $Z \rightarrow ee$  events, at which the nominal energy scales are extracted, and  $Z \rightarrow ll\gamma$  events from which this cross-check will be extracted. Such differences could have biased the final values of the energy scales that are extracted with this method.

In practice, the photon energy is modified by  $\alpha$  in data, and this modification is propagated to the three-body invariant mass and finally the double-ratio  $R$ .  $\alpha$  is progressively varied until the solution  $R = 1$ , which corresponds to the nominal energy scales, is found. This extraction is done separately for unconverted photons, and converted photons with one or two reconstructed tracks. The statistical uncertainty from the fits of the invariant mass distributions is propagated to  $R$  to find the statistical uncertainty on the double-ratio. The systematic uncertainties that have been considered concern the lepton energy scale and energy resolution, the fit range, and the background modelling. The dominant systematic uncertainty comes from the lepton energy scale. No obvious hint of additional effect has been found, but this cross-check is still statistically limited, especially for the converted photons. The results may be found in fig. 4.45 where  $\Delta\alpha$  is the difference between the energy scale extracted from photons in radiative  $Z$  decays and the one extracted from  $Z \rightarrow ee$  events.

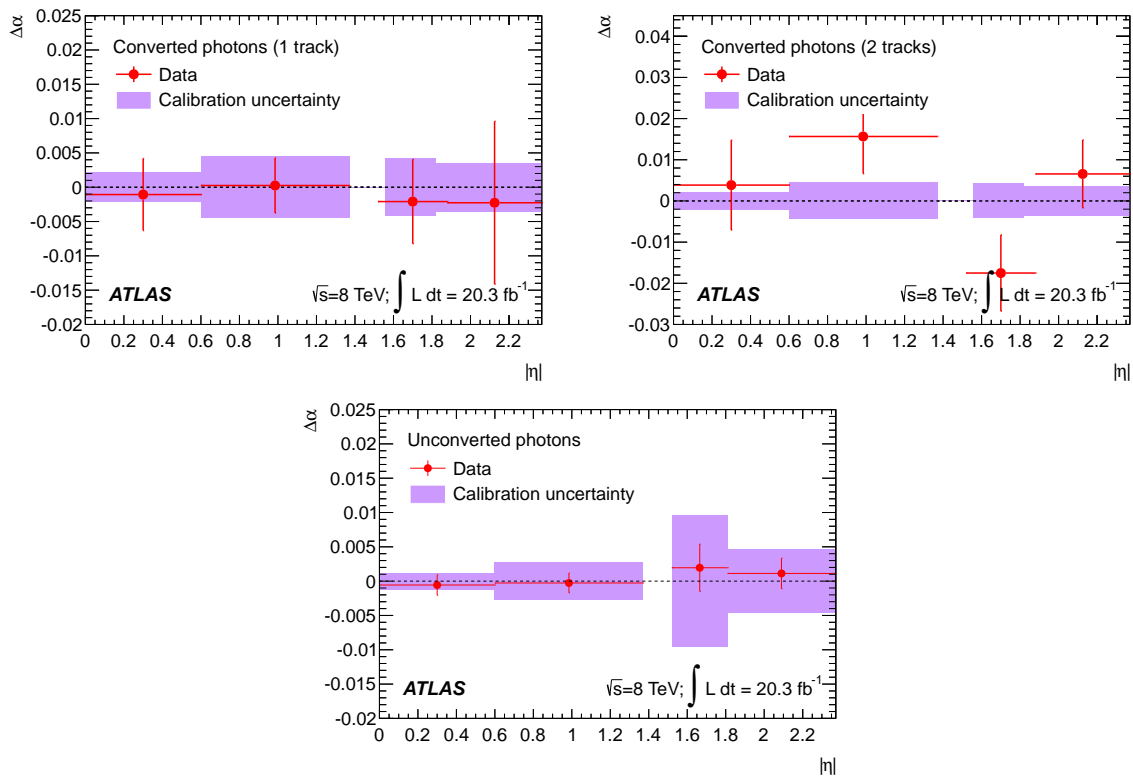


Figure 4.45: Difference between the energy scales extracted from  $Z \rightarrow ee$  events and the photon-energy scale extracted with the double-ratio method in  $Z \rightarrow ll\gamma$  events, as a function of  $|\eta|$  for unconverted photons (bottom), and converted photons with one (top left) or two reconstructed tracks [198]

## 4.8 Electron and photon energy resolution

The main handle on the energy resolution comes from the study of the width of the  $Z \rightarrow ee$  peak observed in our data, but it has the drawback that it actually probes the resolution for electrons at a given energy of  $\langle E_T^{Z \rightarrow ee}(e) \rangle = 40$  GeV while the resolution varies with respect to the energy, following this parametrization :

$$\frac{\sigma_E}{E} = \sqrt{\left(\frac{a}{E}\right)^2 + \left(\frac{b}{\sqrt{E}}\right)^2 + c^2} \quad (4.7)$$

where :

- $a$  corresponds to the impact of the pile-up and electronic noise. Although it varies with the instantaneous luminosity, it is at the order of a few hundreds of MeV
- $b$  corresponds to the sampling term that translates the Poisson variations of the number of particles detected in the showers into a variation of the energy, and it has been measured to be  $b \approx 10\%$ , which had been evaluated in test-beam where there is no matter in front of the calorimeter
- $c$  corresponds to the constant term that represents energy response non-uniformities. From the design of the calorimeter it is expected that  $c = 0.7\%$

An evaluation of the uncertainty on these three parameters is needed, as well as the impact of the uncertainty on the material budget in front of the EM calorimeter. The uncertainty on the constant term  $c$  is taken directly as the uncertainty on the effective constant term that is extracted from  $Z \rightarrow ee$  events at the same time than the in-situ energy scales, as has been described above in subsection 4.6.1 [250].

The uncertainty on the sampling term,  $b$ ,  $\pm 10\%$ , has been evaluated mainly on MC, by comparing the resolution obtained for true unconverted photons of various energies (which are insensitive to the material budget in front of the calorimeter) on various Geant 4 versions with different physics modelling options. This also agrees well with the sampling term that was extracted during the test-beam studies for the ATLAS EM calorimeter [199], and no sign of discrepancy of the sampling term beyond these 10% have been observed in the Run 1 data.

The noise term is suppressed by a factor  $\frac{1}{E}$  and therefore only matters at low energy, where it is hard to find a clean physics process with which it could be studied. Therefore it is studied on bunch-crossings where no interesting physics is expected, using random calorimeter clusters that have the size of the clusters that will be used for electrons or photons. On data, the studied dataset corresponds to events that were recorded after a zero-bias trigger signal, which randomly triggers on any filled bunch-crossing without any requirement on any signal seen in the detector, while for the MC it corresponds to a single-particle simulation of neutrinos, which do not create any signal in the calorimeter. The noise for each of these datasets is estimated as the RMS of the energies of the random clusters, and the uncertainty is the quadratic difference of the noise measured in data and in MC. This uncertainty is almost everywhere of 100 MeV except in  $1.5 < |\eta| < 1.8$  where it grows to 200 MeV.

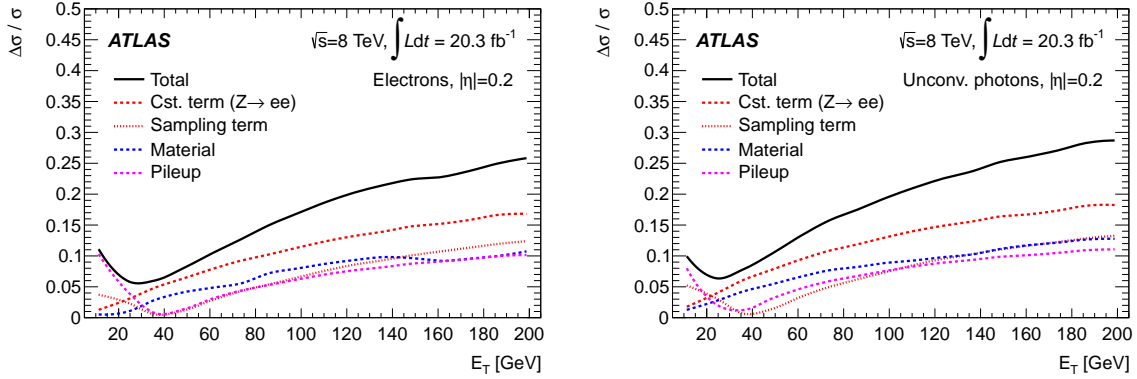


Figure 4.46: Uncertainty on the energy resolution of electrons and unconverted photons as a function of  $E$  for a given  $|\eta|$  bin [198]

The presence of material upstream of the calorimeter increases the energy losses in dead material, and also widens the shower hence increasing the energy lost outside of the clusters, and the dependence of these effects on the energy is complicated. The first effect that additional material creates is a bias of the effective constant term  $c$  on distorted geometries, that has to be taken into account [257] to keep only the dependence on the energy of the resolution variation under a material budget modification, as the effective constant is measured on data, using the  $Z$  peak. To do this a MC sample using a distorted detector geometry is used as the pseudo-data, and an effective constant  $c_{dist}^2$  is extracted from a  $Z \rightarrow ee$  sample generated with this geometry. Then single particle samples are generated, both in the nominal and in the distorted geometry, and the resolution for each of these samples is parametrized as a function of  $E$ ,  $\eta$  and of the type of particles that are being looked at. Then the final uncertainty on the energy resolution is taken as  $\Delta\sigma^2(E, \eta) = \sigma_{dist}^2(E, \eta) - \sigma_{nom}^2(E, \eta) - c_{dist}^2(\eta)$  and only encompass the dependency on  $E$  and on the type of particle. This preserves the uncertainty on the effective constant term extracted from  $Z \rightarrow ee$  events.

For all these uncertainties, the fact that the only uncertainty on the resolution at  $E_T = \langle E_T^{Z \rightarrow ee} \rangle = 40$  GeV should come from the effective constant term extraction method is enforced. The total uncertainty on the resolution is taken as being the quadratic sum of these three uncertainties, and is displayed in fig. 4.46 for electrons and unconverted photons at  $|\eta| = 0.2$ . At the energy we are interested in for  $h \rightarrow \gamma\gamma$  the uncertainty on the resolution is  $\approx 12\%$ , dominated by the uncertainty on the extracted effective constant term from the  $Z \rightarrow ee$  peak.

## 4.9 Comparison between 2011 and 2012 data-taking

### 4.9.1 Layer 1 Gain

The distribution of  $E_{1/2}$  for electrons coming from  $Z \rightarrow ee$  events was found [235] to be unexpectedly different between the 2011 and 2012 runs, in the part of the detector that goes from  $|\eta| = 1.8$  to  $|\eta| = 2.5$ . The only difference that may explain this effect is the re-optimization of the Optimal Filtering Coefficients [4, 201] that has been done

between these two years. For the 7 TeV sample the OFCs were computed considering only the electronic noise, and the pile-up noise was completely neglected. This was obviously not possible anymore in 2012 for which the OFCs were computed considering these two sources of noise. But one of the runs of 2012 have been reprocessed using the older way to compute the OFCs, in order to cross-check the energy distributions before and after this correction. The OFC difference allowed to explain most of the difference of  $E_{1/2}$  that was observed, and showed that the problem was mainly carried by the high-gain electronic chain from the strip cells, but it is not obvious to tell whether it is the 2012 or the 2011 OFCs that have a problem. Therefore it was decided to take the full difference of the layer 1 high-gain energy response between the two kind of OFCs as an additional systematic. This systematic can be as high as 5% (at  $|\eta| = 2.2$ ) but only affects the first layer, which does not carry most of the energy measurement, and only the high-gain while for particles that are of interest to us (with a transverse energy of 40-60 GeV) the most energetic strip cells are always in medium-gain. Still this affects the nominal inter-layer recalibration factor  $\alpha_{1/2}$  that is extracted from muons, for which the energy deposits are only recorded in high-gain in all three layers. This additional uncertainty on  $\alpha_{1/2}$  is also propagated to the uncertainty on the material budget in front of the EM calorimeter, which requires a proper knowledge of the calibration of  $E_{1/2}$ .

### 4.9.2 Crack non-linearity

During the cross-checks of the calibration between 2011 and 2012, it was observed that the distribution of the di-electron invariant mass of  $Z \rightarrow ee$  events where one of the electrons falls into the region of the crack, where the scintillators that are in the crack are taken into account in the energy reconstruction, has some problems in 2011, as is shown in fig. 4.47. Specifically the most probable value is shifted to a fairly low value of  $m_{ee}$ , and the resolution is not as good in 2012. This problem was also seen in the linearity measured with  $Z \rightarrow ee$  (see fig. 41 of [198]), where the bin that corresponds to the crack had a non-linearity that could not be explained by the calibration uncertainties in 2011. In fact, taking scintillators into account in the energy measurements required to add them with the correct weight to the energy measurement of the LAr. The weights used in 2011 were based on an estimation made before the data-taking, which did not had a correct description of the detector geometry. They were updated in early 2012 with the proper detector simulation. It was decided not to reprocess the 2011 dataset with the updated weights, which explains why this feature is still observed at 7 TeV but not at 8 TeV. At the end it was decided to inflate the calibration uncertainty in the crack for 2011 in order to cover the observed non-linearity. This has no importance on the  $h \rightarrow \gamma\gamma$  analysis where this region is completely removed.

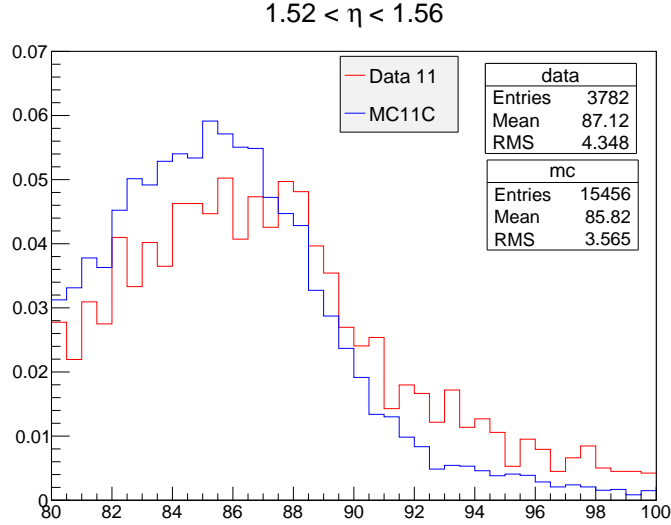


Figure 4.47: Distribution of the di-electron invariant in  $Z \rightarrow ee$  events where one of the electrons falls in the region  $1.52 < \eta < 1.56$ , where the scintillators are used in the particles energy measurement

## 4.10 Possible improvements toward Run II

This sub-part constitutes a brief summary of few of the ideas that could be developed to improve the points mentioned above for the Run 2 of the LHC. This does not imply that all of these will be implemented, as they may also have some drawback that will be mentioned whenever possible. This also does not mean that this list is complete. For instance, the pedestal shift that has been understood as a difference of electronic setting between calibration runs and physics runs will be solved by letting the link between FEB and the trigger board active during the pedestal calibration runs, and will not be mentioned below.

### 4.10.1 Inner detector rail mismodeling

It was already stated that the main method to determine the amount of material upstream of the EM calorimeter, as well as its position, was only done in  $\eta$  bins. In fact another method was developed that also looked at the material variations in  $\phi$ , but it was only used in particular  $\eta$  region where problems were already spotted, such as the beginning of the end-cap. Therefore it was possible to miss localized  $\phi$  variations of the material if they are integrated along  $\phi$  in a given  $\eta$  bin. It was realized only after the implementation of the final Run 1 detector geometry that such a thing happens in the region  $0.6 < |\eta| < 1.37$  close to  $\phi \approx 0$  and  $\pi$  where the support rail of the inner detector is not properly modelled in the simulation, which can be seen in fig. 4.48. In data the electrons are crossing more material than in MC hence losing more energy, which is represented by a larger decrease of the reconstructed  $m(Z \rightarrow ee)$  mass in data than in the MC. This decrease is also broader in  $\phi$  in data. As this deviation is very localized it does not have a big impact on performance, but the future MC samples for the Run 2 will use an improved description of the ID support rail, and this will effectively decrease the constant-term that needs to

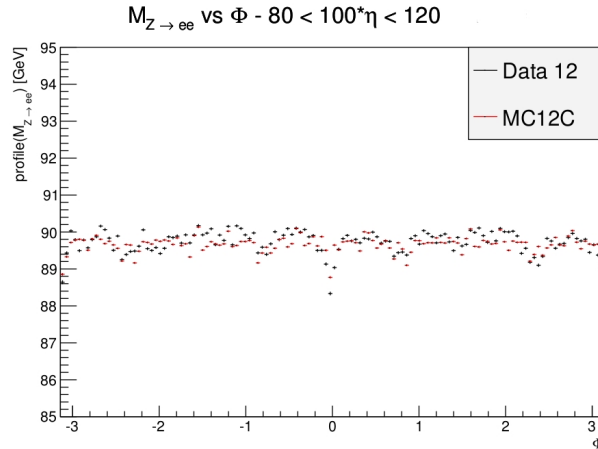


Figure 4.48: Profile of the di-electron invariant mass in  $Z \rightarrow ee$  events as seen on the latest version of the simulation and on 2012 data, in a specific  $\eta$  bin where the ID support rail is not well modelled, as can be seen at  $\phi = 0, \pm\pi$

Particle type	$ \eta  < 0.8$	$0.8 <  \eta  < 1.3$	$1.6 <  \eta  < 2.37$
(Data-MC) $\frac{E7x11-ECluster}{ECluster}$ (current case, $\gamma$ and electron clusters are different)			
El ( $3 \times 7$ ) - Unconv $\gamma$ ( $3 \times 5$ )	$-0.00030 \pm 0.00040$	$-0.00102 \pm 0.00060$	$-0.00054 \pm 0.00040$
El ( $3 \times 7$ ) - Conv $\gamma$ ( $3 \times 7$ )	$-0.00162 \pm 0.00109$	$-0.00458 \pm 0.00102$	$-0.00185 \pm 0.00108$
Using $5 \times 7$ for every object			
El - Unconv $\gamma$	$-0.00044 \pm 0.00025$	$-0.00069 \pm 0.00033$	$-0.00002 \pm 0.00038$
El - Conv $\gamma$	$-0.00116 \pm 0.00092$	$-0.00311 \pm 0.00081$	$-0.00087 \pm 0.00058$

Table 4.9: Evolution of the uncertainty related to the lateral energy leakage if the cluster size is modified

be applied on the MC.

### 4.10.2 Out of cluster leakage

One of the simplest idea to decrease the impact of the mis-modelling of the lateral energy leakage is to increase the size of the clusters : if there is less energy leaking outside of the cluster, mis-modelling will have a milder impact on the energy response. In this context it was checked by how much increasing the cluster to  $5 \times 7$  cells would modify the uncertainty related to the leakage, which is summarized in table 4.9 where it is quite clear that it would improve this uncertainty, especially for converted photons where it improves by almost 0.1%. The drawback of this change in cluster size would be an increase of the noise by a factor of  $\sqrt{\frac{5}{3}}$ . Therefore some study of the impact on the resolution are required before actually modifying the cluster size in the official reconstruction.

## 4.11 Comparison with the CMS calibration

The details of the photon calibration used by the CMS collaboration have been published in [221] (see also [258, 259]). The algorithmic sequence used is roughly similar to the one

for ATLAS, in the sense that it also starts with a set of pre-corrections applied to data, then estimates the energy of the incident particle using a MVA technique, determines the in-situ energy scales with  $Z^0 \rightarrow ee$  events, and then consider uncertainties that are either related to non-linearities or electron to photon extrapolation. But the way each of these steps is done is very different between the two collaborations, and although some of these differences are due to the different calorimeters, some of them correspond to very different choices at the level of the analysis. A quick description of the CMS photon calibration procedure is outlined below, and the comparison of the impact of the calibration within the two experiments will be done at the end of the section (see also [260]). The measurement of the Higgs boson mass within ATLAS will be presented in more details in section 5.2.

**Initial on-detector calibration procedure** A first step of the calibration is done directly on the detector. The response of the different crystals needs to be equalized to ensure the uniformity of the response across the whole calorimeter. This is done using the distribution of the energy coming from (special) minimum bias events, which is expected to be invariant with respect to  $\phi$ , the ratio  $\frac{E}{p}$  measured with electrons from  $Z \rightarrow ee$  and  $W \rightarrow e\nu$  electrons, and also the di-photon invariant mass of  $\pi^0$  and  $\eta$  decays to  $\gamma\gamma$ , that allows to probe the relative response of neighbouring crystals as these decays have a very narrow opening angle. This uniformity of the energy response is re-derived on a monthly basis. In addition to that, the transparency of the crystals is constantly monitored, as it varies with respect to the time during a run because of radiation damages. A system of lasers has been installed which distributes light on all the crystals to give a probe of the transparency, every 40 minutes. The actual level of transparency is taken into account in the energy reconstruction. This can be seen as an equivalent of the electronic calibration procedure that is being done in ATLAS with the specific electronic calibration boards.

**Pre-corrections and Monte-Carlo calibration** Then a first set of pre-corrections is applied and is mostly done to correct the energy lost in inter-module and inter-crystal gaps that are not instrumented. They are also done to recover energy losses upstream of the electromagnetic calorimeter and outside of the clusters. These corrections are derived on Monte-Carlo and as a function of  $\eta$ ,  $E_T$ ,  $R_9 = \frac{E_{3 \times 3}}{E_{super-cluster}}$  and of the size of the super-cluster in  $\phi$ . To some extent this can be seen as an equivalent of the "calibration hits" method that was used on ATLAS in the past [225], although not totally as it does not give the final estimate of the particle energy. This task is done by a multi-variate technique, that is in fact providing the full parametrization of the detector response function individually for every photons (i.e. it determines the distribution of  $\frac{E_{true}}{E_{raw}}$  where  $E_{raw}$  is the super-cluster energy). This response function is parametrized as a Gaussian core with two power laws for the tails, and the multi-variate regression determines the parameters of this function, and the photon energy is taken as the most-probable value of this distribution. This is similar to the boosted regression tree used in ATLAS but allows to use a per-event resolution function that is not available in ATLAS.

**Extraction of in-situ energy scales** The extraction of the in-situ photon energy scale and resolution is different in ATLAS and in CMS. Although they both use  $Z \rightarrow ee$  events

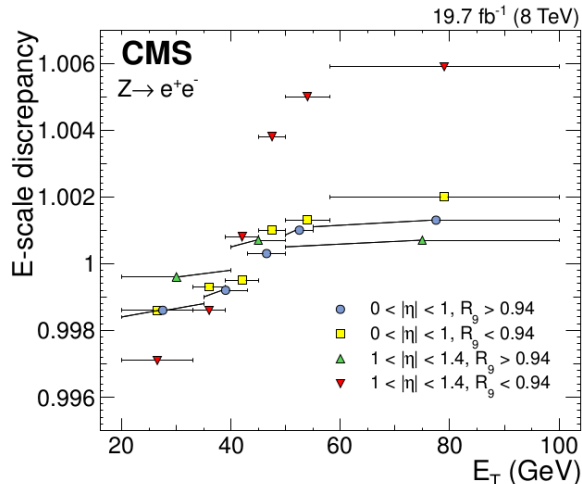


Figure 4.49: Residual discrepancy of the energy scale between data and MC determined during the third step of the in-situ energy scale extraction. The corrections to be applied on data correspond to the inverse of these values [221]

and assume that the values determined with electrons holds for photons too, the extraction is done in a single step in ATLAS while it is done in three different steps in CMS. The first step is done to stabilize the energy scale with respect to time : several data-taking epochs are defined (51 for 2012), and an energy scale is determined for each of these epochs. In the second step both the energy resolution and the energy scale are fitted, in two  $R_9$  and 4  $|\eta|$  regions, which essentially corrects for the material mis-modelling. The last step determines the energy scale and resolution in 20 bins defined by ranges of  $|\eta|$ ,  $R_9$  and  $E_T$  which effectively corrects for a part of the non-linearity observed in data, and the magnitude of this non-linearity is illustrated by fig. 4.49. The energy scale to be applied on data corresponds to a product of the three corrections extracted after each of the fits, and the smearing of the resolution to be applied on the Monte-Carlo is the quadratic sum of the smearing determined in the second and third steps. There are methodological uncertainties connected to the selection requirements, the fit range, but also to the distribution of  $R_9$  that can be different between electrons from  $Z \rightarrow ee$  and di-photon resonances in another energy range. This uncertainty is between 0.05% and 0.1% depending on the position and kinematic of the event.

**Treatment of non-linearities and related uncertainty** One of the most important difference in the assessment of the calibration between ATLAS and CMS has been the understanding and treatment of the non-linearity of the energy response. In ATLAS all the non-linearities that were observed have either been understood and corrected for, or have been treated as additional uncertainties (which was for instance the case of the apparent difference of energy response between high gain and medium gain electronics), while in CMS non-linearities are mostly corrected for by the in-situ energy scales that are binned in  $E_T$ . There is still a remnant non-linearity of the energy response after this step, that is taken as an additional uncertainty, and that may be seen in fig. 4.50. It is estimated by studying mainly  $\frac{E}{p}$  in  $Z \rightarrow ee$  and  $W \rightarrow e\nu$  events, where the momentum is estimated by the inner tracker and the energy by the calorimeter. This non-linearity is then estimated

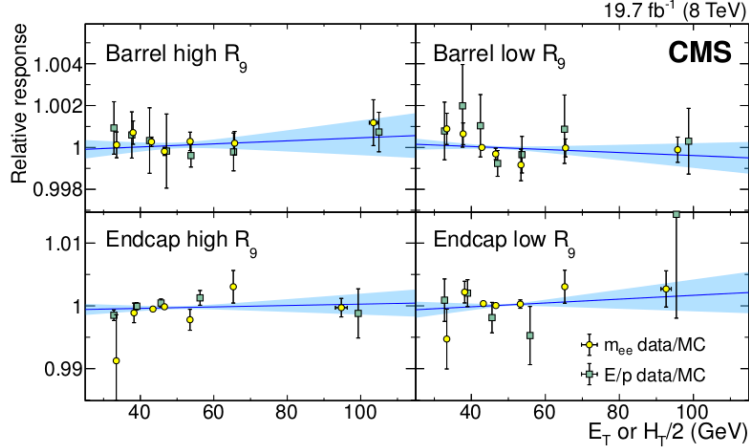


Figure 4.50: Uncertainty band coming from the remnant non-linearity of the energy response in  $Z \rightarrow ee$  or  $W \rightarrow e\nu$  events, using either  $\frac{E}{p}$  or  $m_{ee}$  to estimate the energy response either in bins of  $E_T^e$  or  $H_T/2 = \frac{E_T^1 + E_T^2}{2}$  [221]

from a linear fit to the different points where the energy response has been estimated, and for events considered in the  $h \rightarrow \gamma\gamma$  analysis that have a transverse energy of  $E_T \approx 60$  GeV the uncertainty arising from this differential non-linearity is at the level of 0.1%. For boosted events that have photon energy higher than 100 GeV, this uncertainty is higher, at the level of 0.2%. The CMS EM calorimeter also uses several electronic gains, that are corresponding to different pre-amplifiers, and it was checked that there is no systematic uncertainty induced by the difference of response between these various gains or by the gain switching.

**Treatment of the material mis-modelling** Both the method used to determine the amount of material upstream of the calorimeter and the way its mis-modelling is handled are different between CMS and ATLAS. The estimation of the material budget in CMS comes from the study of radiative energy losses of the tracks, that is estimated by the energy loss (change in the track curvature) between the beginning and the end of the inner tracking region. This study is done for tracks from  $Z \rightarrow ee$  events and low- $p_T$  charged hadrons tracks, which gives the estimated difference of material budget between data and MC that is displayed in fig. 4.51. The two methods are in very good agreement up to  $|\eta| = 1.6$  where the method that uses low- $p_T$  charged hadrons is hard to implement. Unlike ATLAS, the CMS collaboration has not updated its detector simulation with an improved description of the detector geometry, hence it is the difference between data and MC that is taken as an uncertainty. Furthermore some cross-checks have been done, looking at the distribution of the position of photon conversions. The corresponding uncertainty will be treated conservatively as it may have a bigger impact at specific positions. It was assumed to have a deficit of 10% of the material budget at  $|\eta| < 1$  and 20% at  $|\eta| > 1$ , which translates into a 0.06% uncertainty on the Higgs boson mass. In ATLAS the uncertainty on the inner detector material is of 5% and translates into an uncertainty on the Higgs boson mass of 0.07%. The actual reason why the relative impact on the mass is higher in ATLAS, while the relative uncertainty on the material is smaller, is not obvious, and

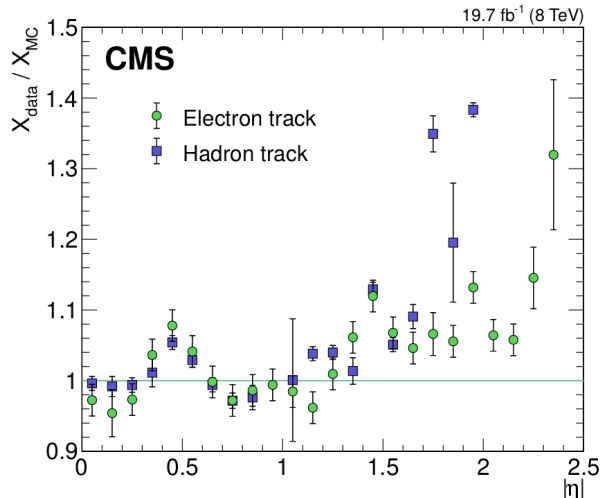


Figure 4.51: Ratio of the estimated material budget between data and MC as a function of  $|\eta|$  for the two methods described in the text [221]

may originate from the fact that there is no material between the tracker and the EM calorimeter in CMS, while there is the cryostat in ATLAS. An increase of the material budget implies an earlier shower, and the uncertainty this is creating may be amplified by the cryostat in which the shower will develop further. In addition to that, in ATLAS there is an additional uncertainty from the material in the cryostat itself and from the material between the pre-sampler and the accordion, at the level of  $0.04X_0$  corresponding to 0.1% on the Higgs boson mass.

**Electro-magnetic shower shapes modelling** Within CMS the mis-modelling of the electro-magnetic shower shapes and its impact on the energy measurement has been estimated by variations of the Geant 4 physics list, while in ATLAS it is taken as a measurement on data of the variation of the size of these shower-shapes with respect to the particles energy or with respect to their nature. The procedure in CMS is more aggressive than the one used in ATLAS, but it is also justified by the fact that the modelling of the electro-magnetic showers is better in CMS than in ATLAS. Until the last results [221] the showers were very well modelled in CMS, but a slight disagreement between data and MC is now observed, as is illustrated by fig. 4.52, although it is much smaller than in ATLAS [243]. At the end the uncertainty on  $m_h$  associated to the modelling of the shower shapes is marginally smaller in CMS (0.05%) than in ATLAS (0.06%).

**Variation of the light absorption with respect to the depth in the crystal** Two of the big differences between electrons and photons in CMS are coming from the difference of tracking material budget and the difference of lateral shower shapes, which has already been described above. The third difference comes from the variation of the light absorption in the crystals with respect to the depth. The side of the crystal that faces the interaction point receives a higher radiation flux and will therefore suffer from a bigger transparency loss. On average the photons start showering later than the electrons, which means that the energy measurement for unconverted photons will not suffer as much from the transparency

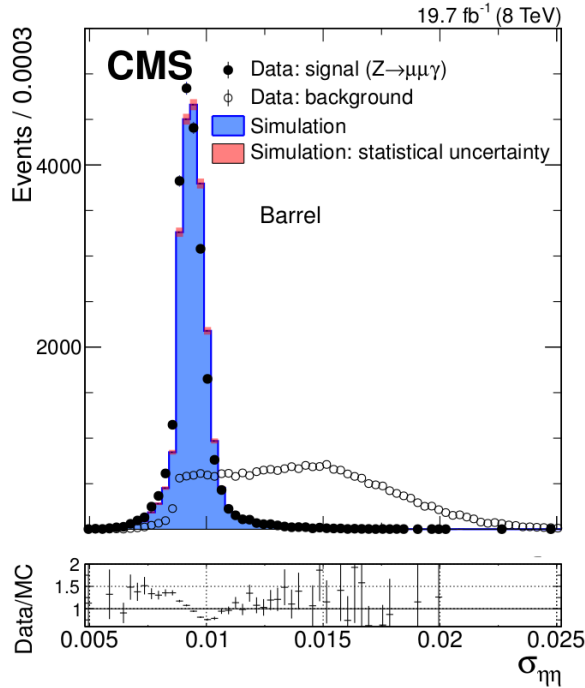


Figure 4.52: Distribution of the shower shape  $\sigma_{\eta\eta}$  (which is the energy-weighted spread along  $\eta$ ) for photons from  $Z \rightarrow \mu\mu\gamma$  [221]

loss than electrons, but the impact on converted photons will be bigger because they consist in two electrons. A modified detector simulation where this variation of the light absorption against the depth in the crystal is implemented was developed and the variation of the energy response between the different simulations is taken as an uncertainty. The important quantity is the difference between the electron and photon energy response, as most of this transparency loss is taken into account by the in-situ energy scales. The energy scale for unconverted photons will be higher than for electrons, which themselves have a higher energy scale than the converted photons, and this means that the effect should be anti-correlated between converted and unconverted photons. This effect is measured by bins of  $R_9$ , where it is estimated give a 0.04% systematic uncertainty on the energy scale of photon with  $R_9 > 0.94$  and a 0.06% uncertainty for  $R_9 < 0.94$ . Taking into account the anti-correlation between the kinds of photons, the total systematic uncertainty this implies on  $m_h$  is of 0.015%.

**Treatment of the resolution** In both ATLAS and CMS the dominant systematic uncertainty on the resolution comes from the extraction of the smearing parameter from the  $Z^0 \rightarrow ee$  mass peak. This fact is reinforced in CMS because the smearing parameters are extracted separately for bins of  $R_9 \times \eta \times E_T$ , which implies that a part of the impact of the noise and sampling term, as well as of the material, are already covered by the binning in which the smearing is extracted. The impact of the systematics uncertainty on the resolution is considered to be negligible within CMS, both for the measurement of  $m_h$  and of the signal strength, and it is not quoted in [221, 261], while in ATLAS it is the dominant experimental uncertainty on the signal strength measurements [89, 262].

	ATLAS	CMS
Statistical uncertainty on $m_h$	0.33%	0.25%
Total energy scale uncertainty	0.21%	0.12%
Energy scale and resolution from $Z \rightarrow ee$	0.04%	0.04%
Energy non-linearity	0.12% (apparent HG/MG difference)	0.08% (remaining non-linearity after energy scales)
Conversion classification	0.02%	Not relevant
The following uncertainties affect both the linearity and electron to photon extrapolation		
Inner detector material	0.07%	0.06%
Rest of the material	0.1% (cryostat)	Nothing
Longitudinal calibration	0.1% ( $\frac{E_1}{E_2}$ calibration)	0.02% (light absorption vs depth)
Lateral shower-shape mis-modelling	0.06% (data-driven, limited by stat.)	0.05% (Geant4 variations)

Table 4.10: Comparison of the systematic uncertainties between ATLAS and CMS [260]

**Comparison of the impact of the calibration on the Higgs boson mass measurement** The impact of the uncertainties on the Higgs boson mass that have been considered in both ATLAS and CMS are compared in table 4.10 (see also [263]). In both detectors the dominant uncertainty is induced by the non-linearity of the energy response, although it has been treated more aggressively in CMS where the biggest part of this non-linearity is taken into account and effectively corrected for by the in-situ energy scales, while in ATLAS it is entirely treated as a systematic uncertainty. In ATLAS the following uncertainties in terms of magnitude are coming from the material budget after the inner detector, and from the inter-layer calibration. The first item has no equivalent in CMS, and although the second one has an equivalent, which is the variation of the light absorption with respect to the depth in the crystals, it is much smaller (although mostly because of the anti-correlation between high and low  $R_9$  photons). The conversion classification uncertainty also does not exist in CMS, because the whole calibration procedure is made to be agnostic of the conversion status of the incoming photon, while it is relevant for ATLAS that uses different MVA calibrations for converted and unconverted, although it is fairly small. Although there are conceptual differences in the way the other systematics are estimated and handled, they turn out to have an equivalent impact on the measurement of  $m_h$  between the two detectors.

Here only the impact of the uncertainties on the energy scale have been discussed, and although it describes most of the systematic uncertainty it does not explain the total uncertainty in sufficient details. The statistical uncertainty needs to be discussed too, and this is directly connected to photon energy resolution. This will be further discussed in section 5.6, although this discussion will be conducted in the context of the width, but it is possible to adapt it to the mass, as will be explained. The fact that the best categories used for the CMS analysis have a better resolution than the best categories used in ATLAS drives the statistical uncertainty estimated by CMS down, although the inclusive resolution is better in ATLAS than in CMS. The precise reasons will be detailed more in section 5.6 too (see also subsection 5.1.3 where it is seen that the uncertainty on the error on the mass is proportional to  $\sigma_{res}^{3/2}$ , where  $\sigma_{res}$  is the resolution).

# Chapter 5

## Upper limit on the BEH decay width and measurement of its mass

### Contents

---

<b>5.1 Overall description of the <math>H \rightarrow \gamma\gamma</math> analyses</b>	<b>168</b>
5.1.1 Selection of events for the $h \rightarrow \gamma\gamma$ analysis	168
5.1.2 Modelling of signal and background processes	171
5.1.3 Event categorization for the mass and width analysis	173
<b>5.2 Measurement of the BEH boson mass</b>	<b>177</b>
5.2.1 Measurement of $m_h$ in the $h \rightarrow \gamma\gamma$ channel	177
5.2.2 Impact of the systematic uncertainties on $m_h$	177
5.2.3 Consistency among classes of events	179
5.2.4 Combination with the $h \rightarrow ZZ^* \rightarrow 4l$ channel	182
5.2.5 Combination with CMS	183
<b>5.3 Modelling of the width</b>	<b>185</b>
5.3.1 Signal model as a function of the width	185
5.3.2 Comparison between different types of Breit-Wigner functions	185
<b>5.4 Main results on the width</b>	<b>188</b>
5.4.1 Overall description of the statistical method and problems	188
5.4.2 Upper limit on the Higgs boson decay width	190
<b>5.5 Checks on the observed non-asymptoticity</b>	<b>198</b>
5.5.1 Presentation of the problem on the full statistical model	198
5.5.2 Impact of the various nuisance parameters	199
5.5.3 Cross-check on a simplified model	199
5.5.4 Comparison with the $h \rightarrow ZZ^* \rightarrow 4l$ channel	201
5.5.5 Look-elsewhere effect and the Leadbetter formula	202
<b>5.6 Impact of the resolution and comparison with CMS</b>	<b>203</b>
5.6.1 Variation of the limit as a function of the resolution	203

## 5.1 Overall description of the $H \rightarrow \gamma\gamma$ analyses

### 5.1.1 Selection of events for the $h \rightarrow \gamma\gamma$ analysis

The events that are considered in the  $h \rightarrow \gamma\gamma$  analysis are selected following a sequence of cuts, which constitutes the inclusive selection. Details of the analysis may be found in [4, 89, 262, 264]. First we look at events that pass a specific di-photon trigger, in our case the trigger requires at least two photons passing the loose identification criteria, one with a  $p_T$  higher than 35 GeV and a second one with  $p_T > 25$  GeV. Then a first set of cuts is applied to remove temporary detector defaults, as well as events potentially coming from cosmic-rays. This is followed by a series of cuts about the kinematics of the event, especially on the  $p_T$  of the two photons and on the di-photon invariant mass, which are here to remove part of the dominant background, that is the di-photon background. The last cuts insure that none of the photons in the di-photon pair comes from a mis-identified jet faking a photon. The exact sequence is applied as follows :

- Trigger requirement : the event should pass the g35\_loose\_g25\_loose trigger
- Good Runs Lists : the lumi-blocks during which at least one of the sub-detector was not fully operational are removed. A lumi-block typically corresponds to 60 seconds
- Event quality : data-quality flags are checked to insure the integrity of the data in the event, especially the quality of the information from the calorimeter. For instance these flags are removing noise-bursts that can be observed in the LAr calorimeters
- Primary vertex : the existence of a primary vertex in the event is checked for, which is expected to remove events coming from cosmic-rays. This only impacts a few low-luminosity runs of the 2011 datasets
- Pre-selection : we check the existence of two photons with  $p_T > 25$  GeV and that are falling inside the detector acceptance ( $|\eta| < 2.37$ , with the part  $1.37 < |\eta| < 1.56$  that corresponds to the crack removed). After this point only the two highest- $p_T$  photons in the event are considered
- Relative  $p_T$  cuts : the leading/sub-leading photons are required to pass the cuts  $\frac{p_T}{m_{\gamma\gamma}} > 0.35, 0.25$
- Identification criteria : the two selected photons are asked to pass the tight identification criteria, which removes a sizeable part of the background generated by  $\pi^0 \rightarrow \gamma\gamma$  decays
- Isolation criteria : in order to further reduce the impact of jet backgrounds, an isolation requirement is applied on the photons, by asking that the scalar sum of the  $p_T$  of the tracks coming from the same primary vertex than the di-photon pair and in a cone of  $\Delta R < 0.2$  around the photon is less than 2.6 GeV, and that the amount

of energy from topological clusters [204] in the calorimeter in a cone of  $\Delta R < 0.4$  is less than 6 GeV

- $m_{\gamma\gamma}$  window requirement : the di-photon mass of the selected pair is asked to be between 105 and 160 GeV

During the previous sequence several corrections need to be applied, and will be described below. First the energy of the particles is corrected by the calibration procedure that has been described in the previous part. Then the computation of the di-photon mass, as well as of the track isolation, requires a proper knowledge of the primary vertex, which is achieved using a neural-network based on several variables from the calorimeter pointing and the tracker. The calorimetric isolation also needs to be corrected for the impact of the pile-up in the event, and for the impact of the energy of the photon leaking into the isolation region.

### Selection of the primary vertex

As the analysis was evolving the method used to select the primary vertex corresponding to a  $h \rightarrow \gamma\gamma$  event evolved too, but the basic building blocks remained similar.

The first method that has been considered is the pointing [89, 176, 265, 266] that uses the barycentre of the energy deposits in the first and second layer of the calorimeter. These two positions are fitted by a straight line and extrapolated back to the beam axis, which gives an estimate of the  $z$  of the primary vertex,  $z_{pointing}$ . In the case of converted photons where the two tracks are reconstructed, and both have hits in the SCT, the information from the middle layer is removed and the position of the conversion vertex is used instead, which is much more precise. Then the choice of the primary vertex can be done by selecting the vertex with the  $z$  the closest to  $z_{pointing}$ . The resolution on  $z_{pointing}$  is of 15 mm on average, and improves for two-tracks conversions where it goes down to an order of 1 mm.

The second approach uses the information from the tracker, because the primary vertex from which the actual hard-scattering originates is expected to have a higher track activity than the others. The most naive variable to check for such an effect is  $\sum p_T^2$  where the sum runs on all the tracks that are associated to a given vertex. In the case of the production of a heavy particle with a hard scattering we expect to have a higher hadronic activity from the proton remnants that will recoil against the produced particle. The information from this variable can be combined with the information from the pointing, by combining their likelihoods, which combines the advantages of both the methods and when the vertex selected by the highest  $\sum p_T^2$  will not be the correct one, it will still be constrained by the pointing, hence it will not have a big impact on the mass resolution. Fig. 1 of [267] shows the Higgs boson mass resolution in the diphoton channel when the primary vertex is selected with the highest  $\sum p_T^2$  or with the pointing. This last method improves largely the resolution. The likelihood method is presented in [89].

The last approach [268], which is the one that had been used for the final Run 1 analyses, uses a neural-network where the previous variables are used as input, and a few others are added. These additional variables are :

- The scalar sum of all the tracks associated to a given vertex,  $\sum p_T$

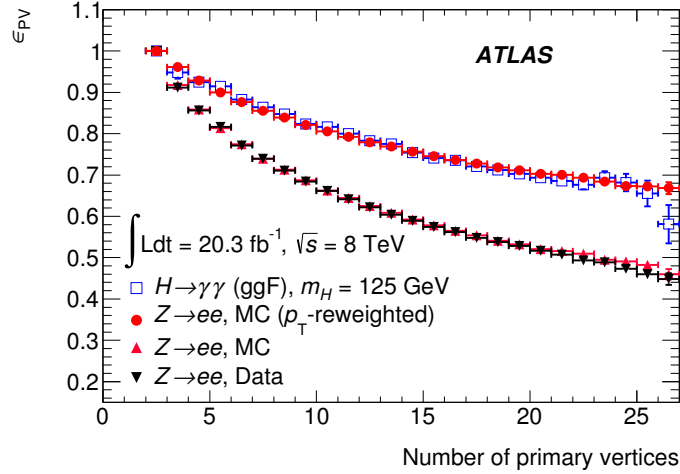


Figure 5.1: Efficiency of selecting a primary vertex within 0.3 mm of the true one, using the neural network algorithm, for events from simulation of  $h \rightarrow \gamma\gamma$  and  $Z \rightarrow ee$ , as well as from data for  $Z \rightarrow ee$  events. For  $Z \rightarrow ee$  the electron tracks are removed from the event before running the neural network [262]

- $\Delta\phi$  between the direction of the selected  $h \rightarrow \gamma\gamma$  candidate and the direction of the vectorial sum of the tracks associated to a given vertex
- The pull between the  $z$  reconstructed with the pointing and with  $\sum p_T^2, \frac{z_{pointing} - z_{p_T^2}}{\sigma_{pointing}}$

The first two variables should improve the selection of the hard-interaction vertices, for which the distribution of the tracks is not isotropic, i.e. for which the proton remnants are recoiling against another particle without tracks, which is typically the case we are interested in. At the end, with this algorithm, the efficiency of selecting a primary-vertex that is within  $\pm 15$  mm of the true one is of 93%, and the contribution of the opening angle to the di-photon mass resolution is negligible. The efficiency to select a primary vertex within 0.3 mm of the true one with this algorithm is shown in fig. 5.1 as a function of the pile-up. The performance obtained from a simulated sample of  $h \rightarrow \gamma\gamma$  decays are compared with those coming from  $Z \rightarrow ee$  samples, both from data and MC, where the tracks coming from the  $Z$  boson have been removed from the event before running the neural network. As the  $p_T$  of the electromagnetic particles in  $Z$  and  $h$  decay are different, the  $p_T$  of the electrons in the  $Z$  MC sample is reweighted to the one of the photon in the simulated  $h \rightarrow \gamma\gamma$  sample, which allows for a fair comparison of the performance obtained on the two different samples.

### Correction to the calorimetric isolation

The goal of the isolation is to quantify the level of hadronic activity around the photon, hence giving a way to determine how likely is a photon to originate from a  $\pi^0$  decay happening inside a jet. Ideally it should only represent the energy that comes from the same primary-vertex than the photon itself, which means that it should not depend on the level of pile-up, neither on the  $p_T$  of the particle. But, in a high pile-up environment there are soft energy deposits coming from all the vertices that are increasing the value of

the calorimetric isolation. A way to suppress this effect have been developed [269]. In the same way, to make sure that no energy coming from the photon is included in the isolation cone, a cluster of  $5 \times 7$  cells (in  $\eta \times \phi$ ) is removed from the isolation cone. But some of the energy of the photon can still leak outside of this cluster, hence artificially increasing the value of the isolation energy too. This is also corrected for, and both these corrections are described below.

**Photon energy leaking inside the isolation cone** The energy leakage coming from an electro-magnetic particle into its isolation cone has been studied on single-particle MC samples where the pile-up has not been simulated, which insures that any contribution to the isolation cone would originate from the particle energy leakage [269]. It is expected that this leakage will depend on the energy of the particle, but also on its type. For instance a converted photon will have a bigger leakage because it actually consists of two electrons with an opening angle between each other. This variation was parametrized by a linear function of the  $p_T$  where the slope and the origin of the function are fitted separately for each type of particle, and this fit is done in nine different regions in  $|\eta|$ .

**Ambient energy correction** As was explained above the electronic shaping of the EM calorimeter has been done to cancel the impact of pile-up on average, but there are remaining Poisson fluctuations in the number of primary vertices that are impacting the resolution of the cell energy at an event-by-event level. This impacts the distribution of the calorimetric isolation too, that would become broader with an increasing pile-up, and the efficiency of a cut on the isolation would not be constant with respect to the number of pile-up events. To correct for this an event-by-event correction has been developed, and is based on the energy density of the event [269]. In each event, jets of radius  $R = 0.5$  are built, using every topo-cluster of positive energy in the event. For each jet the transverse momentum density is computed, as the ratio of the jet transverse momentum to of its area, and the energy density of the event  $\rho$  is defined as the median of this distribution. Then, assuming  $A$  is the size of the isolation area, it is possible to correct the impact of pile-up on the isolation of each particle, by subtracting  $A \times \rho$ .

## 5.1.2 Modelling of signal and background processes

### Analytical description of the signal

The shape of the invariant mass of the di-photon system in  $h \rightarrow \gamma\gamma$  events has been studied using Monte-Carlo samples, using a full simulation of the detector, and an analytical description of the signal has been derived. This distribution can be seen in fig. 5.2 for the inclusive case, where it is clear that the core of this distribution is Gaussian in first approximation, which corresponds to what we expect for the resolution, but has a slightly larger tail at low  $m_{\gamma\gamma}$ . This tail corresponds to converted photons, where one of the two electrons of the conversion pair lose energy by radiating soft photons, hence decreasing the reconstructed invariant mass of the di-photon pair. This kind of distribution is well described by the Crystal-Ball function (CB) [270], which is defined as follows, if we denote

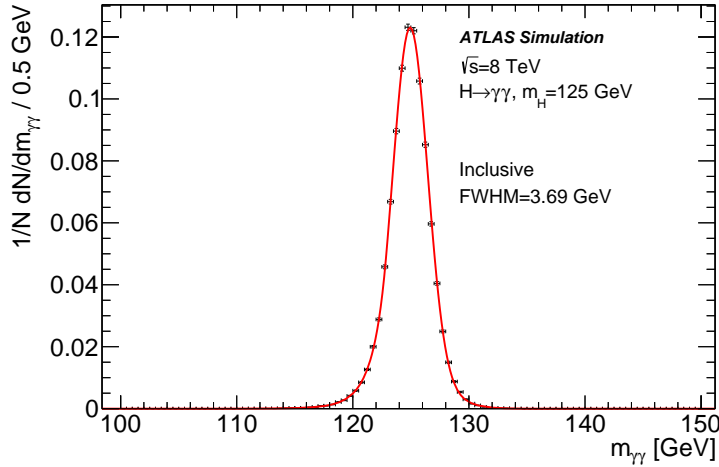


Figure 5.2: Distribution of the reconstructed di-photon invariant mass for simulated  $h \rightarrow \gamma\gamma$  events with  $m_H = 125$  GeV and  $\Gamma_H = 4$  MeV [264]

$$t = \frac{m_{\gamma\gamma} - m_H}{\sigma_m} :$$

$$N \cdot \begin{cases} e^{-t^2/2} & \text{if } t > -\alpha \\ \left(\frac{n}{|\alpha|}\right)^n \cdot e^{-|\alpha|^2/2} \cdot \left(\frac{n}{|\alpha|} - |\alpha| - t\right)^{-n} & \text{otherwise} \end{cases} \quad (5.1)$$

Although this describes the core of the distribution very well, it was noticed that there were tails at high and low  $m_{\gamma\gamma}$  that were not properly described by this distribution. A broad Gaussian component has been added to the signal model to improve the description of the distribution, but its fraction is very small with respect to the CB. The signal model is then :

$$f_s = f_{CB} CB(m_{\gamma\gamma} | \mu_{CB}, \sigma_{CB}, n, \alpha) + (1 - f_{CB}) Gaus(m_{\gamma\gamma} | \mu_{gaus}, \sigma_{gaus}) \quad (5.2)$$

Where the fraction of Crystal-Ball component ( $f_{CB}$ ) in the model is always higher than 95%. Except for  $n$  that is fixed at 10, the value of all the parameters in the model are determined from a fit of the Monte-Carlo samples, using the following recipe. Several MC samples are generated at different values of  $m_H$ , and the signal model is fitted separately on each of the samples. The parameters  $\mu_{CB,gaus}$  and  $\sigma_{CB}$  are expected to vary linearly with respect to  $m_h$ . It is therefore possible to express them as a function of  $m_h$ , and as we have their values at several points of  $m_h$  it is possible to fit the slope and the offset of this function, taking the origin at  $m_h = 125$  GeV.  $\sigma_{gaus}$  is not fitted by itself but expressed as  $\sigma_{gaus} = \kappa \sigma_{CB}$  and it is the  $\kappa$ , which is a constant, that is fitted. In this process  $\alpha$  is fitted only once on the MC at  $m_h = 125$  GeV. We will see later that we need to define categories of events to improve the analysis performance, and the signal model will be extracted separately for each of the categories.

### Description of the background and its uncertainty

The main component of the background in the  $h \rightarrow \gamma\gamma$  analysis after selection comes from prompt di-photon event ( $\approx 75\%$  of the total background), essentially through  $q\bar{q} \rightarrow \gamma\gamma$

although there is also a non-negligible contribution from  $gg \rightarrow \gamma\gamma$ , that is already at one-loop at LO but still accounts for  $\approx 10\%$  of this background, and from  $qg \rightarrow q\gamma\gamma$  where one of the photons is a final state radiation of a quark. The two other important background are the gamma-jet (20%) and di-jet processes (5%), where the jets are mis-identified as photons. Although these processes have a much bigger cross-section, the procedure of photon identification is sufficiently powerful to reject most of these events. Still even after the  $h \rightarrow \gamma\gamma$  selection the cross-section for the background events is high, but as their  $m_{\gamma\gamma}$  distribution follows a smoothly falling form, it is possible to use an analytical function to parametrize it, and the actual estimation of the background comes from a fit of the data. But the real analytical expression of the  $m_{\gamma\gamma}$  distribution is not known, hence the choice of a specific function introduce a new uncertainty that has been implemented on ATLAS by using the "spurious signal" method [271]. This method also constitutes the basis on which the specific form that will be used to fit the background on data will be chosen.

**The spurious signal** The goal of the spurious signal is to represent the potential bias of the fitted number of signal coming from the choice of the functional form used to describe the background shape. High-statistics Monte-Carlo samples have been generated for the  $\gamma\gamma$ , gamma-jet and di-jet background processes, and are used to study the potential background shapes. For each of these shapes a full signal plus background fit is performed, using the signal shape described above. This fit will give a non-zero value for the number of signal events, which gives the value for the spurious signal. The spurious signal will be considered as an additional uncertainty on the fitted number of events, given that if both the simulation and the tested functional form were perfectly describing the data, the number of signal events returned by the fit should be 0. In this sense, the size of the spurious signal is small if the tested function is close to the actual shape of the background  $m_{\gamma\gamma}$  distribution.

**Choice of a functional form** The background shape is determined separately in each category, and to chose it a broad range of functions are tested. The list of functions includes for instance several kinds of polynomials, and exponential of polynomials. First, the functions that clearly do not fit the high-statistics MC or that are creating fit convergence problems are discarded. For each of the remaining background models, the three following parameters are considered in order to select the best model : the expected number of signal events in this category  $N_{SM}^{sig}$ , the spurious signal  $N_{spur}$  and the uncertainty on the number of background events  $\sigma_{bkg}$  which is extracted from the fit of a pure background Asimov dataset. The chosen signal should pass at least one of these two criteria :

- $N_{spur} < 20\% \sigma_{bkg}$
- $N_{spur} < 10\% N_{SM}^{sig}$

If more than one parametrization passes these tests, the one with the lowest spurious signal is kept, although there are usually few parametrizations that pass this test.

### 5.1.3 Event categorization for the mass and width analysis

To fully benefit from the variation of resolution and of the signal-to-background ratio in the dataset that has been selected for the  $h \rightarrow \gamma\gamma$  analysis, it is possible to define categories

of events. Afterwards the full likelihood of this analysis will be defined as the product of the individual likelihoods of each of the categories. The constraint terms on the nuisance parameters associated to uncertainties that are correlated among categories only appear once in the full likelihood. To define the individual likelihoods one needs to re-evaluate the parameters of the signal model, re-define the functional form used for the background and re-derive the value of all the systematic uncertainties for each of these categories. This allows to isolate particular classes of events that have poor performance, while not excluding them from the analysis. At the end the measurements will mainly be driven by the few categories that have a good resolution, a high  $\frac{S}{B}$  and low uncertainties. The presence of the other categories allows to slightly improve the performance but their impact is smaller. For the measurement of the Higgs boson mass the most important uncertainties are those impacting the photon energy scale, but they need to be propagated to the mass itself. The method used to do that is described below.

### Propagation of the energy scale uncertainty to the mass

The uncertainties on the energy scale of individual electromagnetic particles, as a function of their position, type and momentum are derived from the electromagnetic calibration. This needs to be converted into an uncertainty on one of the parameter of the signal model, namely  $m_h$  here. As this conversion mainly implies kinematic effects it can be done using MC samples, on which this kinematic is well modelled. The nominal  $h \rightarrow \gamma\gamma$  MC is modified by injecting an upward or a downward bias on the photon energy of the size of the uncertainty that is being probed. The full  $m_{\gamma\gamma}$  distribution of this biased MC is then re-derived, and the signal model is fitted on this distribution to obtain the value of  $m_h$  after the energy scale bias,  $m'_h$ . The uncertainty on the mass is then taken as the relative difference between the nominal  $m_h$  and  $m'_h$  :  $\delta = \frac{m'_h - m_h}{m_h}$ . This method is applied separately for each source, and the size of the uncertainty induced by a given source is evaluated separately in each category.

The uncertainty on the energy and vertex position resolution are propagated to the mass resolution using a similar method.

### Other uncertainties

Although the uncertainties on the photon energy scale and on their energy resolution are the most important for the measurement of the Higgs boson mass and the analysis of the Higgs boson decay width, few others have been implemented too [272]. The first one concerns the modelling of the background, because the spurious signal only represents an uncertainty on the fitted number of signal events, and not directly on the mass, therefore a more refined method was needed. The second effect corresponds to uncertainties on the expected number of events in the various categories, as the different signal models in the different categories may imply a shift of the Higgs boson mass if the number of events in each category changes.

**Uncertainty on the modelling of the background** The spurious signal method is not sufficient to estimate an uncertainty on the Higgs boson mass coming from the mis-modelling of the background, as it only gives an estimate of the potential bias of the fitted

number of signal events. Yet it was possible to design another method to estimate the uncertainty on the mass, which is based on the same high-statistics MC samples that were used to extract the spurious signal. A signal template, generated in the same way as an Asimov dataset, is overlaid on top of this high-statistics MC, and the fit of the mass is performed on this S+B pseudo-dataset. The difference between the fitted mass and the true injected mass gives an estimate of the uncertainty, but this fit is done at various mass points and it is actually the maximal deviation between the true injected mass and the estimated one that is taken as an uncertainty. Depending on the category this uncertainty has an impact of 0.05% to 0.20% on the Higgs boson mass.

**Uncertainty from event migrations between categories** There are potential sources of uncertainties coming from the relative variation of the signal yield in each category with respect to each others. These uncertainties are treated as uncertainties on the expected number of events in each category, although they are signed in order to impose the fact that the total number of events should stay constant, and hence the increase in the yield of one category implies its decrease in another category. The mis-modelling of the conversion reconstruction creates such a migration of true unconverted photon into the converted category, and vice-versa. The estimation of the fraction of true converted photon has been explained in subsection 4.7.1. Another effect that creates that kind of variation is the mis-modelling of the Higgs boson  $p_T$  spectrum [89], that creates a migration of the expected number of events between the high- $p_{T_i}$  and low- $p_{T_i}$  categories. This has been estimated by varying the renormalization scale, factorization scale, and resummation scales associated to the bottom and top quarks in HRes 2 [82, 83].

**Uncertainties on the total signal yield** Several effects may affect the expected total number of events. First the theory uncertainty on the Higgs boson production cross-section is provided by the LHC Higgs cross-section working group [81] and corresponds to the propagation of the uncertainty on the PDF sets and on  $\alpha_S$ . The uncertainty on  $\alpha_S$  corresponds mainly to an uncertainty on the renormalization scale. The uncertainty is currently at the level of 10% for the gluon fusion production cross-section, which is dominant, and 5% for the  $h \rightarrow \gamma\gamma$  branching ratio. But there is also a set of experimental uncertainties that can give this effect, such as the uncertainty on the trigger efficiency, on the photon identification and on the isolation efficiency, but are all at the level of 1% for the 2012 dataset. There is also an uncertainty on the luminosity recorded by ATLAS which is of 2.8% in 2012.

### Procedure of optimization and selected categorization

In order to find the best categories for the mass measurement, several categorization were tried although they were all relying on our understanding of the detector and on the variation of the signal-to-background ratio with respect to a few variables. For each of these categorization the full statistical model was derived, and an Asimov dataset was built for  $m_H = 126.5$  GeV and  $\mu = 1$ . A fit of this dataset gives the expected error on the mass,  $\delta m_h$ , and the categorization that was finally chosen is the one that gives the smallest  $\delta m_h$ . The dominant uncertainty comes from the statistical power of the available dataset, which depends on the mass resolution  $\sigma_{res}$  and it may be shown that the error

varies as  $\delta m_H \propto \sigma_{res}^{3/2}$  (see appendix B) and hence the quality of a given categorization depends a lot on its ability to isolate classes of events that have a high-resolution. These few categories will dominate the mass measurement and the other ones will essentially be factorized out in the likelihood ratio. In this respect the categories that will be chosen to do the mass measurement are also the best candidate to derive an upper limit on the width too, as in this analysis we are interested at excluding a potential widening of the peak that cannot be explained by the effect of the resolution, which is easier if the resolution is in itself smaller.

The chosen categorization splits the dataset in ten categories as a function of  $\eta$  of the two photons in the pair, whether they are converted or not, and as a function of  $p_{T_t}$  of the selected pair. The  $p_{T_t}$  is defined as follows :

$$p_{T_t} = |\vec{p}_T^{\gamma\gamma} \times \hat{t}| \text{ where } \hat{t} = \frac{\vec{p}_T^{\gamma 1} - \vec{p}_T^{\gamma 2}}{|\vec{p}_T^{\gamma 1} - \vec{p}_T^{\gamma 2}|} \text{ and } \vec{p}_T^{\gamma\gamma} = \vec{p}_T^{\gamma 1} + \vec{p}_T^{\gamma 2}$$

and  $\hat{t}$  is called the thrust axis. The categories for the mass and width analysis [264] are then defined as follows :

- First define a central category where both photons have  $|\eta| < 0.75$
- A transition category where at least one photon falls into  $1.3 < |\eta| < 1.8$
- And a last category for the rest of the events

These categories are further split as a function of the conversion status of the photons, with the events where the two photons in the pair are unconverted on one side, and the events where at least one photon is converted on another. A last separation is applied in the "central" and "rest" categories that are further split in two categories, delimiting the two sub-categories of events by adding a cut on  $p_{T_t}$  at 70 GeV.

It was noticed that adding a VBF category could slightly improve the final error on the Higgs boson mass, although not by a big factor and it would have required to add all the systematic uncertainties related to the jet identification and energy response, therefore it was decided to stay with this simpler 10 categories model, without any categorization related to the associated production modes. The exact definition of the categories, as well as some of the most important parameters of their models is given in table 5.1.

	Conv. status	$ \eta $ region	$p_{T_t}$ cut	Background shape	$n_{sig}^{exp,SM}$	Resolution [GeV]
Category 1	Unconv.	$ \eta  < 0.75$	$p_{T_t} < 70$ GeV	Exp. Poly. 2	59.3	1.35
Category 2			$p_{T_t} > 70$ GeV	Exponential	7.1	1.21
Category 3	Unconv.	Rest	$p_{T_t} < 70$ GeV	Exp. Poly. 2	96.2	1.53
Category 4			$p_{T_t} > 70$ GeV	Exponential	10.4	1.36
Category 5	Unconv.	Transition	None	Exp. Poly. 2	26.0	1.86
Category 6	Conv.	$ \eta  < 0.75$	$p_{T_t} < 70$ GeV	Exp. Poly. 2	37.2	1.52
Category 7			$p_{T_t} > 70$ GeV	Exponential	4.5	1.35
Category 8	Conv.	Rest	$p_{T_t} < 70$ GeV	Exp. Poly. 2	107.2	1.88
Category 9			$p_{T_t} > 70$ GeV	Exponential	11.9	1.64
Category 10	Conv.	Transition	None	Exp. Poly. 2	42.1	2.41
Inclusive	None	None	None	Exp. Poly. 2	402	1.67

Table 5.1: Summary of the definition of the categories, of the chosen background shape in each of the category, of the expected number of signal events, and the signal resolution corresponding to half of the smallest range containing 68.8% of the events. The resolution and the number of expected signal events corresponds to the 2012 dataset only [264]

## 5.2 Measurement of the BEH boson mass

### 5.2.1 Measurement of $m_h$ in the $h \rightarrow \gamma\gamma$ channel

The mass of the BEH boson is estimated [264] from a combined signal plus background fit to the ten categories that have been defined above, in the 2012 and 2011 datasets. This fit is done with an unbinned likelihood that is constructed as in eq. 2.3, where the signal and background PDFs used for each category are those defined above. All the uncertainties are represented by constrained nuisance parameters in the likelihood, and are profiled out during the fit. The signal strength  $\mu$  is also treated as a free parameter in the fit. The result of this fit as well as the fitted dataset may be seen in fig. 5.3, where the events corresponding to the various categories are weighted by the  $\frac{S}{B}$  of their category for illustrative purpose. The  $h \rightarrow \gamma\gamma$  peak can clearly be observed over the smooth background, and the maximum-likelihood estimate of  $m_H$  and  $\mu$  gives  $m_H = 125.98 \pm 0.50$  GeV with  $\mu = 1.29 \pm 0.30$ . This error can be divided into its statistics and its systematic components, by fixing the nuisance parameters to their best-fit values, which deprives the fit from the additional freedom that represents the systematic uncertainties. Then the systematic uncertainty is determined as the quadratic difference between the full error and its statistical component. This gives  $m_H = 125.98 \pm 0.42$  (*stat*)  $\pm 0.28$  (*syst*) GeV. At  $\mu = 1.3$  the expected statistical error on  $m_h$  is of 0.35 GeV, and it has been estimated from toys that 16% of the experiments generated at  $\mu = 1.3$  have an uncertainty on the mass at least as high as 0.42 GeV. It can be shown that the statistical uncertainty on the mass varies as  $\delta m_h \propto \frac{\sigma_{res}^{3/2}}{\mu}$  where  $\sigma_{res}$  corresponds to the resolution, and for  $\mu = 1$  the expected statistical uncertainty is 0.45 GeV.

### 5.2.2 Impact of the systematic uncertainties on $m_h$

In the  $h \rightarrow \gamma\gamma$  channel, the dominant systematic uncertainty on the measurement of the Higgs boson mass comes from the photon energy scale uncertainty, followed by the background modelling which has a non-negligible impact too. Every other uncertainties (for instance those regarding the signal yield) have been implemented in the statistical

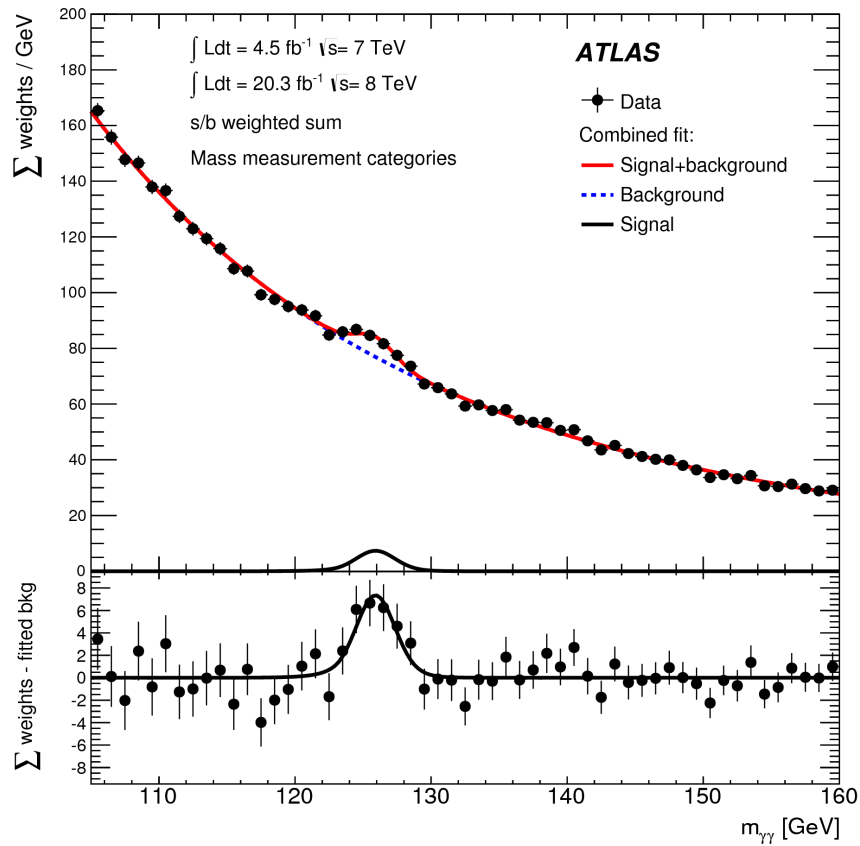


Figure 5.3: Di-photon invariant mass spectrum for pairs selected by the  $h \rightarrow \gamma\gamma$  selection criteria. Each event is weighted by the  $S/B$  ratio of the category it falls in. [264]

Class	Central		Unconverted Rest		Transition	Central		Converted Rest		Transition
	low $p_{Tt}$	high $p_{Tt}$	low $p_{Tt}$	high $p_{Tt}$		low $p_{Tt}$	high $p_{Tt}$	low $p_{Tt}$	high $p_{Tt}$	
$Z \rightarrow e^+e^-$ calibration	0.02	0.03	0.04	0.04	0.11	0.02	0.02	0.05	0.05	0.11
LAr cell nonlinearity	0.12	0.19	0.09	0.16	0.39	0.09	0.19	0.06	0.14	0.29
Layer calibration	0.13	0.16	0.11	0.13	0.13	0.07	0.10	0.05	0.07	0.07
ID material	0.06	0.06	0.08	0.08	0.10	0.05	0.05	0.06	0.06	0.06
Other material	0.07	0.08	0.14	0.15	0.35	0.04	0.04	0.07	0.08	0.20
Conversion reconstruction	0.02	0.02	0.03	0.03	0.05	0.03	0.02	0.05	0.04	0.06
Lateral shower shape	0.04	0.04	0.07	0.07	0.06	0.09	0.09	0.18	0.19	0.16
Background modeling	0.10	0.06	0.05	0.11	0.16	0.13	0.06	0.14	0.18	0.20
Vertex measurement	0.03									
Total	0.23	0.28	0.24	0.30	0.59	0.21	0.25	0.27	0.33	0.47

Figure 5.4: Relative magnitude (in %) of the main uncertainties on the Higgs boson mass measurement, given by categories and using a merging of all the systematics into seven main classes [264]

model, but their impact on the mass measurement is mild hence they will not be discussed further below. The magnitude of the uncertainty on the mass scale, which is given as an input to the statistical model, is shown in fig. 5.4, where all the uncertainties that were described before have been grouped in a few groups depending on their source. In this table the "LAr cell non-linearity" corresponds to the combined effect of the pedestal shift between data and MC, and of the apparent difference of energy response between the high and medium gain electronic read-out, although it is clearly dominated by the second effect. In most of the categories, and especially in those that are the best in terms of resolution and signal-to-background ratio, this non-linearity is the biggest uncertainty, and it is followed by the out-of-cluster leakage for categories associated to converted photons and the inter-layer calibration for those with unconverted photons.

Depending on the specificities of the measurement that is being conducted, the uncertainties may decrease after the fit because the data may bring additional information on one of the source of uncertainties that is included in the model. In such a case the nuisance parameters, whose best-fit value should be close to 0 with an error of 1, will be over-constrained and potentially pulled away from 0. These pulls are shown in fig. 5.5. At the same time the individual impact of each of the source of uncertainties on the total error on the mass may be measured, which is done by actually estimating what is the variation of the conditional best-fit of  $m_h$  under a variation of  $\pm 1\sigma$  of the nuisance parameter associated to a given source of uncertainty around its best-fit value, which is also shown in fig. 5.5. The associated nuisance parameter is actually fixed to its  $\pm 1\sigma$  value during the fit. As expected the apparent energy difference between the two electronic gains has the biggest impact on  $m_h$ , and it is closely followed by the impact of the uncertainties on the simulation of the liquid-argon calorimeter on the determination of the material budget in front of the pre-sampler, as well as the uncertainty on the extrapolation of the inter-layer calibration scale from muons to photons.

### 5.2.3 Consistency among classes of events

To ensure the stability of this measurement, it has been produced in several different sub-samples of the data, and the compatibility between these different sub-samples have been checked. This is summarized by fig. 5.6 where the consistency of this measurement with respect to the level of pile-up in the event, the conversion status of the photons in the

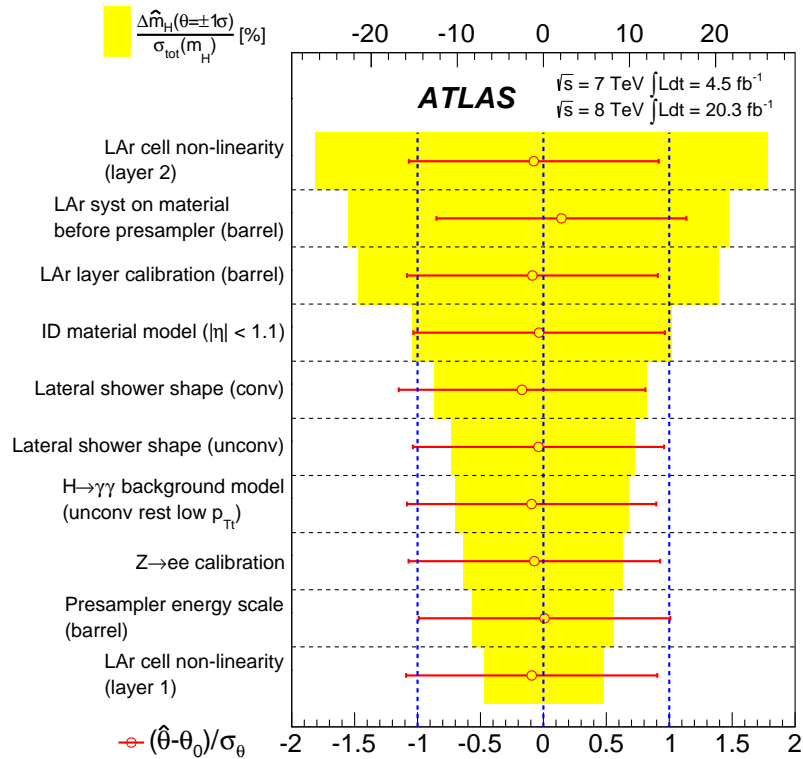


Figure 5.5: Impact of the main systematic uncertainties on the mass measurement in the  $h \rightarrow \gamma\gamma$  channel and pull of the related nuisance parameters. The various systematic uncertainties are ranked by the magnitude of their impact on the mass measurement [264]

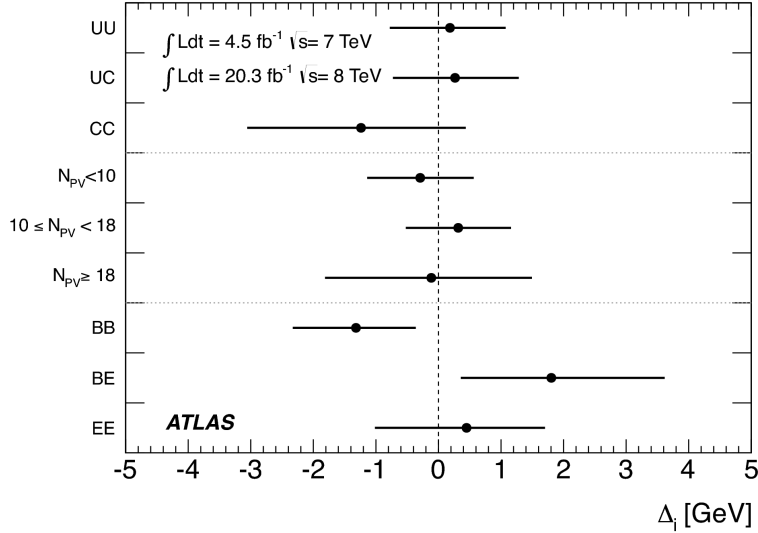


Figure 5.6: Difference between the best estimate of  $m_h$  in different categories of events and its combined value [264]. The notations used are the following : UU when the two photons are unconverted, CC if both are converted and UC if there is one of each. BB if both are in the barrel, EE for both in the end-cap and EB if there is one of each

pair and the position of the two photons within the detector is shown. To do this check an alternative statistical model is used where a common central value  $m_h$  exists for the mass, but for a given sub-sample there is an additional parameter  $\Delta_i$  that captures the variations of the best-fit of the mass in this category with respect to the combined one, and hence allows to determine how compatible the different categories are with respect to each others. There is one model of this kind by sub-sample, where only the  $\Delta_i$  corresponding to the sub-sample that is being tested is included, and it is these values of the  $\Delta_i$  that are shown in fig. 5.6, for the three different ways of defining the sub-samples of the data. In all the sub-samples that have been tested the  $\Delta_i$  are found to be compatible with 0. The same test has also been conducted with respect to the conversion topology, the instantaneous luminosity, the photon isolation and the data taking periods and gave similar results.

The 2011 dataset has also been included in this measurement, although its statistical power is much smaller than the one from the 2012 sample. A similar cross-check was derived to assess the compatibility between these two datasets, where the parameter  $m_h$  represented only the mass fitted in 2012 and the mass peak of the 2011 dataset was allowed to be shifted by a parameter  $\Delta$ , i.e. in the statistical model for the 2011 category the mass was  $m_h^{11} = m_h^{12} + \Delta$ . The scan of the full likelihood describing the combination of the 2011 and 2012 dataset is shown in fig. 5.6, where a tension with respect to the hypothesis  $\Delta = 0$  can be observed. The significance of this tension has been evaluated using pseudo-experiments and found out to be at the level of  $2.1\sigma$ . This is compatible with a statistical fluctuation between the two years, and despite specific cross-checks of the difference of calibration between the two years no effect that could explain this difference has been found. Furthermore it should be noted that the significance of the  $h \rightarrow \gamma\gamma$  peak is much weaker in 2011 than 2012, and it would not have been observed with 2011 alone.

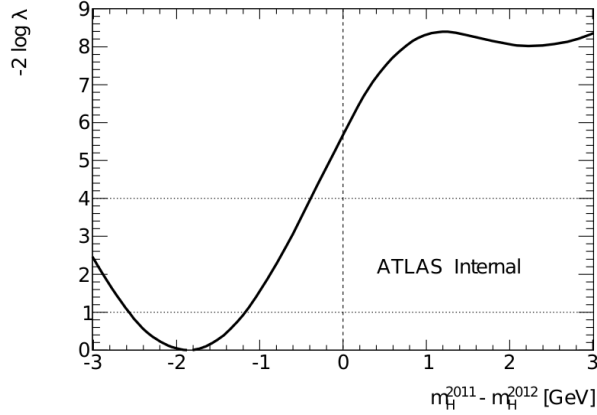


Figure 5.7: Scan of the likelihood with regard to the difference of Higgs boson mass between 2011 and 2012 [272]

### 5.2.4 Combination with the $h \rightarrow ZZ^* \rightarrow 4l$ channel

The measurement of the mass in the  $h \rightarrow \gamma\gamma$  channel has been combined [264] with its measurements in the  $h \rightarrow ZZ^* \rightarrow 4l$  channel, which is the other high-precision channel. In this channel most of the energy is carried by the on-shell Z boson, for which a Z-mass constraint is imposed, and this implies that for this boson the only relevant energy scale uncertainties are those related to the method of energy scale determination. The energy of the leptons from the off-shell bosons is much smaller and may be subject their energy scale uncertainties may be inflated without this having an impact on the uncertainty on the Higgs boson mass. Therefore the systematic uncertainty on  $m_h$  from the  $h \rightarrow ZZ^* \rightarrow 4l$  channel is very small, at the level of  $\pm 0.03\%$  for both the electron and muon energy scales, and the total error on  $m_h$  is completely driven by the observed number of events in the peak region. The mass measured in this channel is  $m_h = 124.51 \pm 0.52$  (*stat*)  $\pm 0.06$  (*syst*) GeV (see also [263] where the systematic error is 0.04 GeV).

The combined likelihood for the  $h \rightarrow ZZ^* \rightarrow 4l$  and  $h \rightarrow \gamma\gamma$  channels is determined by multiplying the individual likelihoods, which allows to produce the same measurement. The confidence interval obtained for  $(\mu, m_h)$  separately for the  $h \rightarrow ZZ^*$ ,  $h \rightarrow \gamma\gamma$  and for their combination is shown in 5.8. Although this interval is clearly smaller after the combination we can see a slight tension between the two individual channels, which will be discussed later. The best fit of the mass is obtained for  $m_h = 125.36 \pm 0.37$  (*stat*)  $\pm 0.18$  (*syst*). The uncertainty induced by each of the source of systematic effect has been evaluated separately, which is done by performing the fit of  $m_h$  with the related nuisance parameter fixed to its best fit value, and the systematic uncertainty from this effect is estimated as the quadratic difference between the total uncertainty with every parameter free, and the total uncertainty with the nuisance parameter fixed in the fit. This is shown in fig. 5.9 and the dominant uncertainty on the combined  $m_h$  comes from the impact of the mis-modelling of the liquid-argon calorimeter on the determination of the material. Naively the inversion between this uncertainty and the liquid-argon cell non-linearity is not expected, and it is not seen on an Asimov dataset of this problem, hence it likely originates from statistical fluctuations of the distribution of the position of  $h \rightarrow ZZ^* \rightarrow 4l$  events. Below, the next sources of uncertainties in terms of importance are the electron-to-photon

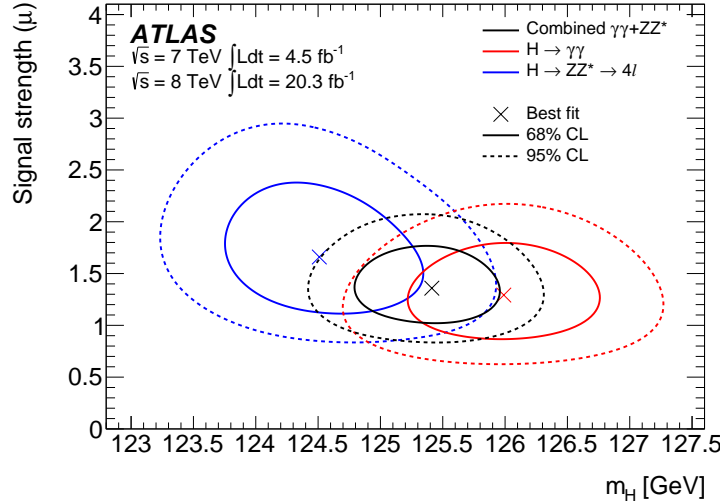


Figure 5.8: Iso-likelihood contours in the  $\mu - m_H$  plan corresponding to the 68% and 95% C.L. contours, separately for the  $h \rightarrow \gamma\gamma$ ,  $h \rightarrow ZZ^* \rightarrow 4l$  channels and for their combination [264]

extrapolation of the lateral leakage, the extrapolation of the inter-layer calibration scale from muons to photons, and the uncertainties from the method of energy scale setting in  $Z \rightarrow ee$  events.

The tension between the two channels has been studied by using a combined mass between the two channels, but adding a parameter  $\Delta$  to the mass of one of the two channel, and in the case of an identical resonance between the two channels we expect to find  $\Delta = 0$ . The maximum-likelihood estimate gives a value  $\Delta = 1.47 \pm 0.67(stat) \pm 0.28(syst)$  GeV, which is an improvement of compatibility with respect to the previous measurement [273] where the  $h \rightarrow \gamma\gamma$  mass was  $126.8 \pm 0.2(stat) \pm 0.7(syst)$  GeV [274], which is partially due to a decrease of  $450 \pm 300$  MeV (dominated by the effects of  $E_1/E_2$  calibration and of the gain calibration [275]) of the mass measured in the  $h \rightarrow \gamma\gamma$  channel that was expected from the improved calibration. The significance of this tension has been evaluated with pseudo-experiments, that are shown in fig. 5.10, and is at the level of 5% ( $2.0\sigma$ ), which is compatible with a statistical fluctuation.

### 5.2.5 Combination with CMS

Recently a combined measurement of the Higgs boson mass with the Run 1 data in the  $h \rightarrow \gamma\gamma$  and  $h \rightarrow ZZ^* \rightarrow 4l$  has been released [263]. The result is  $m_h = 125.09 \pm 0.21(stat) \pm 0.11(syst)$  GeV

Systematic	Uncertainty on $m_H$ [MeV]
LAr syst on material before presampler (barrel)	70
LAr syst on material after presampler (barrel)	20
LAr cell nonlinearity (layer 2)	60
LAr cell nonlinearity (layer 1)	30
LAr layer calibration (barrel)	50
Lateral shower shape (conv)	50
Lateral shower shape (unconv)	40
Presampler energy scale (barrel)	20
ID material model ( $ \eta  < 1.1$ )	50
$H \rightarrow \gamma\gamma$ background model (unconv rest low $p_{Tt}$ )	40
$Z \rightarrow ee$ calibration	50
Primary vertex effect on mass scale	20
Muon momentum scale	10
Remaining systematic uncertainties	70
<b>Total</b>	<b>180</b>

Figure 5.9: Impact of the main systematic uncertainties on the combined mass measurement and pull on the related nuisance parameters. The various systematic are ranked by the magnitude of their impact on the mass measurement [264]

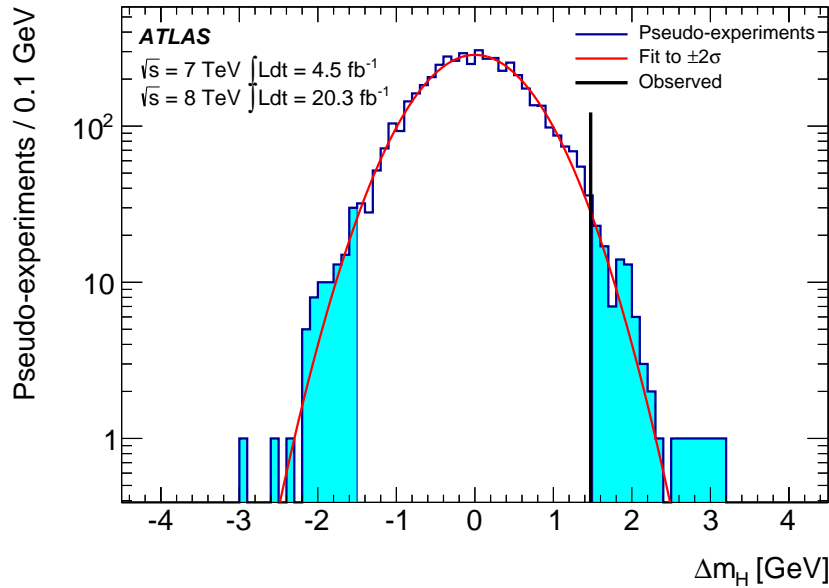


Figure 5.10: Distribution of the mass difference between the  $h \rightarrow \gamma\gamma$  and  $h \rightarrow ZZ^* \rightarrow 4l$  channels constructed with pseudo-experiments (assuming a common mass for the generation), and its value observed on data [264]

## 5.3 Modelling of the width

### 5.3.1 Signal model as a function of the width

The actual reconstructed invariant mass distribution generated by the decay of a BEH boson into two photons is in fact the convolution of the detector resolution, and of the underlying distribution coming from the Higgs boson propagator who has a natural non-zero width. Within the standard model the Higgs boson width (see paragraph 1.3.3) is of 4 MeV for a Higgs boson with  $m_H = 125$  GeV, which is completely negligible with respect to the invariant mass resolution of the detector, that is higher than 1 GeV everywhere. The signal model that was described above has been derived with such a sample where the width is negligible, and it is therefore reasonable to assume that it describes only the detector response and the resolution on the primary vertex, and nothing else. Then, if one wants to model a distribution based on a non-zero decay width, one only has to fold this resolution model with the proper propagator that models the natural width. This is the method that was used in this analysis, using a non-relativistic Breit-Wigner (BW) as a propagator, and doing the convolution with Fast Fourier Transforms (FFTs), which offers the best performance in term of speed and numerical stability. Although the non-relativistic Breit-Wigner is known to be an approximation at small width, and would not represent the true propagator at large width, it allows to give an effective limit on the width and it is this that is used here [264]. Another possibility, although it is also effective, would have been to use a relativistic Breit-Wigner while a complete model would also take into account the opening of the various decay channel, although it has to make explicit assumptions on the position of the threshold for the various decay channels. In order to be consistent with the limit in the  $h \rightarrow ZZ^* \rightarrow 4l$  decay channel, we decided to keep using a non-relativistic Breit-Wigner. Furthermore its convolution with a Gaussian is analytically known and is called a Voigtian [276], which makes it easier to use in the  $h \rightarrow ZZ^* \rightarrow 4l$  channel where the signal model is a sum of Gaussians [277]. Furthermore the impact of interferences between the background  $gg \rightarrow \gamma\gamma$  and  $gg \rightarrow h \rightarrow \gamma\gamma$  is neglected, and will be discussed in another chapter.

The complete model of the data as well as its signal component is shown in fig. 5.11 for three different widths. From this plot it is clear that the difference of signal shape between various width hypothesis is very small in the low width regime, because the effect of the detector resolution dominates, which justifies that it is indeed safe to assume that the signal model extracted from a MC sample with  $\Gamma_H = 4$  MeV represents mainly the experimental resolution.

### 5.3.2 Comparison between different types of Breit-Wigner functions

The non-relativistic Breit-Wigner function is expressed as follows :

$$BW_{NR}(m_{\gamma\gamma}|m_H; \Gamma_H) = \frac{k}{(m_{\gamma\gamma} - m_H)^2 + \frac{1}{4}\Gamma_H^2} \quad (5.3)$$

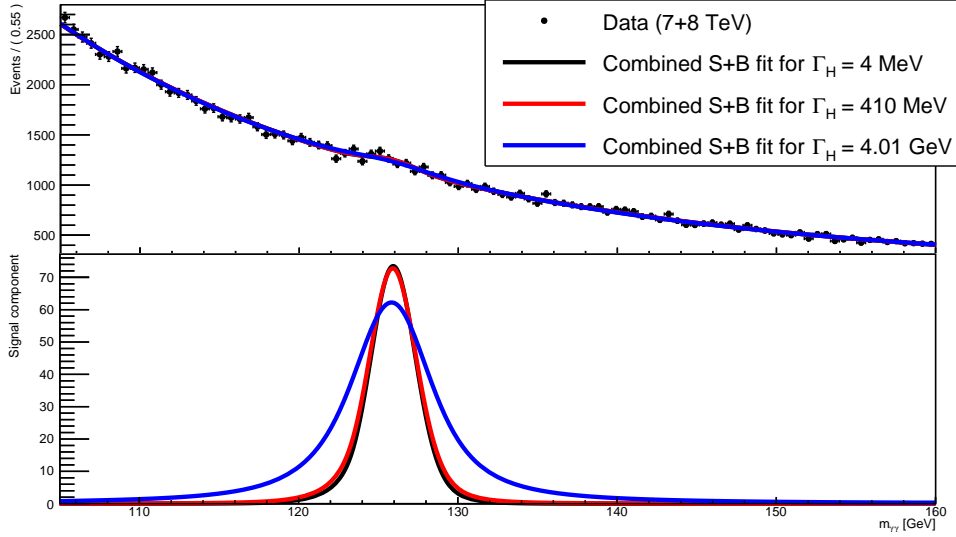


Figure 5.11: Modelling of the data (top) and of its signal component only (bottom) for three different values of the width. The data plotted in the top plot corresponds to the full Run 1 statistics

where  $k$  is a normalization factor. This is a good approximation at low width. The relativistic Breit-Wigner is :

$$BW_R(m_{\gamma\gamma}|m_H; \Gamma_H) = \frac{k'}{(m_{\gamma\gamma}^2 - m_H^2)^2 + m_H^2 \Gamma_H^2} \quad (5.4)$$

which is equivalent to the non-relativistic version for low widths. The difference between these two distributions for the Z boson may be seen in fig. 5.12, where we see that the difference between these two distributions is small and affects only its tails. For the Z boson a third type of Breit-Wigner function, which is called "improved" in fig. 5.12, exists [104] and takes into account the fact that the decay width is a running parameter. Given that there are no new decay channel opening at a threshold close to the Z boson mass pole this running is dominated by the opening of the phase space and a simple parametrization of this effect can be derived, which is not true anymore in the case of the Higgs boson as the threshold for the  $h \rightarrow WW$  and  $h \rightarrow ZZ$  are not far from the pole, in the case of a high width. This improved BW is expressed as follows :

$$BW_{improved}(m_{\gamma\gamma}|m_H; \Gamma_H) = \frac{k'' m_{\gamma\gamma}^2}{(m_{\gamma\gamma}^2 - m_H^2)^2 + (\frac{m_{\gamma\gamma}^2 \Gamma_H}{m_H})^2} \quad (5.5)$$

and in particular this is increasing the tail at high invariant mass, which is expected as it is where the phase space is the biggest.

Such an "improved" Breit-Wigner for the Higgs boson can even be "improved" more by requiring a parametrization of all the contributions to the Higgs boson propagator by having  $\Gamma_H(m_{\gamma\gamma})$  for instance in formula 5.5. As the threshold for  $h \rightarrow ZZ$  and  $h \rightarrow WW$  are not very far from the pole, it is much more complicated [105, 138]. A small study was done to assess that the difference on the limit induced by using a relativistic or a non-relativistic BW in the signal model, and is summarized by fig. 5.13. Several signal-only

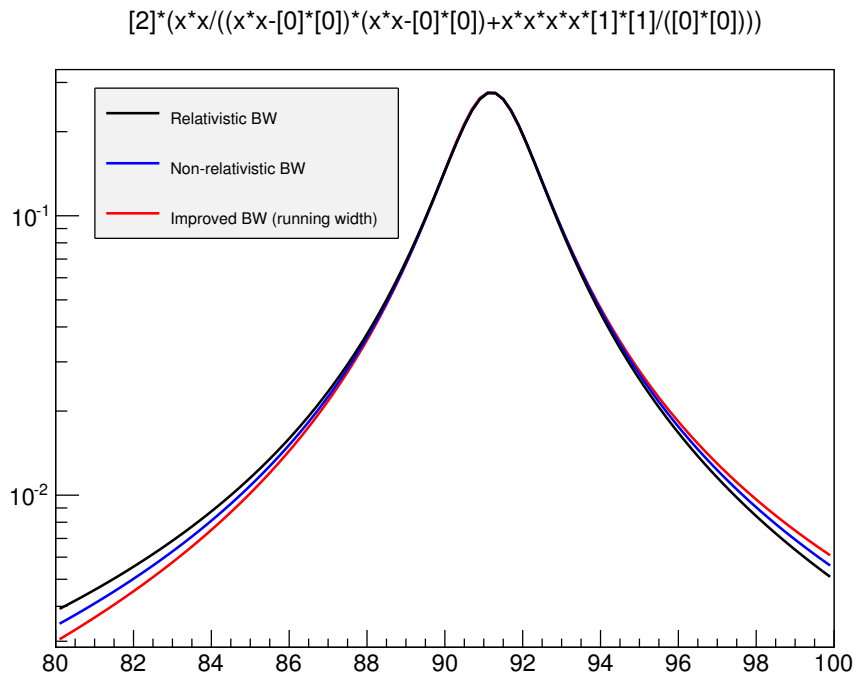


Figure 5.12: Comparison of the distribution of the invariant mass coming from various type of Breit-Wigner distributions for the Z boson

pseudo-experiments are generated at different values of the width and with a signal model based either on a relativistic or non-relativistic BW. In these toys the resolution is set to 0 and there is no background. All the toys are fitted twice, once by each of the two types of BW, and the relative difference between the best-fit value from the two fits quantifies the importance of the difference between the two types of BW. This difference is found negligible. Nine width points are tested, ranging from 1 to 9 GeV, and for each point a set of 1000 pseudo-experiments is generated. The median of the relative difference of best fit between the two types of BW represents the expected bias coming from using the wrong type of BW, and this corresponds to the content of fig. 5.13. As expected the difference between the two BWs is the smallest at low  $\Gamma$  and slowly increases with  $\Gamma$ . But it stays below 1 % up to 9 GeV, which is a fairly low bias and corresponds to a width point at the border of the range we will be testing in this analysis. Therefore we consider that it is safe to neglect the difference between these two kind of propagators.

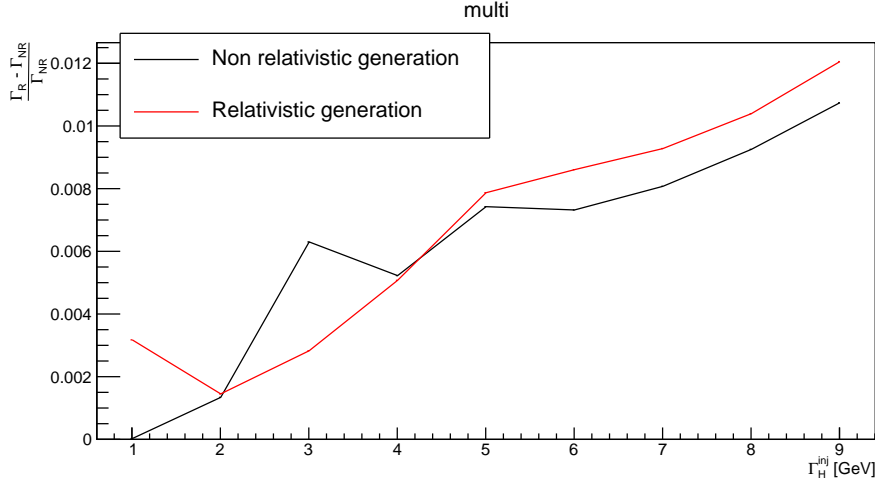


Figure 5.13: Median difference in the best fit of the width obtained between a signal model based on a relativistic or non-relativistic BW, for various value of the true width. At each width point two set of toys are generated, using either a relativistic or non-relativistic BW for the generation

## 5.4 Main results on the width

### 5.4.1 Overall description of the statistical method and problems

For the statistical model, the only difference between the Higgs boson mass measurement and the upper limit on the width is in the signal model. All the uncertainties that have been considered are the same between the two analyses, as well as the modelling of the background and the categories that have been considered. The meaning of the signal strength  $\mu$  is similar in both analyses, in the sense that it corresponds to a scale factor between the fitted number of signal events and what is expected in the Standard Model, but a model predicting a decay width modified with regard to the SM has no reason to predict the same number of events, hence it was decided to let  $\mu$  free in the fit. The Higgs boson mass  $m_H$  is also let free in the fit given that if the tested width is different from the true one the best fit of the mass may be shifted, especially given that the  $h \rightarrow \gamma\gamma$  peak lies on top of a falling background.

#### Scan of the likelihood

If we assume that the large-sample limit is valid, we can extract the upper limit on the width directly from the scan of the profiled likelihood ratio that is shown on fig. 5.14. In this scan the width is forced to be positive, as a negative value would not have any physical sense, and if we consider only the expression of the BW in eq. 5.3 allowing the width to be negative would create a degeneracy in the model. The test-statistic that is used in fig. 5.14 is the two-sided test-statistic  $\tilde{t}_\Gamma$  which is equivalent to the Feldman-Cousins test-statistic [158] (see also paragraphs 2.2 and 3.4 of [156]). It is also the one used in CMS [261] (see also the preliminary results published in [278]). In this case the upper limit on the width at 95% C.L. is obtained for a variation of the log-likelihood ratio of 3.84, which gives an observed (expected for the SM) upper limit at  $\Gamma_H = 4.4$  GeV (5.4) for the full Run 1 dataset. To quantify how much of the improvement comes from the fact that the signal

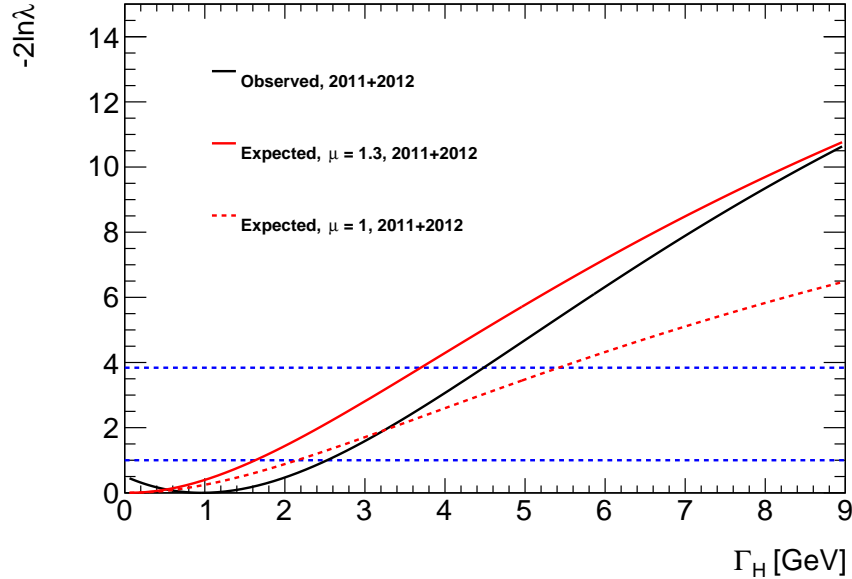


Figure 5.14: Scan of the profiled log-likelihood ratio as a function of the width. All the parameters are profiled out expect for the width, which is the only parameter of interest

strength profiled at  $\Gamma = \Gamma_{SM}$  is higher than in the SM, an expected limit was derived on an Asimov dataset generated at  $\mu = 1.3$ , which yield to an expected 95% CL upper limit of 3.8 GeV and explains part of the fact that the observed limit is stronger than expected in the SM. Furthermore the best fit of the width in the data, that corresponds to the minimum of the scan of the profiled likelihood-ratio, is at 800 MeV instead of the 4 MeV that are expected in the SM. This large fitted width is driven by the difference of  $m_H$  measured in the 2011 and 2012 dataset (see for instance chapter 7.5.2 of [89]), which effectively broadens the mass peak, and explains why the observed limit is slightly weaker than what is expected for an Asimov at  $\mu = 1.3$ .

### Checking the validity of the large sample limit

But the validity of the large-sample limit needs to be checked for. In order to do this we explicitly built the distribution of the test-statistics from toy pseudo-experiments and we will compare this distribution to the one that is expected under the large-sample limit. In fig. 5.15 the distribution of the test-statistics obtained from the pseudo-experiments is overlaid with the expectation from the asymptotic formula which is a  $\chi^2$  distribution, since the test-statistics is double-sided. The value of the test-statistics that is measured on the data and on a SM-like Asimov dataset (obtained with  $\Gamma_h = 4$  MeV) is also presented, as it allows to estimate the p-values. These toys are generated with the complete signal model that has been described above, which includes a convolution by category. The likelihood is therefore very CPU-time consuming to evaluate, which explains the limited statistics in fig. 5.15. Therefore it is hard to check by eye whether the large-sample limit is valid or not. The actual check comes from a comparison of the p-values that are obtained with these two distributions, which are computed as the integral of the test-statistic distribution for the measured value of the test-statistics up to  $+\infty$ . The statistical precision on the

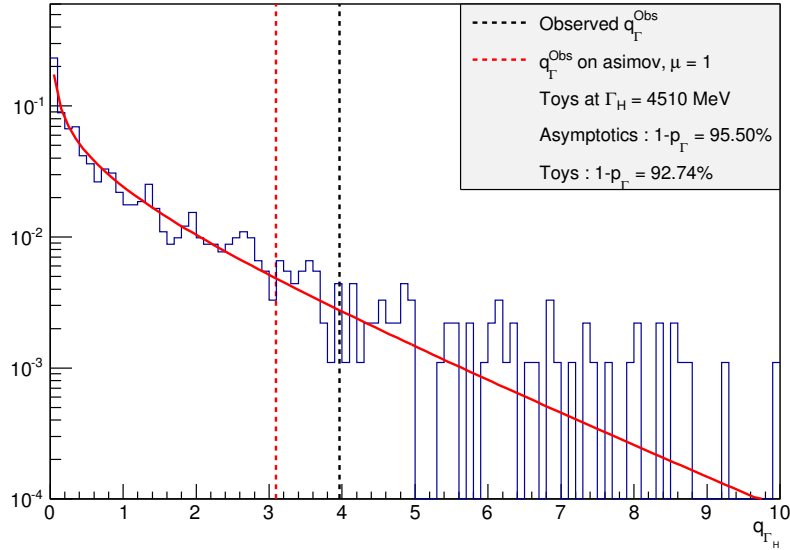


Figure 5.15: Distribution of the test-statistic obtained either from the asymptotic formulae (red curve) or from the pseudo-experiments (blue histogram), for an tested width of 4.51 GeV. The dotted lines corresponds to the value of the test-statistics. The Asimov dataset is generated with a width of 4 MeV

p-value obtained from the toys is at the level of 1% or better depending on the width that is tested, while the difference between the p-value obtained from the pseudo-experiments and the one from the asymptotic formulae is of 3% for fig. 5.15, hence it seems clear that the asymptotic formulae are not valid in our case.

Therefore the whole statistical interpretation for the width, whose results will be given below, is based on pseudo-experiments, and pseudo-experiments only. Five sets of pseudo-experiments are generated at five different width points, and each of these sets contain between 300 and 1000 pseudo-experiments. The p-value of each of the width points is computed, and the variation of the p-value as a function of the width is fitted with an exponential function, which was found out to give an accurate description of this shape. At the end the upper limit at 95% CL comes from the intercept between this exponential fit and the line defined by  $p - value = 5\%$ .

## 5.4.2 Upper limit on the Higgs boson decay width

**Published results :**  $CL_{s+b}$  and  $\tilde{t}_{\Gamma}$

The results presented below have been published in [264], and are the first direct limit on the width from the  $h \rightarrow \gamma\gamma$  channel published by ATLAS. They are based on the two-sided test-statistics  $\tilde{t}_{\Gamma}$ , and use the method described above to extract the actual upper limit at 95% CL. The observed test-statistics is evaluated on data, and all the parameters except for the width are left free during the fits. The distribution of the test-statistics extracted from pseudo-experiments is determined at five different width points, and all the distributions are shown if fig. 5.15 and fig. 5.16. In the generation of the pseudo-

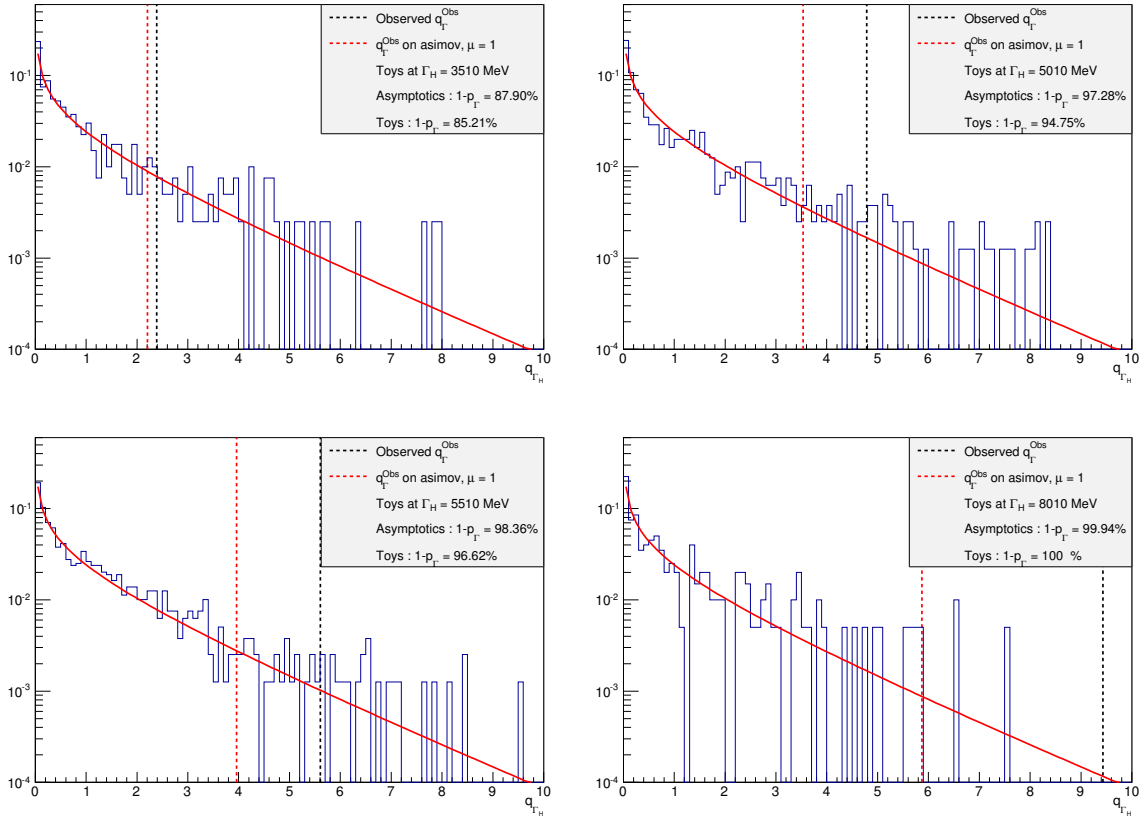


Figure 5.16: Distribution of the test statistics for different tested widths. The convention and information presented in these plots are the same than in 5.15. In the 4 plots the Asimov dataset is generated with  $\Gamma = 4$  MeV

experiments the nuisance parameters (including  $\mu$ ) are fixed at their value profiled on data for the width that is being tested, i.e. at  $\hat{\theta}(\Gamma_{inj})$ . As the generation of the pseudo-experiments is time-consuming (up to 4 CPU-days for one pseudo-experiment), we decided not to generate another set to determine the expected exclusion limit, but to re-use the distribution generated with the nuisance parameters profiled on data.

Having both the distribution of the test-statistics and its measured value allows to extract the p-values and hence the 95% CL upper limit on the width, which is shown in fig. 5.17. The p-values extracted from the toys is limited by the statistics of the generated set of toys, and this statistical uncertainty is estimated as  $\sqrt{\frac{p_{\Gamma}(1-p_{\Gamma})}{N_{toys}}}$  where  $p_{\Gamma}$  is the p-value of a given hypothesis and  $N_{toys}$  the number of pseudo-experiments generated for this hypothesis. This is shown on fig. 5.17. As the exponential fit of  $p_{\Gamma} = f(\Gamma)$  exploits the correlation that exists between the different points, it gives a sizeable reduction of this statistical uncertainty, and this is what corresponds to the dotted band in fig. 5.17, which is the  $1 \sigma$  statistical uncertainty extracted from the fit. The p-values extracted from the asymptotic formulae for the distribution of the test-statistics are also shown in fig. 5.17, and they do not have a statistical uncertainty since they come from an analytical description of the distribution. One should note that the 95% C.L. limit obtained for the expected p-value with the asymptotic formula in fig. 5.17 (5.4 GeV for  $\mu = 1$ ) is exactly the

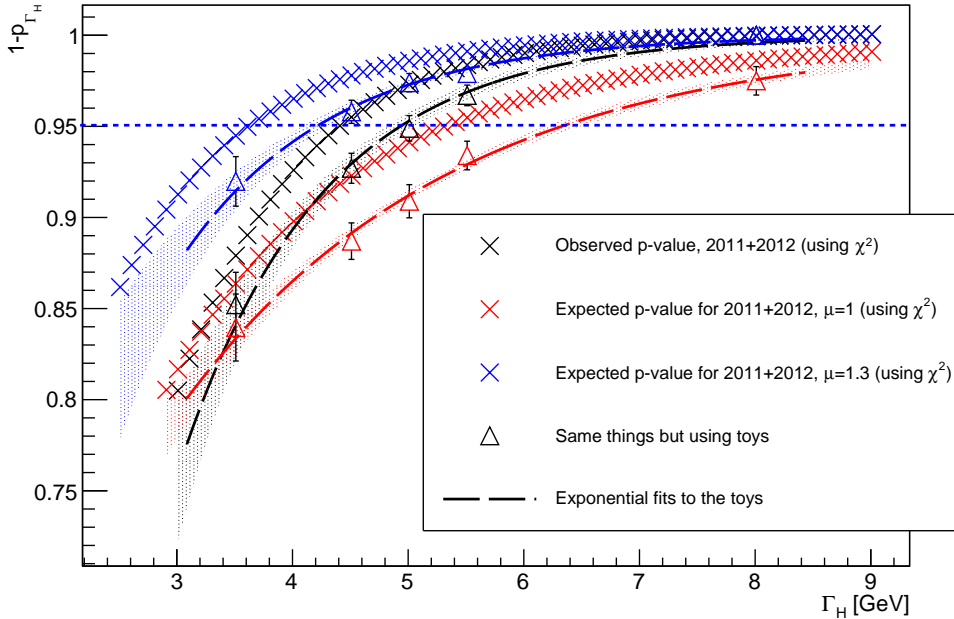


Figure 5.17: Confidence level for different width hypothesis, coming either from pseudo-experiments (see fig. 5.16) or from the asymptotic formulae. The dotted band correspond to the statistical  $1\sigma$  error band

same than the one that would be deduced from fig. 5.14 by the crossing of the likelihood curve with  $-2 \ln \lambda = 3.84$ . It is clear that the limit extracted from the toys is weaker than from the asymptotic formula, by  $\approx 15\%$ . The published value is extracted from the pseudo-experiments, and the observed 95% CL exclusion limit (expected for  $\mu = 1$  or 1.3) is at  $\Gamma_H < 5$  GeV (6.2 or 4.2).

### $CL_s$ and $p_0$

The use of the two-sided test-statistics  $\tilde{t}_\Gamma$  was motivated by the need to use the same statistical method between experiments, and between the two precision channels ( $h \rightarrow \gamma\gamma$ ,  $h \rightarrow ZZ \rightarrow 4l$ ), which allows for a proper comparison between the different results, and also by the note [279]. But this note only deals with measurement that are done near a physical limit, and not with upper limits, although it was used several time to justify the use of  $\tilde{t}_\Gamma$  in the determination of upper limits, such as in [280]. The real recommendation to set an upper limit is the use of the  $CL_s$  method [157] which should be complemented with the value of the  $p_0$  of the background hypothesis as  $CL_s$  will never be able to exclude the background. These numbers were extracted after the publication of [264], and are presented below.

The  $CL_s$  confidence level is computed as  $CL_s = \frac{CL_{s+b}}{1-p_b}$ , where  $CL_{s+b}$  is the confidence level extracted by using the one-sided test-statistics  $\tilde{q}_\Gamma$ , and  $p_b$  is the p-value of the hypothesis being tested when the pseudo-experiment is generated under the background hypothesis (which is  $\Gamma = \Gamma_{SM} = 4$  MeV in our case), therefore it requires generating another set of toys.  $p_b$  is then computed as  $p_b = \int_0^{q_\Gamma^{obs}} f(\tilde{q}_\Gamma | \Gamma = \Gamma_{SM}) d\tilde{q}_\Gamma$ , where  $f(\tilde{q}_\Gamma | \Gamma = \Gamma_{SM})$

is the distribution of the test-statistics. The toys that were generated to determine the exclusion level of fig. 5.17 are used to determine the value of  $CL_{s+b}$  although for the toys that have  $\hat{\Gamma} > \Gamma_{inj}$  the value of the test-statistics  $\tilde{q}_T$  is set to zero, which changes the actual distribution. The distribution for both the  $s+b$  and background-only pseudo-experiments is shown on fig. 5.18. The test-statistics measured on the Asimov dataset of a given hypothesis is expected to be equal to the median of the distribution of the test-statistics constructed from the pseudo-experiments generated under this hypothesis, up to potential statistical fluctuations of the nuisance parameters if they are not fixed to the value that is profiled on data during the generation of the Asimov. As the toys are generated with all the nuisance parameters profiled on data, including  $\mu$ , the proper Asimov to which the median of the toys should be compared is the one created at  $\hat{\mu}(\Gamma_{SM}) = 1.3$ , which indeed roughly corresponds to the median of the toys, as seen in fig. 5.18.

The value of  $CL_s$  extracted from these distributions is then constructed and shown on fig. 5.20. In the large sampling limit the expected 95% CL exclusion limit from  $CL_s$  is the same than the asymptotic limit of fig. 5.16, because the penalty that comes from the  $1 - p_b$  is 0.5 for the expected which exactly compensates the change from the two-sided to the one-sided test-statistics. However even if  $1 - p_b = 0.5$  the corresponding expected  $CL_s$  limit for the toys will differ from the expected  $CL_{s+b}$  limit because the change from the two-sided test-statistics to the one-sided test-statistics will not be exactly a factor 2 on toys (contrary to the asymptotics) and therefore will not exactly compensate  $1 - p_b = 0.5$ . For the observed limit since  $1 - p_b \neq 0.5$  the difference can be larger. The observed (expected at  $\mu = 1$ ) 95% CL exclusion limit is then at 5.3 GeV (7.2 GeV). Due to the broadening of the  $h \rightarrow \gamma\gamma$  mass peak induced by the statistical fluctuation between the best-fit of the mass in 2011 and 2012, the observed data were more compatible with the bigger width hypothesis than expected, hence decreasing  $p_b$ , which explains why the degradation of the exclusion limit is worse for the expected than the observed limit.

The p-value of the background hypothesis,  $p_0$ , was computed too, in order to check that the SM value of the width is not excluded by the data. This is done with the one-sided test-statistic  $q_0$  and requires to run a set of pseudo-experiments that are both generated and tested at  $\Gamma = \Gamma_{SM} = 4$  MeV, whose distribution is shown in fig. 5.21. Then the observed test-statistics  $q_0^{obs}$  is evaluated on data and  $p_0$  is obtained by integrating the distribution of  $q_0$  from its observed value up to  $+\infty$ . The measured  $p_0$  is at the level of 15% and clearly does not exclude the SM value for the width.

### Impact of the systematic uncertainties

In order to check the impact of systematic uncertainties, a cross-check was done where all the nuisance parameters associated to an uncertainty were fixed to 0, and this corresponds to what is shown in fig. 5.22. If we assume that the asymptotic formulae are valid and can be used to extract the upper limit on the width from the scan of the likelihood, the impact of the nuisance parameters on this limit is negligible. It is the biggest for the expected limit at  $\mu = 1.3$ , and changes the limit by 100 MeV, when the limit itself is at 4.4 GeV. To cross-check that it was not coming from a bug in the implementation of the uncertainty, it was decided to increase the size of the resolution uncertainty, which is expected to have the most important effect on the limit, and re-do the scan of the likelihood with the increased uncertainties, which is shown in fig. 5.23. The limit clearly worsens when this uncertainty

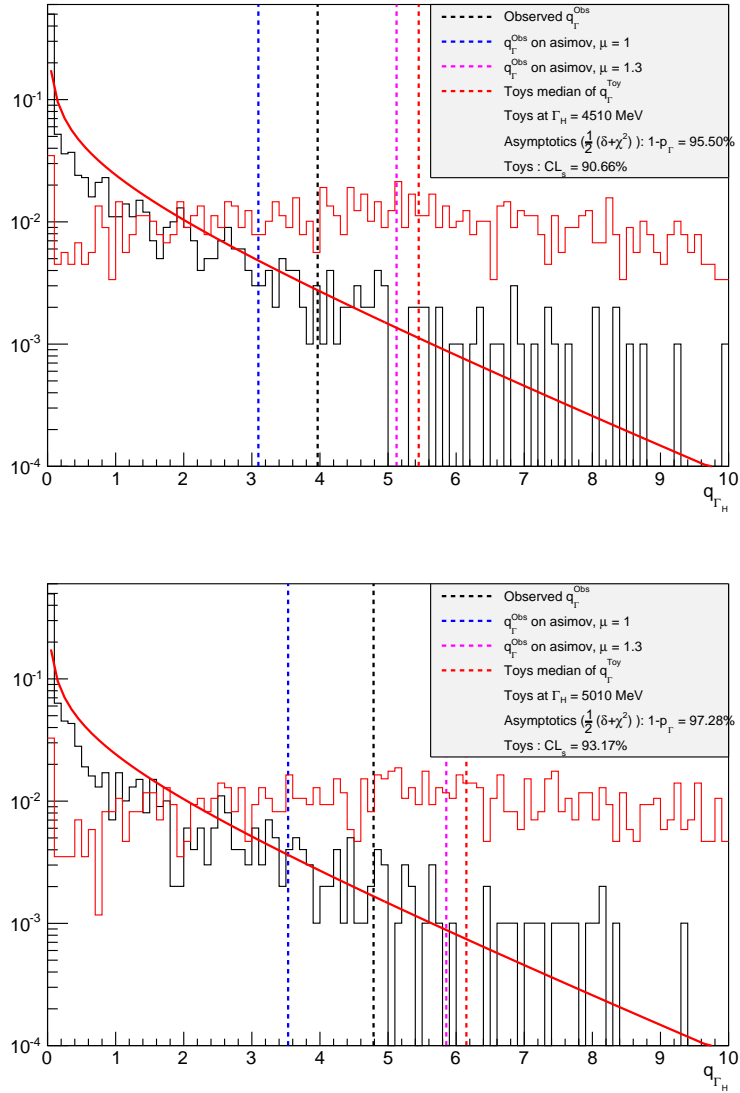


Figure 5.18: Distribution of the test-statistics from the pseudo-experiments, for the cases that are entering in the definition of  $CL_s$ . The red histogram corresponds to the background-only pseudo-experiments and the black to the  $s + b$ . The other points are shown in fig. 5.19

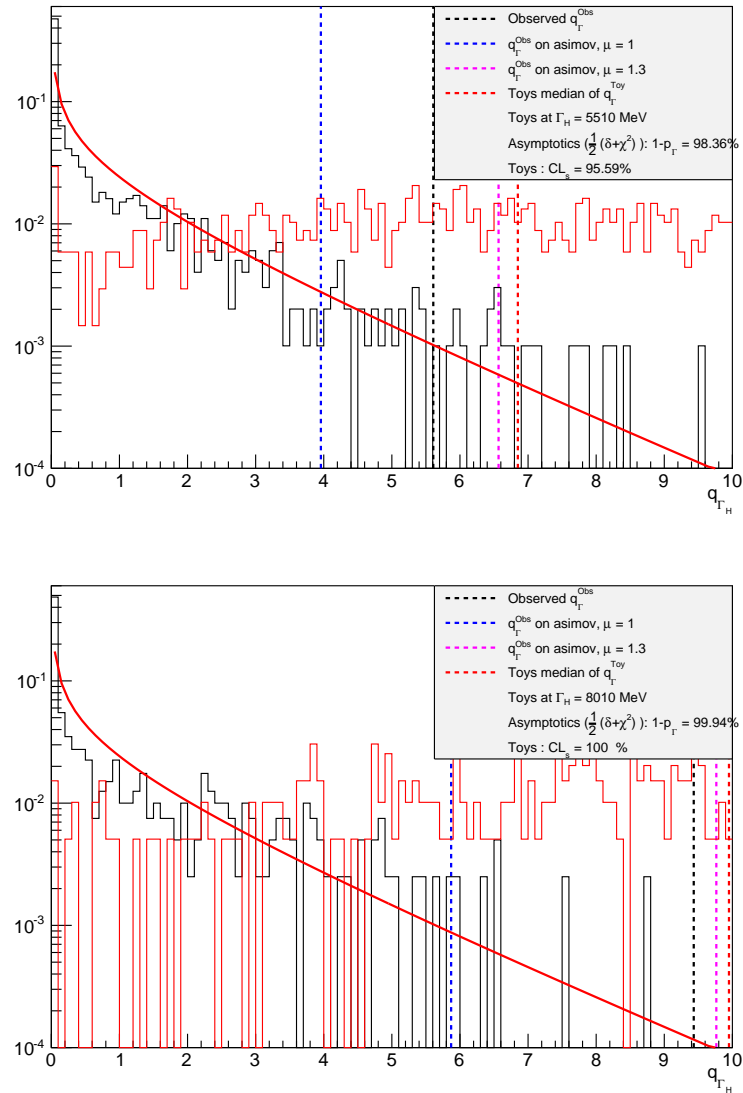


Figure 5.19: Distribution of the test-statistics from the pseudo-experiments, for the cases that are entering in the definition of  $CL_s$ . The red histogram corresponds to the background-only pseudo-experiments and the black to the  $s + b$

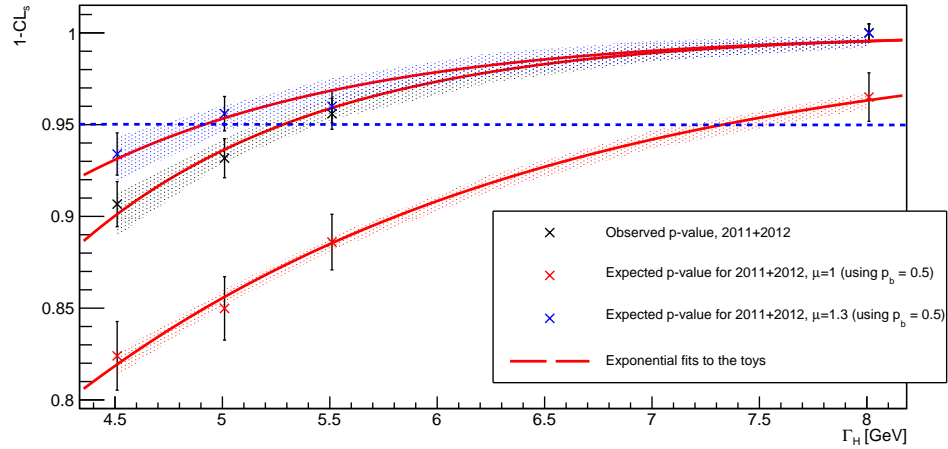


Figure 5.20: Confidence level extracted with the  $CL_s$  method and corresponding exclusion limit

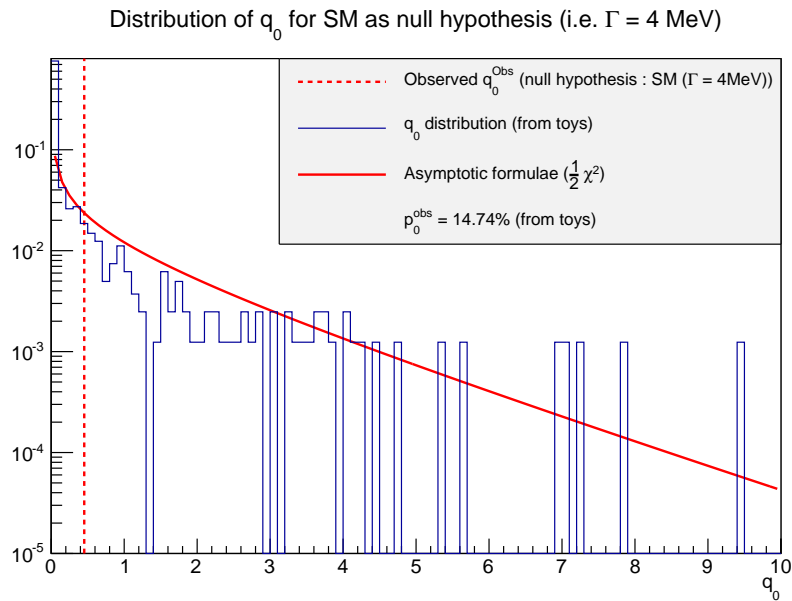


Figure 5.21: Distribution of the test-statistic  $q_0$  used to determine  $p_0$  in order to check whether the background is excluded

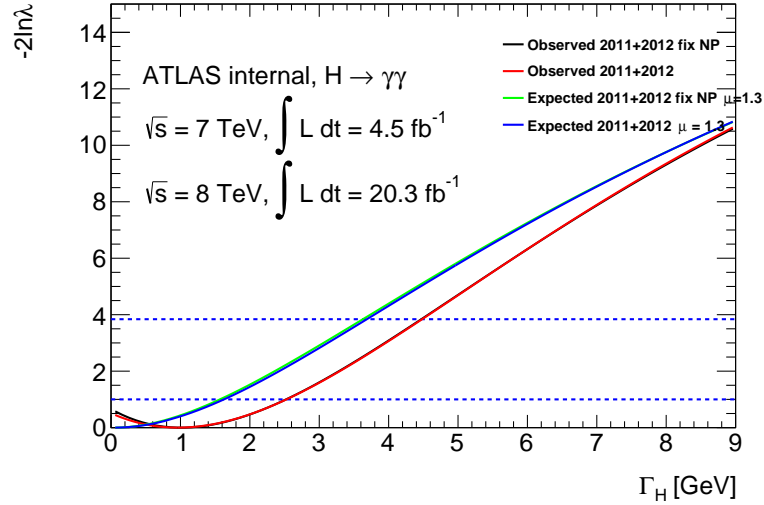


Figure 5.22: Scan of the profiled log-likelihood ratio as a function of the width, both for the data and for an Asimov generated at the observed  $\mu = 1.3$ , and with the nuisance parameters either profiled or fixed to  $\theta = 0$

is increased but it reaches a value of the limit beyond which it cannot worsen anymore, because the resolution uncertainty starts to be over-constrained by the data, as it is not possible to have a negative resolution. The fact that this limit is not sensitive to the systematic uncertainties included in the statistical model clearly shows how statistically limited this limit is.

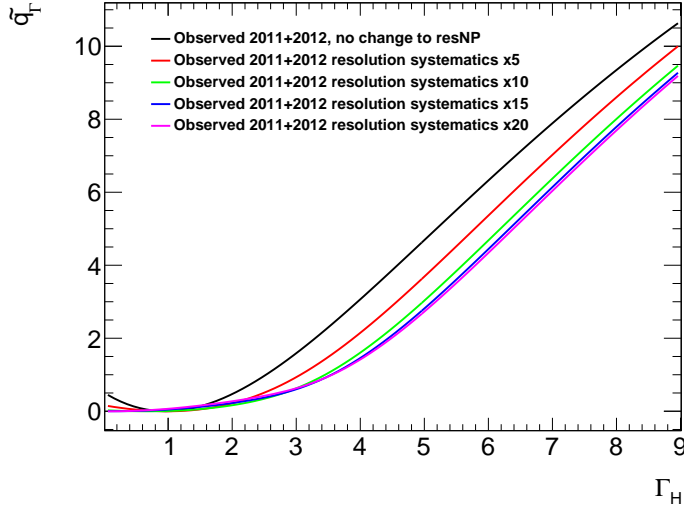


Figure 5.23: Scan of the profiled log-likelihood ratio as a function of the width on the data and for increasing values of the systematic uncertainty on the resolution

## 5.5 Checks on the observed non-asymptoticity

The fact that we were not in a case where the large sample limit is valid and that we could not use the asymptotic formulae to extract the significance of the different width hypothesis has been an important problem in this analysis. This limit was expected to be valid, because the dataset involved in the  $h \rightarrow \gamma\gamma$  analysis is fairly large, and every other analyses conducted in this channel have been able to use this approximation, even when the available statistics was much smaller, as was demonstrated in [281]. Therefore several cross-checks were conducted to insure that it was not a bug, to understand the origin of this non-asymptotic behaviour, and to try to find potential alternative asymptotic formulae.

### 5.5.1 Presentation of the problem on the full statistical model

In order to understand the origin of this non-asymptotic behaviour we still study only one value of  $\Gamma_H$ , and therefore generate toys at only this value. Furthermore, in order to check whether a specific region of  $\hat{\Gamma}$  was affected we decided not to use the usual variants of the test-statistics, but a slightly different one that clearly separates the region  $\hat{\Gamma} < \Gamma_{inj}$  and  $\hat{\Gamma} > \Gamma_{inj}$ . It is still based on profiled log-likelihood ratios but when  $\hat{\Gamma} > \Gamma_{inj}$  the test-statistics is multiply by  $-1$  and becomes  $2 \ln \lambda$ , then the region where  $\hat{\Gamma} > \Gamma_{inj}$  will have negative values of the test-statistics while they will be positive for the region where  $\hat{\Gamma} < \Gamma_{inj}$ . This will be called the uncapped log-likelihood ratio in the following, and its distribution is shown in fig. 5.24 for one width value, from which we see an asymmetry between the two sides of this test-statistics, while in case of a perfectly asymptotic behaviour we would expect that both sides follow a  $\frac{1}{2}\chi^2$  distribution. The positive side, that corresponds to a best fit of the width narrower than the one injected to generate toys, is the one that is the further away from this distribution. This also means that when we used  $\tilde{t}_\Gamma$ , where both sides are merged together, we were in fact closer to the asymptotic case than if we used  $\tilde{q}_\Gamma$

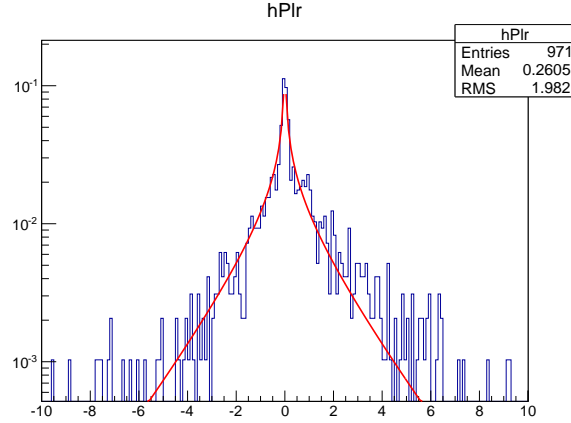


Figure 5.24: Distribution of the uncapped log-likelihood ratio from toys generated with the full statistical model at  $\Gamma_{inj} = 3.71$  GeV

as this second test would discard the region that is properly described by the asymptotic formulae.

### 5.5.2 Impact of the various nuisance parameters

In order to check that there are no problems in the implementation of the statistical model, several sets of a few hundred toys were generated at  $\Gamma_{inj} = 3.71$  GeV but with different nuisance parameters fixed during the fits, either at 0 for the nuisance parameters associated to a systematic uncertainty, or to their values profiled on data. The goal of this study is to find a parameter, or a subset of parameters, that would explain this non-asymptotic behaviour. Then the integral  $\int_{\tilde{q}_\Gamma^{low}}^{+\infty} f(\tilde{q}_\Gamma) d\tilde{q}_\Gamma$  is computed on each of these set of toys as a function of  $q_\Gamma^{low}$ , and this corresponds to the figures displayed in fig. 5.25. One can note that if we set  $\tilde{q}_\Gamma^{low}$  equal to the observed value of test-statistics on data for  $\Gamma = 3.71$  GeV, this integral directly corresponds to the p-value of the hypothesis  $\Gamma_h = 3.71$  GeV. This value may be computed from the asymptotic formulae too, and we will be able to compare in which case we recover the large-sample limit. We clearly see from fig. 5.25 that fixing the nuisance parameters associated to systematic uncertainties has no impact on the behaviour of the test-statistics, but if we fix the mass during the fit too, we then recover the behaviour that we expect under the large-sample limit. Therefore the most important parameter seems to be  $m_h$ , and more specific checks related to this hypothesis may be devised.

### 5.5.3 Cross-check on a simplified model

In order to rule out possible numerical instabilities and problems in the implementation of the model, a very simple toy model reproducing a similar experiment has been devised. It is made of a simple exponential background on top of which a Gaussian signal is added. The number of signal and background events roughly reproduced those of the  $h \rightarrow \gamma\gamma$  analysis. As this model is very simple it allows to generate a large number of pseudo-experiments, on which  $\chi^2$  fits are performed with both the resolution of the Gaussian

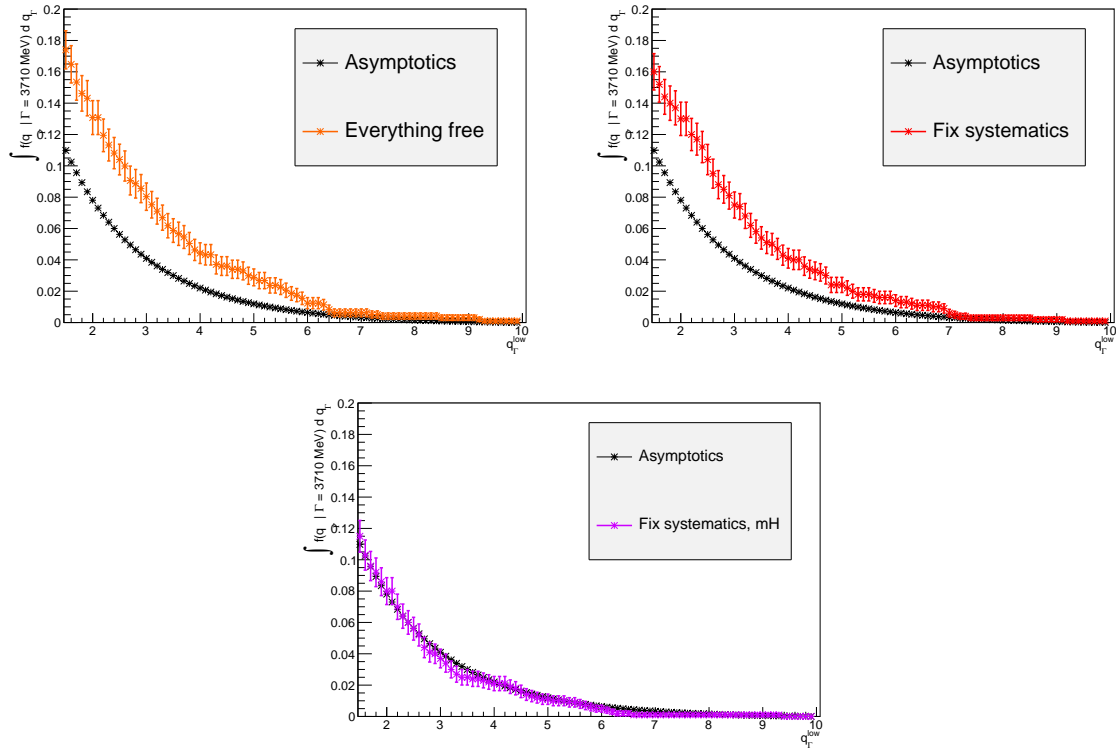


Figure 5.25: Value of  $\int_{q_{\tilde{\Gamma}}^{low}}^{+\infty} f(q_{\tilde{\Gamma}} | \Gamma = 3.71 \text{ GeV}) d q_{\tilde{\Gamma}}$  as a function of  $q_{\tilde{\Gamma}}^{low}$ , using the distribution  $f(q_{\tilde{\Gamma}} | \Gamma = 3.71 \text{ GeV})$  constructing on toys and fixing different parameters

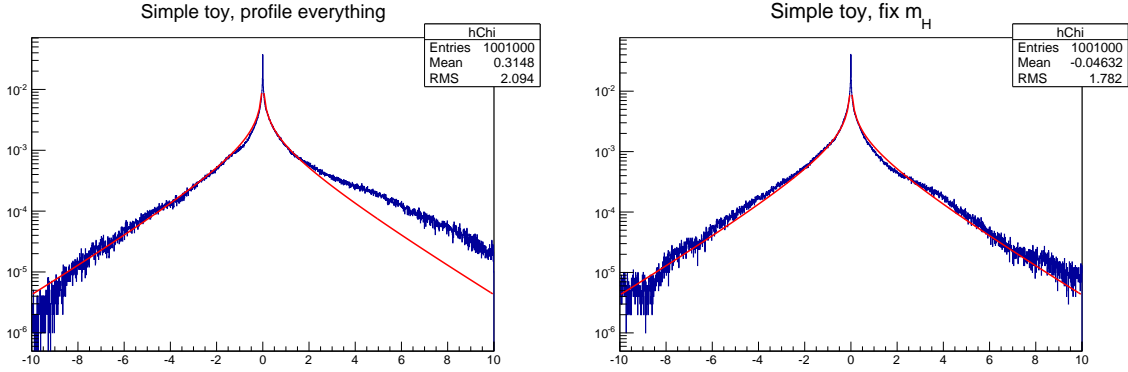


Figure 5.26: Distribution of the test-statistics  $\Delta\chi^2$  on simple toys, with one case where  $m_h$  is free in the fit (left) and the other where it is fixed (right)

fixed at its tested value or left free. The test-statistics used is then the  $\Delta\chi^2$  between these two fits, which is equivalent to the log-likelihood ratio in the case of  $h \rightarrow \gamma\gamma$  where the number of events is sufficient to consider that the distribution of the content of each bins follows a Gaussian distribution. Two sets of toys are analysed, one where  $m_h$  is left free during the fits and the other where it is fixed, and both these results are shown in fig. 5.26. These toys are well reproducing the qualitative result that we got earlier that most of the asymptotic behaviour is lost when the mass is released, and that it is indeed a statistical effect that needs to be taken into account in the analysis. Even when the mass is fixed the distribution of the test-statistics is not perfectly asymptotic, but it is much closer to what is expected and it would be sufficiently close to actually use the asymptotic formula in this analysis.

#### 5.5.4 Comparison with the $h \rightarrow ZZ^* \rightarrow 4l$ channel

Once the non-asymptotic behaviour of the test-statistics was observed in the  $h \rightarrow \gamma\gamma$  channel, the same cross-check was asked for the  $h \rightarrow ZZ^* \rightarrow 4l$  channel, where the distribution of the test-statistics coming from the toys was shown to be very close to what is expected from the asymptotic formula, as may be seen in fig. 5.27. There are important differences between the two channels, but only two were believed to be important in this comparison, the first one being the difference of background which is much smaller and flat for the  $h \rightarrow 4l$  decay channel, and the second is the difference of significance that comes from the fact that the best fit of  $\mu$  in the  $4l$  channel is very high (1.7) [264, 282] yielding a higher signal significance ( $\approx 8$  for  $h \rightarrow ZZ^* \rightarrow 4l$  and  $\approx 5$  for  $h \rightarrow \gamma\gamma$ ). Using the simple toy model described in subsection 5.5.3 we were able to check both these hypotheses. First the exponential background was replaced by a flat function, while the significance was kept unchanged at  $\approx 5$ , and we observed that the non-asymptotic behaviour remained. In a second step the number of signal events was changed in order to keep  $\frac{S}{B}$  constant and increase  $\frac{S}{\sqrt{B}}$  to the value corresponding to the one of the  $4l$  channel. In this latter case the distribution of  $\Delta\chi^2$  from toys properly matched the one from the asymptotic formulae, and it was further checked that at constant  $\frac{S}{\sqrt{B}}$  the impact of varying  $\frac{S}{B}$  was only mild (while we were still in a regime where  $\chi^2$  fits are valid).

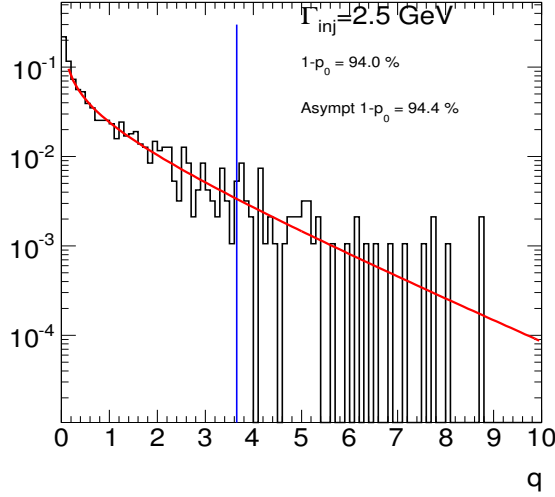


Figure 5.27: Distribution of the test-statistics for the width, constructed from toys in the  $h \rightarrow ZZ^* \rightarrow 4l$  decay channel [283]

### 5.5.5 Look-elsewhere effect and the Leadbetter formula

At the time of the discovery of the BEH boson a similar problem had been observed and is described precisely in [284, 285]. In summary, during the preparation of the statistical method to be used for the BEH boson searches it had been noticed that letting the mass free in the fits needed to evaluate  $q_0$  creates a departure from the asymptotic formulae for  $q_0$ , whose reason will be explained below. The solution was to fix the mass in the fits, and evaluate  $q_0$  at different masses. The distribution of  $q_0$  was then asymptotic at each mass point, and a local  $p_0$  was quoted separately for each of these points, and the global  $p_0$  was then determined using the method of Trial Factors that is defined in [286]. For the discovery, the energy scale uncertainties were included in the model. This consists in the following modification :  $m_h \rightarrow m'_h = m_h(1 + \delta\theta)$  where  $\theta$ , although it is constrained by a Gaussian, is a free parameter. This means that even if  $m_h$  is fixed in the fit the parameter  $\theta$  and therefore  $m'_h$  can still move, hence the distribution of  $q_0$  will not follow perfectly the asymptotic formulae although it is a small deviation. Such a scenario was studied by Leadbetter in [287] where a modified asymptotic formula was derived to deal with such cases. This formula adds an exponential component to the usual  $\chi^2$  formula, where the slope of the exponential is 1/2 and the exact fraction of exponential and  $\chi^2$  depends on the specific problem. The origin of the problem comes from the definition of the parameters of the statistical model : the asymptotic formulae assume that all the parameters are well defined under all the tested hypotheses, but in the case of a discovery the mass is not defined under the background hypothesis, as there should be no mass peak. In such a case the best-fit can correspond to any statistical fluctuation that happens in the fit range, and not only to the fluctuation that are happening at a specific point, hence there are more statistical fluctuations than what is described by the asymptotic formulae. In the Leadbetter formula the fluctuations that may be chosen by the fit are limited by the Gaussian constraint, and the further away the fluctuations are from the mass point that is being tested, the bigger they need to be to overcome the penalty from

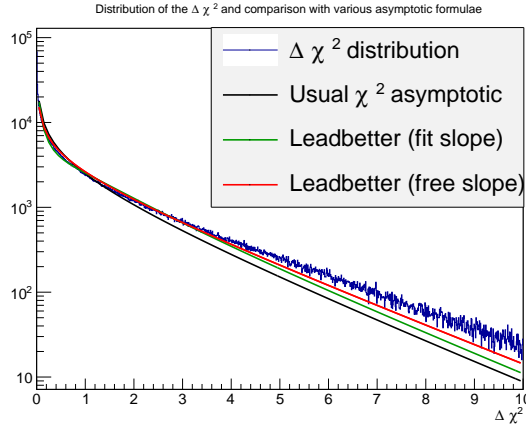


Figure 5.28: Distribution of the test-statistics  $\Delta\chi^2$  constructing on simple toys, and comparison with the usual asymptotic formula and with the Leadbetter formula

the constraint. It is not obvious that this explanation is still valid in the case of the upper limit on the width, as the background hypothesis is then  $\Gamma_{SM}$  and the mass is still a well defined parameter under this hypothesis, but given that fixing the mass gives a sizeable improvement in the distribution of  $q_\Gamma$  it could be a possible explanation. A comparison between the distribution extracted from the toys and the Leadbetter formula is shown in fig. 5.28. There is a clear improvement with respect to the usual  $\chi^2$ . As a cross-check it was tried to fit the slope of the exponential in the Leadbetter formula too, to verify that it indeed had the proper value of  $1/2$ , and we can see that it is not exactly the case although the fit is essentially driven by the region at low  $\Delta\chi^2$ . When the slope is fixed at its nominal value the description of the tail at high  $\Delta\chi^2$  is much better. This explanation also gives a reason why a higher significance improves the asymptotic behaviour, as the existence of the exponential component describes the possibility of fitting statistical fluctuations in the neighbourhood of the mass peak, but the more significant the peak becomes the less likely it is to find a statistical fluctuation that is at least as significant.

## 5.6 Impact of the resolution and comparison with CMS

### 5.6.1 Variation of the limit as a function of the resolution

As setting an upper limit on the width essentially consists in studying how broad the  $h \rightarrow \gamma\gamma$  mass peak is, we expect that the parameter that impacts the most the performance of the analysis is the resolution, and this was qualitatively cross-checked on a simplified model. This model consists in a simple exponential background, and a Voigtian signal. The Voigtian corresponds to an analytical implementation of the convolution of a Gaussian with a non-relativistic Breit-Wigner [276] and is therefore a powerful tool to make a simple modelling of the signal that has statistical and physical properties that are close to the full model. The width of the Breit-Wigner of the Voigtian is fixed to 4 MeV while its resolution is progressively varied from 250 MeV to 4 GeV, by steps of 250 MeV. At each

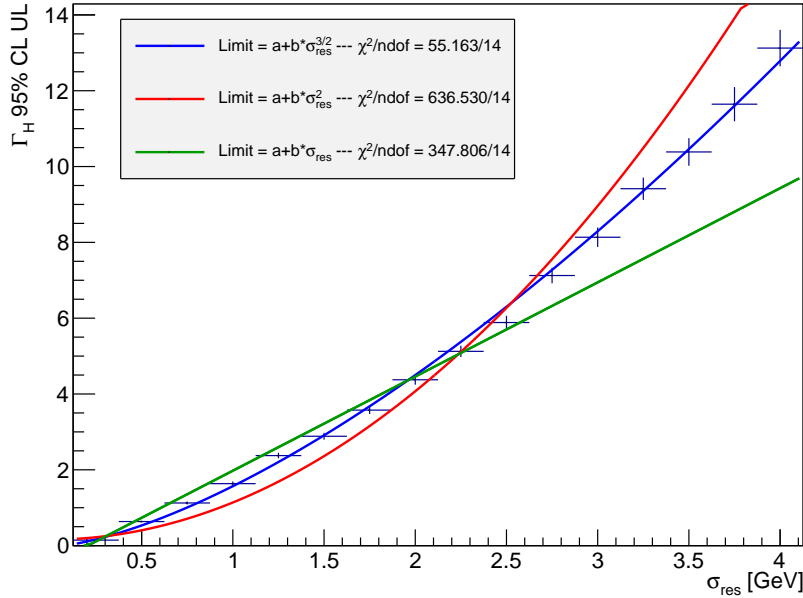


Figure 5.29: Value of the median 95% CL upper limit determined with the asymptotic formulae on 100 toy pseudo-experiments, for various values of the resolution

point a set of 100 pseudo-experiments are generated, and for each of these toys a 95% C.L. upper-limit on the width is determined from a scan of the profiled log-likelihood ratio, which is done by steps of 250 MeV. The median of the distribution of the upper limits is considered as being the most representative value for the limit for a given value of the resolution, and is displayed in fig. 5.29. As expected the exclusion limit worsens when the resolution is degraded, and a few simple polynomials have been tried to parametrize this variation. The best description is given by a power  $\frac{3}{2}$  of the resolution, i.e.  $\Gamma_{UL}^{95\% CL} \propto \sigma_{res}^{3/2}$ . A similar result was obtained for the mass measurement where, for a simple model, it is shown (see subsection 5.1.3) that the statistical uncertainty on  $m_h$  increases as a power  $\frac{3}{2}$  of the resolution. It is possible to adapt this demonstration for the case of the width. Both of these calculations have been outlined in appendix B. The same study can be done to estimate the dependency of the upper limit on the signal to noise ratio, which is summarized by fig. 5.30 where the dependency is shown to be in  $\Gamma_{UL}^{95\% C.L.} \propto \frac{1}{(S/B)^{0.3}}$ .

Although the computation sketched in appendix B also gives the dependency of the limit on  $S$  and  $B$  it is harder to translate it in a variation with respect to  $S/B$  than it was to translate it in a dependency with respect to the resolution. Indeed the different terms involved in the final expression of the limit are not exact powers of  $S/B$  while they were exact powers of  $\sigma_{res}$ , and therefore the exponent determined in the fit of fig. 5.30 cannot be compared to a value determined analytically.

### 5.6.2 Upper limit on the width from the CMS collaboration

As the upper limit on the width degrades very quickly when the resolution worsens, extracting categories that have a higher resolution matters even more than in a typical

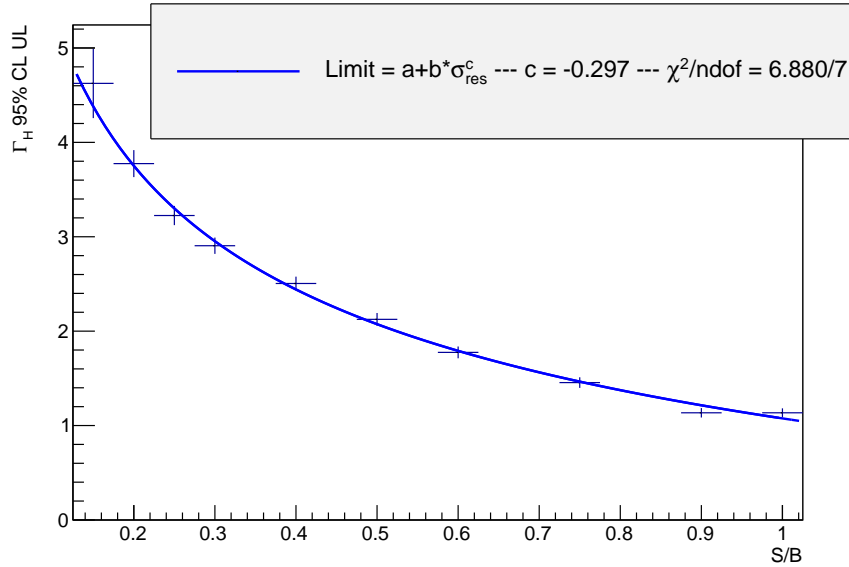


Figure 5.30: Value of the median 95% CL upper limit determined with the asymptotic formulae on 100 toy pseudo-experiments, for various values of the the signal to background ratio

analysis. This is also the case in the mass measurement, and for both of these analyses it is in fact the two or three best categories that will drive the measurement. The CMS  $h \rightarrow \gamma\gamma$  analysis is extensively based on multi-variate techniques, and a per-event estimation of the resolution enters in both the MVA used for the selection of the events and for their categorization. Effectively this allows to remove regions that have a low resolution already during the selection, for instance the high- $\eta$  region of the end-cap ( $|\eta| > 2$ ), where the radiation-induced degradation of the resolution had a bigger impact, is almost completely removed [261]. The variation of the resolution inside the CMS detector is larger than in ATLAS, which means that the resolution of the inclusive signal peak is slightly better in ATLAS, as may be seen from fig. 5.31, but for its best categories CMS is able to extract classes of events that have a better resolution than the best categories ATLAS can define, as can be shown from table 5.2, where the parameters of the untagged categories are shown. CMS also uses categories that isolates specific production modes although they are expected to have only a mild impact for the width and mass analysis, and should mainly matter for the Higgs boson couplings measurement. For the two experiments the best category isolates central and boosted di-photon pairs, where both the resolution and signal-to-background ratio are the best, but the resolution for this central part of the detector is better in CMS than in ATLAS, which explains why the CMS result is better [271], with an observed 95% CL upper limit (expected) at 2.4 GeV (3.1 GeV), and also why the CMS statistical uncertainty on the mass is smaller, at 0.31 GeV instead of 0.42 GeV for ATLAS [264].

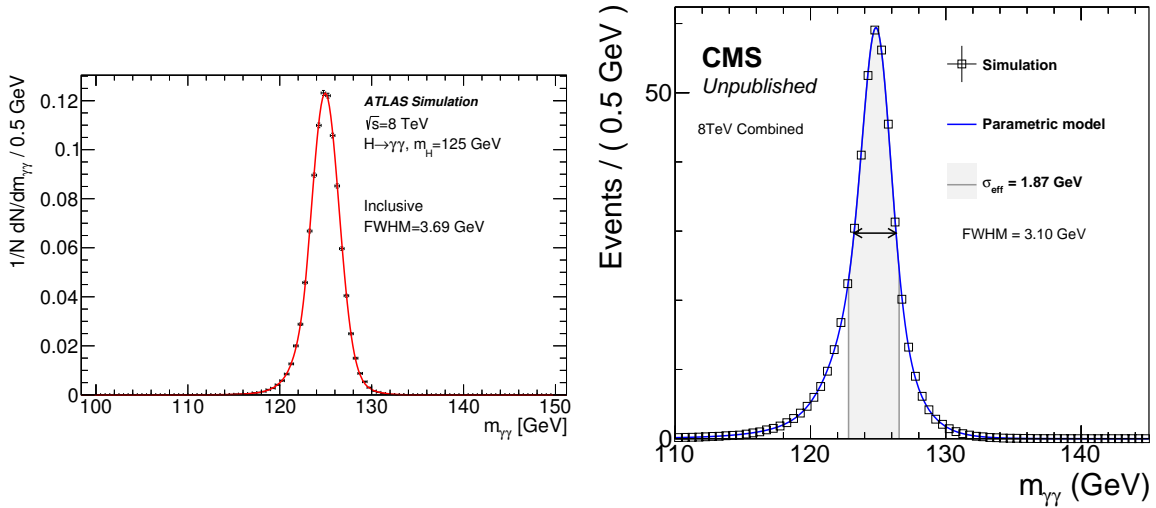


Figure 5.31: Inclusive di-photon mass distribution and its corresponding signal model for ATLAS (left) [264] and CMS (right) [261], for the 8 TeV samples. The effective resolution  $\sigma_{eff}$ , defined in table 5.2, is 200 MeV better in ATLAS (1.67 GeV) than in CMS (1.87 GeV)

Category	$n_{sig}^{exp}$	$\sigma_{eff}$ [GeV]	$\frac{S}{B}$ in signal region
CMS			
Untagged 0	6.0	1.05	0.42
Untagged 1	50.8	1.19	0.12
Untagged 2	117.	1.46	0.07
Untagged 3	153.	2.04	0.03
Untagged 4	121.	2.62	0.01
ATLAS			
Unconverted central low $p_{T_t}$	59.3	1.35	0.07
Unconverted central high $p_{T_t}$	7.1	1.21	0.25
Unconverted rest low $p_{T_t}$	96.2	1.53	0.03
Unconverted rest high $p_{T_t}$	10.4	1.36	0.10
Unconverted transition	26.0	1.86	0.03
Converted central low $p_{T_t}$	37.2	1.52	0.06
Converted central high $p_{T_t}$	4.5	1.35	0.19
Converted rest low $p_{T_t}$	107.2	1.88	0.03
Converted rest high $p_{T_t}$	11.9	1.64	0.07
Converted transition	42.1	2.41	0.02

Table 5.2: Some parameters for the performance of the mass and width analysis in the  $h \rightarrow \gamma\gamma$  channel, taken from [261] for CMS (for some categories) and [264] for ATLAS. Only the numbers for the 8 TeV datasets, which carries most of the statistical power, are quoted here.  $\sigma_{eff}$  correspond to half of the smallest range containing 68.3% of the events. For CMS, S/B is computed in  $\pm\sigma_{eff}$  while for ATLAS it is computed in the window containing 90% of signal events

# Chapter 6

## Interferences between $gg \rightarrow h \rightarrow \gamma\gamma$ and $gg \rightarrow \gamma\gamma$

### Contents

---

<b>6.1</b>	<b>Monte-Carlo generation of interferences</b>	<b>208</b>
6.1.1	Precision of the Sherpa 2 computation	208
6.1.2	Implemented Higgs boson propagator	209
6.1.3	Cross-check of the output cross-sections	209
6.1.4	Reweighting of the cross-section to the Standard Model	211
<b>6.2</b>	<b>Detector effect folding</b>	<b>212</b>
6.2.1	Simulation of photon conversions	212
6.2.2	Identification and reconstruction efficiencies	212
6.2.3	Implementation of the mass resolution	213
<b>6.3</b>	<b>Parton shower tuning</b>	<b>215</b>
6.3.1	Principle of the optimization	215
6.3.2	State of the art description of the Higgs boson $p_T$ distribution	216
6.3.3	Results for the tuning	216
<b>6.4</b>	<b>Impact of interferences on the measurement of <math>m_h</math></b>	<b>221</b>
6.4.1	Generation of pseudo-Asimov datasets	221
6.4.2	Main results on the mass shift	221
6.4.3	Systematic effects affecting the mass shift	224
6.4.4	Results by categories	226
6.4.5	Conclusions	228

---

All the results produced in the  $h \rightarrow \gamma\gamma$  channel during the first Run of the LHC, in both ATLAS and CMS, had an improper treatment of the interferences that exists between the main signal process ( $gg \rightarrow h \rightarrow \gamma\gamma$ ) and the  $gg \rightarrow \gamma\gamma$  background process. Only their impact on the total yield was taken into account, as it is expected that interferences decrease the total cross-section of  $\approx 2\%$  [110, 227]. But it is also expected that the

interference sizeably modifies the di-photon invariant mass distribution, as was initially noticed in [111], and as may be seen in fig. 1.14. This was neglected as no Monte-Carlo were available to study this effect. This became available at the end of 2013 with the release of Sherpa 2 [288] in which a specific "plug-in" implemented the computation that had been published a few month earlier in [112]. This chapter will present a study that aimed at understanding the actual content of this plug-in, how it should be configured, and how to generate samples that may be used in physics analyses in the future. In addition to [111] and [112] several theory papers where published recently on the  $h \rightarrow \gamma\gamma$  mass shift induced by the interferences [111, 113, 116] (see also a rough prospective study in ATLAS [289]).

## 6.1 Monte-Carlo generation of interferences

### 6.1.1 Precision of the Sherpa 2 computation

The interference plug-in of Sherpa 2 is an implementation of the computation published in [112], which is itself based on a NLO computation of the signal and on the NLO computation of the  $gg \rightarrow \gamma\gamma$  background that was published in [114], and therefore the interference term is itself computed at NLO too. There are some subtleties to take into account in this description : in the interference one need to match signal and background diagrams that have the same initial and final states, and at the LHC this corresponds mostly to processes that are initiated by two gluons and have two photons in the final state. But there is also a non-negligible part coming from processes initiated by one quark and one gluon where the quark may emits one gluon, which will interact with the initial state gluon to create one Higgs by gluon fusion (see section 1.5 and figure 1.13). For the signal this is a NLO diagram of gluon fusion but a similar background process can arise as a tree level diagram, where the initial quark will absorb one gluon, and then emit two photons by bremsstrahlung, and there is only one gluon in this process. For the gluon-gluon initiated process it has been possible to interface the Sherpa event generation of interferences with a Parton Shower that mimic the impact of higher order parton emission, although it only modifies the momentum distribution of the initial and final state partons. For the leading order quark-gluon interference processes this has not been possible, and it is not obvious why, although it probably comes from the fact that the total interference cross-section for the quark-gluon initiated part is 0 at leading-order, as may be seen in fig. 1.14. This is not a problem when we are interested in the inclusive distributions, as it has been checked that this problem was neither impacting the total cross-section nor the invariant mass spectrum, but it is a sizeable problem when we are interested in the  $p_T$  spectrum as we have been for the  $m_h$  and  $\Gamma_h$  analyses, or as it was proposed to do in order to infer an upper limit on the width in [112]. Furthermore it will be shown below that even for the gluon-gluon initiated processes the inclusion of the Parton Shower creates a sizeable dependency on the parton shower resummation scale, and is therefore also a problem for analyses that rely on the description of the  $p_T$  spectrum.

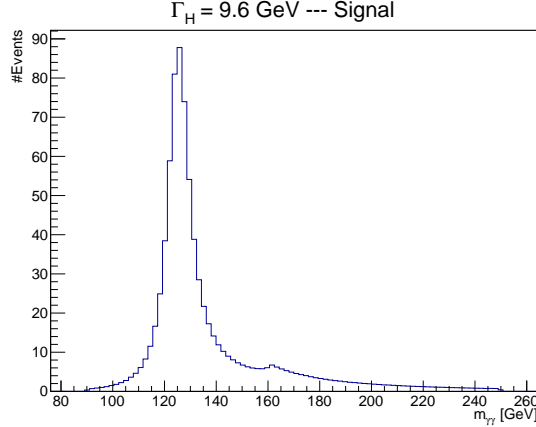


Figure 6.1: Di-photon mass distribution from  $gg \rightarrow h \rightarrow \gamma\gamma$  events generated by Sherpa 2 for  $\Gamma_h = 9.6$  GeV

### 6.1.2 Implemented Higgs boson propagator

Close to the pole and in the low mass regime it is not possible to differentiate between the various type of propagators that may be used to describe the Higgs boson. The invariant mass distribution of the di-photon pair in  $gg \rightarrow h \rightarrow \gamma\gamma$  events is displayed in fig. 6.1 and does not correspond at all to the Breit-Wigner distribution that is naively expected for the decay of a resonance, especially not in the high invariant mass tail where a small bump appears at  $\approx 160$  GeV ( $\approx 2m_W$ ). In fact in this module of Sherpa the total width of the Higgs boson is kept constant at its input value  $\Gamma_h$ , while the exact dependence of the partial decay width of  $h \rightarrow \gamma\gamma$  on  $m_{\gamma\gamma}$  has been implemented. This partial width is expressed as follows [102] :

$$\Gamma(h \rightarrow \gamma\gamma) = \frac{G_\mu \alpha^2 m_h^3}{128\pi^3 \sqrt{2}} |A_1^H(m_{\gamma\gamma}) + \sum_f N_c Q_f^2 A_{1/2}^H(m_{\gamma\gamma})|^2 \quad (6.1)$$

where  $A_1^H$  and  $A_{1/2}^H$  are two well defined complex function whose imaginary part is 0 below the kinematical threshold of the W (for  $A_1$ ) or of the top (for  $A_{1/2}$ ). These two functions can be computed [102], but given that the most problematic feature in fig. 6.1 happens at the  $2m_W$  kinematic threshold we are only interested in the evolution of  $A_1^H$ , which is displayed in fig. 6.2. The strong variation of  $A_1^H$  at  $m_{\gamma\gamma} = 2m_W$  explains the additional bump that is seen at this mass on the di-photon invariant mass spectra, as there is a strong change in the trend of the partial decay width at this point that is not compensated by the total decay width, which is constant. Furthermore the increase of the partial width as  $m_h^3$  also explains the stronger tail at high invariant mass than what is naively expected from a Breit-Wigner distribution. For the description of the mass shift we are interested in the description of the mass lineshape near the pole and therefore are not sensitive to the exact modelling of the tails of the distribution.

### 6.1.3 Cross-check of the output cross-sections

The cross-section predicted by Sherpa 2 has been cross-checked against state-of-the-art NLO computations, and this comparison is summarized in table 6.1. It is slightly higher

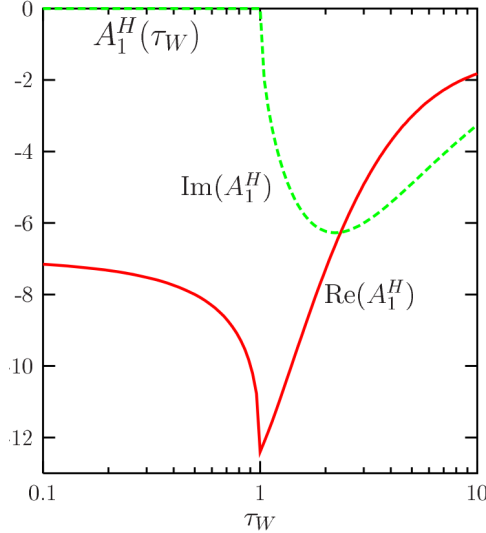


Figure 6.2: Variation of the  $A_1^H$  function that is ruling the evolution of the  $h \rightarrow \gamma\gamma$  partial decay width [102]. The variable  $\tau_W$  is defined as  $\tau_W = \frac{m_{\gamma\gamma}^2}{(2m_W)^2}$  hence is equal to 1 at the  $2m_W$  kinematical threshold

	Sherpa 2.0.0	HNNLO	Yellow Report
$\sigma \times BR$ (in $fb$ ) for $gg \rightarrow H \rightarrow \gamma\gamma$	$32.005 + / - 0.002$	$30.27 \pm 0.01$	$30.65 \pm 0.01$

Table 6.1: Comparison between results from Sherpa 2, HNNLO at NLO [290], and NLO results from Yellow Report 3 [81]

than the output of HNNLO at NLO and of the NLO results quoted in the Yellow Report [81], by  $\approx 6\%$ . This corresponds to the expected difference [81] between the NLO computation done with only the top loop in the infinite mass limit, which is implemented in Sherpa 2, and with the bottom and top loop treated in the finite mass scheme, as it is used in HNNLO or in the Yellow Report. As the signal cross-section will be rescaled to the state-of-the-art signal NNLO cross-section which is computed in the Yellow Report [81], which gives a k-factor of 1.45, it is not a problem. An uncertainty of  $\pm 10\%$  is taken on this k-factor, which corresponds to the combination of the PDF and  $\alpha_s$  uncertainties for the NNLO computation. The square-root of this k-factor will also be applied on the interference term, and this uncertainty propagated to the interference template.

For the  $gg \rightarrow \gamma\gamma$  background, no computation exists beyond NLO and it is not possible to quote an estimate of the background k-factor. The gluon fusion signal produces harder radiations than the background, because the top quarks in the gluon fusion triangle are heavier than the light quarks in the  $gg \rightarrow \gamma\gamma$  box which explained why LO to NLO background k-factor was smaller for the background than for the signal, and it is expected that the same argument is valid for the NLO to higher orders k-factor. We decided to vary  $k_B$  between 1 and 2, and to quote this variation as an error on the interference template to which the square-root of the background k-factor is applied as a scaling factor. As the description of the background part itself will be taken from an analytic fit to the data, it is not needed to apply this k-factor to the background itself.

### 6.1.4 Reweighting of the cross-section to the Standard Model

An increase of the Higgs boson width can only happen in a new physics scenario, and depending on the scenario one is considering it may happen in different ways : it can either modify the gluon fusion (and the  $h \rightarrow \gamma\gamma$  decay one also, even if its impact is probably negligible) loop, or just create a new decay channel that has a sizeable decay width and does not modify the loops. Within Sherpa the second scheme has been chosen : the  $h \rightarrow \gamma\gamma$  partial width is left constant while the total width is varied, which gives a scaling of the  $h \rightarrow \gamma\gamma$  branching ratio as the inverse of the width that is propagated to the cross-sections  $gg \rightarrow h \rightarrow \gamma\gamma$  that Sherpa gives as an output. In this analysis we do not want to depend on the total cross-section but only on the lineshape of the Higgs boson, and therefore we need to apply an additional weight to rescale this total cross-section to the Standard Model. This scaling can be derived [112] within the  $\kappa$  framework used for the couplings [99], which only assumes the tensor structure of the Standard Model which implies that every couplings may only be rescaled by a scalar. The Feynman diagrams in which we are interested are shown in fig. 1.13, and if we decide to treat these diagrams in the effective theory where the  $\kappa_g, \kappa_\gamma$  are not resolved we can derive a rescaling of these diagrams in order to keep the total signal plus interference cross-section constant. The signal cross-section gets rescaled as  $S = \frac{\kappa_g^2 \kappa_\gamma^2}{\Gamma_h / \Gamma_h^{SM}} S_{SM}$  and the interference cross-section as  $I = \kappa_g \kappa_\gamma I_{SM}$ . If we denote  $c_{g\gamma} = \kappa_g \kappa_\gamma$  it is possible to derive a way to determine  $c_{g\gamma}$  from the fact that we want to keep constant  $S + I = S_{SM} + I_{SM}$ , which is done in this way :

$$c_{g\gamma}^2 \sigma_S^{sherpa}(\Gamma_h) + c_{g\gamma} \sigma_I^{sherpa}(\Gamma_h) = \sigma_S^{sherpa}(\Gamma_h^{SM}) + \sigma_I^{sherpa}(\Gamma_h^{SM}) \quad (6.2)$$

where  $\sigma_{S,I}^{sherpa}(\Gamma_h)$  corresponds to the total  $gg \rightarrow \gamma\gamma$  cross-sections that are determined by Sherpa for a given width, and this equivalent to equation 6 of [112]. The cross-sections above are the mass integrated cross-sections and we have  $\sigma_I^{sherpa}(\Gamma_h) = \sigma_I^{sherpa}(\Gamma_h^{SM})$  while  $\sigma_S^{sherpa}(\Gamma_h) = \sigma_S^{sherpa}(\Gamma_h^{SM}) \frac{\Gamma_h^{SM}}{\Gamma_h}$ . Another way to look at this problem is to think to a fit of a differential cross-section (with respect to the di-photon invariant mass  $m_{\gamma\gamma}$ ) :

$$\frac{d\sigma}{dm_{\gamma\gamma}} = c_{g\gamma}^2 \frac{d\sigma_S^{sherpa}}{dm_{\gamma\gamma}} + c_{g\gamma} \frac{d\sigma_I^{sherpa}}{dm_{\gamma\gamma}} + \frac{d\sigma_{bkg}}{dm_{\gamma\gamma}} \quad (6.3)$$

where the three parameters of interest are  $m_h, \Gamma_h$  and  $c_{g\gamma}$  in the general case. If we are interested only in the SM case  $c_{g\gamma}$  and  $\Gamma_h$  are fixed to their SM values (1 and  $\Gamma_h^{SM} = 4$  MeV) and only  $m_h$  is fitted. In general, this implies a variation of both the signal and interference cross-sections with respect to the width, only their sum being constant. Once these two cross-sections are known they can be used to reweight the signal and interference Monte-Carlo samples to be used later, so that the analysis will only be sensitive to variations of the lineshape and not to variations of the number of events. But this reweighting is perfect only for pure  $gg \rightarrow \gamma\gamma$  samples and do not account for the associated production modes, that do not produce a cross-section proportional to  $c_{g\gamma}$  or  $c_{g\gamma}^2$ . The inclusion of these modes either requires to make explicit assumptions on which part of the effective  $c_{g\gamma}$  comes from the gluon fusion modifier and which comes from the  $h \rightarrow \gamma\gamma$  decay modifier, or to produce a global fit where additional channels can bring additional constraints on  $\kappa_\gamma$  separately from  $\kappa_g$ .

## 6.2 Detector effect folding

As this specific Sherpa module generates weighted events the relative uncertainty on the cross-section will be  $|\frac{\delta\sigma}{\sigma}| = |\frac{\sum w^2}{\sum w}|$ , where the numerator will have a small but finite value, while the denominator will be close to 0 because the cross-section of the interference term is 0 at leading order, and the negative and positive weights corresponding to different events will cancel each others. Given that the interference cross-section is not strictly 0 and that the weights are fairly small the ratio  $\frac{\delta\sigma}{\sigma}$  is under control but, in order to achieve a relatively small statistical uncertainty on these templates, it requires a lot of events : for instance generating 400000 events still gives an error of  $\approx 25\%$  on the interference cross-section. In most cases the datasets that were used contained more than 200 million events, which is clearly too much to go through a realistic detector simulation. Instead a framework that does a fast smearing and a fast folding of the efficiencies has been developed, and its main components are described below.

### 6.2.1 Simulation of photon conversions

As the energy resolution of the photons is very different between converted photons and unconverted, it is important to have a proper description of the probability for a photon to convert. To do so a two-dimensional map of the fraction of converted photon has been constructed on a Monte-Carlo sample generated with the full detector simulation. The sample that had been used corresponds to single-photon events and implements the last description of the detector material budget, and had been previously used to train the calibration MVA [226]. The  $(\eta \times \phi)$  map that is constructed in this way may be found in fig. 6.3. A tentative to produce a 3D map where the dependency on the photon  $p_T$  was implemented as well has been done, but given that this dependency is negligible the simpler 2D map was kept.

For each photon a random number is generated in  $[0, 1]$  according to an uniform probability distribution. If this random  $r$  is smaller than the fraction of converted photons  $f$  in the  $(\eta \times \phi)$  bin the photon falls in, we classify this photon as being converted, otherwise it is unconverted. Once  $h \rightarrow \gamma\gamma$  samples are generated using this logic we have an overall fraction of converted photons of 28% while on the official  $h \rightarrow \gamma\gamma$  samples, which uses the full detector simulation and PowHeg-Pythia [86–88] to generate the events, it is of 30%. We considered the difference between these two numbers to be negligible.

### 6.2.2 Identification and reconstruction efficiencies

The selection efficiency of  $h \rightarrow \gamma\gamma$  events is known to vary as a function of the  $p_T$  of the photon in the events, on their pseudo-rapidity, and on whether or not one of the two photons have converted. This dependency had been computed before to create the fast smeared Monte-Carlo [291] that has been used to generate large background samples to study the spurious signal and chose the background shape used in the  $h \rightarrow \gamma\gamma$  analysis. Therefore we decided to use these numbers. They actually give a per-photon efficiency, and have been derived in 4  $\eta$  and 4  $p_T$  bins. These efficiencies are applied as a multiplicative

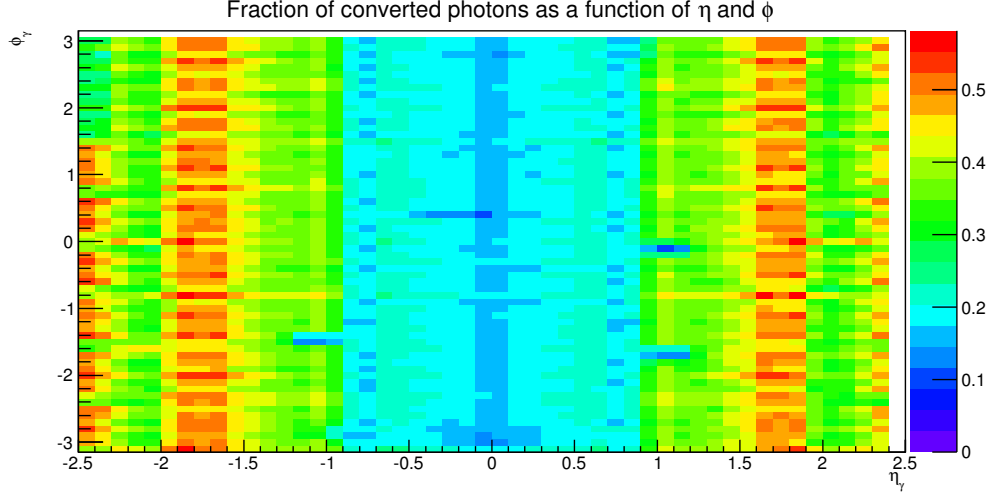


Figure 6.3: Two-dimensional map ( $\eta \times \phi$ ) of the fraction of converted photons obtained from a single photon MC that used the last detector material description

factor to the Monte-Carlo event weights, i.e. the weight that are used to create the final datasets are  $w' = \epsilon_{\gamma 1} \epsilon_{\gamma 2} w$ , and this is done separately for every event.

A second approach can be applied, based on a method that was designed for the differential cross-section analysis [292]. For this analysis, global factors were derived to unfold the impact of detector efficiency, and the efficiencies obtained with the per-event weights and with the global factors can be compared. This is done on table 6.2 at several stages of the analysis, and the final efficiencies differs by a few per-cents. At the same time it was realized that the efficiency obtained with the global folding factors was higher than the one that was obtained for the mass [264] and couplings [262] analyses, therefore it was decided to rescale all the efficiencies to the smallest value, which corresponds to the one of the couplings analysis that is  $\approx 2\%$  lower (a small change in the isolation efficiency occurred between the mass and couplings papers), as it is the most conservative number.

### 6.2.3 Implementation of the mass resolution

The implementation of the energy and vertex position resolution is done at the level of the di-photon invariant mass, separately for each events, and is based on the resolution model that have been determined for the mass analysis [264]. For each di-photon pair, the category to which it belongs is determined, depending on the  $\eta$ ,  $p_T$  and the randomized conversion status of the photons. This provides a model of the mass resolution for this event, which has been described in subsection 5.1.2. In this model the value of  $m_H$  is replaced by the current value of the di-photon invariant mass, and this completely determines the model. A new, smeared, value for the invariant mass is then randomly drawn on this model, and is used as the reconstructed invariant mass of the current event. This effectively implements the convolution between the underlying physics and the detector resolution.

Although this method is perfect when the event generation is interfaced with a Parton Shower, it does not work for the fixed order computation. In Sherpa divergence subtraction

$p_T$ bin	0-20	20-30	30-40	40-50	50-60	60-80	80-100	100-200
(1) Truth, no cut ( $\eta < 5$ ), w/ iso	0.617	0.484	0.335	0.240	0.177	0.116	0.065	0.012
(2) Truth, w/ cuts, no crack cut, w/ iso	0.390	0.312	0.212	0.150	0.109	0.070	0.039	0.007
(3) Truth, w/ cuts, no crack cut, no iso	0.392	0.317	0.218	0.154	0.112	0.073	0.040	0.008
(4) Truth, w/ cuts, w/ crack cut, no iso	0.339	0.275	0.189	0.134	0.097	0.063	0.035	0.007
(5) Truth, w/ cuts, w/ crack cut, w/ iso	0.338	0.270	0.184	0.130	0.094	0.061	0.034	0.006
(6) Truth, w/ cuts, unfolded, w/ iso	0.254	0.203	0.138	0.096	0.070	0.045	0.025	0.005
(7) Smeared, w/ cuts, w/ iso	0.264	0.212	0.146	0.102	0.074	0.048	0.026	0.005
Efficiency (from global folding : (6)/(2)) (in %)	65.20	65.13	64.88	64.4	64.29	64.29	64.34	65.60
Efficiency (from per-event weights : (7)/(2)) (in %)	67.86	68.15	68.53	68.47	68.47	68.34	68.14	69.13
Difference of efficiency (in %)	4.01	4.54	5.46	6.12	6.29	6.11	5.73	5.25

Table 6.2: Value of the cross-sections (in  $fb^{-1}$ ) and of the efficiencies in several  $p_T$  bins, compared between the methods to apply the resolution and efficiency folding. "w/ cuts" corresponds to the acceptance cuts on  $|\eta|$ ,  $\frac{p_T}{m}$ . Values (1) to (6) correspond to [292]

is handled using correlated events : a given event is in fact made of several sub-events, that are all weighted and whose weights are correlated among one another. Although all these sub-events have the same  $m_{\gamma\gamma}$  they are usually very different in  $\eta$  and  $\phi$ , and may fall in different categories. If after the smearing the various sub-events have a different mass, the divergence subtraction is lost and the mass spectrum becomes meaningless. In that case the mass smearing is determined only for the first sub-event and the same mass variation is applied to all the following sub-events, which allows not to lose the divergence subtraction property.

## 6.3 Parton shower tuning

### 6.3.1 Principle of the optimization

The accuracy of the description of the  $p_T$  distribution generated by Sherpa is only NLO in the matrix elements, with additional initial and final states radiations generated by a parton shower, and within Sherpa the default parton shower program is CSS++ [293] and the matching between parton emissions from matrix elements and from the shower is done via MC@NLO. This does not correspond to the best description of the Higgs boson  $p_T$  that may be achieved, which comes from HRes 2 [82], but it is possible to tune the parton shower to try to improve this description. This is done by a modification of the parameter CSS\_IS\_AS\_FAC, which modifies the behaviour of the parton shower for initial state radiation in the way that will be described below. Obviously for  $h \rightarrow \gamma\gamma$  the parton shower has no impact on final state particles (except through the change of the boost).

Effectively a parton shower program does an iterative resolution of the DGLAP equations [65–67] to determine the splitting of the partons and their kinematics after the splitting. In the initial state this is done backward in time : we start from the partons that collide and we reconstruct their history to determine if they come from a splitting, and how their momentum has been modified in this splitting. This modifies the momentum of the colliding partons, and therefore this also modifies the momentum of the particles that will be produced in the collision. If we denote  $q_i$  the parton density function for the quark family  $i$  and  $g$  the density of the gluon, the DGLAP equation is expressed as follows [294, 295] :

$$\frac{dq_i(x, \mu^2)}{d\log\mu^2} = \frac{\alpha_s}{2\pi} \int_x^1 \frac{d\xi}{\xi} (q_i(\xi, \mu^2)P_{qq}\left(\frac{x}{\xi}\right) + g(\xi, \mu^2)P_{qg}\left(\frac{x}{\xi}\right)) \quad (6.4)$$

$$\frac{dg(x, \mu^2)}{d\log\mu^2} = \frac{\alpha_s}{2\pi} \int_x^1 \frac{d\xi}{\xi} \left( \sum_i q_i(\xi, \mu^2)P_{gq}\left(\frac{x}{\xi}\right) + g(\xi, \mu^2)P_{gg}\left(\frac{x}{\xi}\right) \right) \quad (6.5)$$

where the functions  $P_x(\frac{x}{\xi})$  are the splitting kernels that give the probability for an initial parton to emit another parton that carries a fraction  $\frac{x}{\xi}$  of its momentum. These splitting functions may be seen in term of Feynman diagrams in fig. 6.4 and are functions of  $\alpha_s$ .

In the DGLAP equation  $\alpha_s$  is evaluated at an energy scale  $Q^2$  that corresponds to the energy scale of the process being considered. The idea behind the tuning of CSS\_IS\_AS\_FAC is to modify this energy scale by a multiplicative factor, i.e. we do the following replacement :  $\alpha_s(Q^2) \rightarrow \alpha_s(\text{CSS\_IS\_AS\_FAC} \times Q^2)$ . Due to the running of  $\alpha_s$  a bigger CSS\_IS\_AS\_FAC implies a smaller  $\alpha_s$  hence less emissions of jets by the initial state partons

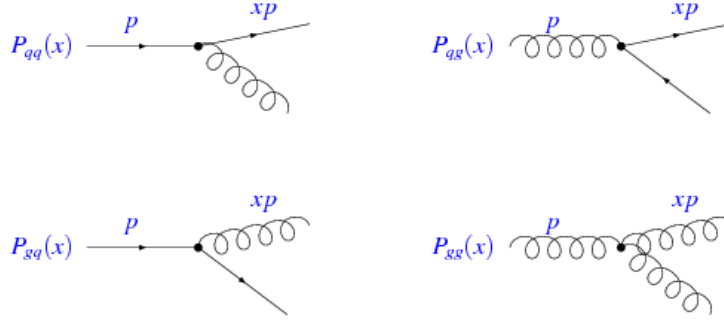


Figure 6.4: Feynman diagrams corresponding to the various splitting function described in the text [296]

and a lower  $p_T$  for the Higgs boson produced in the process  $gg \rightarrow h \rightarrow \gamma\gamma$ . On the contrary a very small value for this parameter implies a large cross-section for the production of high- $p_T$  Higgs bosons. If we have a prior knowledge for the  $p_T$  distribution of Higgs bosons in the  $gg \rightarrow H$  process we can search the value of CSS\_IS\_AS\_FAC that gives the best agreement between this prior distribution and the one that is determined by Sherpa 2. It is not directly possible to tune the  $p_T$  spectrum generated by the interference term, because we do not have any previous knowledge of this distribution. But we may tune the distributions obtained for the signal and re-use the value determined for CSS\_IS\_AS\_FAC on the interference and background samples.

### 6.3.2 State of the art description of the Higgs boson $p_T$ distribution

The best description of the Higgs boson  $p_T$  distribution in the gluon fusion process comes from HRes 2 [82, 83] which is NNLO in  $\alpha_s$  and where the quark triangle has been computed with finite top and bottom masses at NLO, and this impacts the  $p_T$  distribution especially at low  $p_T$  where the addition of the bottom mass contribution has a sizeable impact, as may be seen on fig. 6.5. The emission of soft gluons is described using the technique of large logarithm resummation, up to NNLL in HRes 2, and gives a more accurate description of the  $p_T$  than a parton shower Monte-Carlo. The official Monte-Carlo samples used for  $h \rightarrow \gamma\gamma$  in ATLAS are generated with PowHeg which is interfaced with Pythia 8 for the parton shower. A detailed comparison between HRes 2 and PowHeg-Pythia8 may be found in [89], where a reweighting of the  $p_T$  distribution of PowHeg-Pythia8 to the distribution determined on HRes 2 had been derived. This reweighting has been applied on all the samples that are used for the final  $h \rightarrow \gamma\gamma$  analyses of the Run 1.

### 6.3.3 Results for the tuning

The best value of CSS\_IS\_AS\_FAC is determined from the best compatibility between the  $p_T$  distribution from Sherpa 2 and the one either from HRes 2 or from the reweighted (to HRes) PowHeg-Pythia8 sample. The comparison with HRes 2 should be done with the true value of the  $p_T$  before any detector effect as HRes 2 cannot implement such effect, while the comparison with PowHeg-Pythia8 should be done after having applied the efficiency

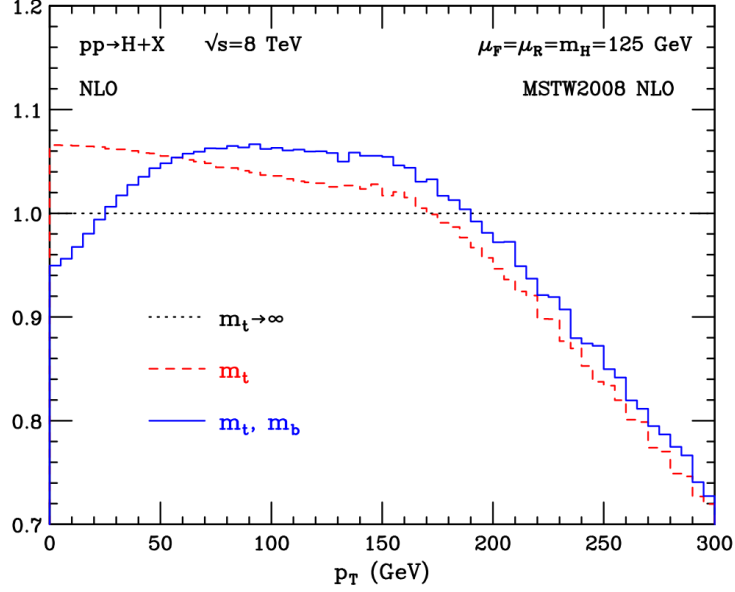


Figure 6.5: Distribution of the Higgs boson  $p_T$  determined with HRes 2.0 with different approximations. All the curves are normalized to the infinite top mass approximation [82]

and smearing functions, as this sample went through a full detector simulation. Both of these tunings have been produced.

First, Higgs boson signal samples are generated using Sherpa at several points of CSS\_IS\_AS\_FAC, and their  $p_T$  distributions are compared with those from PowHeg-Pythia8, which may be seen in fig. 6.6. Just after  $p_T^{\gamma\gamma} = 120$  GeV there is a clear drop in the number of events in Sherpa with regard to PowHeg, which originates from the value of the resummation scale, that is set at  $m_H$  in Sherpa. This means that the parton shower may generate parton emission up to  $p_T \approx m_H$  and will not have much impact above, where all the parton emission will have to be described by an underlying matrix element. But this corresponds to the CSS++ parton shower with the MC@NLO procedure, and PowHeg works differently and is still able to create parton emission above  $m_H$ . At a very high- $p_T$  ( $> 250$  GeV) both parton shower modules will have the same behaviour as all the parton emissions will come from the matrix elements in both cases, and this is shown in fig. 6.7 although the statistics quickly becomes small at high- $p_T$ . Furthermore it is not possible to cancel the deficit of events that is observed after  $p_T^{\gamma\gamma} = m_H$  with an adequate tuning, as the parton shower has no effect in this region.

Although fig. 6.6 seems to hint that CSS\_IS\_AS\_FAC = 1.5 is the best value, it is not easy to determine it only from this plot. The fraction of events falling in three broad  $p_T$  bins (in GeV) for the various Monte-Carlo samples is given in table 6.3 at a truth level and in table 6.4 at a detector level. In principle the tuning extracted from these two tables should be the same, but there is a slight disagreement as the optimization done at truth level tends to favour CSS\_IS\_AS\_FAC = 1 and the one done at detector level favours CSS\_IS\_AS\_FAC = 1.5, although the difference in term of fraction of events in each of the  $p_T$  bins is not big. We decided to use CSS\_IS\_AS\_FAC = 1.5 in the generation of our Monte-Carlo samples.

Figures 6.8, 6.9 and 6.10 show the  $p_T$  spectrum obtained with MC@NLO and with the

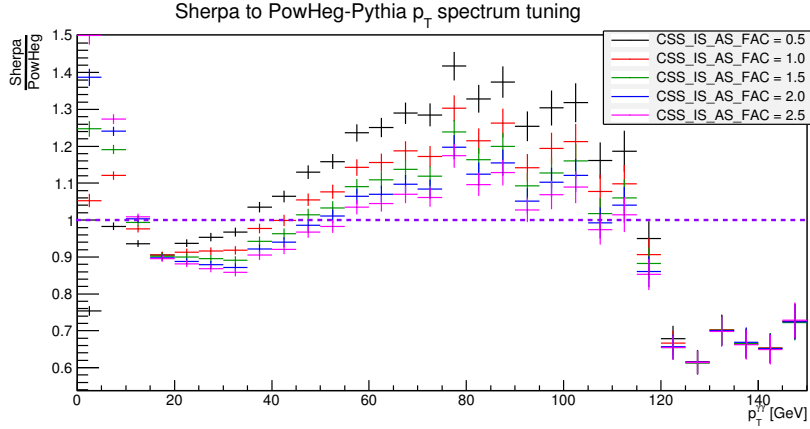


Figure 6.6: Ratio of the  $p_T$  distribution generated by Sherpa to the one generated by PowHeg-Pythia8 reweighted to HRes 2, for several values of CSS\_IS\_AS\_FAC

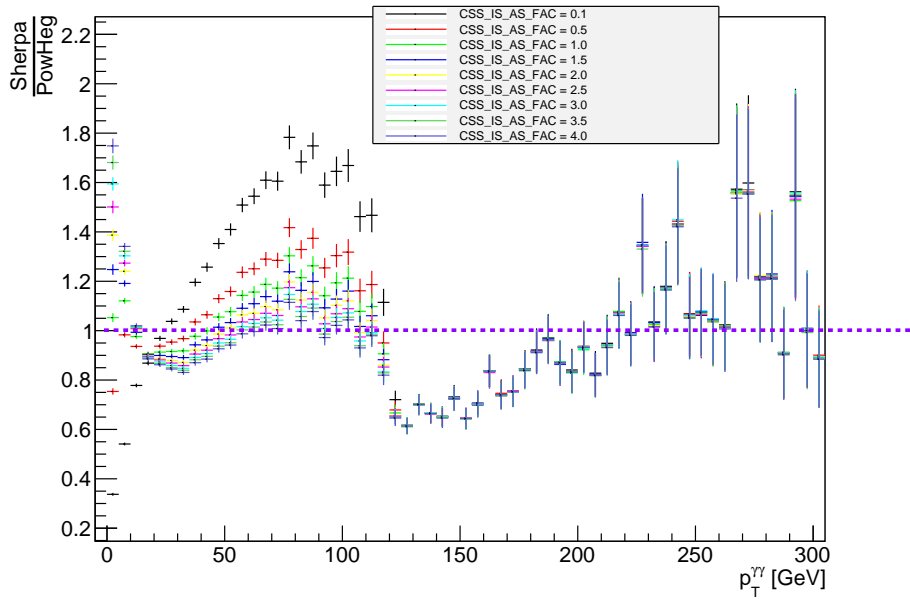


Figure 6.7: Ratio of the  $p_T$  distribution generated by Sherpa to the one generated by PowHeg-Pythia8 reweighted to HRes 2, for several values of CSS\_IS\_AS\_FAC, and up to a high  $p_T$

CSS_IS_AS_FAC	frac $p_T$ 0-30	frac $p_T$ 30-80	frac $p_T$ 80-500
0.5	55.92	34.65	9.43
1.0	58.61	32.47	8.93
1.5	60.02	31.32	8.67
2.0	60.96	30.54	8.49
HRes 2	57.9	32.9	9.2

Table 6.3: Fraction of events falling in three broad  $p_T$  bins (in GeV) at a truth level, either from HRes 2.0 or from Sherpa, and for different values of CSS\_IS\_AS\_FAC

CSS_IS_AS_FAC	frac $p_T$ 0-30	frac $p_T$ 30-80	frac $p_T$ 80-500
0.5	57.13	33.76	9.10
1.0	59.71	31.65	8.64
1.5	61.10	30.51	8.39
2.0	62.00	29.76	8.24
PowHeg-Pythia8	61.39	30.15	8.46

Table 6.4: Fraction of events falling in three broad  $p_T$  bins (in GeV) at a detector level, either from PowHeg-Pythia8 reweighted to HRes 2 or from Sherpa, and for different values of CSS\_IS\_AS\_FAC

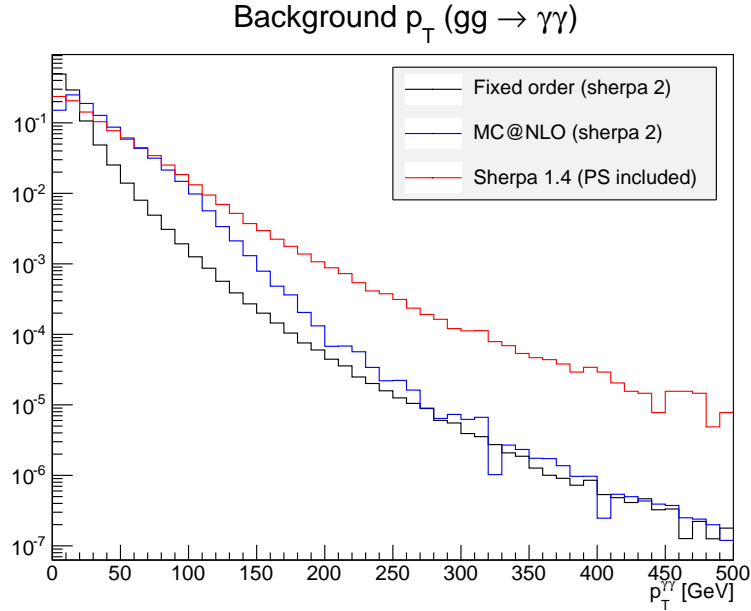


Figure 6.8:  $p_T$  spectrum generated by background  $gg \rightarrow \gamma\gamma$  processes with Sherpa 2 (with and without Parton Shower) and with the previous version of Sherpa (used for Run 1 analyses)

fixed order calculation used in [112] and [289]. Using the fixed order computation, one had a mass shift at high transverse momentum which is much smaller (see fig. 1.16) and this can be used in order to have two sets of categories with different mass shifts (for a fixed width) and therefore help to constrain the width. Unfortunately this is largely diluted with MC@NLO and cannot be used. It has been proposed (for instance in [297]) to use instead the mass coming from the  $h \rightarrow ZZ^*$  analysis (see section 5.2) which is much less sensitive to interference effects.

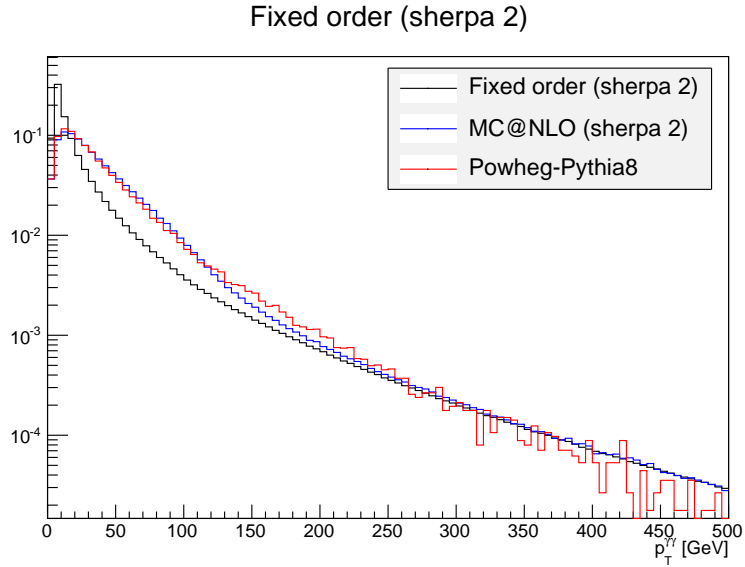


Figure 6.9:  $p_T$  spectrum generated for the  $gg \rightarrow h \rightarrow \gamma\gamma$  signal processes with Sherpa 2 (with and without Parton Shower) and with PowHeg-Pythia8 (used for Run 1 analyses)

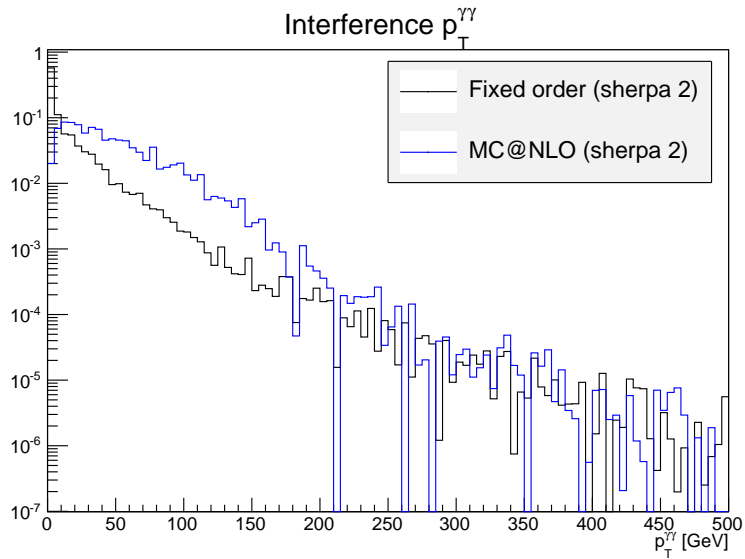


Figure 6.10:  $p_T$  spectrum generated for the interference term between  $gg \rightarrow H \rightarrow \gamma\gamma$  and  $gg \rightarrow \gamma\gamma$  processes with Sherpa 2 (with and without Parton Shower)

## 6.4 Impact of interferences on the measurement of $m_h$

### 6.4.1 Generation of pseudo-Asimov datasets

In order to determine the mass shift, two datasets representative of the  $h \rightarrow \gamma\gamma$  analysis are needed : one with the interferences included and one without. To this purpose we use large signal and interference samples (including both g-g and q-g initiated components, see subsection 1.5.1 and fig. 1.13) that are generated with the Sherpa 2 Monte-Carlo generator, tuned in the way that has been presented above, and scale them to a luminosity of  $20 \text{ fb}^{-1}$  (corresponding to the  $\sqrt{s} = 8 \text{ TeV}$  dataset). Furthermore an additional normalization factor  $k_S$  is applied to rescale this cross-section computed at NLO to the value of the Yellow Report 3 [81], which gives  $k_S = 1.45 \pm 10\%$  (where the uncertainty accounts for uncertainties on the PDFs and on  $\alpha_S$ ). A similar factor  $k_B$  is applied on the background and although it is not known as no higher-order background computation is available, we chose it to be  $k_B = k_S$  as a nominal value and a conservative uncertainty will be assessed by applying large variations on this parameter (from 1 to  $k_S$ ). Because of the difference of the quark mass in the  $gg$ -induced (box) background and signal triangle loops the background is expected to receive a smaller k-factor between NLO and NNLO than the signal, because the top-quarks will emit harder radiations [298] and also because there is an additional term from short-distance renormalization for the signal, that does not exists for the background (eq. 23 of [114]). The formula 6.3 is then changed to :

$$\frac{d\sigma}{dm_{\gamma\gamma}} = c_{g\gamma}^2 k_S \frac{d\sigma_S^{sherpa}}{dm_{\gamma\gamma}} + c_{g\gamma} \sqrt{k_S k_B} \frac{d\sigma_I^{sherpa}}{dm_{\gamma\gamma}} + k_B \frac{d\sigma_{bkg}}{dm_{\gamma\gamma}} \quad (6.6)$$

A last normalization factor is applied to take into account the contribution of the associated production processes, which is done by rescaling the signal template by a factor of  $\frac{N_h^{tot}}{N_h^{gg \rightarrow h}}$ . This fraction of  $gg \rightarrow h$  events is given in table 6.5, and we only rescale the signal template because we assume that there is no interference that involves these associated production processes as the background is much smaller.

The background template is directly taken from a fit to data, using the background shape presented in subsection 5.1.2 to do the fit, and there is one  $S + B + I$  template per event category, which is required to produce combined  $S + B$  fit to the 10 categories defined for the mass analysis. Despite this procedure the generated samples are not exact Asimov datasets, as there are still statistical fluctuations in the Monte-Carlo templates, especially for the interference templates.

### 6.4.2 Main results on the mass shift

The fit of the Higgs boson mass is carried out on this pseudo-Asimov datasets, and the comparison of the mass fitted between the templates with and without interferences allows an estimation of the impact of interferences between signal and background processes on the best estimate of the Higgs boson mass. The rescaling of the interference and signal templates to the SM requires to solve equation 6.2, which has two solutions in  $c_{g\gamma}$  : one of

Category	$gg \rightarrow H$ fraction (%)
1	90.33
2	58.95
3	90.18
4	59.00
5	86.81
6	90.39
7	59.55
8	90.07
9	60.30
10	86.84

Table 6.5: Fraction of Higgs bosons produced by gluon with respect to the total number of produced Higgs bosons (for a mass of 125.4 GeV [299]). The numbering of the categories is the same than in table 5.1

each sign. One of these solutions increases the total number of events with respect to the case where the interferences are not considered hence will be called "constructive". Incidentally it also corresponds to a case where the mass spectrum increases, i.e. is on average at a higher value than without interferences. The second solution which decreases both the number of events and the mass spectrum will be called "destructive" and corresponds to the actual Standard Model ( $c_{g\gamma} = 1$  in the exact SM), and interferences should decrease the number of events at very high-mass to allow for unitarity conservation at high-energy [300]. In the following we are only interested in assessing the impact of interferences in the SM, hence we decided to assess only the impact of interferences in the destructive case. The interference template for the Standard Model case may be seen in fig. 6.11.

The measurement of the mass on each of these templates uses the same modelling of the data and procedure as the one that had been presented in section 5.2, with a combined signal and background fit to the 10 mass categories. The only difference comes from the use of a binned likelihood, with bins of 10 MeV, instead of an unbinned likelihood that can not be used for the interference templates that require several hundred of millions of events with small weights. This fit is actually done two times, iteratively and using the result of the first as starting point to the second. The stability of this result has been checked with respect to the bin size, and by comparing the result of the fit to a full likelihood scan. Given that these MC templates are not exact Asimov datasets the production has been split in four samples, and the mass shift have been separately assessed for each of these samples which allow to check that the size of each sample is large enough since the standard deviation computed by comparing one sample to another is small enough. These results are summarized in table 6.6, that show a constant decrease of 35 MeV of the Higgs boson mass estimate within the Standard Model due to interferences, and also show that the RMS of this result computed over four different sample is completely negligible, therefore the impact of Monte-Carlo statistical fluctuations on this estimation of the mass shift will not be considered further.

In the case for the template generated in the destructive scheme and in which the interferences are implemented we expect to find back the number of events that have been used in the mass analysis as a prediction of the SM, hence the result of the fit should

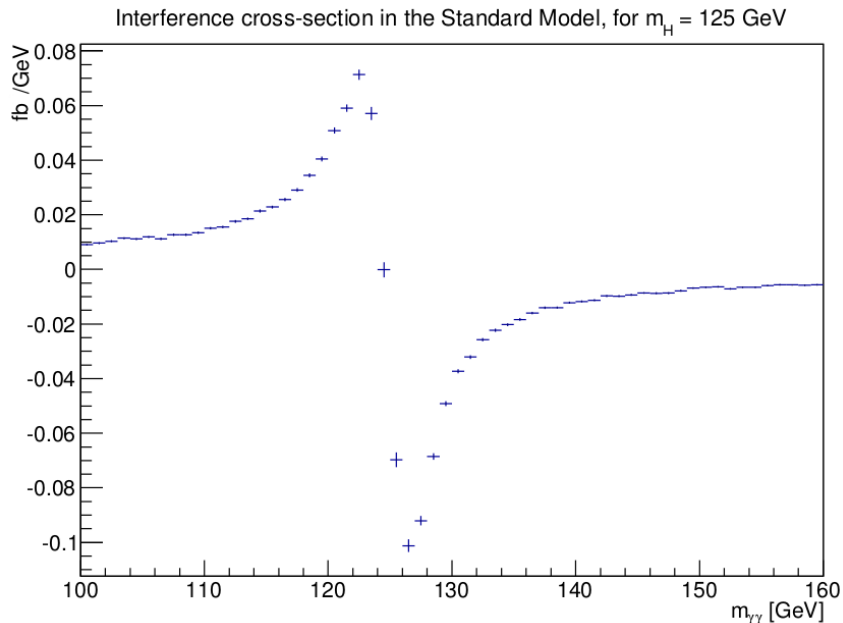


Figure 6.11: Detector-level di-photon mass distributions induced by interferences between  $gg \rightarrow \gamma\gamma$  and  $gg \rightarrow h \rightarrow \gamma\gamma$  within the Standard Model, in  $fb/GeV$  (after all cuts applied in the  $h \rightarrow \gamma\gamma$  analysis)

Int. type	With/out interf.	Quantity	Sample 1	Sample 2	Sample 3	Sample 4	Mean	RMS
destructive	no I	$m_h$	124.998	124.998	124.997	124.997		
		$\mu$	0.995	0.995	0.995	0.994		
	w/ I	$m_h$	124.963	124.962	124.962	124.962		
		$\mu$	0.988	0.988	0.988	0.988		
		$\Delta m_h [MeV]$	-34.7	-35.4	-35.0	-34.8	-35.0	0.3

Table 6.6: Summary of the Higgs boson mass fit for different templates (with or without interference) for an injected Higgs mass of 125 GeV and for  $k_B = k_S = 1.45$

give  $\mu = 1$ , and the best fit of the signal strength is indeed close to it, as seen in fig. 6.6. This result already implements the rescaling of the efficiencies of our smeared MC to the efficiencies estimated during the couplings analysis which was mentioned earlier, and the impact of this rescaling on the mass shift has been checked and was at the order of 2 MeV, hence can be neglected. We also expect a closure for the best-fit of  $m_h$  on the S+B samples (without interferences), as it should give back the value of  $m_h$  injected for the generation of the MC samples, and it is indeed the case. In addition to this closure, the results obtained on the four samples do not display a big variance, hence it is safe to quote a mass shift of  $\Delta m_h = -35 \pm 0.3$  MeV for the standard model case. This means that if we were to correct for the effect of interferences in the mass measurement, the Higgs mass measured by ATLAS in the  $\gamma\gamma$  channel [264] would be 35 MeV higher. Here the RMS of these four samples has been quoted as a statistical error, and the same notation will be used below. Several samples had to be generated to study systematic effects, using different settings of the MC generators. For these additional samples, no statistical error will be quoted as only one sample per setting has been generated. Given the size of the statistical error for the main templates, it is expected to be negligible for the templates with systematic variations too.

### 6.4.3 Systematic effects affecting the mass shift

#### k-factor variations

One important systematic uncertainty comes from the imperfect knowledge of the signal and background cross-sections, which needs to be propagated to the templates. In this process the signal template is scaled by  $k_S$  and the interference template by  $\sqrt{k_S k_B}$  (see subsection 6.4.1). As it is taken from data, the background template is not rescaled by any k-factor. First the signal k-factor  $k_S$  has been varied by  $\pm 0.1$  which roughly corresponds to its uncertainty ( $\pm 7\%$ ), and the impact on the estimation of the mass shift was at the order of 1 MeV, which is negligible. As the signal varies linearly with  $k_S$  while the interference term varies only with  $\sqrt{k_S}$  the increased interference cross-section does not imply a bigger mass shift as the signal is more significant and there is, to some extent, a partial cancellation of this uncertainty. The background k-factor is unknown hence requires to be varied over a large range in order to have a fair estimation of the associated uncertainty on the mass shift. Two values have been taken (1 and  $k_S$ ) and the mass shift has been estimated for each of these values. As  $k_B$  only enters within the interference cross-section, it directly translates in a variation of the mass-shift without any possible cancellation of this effect, hence giving a bigger uncertainty. This variation of the mass shift against the value of the k-factors is given in table 6.7 where one may see variation of  $\approx 6$  MeV of the mass shift coming from these extreme variations of  $k_B$ , within the Standard Model.

#### Scale variations

Within this problem three QCD scales have to be considered : renormalization ( $\mu_{Res}$ ), factorization ( $\mu_{Fac}$ ) and resummation ( $\mu_{Res}$ , linked to the parton shower). For the central value of  $\Delta m_h$  presented in this document, the value of these scales have all been chosen to be of  $m_{\gamma\gamma}$ , and an additional theory uncertainty has to be evaluated due to the fact the

	$k_s = 1.35$	$k_s = 1.45$	$k_s = 1.55$
$k_B = 1$	$-29.9 \pm 0.2$	$-29.0 \pm 0.2$	$-28.1 \pm 0.2$
$k_B = k_S$	$-34.7 \pm 0.3$	$-34.9 \pm 0.3$	$-35.1 \pm 0.3$

Table 6.7: Variation of the mass shift induced by the interferences against the value of the background k-factor  $k_B$  and signal k-factor  $k_S$

	Renormalization ( $\mu_{Ren}$ )	Factorization ( $\mu_{Fac}$ )	Resummation ( $\mu_{Res}$ )
Down	$\frac{m_{\gamma\gamma}}{2}$	$\frac{m_{\gamma\gamma}}{2}$	$\frac{m_h}{4}$
Nominal	$m_{\gamma\gamma}$	$m_{\gamma\gamma}$	$m_{\gamma\gamma}$
Up	$2m_{\gamma\gamma}$	$2m_{\gamma\gamma}$	$2m_{\gamma\gamma}$

Table 6.8: Summary of the different scale variations used in the evaluation of theory uncertainties, for  $k_B = k_S = 1.45$

exact value of this scale is not known. To do so we use the standard method of varying these three scales. This variation is taken to be of a factor 2 for  $\mu_{Ren}$  and  $\mu_{Fac}$ , which corresponds to the standard scale variation, but it is higher for  $\mu_{Res}$ . For the background the central value for the resummation scale is usually taken as  $m_{\gamma\gamma}$  while for the signal is often suggested to be close to  $\frac{m_h}{2}$ , therefore it is not clear which value should be used in the generation the interference template. Furthermore this scale is very important for the result of this document, as it completely modifies the impact of interferences in the high- $p_{T_t}$  categories, therefore a conservative approach has been chosen for the uncertainty linked to this scale. The maximal envelope of the variations used for the signal and the one used for the background has been considered, which corresponds to  $\mu_{Res} = \frac{m_h}{4} \rightarrow 2m_{\gamma\gamma}$ . Only the two extrema of this interval have been evaluated. All these scale variations are summarized in table 6.8.

Within Sherpa 2.0, evaluating the impact of a new value for these scales requires to create full new signal and interference samples. The mass shift  $\Delta m_h$  is estimated by using signal and interference templates that are generated with the same settings for the three scales, while the background does not suffer from this uncertainty as it comes from a fit to data. In a first step, this has been done by varying each of these three scales separately. This cannot capture the behaviour of potential non-trivial interplays between the three scales, which is estimated in a second step by varying coherently the three scales at once and in the same direction (i.e. all the scales are at "nominal", "up" or "down" at the same time). This last setting does not display any obvious effect that could not be explained by the individual scales variations, and it was therefore decided not to investigate the potential effect of incoherent scale variations as the three scales do not seem to display a non-trivial interplay. The biggest effect is observed for the samples where all the scales are varied at once, and is at the level of  $\pm 5$  MeV. It is clearly dominated by the variation of the factorization scale, which has been understood to be coming from the relative variation of the cross-section of the interference term compared to the signal. Despite having a big impact on the  $p_T$  spectrum, the resummation scale has a fairly small impact on the mass shift, because it does not impact the cross-sections at all. Furthermore the categories that give the biggest statistical power in the measurement of  $m_h$  correspond to low  $p_{T_t}$  categories [301] where the relative impact of the variation of  $\mu_{Res}$  is small (see subsection

Variations	Nominal	$\mu_{Ren}$ up	$\mu_{Ren}$ down	$\mu_{Fac}$ up	$\mu_{Fac}$ down	$\mu_{Res}$ up	$\mu_{Res}$ down	All up	All down
$m_h$ (S+B)	124.997	124.997	124.998	125.000	124.998	125.000	124.997	124.998	124.997
$\mu$ (S+B)	0.995	0.982	0.983	0.835	1.181	1.057	0.947	0.911	1.151
$m_h$ (S+B+I)	124.962	124.961	124.963	124.960	124.967	124.962	124.961	124.959	124.967
$\mu$ (S+B+I)	0.988	0.976	0.977	0.831	1.172	1.05	0.941	0.906	1.143
$\Delta m_H [MeV]$	-34.9	-36.6	-34.8	-38.3	-30.7	-36.0	-35.8	-39.4	-30.7

Table 6.9: Estimated mass shift ( $\Delta m_h$ ) due to the impact of interferences, for different QCD scales variations

Cat.	1	2	3	4	5	6	7	8	9	10
Nomin.	$-41.2 \pm 1.0$	$-1.8 \pm 0.6$	$-54.4 \pm 0.2$	$-12.8 \pm 0.8$	$-59.2 \pm 0.7$	$-39.0 \pm 0.8$	$-1.3 \pm 0.7$	$-55.7 \pm 0.7$	$-10.5 \pm 0.7$	$-61.7 \pm 1.2$
$\mu_{Ren}^{up}$	-43.3	-0.1	-54.6	-14.9	-59.2	-38.7	-0.2	-58.5	-13.8	-65.4
$\mu_{Ren}^{down}$	-41.0	-2	-54.5	-11.1	-59.4	-40.1	-1.8	-56.4	-9.8	-63.8
$\mu_{Fac}^{up}$	-45.0	-1.7	-57.9	-14.2	-65.1	-41.4	-4.3	-61.3	-13.7	-69.1
$\mu_{Fac}^{down}$	-36.1	-0.5	-48.7	-11.1	-54.8	-34.9	0.6	-49.2	-9.9	-56.6
$\mu_{Res}^{up}$	-40.3	-14.9	-54.7	-23.6	-60.4	-39.9	-15.0	-57.1	-23.0	-61.5
$\mu_{Res}^{down}$	-41.8	12.2	-55.3	2.5	-59.2	-39.5	11.3	-58.0	3.7	-66.5
all up	-43.8	-17.2	-58.0	-30.5	-67.1	-42.4	-16.5	-59.5	-28.8	-69.4
all down	-37.5	10.4	-51.1	1.0	-52.7	-34.6	9.5	-52.5	2.2	-55.4
$k_B = 1$	$-34.2 \pm 0.9$	$-1.5 \pm 0.6$	$-45.1 \pm 0.3$	$-10.6 \pm 0.3$	$-48.6 \pm 0.6$	$-32.2 \pm 0.6$	$-1.1 \pm 0.6$	$-46.2 \pm 0.6$	$-8.7 \pm 0.6$	$-51.1 \pm 1$

Table 6.10: Estimate of  $\Delta m_h$  by categories (in MeV), together with the uncertainty coming from scale variations, for  $k_S = 1.45$  and  $k_B = 1.45$  (unless specified otherwise). The numbering scheme is the same than in table 5.1

6.4.4).

## 6.4.4 Results by categories

The same analysis has been conducted category by category, and these results are summarized in tab. 6.10. Here the individual likelihood of the category that is being looked at is used, and fits to both the S+B and S+B+I of this category are performed to extract  $\Delta m_h$ . As expected the categories where the interference term has the biggest impact corresponds to low  $p_{T_t}$  categories, and it is much smaller at high  $p_{T_t}$ . The impact of the interference is also larger in the regions that are at higher  $\eta$  as the level of background becomes larger. It also larger in the barrel-endcap transition region where the resolution is worse. All the variations of the scales are shown in 6.10, but with only the impact of the most extreme k-factor variation ( $k_B = 1.45 \rightarrow 1$ ) as the variation of  $k_S$  has a small impact.

For the low  $p_{T_t}$  and crack categories the conclusion is the same than in the full fit, as the factorization scale has the dominant impact while the renormalization and resummation scales have a fairly small impact. But in the high  $p_{T_t}$  categories the dominant uncertainty comes from variations of the resummation scale, that can even change the sign of  $\Delta m_h$  when  $\mu_{Res}$  is small. In the plain fixed-order NLO computation, the impact of interferences on the high- $p_{T_t}$  categories is completely negligible as it has an effect that affects mainly the very low- $p_T$  region, where most of the background events are found. Therefore in NLO+PS samples most of the interference cross-section in high- $p_{T_t}$  categories will be induced by additional radiations coming from the parton shower, that does not give any emission above  $p_T = \mu_{Res}$ . This means the region  $p_T^H > \mu_{Res}$  is described by the fixed-order computation, and it is a feature of the shower used in sherpa that the transition between these two region is very sharp around  $\mu_{Res}$  [302], although there is an ongoing effort to improve its description [303]. At fixed-order the high- $p_{T_t}$  interference cross-section is dominated by the quark-gluon initiated process (denoted "LO (qg)" in fig. 1.13), as it

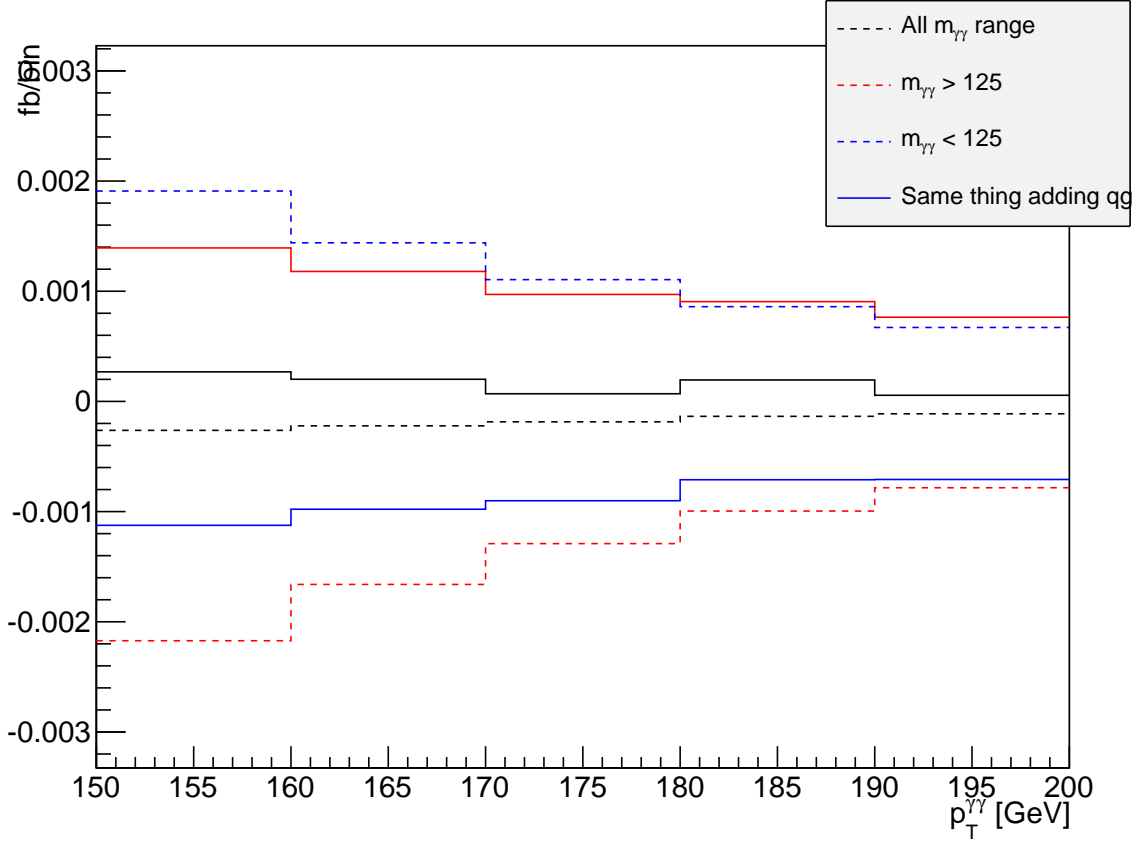


Figure 6.12: Di-photon  $p_T$  spectrum at fixed-order for the full (gg+qg) and gluon-initiated only components of the interference term. The difference between the full and dotted lines gives the qg term, which is 0 over the whole  $m_{\gamma\gamma}$ , and has therefore been splitted into  $m_{\gamma\gamma} < m_h$  and  $m_{\gamma\gamma} > m_h$

is seen in fig. 6.12. As the total cross-section for this term is null, it has been split into two sides in fig. 6.12 : one above the Higgs pole and one below, each having a non-zero cross-section. At any given  $m_{\gamma\gamma}$ , this term as an opposite sign with respect to the gluon-induced process (at leading order while at NLO the change of sign of the gluon induced process is slightly shifted in  $m_{\gamma\gamma}$ , see fig. 1.14), and it is dominating at high  $p_T^{\gamma\gamma}$  as may be seen in fig. 6.12. This explains the change of sign of  $\Delta m_h$  : when the resummation scale is smaller than  $p_T \approx 100$  GeV (which roughly corresponds to  $p_T^{\gamma\gamma} = 70$  GeV), the impact of the gluon-induced interference term is not sufficient in the high- $p_{T_t}$  category to balance out the one of the quark-gluon induced process and get back  $\Delta m_h < 0$ . As soon as the resummation scale becomes higher than 100 GeV ( $\mu_{Res} = m_{\gamma\gamma}$ ) there is a contamination from the gluon-induced interference process that can balance the quark-gluon one and give back  $\Delta m_h < 0$ , as it has a higher total cross-section. Using an even higher resummation scale ( $2 m_{\gamma\gamma}$ ) increases further the cross-section of the gluon-initiated interference term in the high- $p_{T_t}$  categories, as it increases the magnitude of migration from low to high  $p_{T_t}$  categories, and hence it decreases further  $\Delta m_h$ .

### 6.4.5 Conclusions

An estimate of the impact of the interferences between signal and background processes has been estimated and found out to be small, at  $\Delta m_h = 35 \pm 8$  MeV, where the uncertainty is the quadratic sum of the uncertainty due to the k-factors and the one from scale variations (a correction for this effect would increase the value of the mass quoted). It has been safely neglected for the current published values [130, 263, 264] but can become important for the next runs, when the uncertainty will decrease. At this stage there are still uncertainties on the  $p_T$  distribution which is poorly described by the current best theoretical tools. Hence its impact on the high- $p_{T_i}$  categories has large uncertainties due to the resummation scale used. One should note that there is currently some work ongoing inside the theory community to improve the describe of the  $p_T$  spectrum, by performing an analytical resummation. Therefore it will probably be possible to achieve an accurate description of the  $p_T$  spectrum of the interference term in the coming years, which will help to have a better knowledge of the full interference term, in all the categories. In addition there is a new computation of the interference in h+2jets that could be taken into account [116].

# Conclusion

The outstanding performance of both the LHC and the ATLAS detector during this first run of the LHC have allowed for a harvest of mature results, especially in the sector of the Higgs boson, which has just been discovered. The aim of this thesis was to summarize the current understanding of the  $h \rightarrow \gamma\gamma$  lineshape that we have been able to derive with the data recorded by the ATLAS detector.

The details of the final electro-magnetic calibration procedure, whose development yielded to a very good understanding of the ATLAS electro-magnetic calorimeter, has been explained in chapter 4. In this chapter the uncertainties related to the extrapolation of the energy scale from electrons to photons are derived. They are mainly related to the material modelling uncertainty, to the lateral leakage mis-modelling, as well as the uncertainties related to the non-linearity of the energy response (which is mainly induced by the apparent difference of energy response between the different electronic gain chains). The set of pre-corrections applied on data, which are mainly targeting an improvement of the energy resolution, are also described.

This improved calibration procedure brought a sizeable improvement to the systematic uncertainty on the Higgs boson mass, from 700 MeV [274] to 280 MeV [264]. The final Run I measurement of the Higgs boson mass using the ATLAS data has been presented too with  $m_h = 125.98 \pm 0.42$  (*stat*)  $\pm 0.28$  (*syst*) GeV for the  $h \rightarrow \gamma\gamma$  channel alone, and of  $m_h = 125.36 \pm 0.37$  (*stat*)  $\pm 0.18$  (*syst*) GeV when it is combined with the  $h \rightarrow 4l$  channel. The impact of the different uncertainties on this measurement have been explained too. In the same effort [264], an upper limit on the Higgs boson width using a direct fit of the lineshape has been set, at  $\Gamma_h < 5.3$  GeV at 95% C.L. using the  $CL_s$  method, and this analysis has been detailed in this manuscript.

Finally a first study of the impact of interferences between signal and background processes on the distribution of the di-photon invariant mass in the  $h \rightarrow \gamma\gamma$  decay channel is shown. An estimate of the impact of this effect on the measurement of the Higgs boson mass is given, and has been found out to be small (35 MeV) but it will be more important for the next Run of the LHC, where the statistical uncertainty is expected to shrink by a factor of more than 3. Most of the theory uncertainties that are, so far, limiting the use of this number in an actual analysis are given. This study is expected to be more important for the Run II of the LHC as it has an impact on the estimate of the width and on the estimate of the mass, which have so far been neglected, and because we expect an improved description of the  $p_T$  spectrum of interferences. Furthermore if a proper modelling of the  $p_T$  spectrum is achieved, the method outlined in [112] where the variation of the mass shift with respect to  $p_T$  of the di-photon pair is used to infer a limit on the width, could be developed and applied on the future ATLAS data.



# Appendix A

## Distribution of the reconstructed $Z^0$ boson mass in $Z^0 \rightarrow ee$ events profiled along $\phi$ in narrow $\eta$ bins

In this appendix all the reconstructed  $Z^0 \rightarrow e^+e^-$  mass distributions that were required to derive to high-voltage corrections that have been described in subsection 4.3.3 are displayed. They correspond to profiles of the Z boson mass in  $Z^0 \rightarrow ee$  events along  $\phi$ , in narrow  $\eta$  bins. As the short-circuits have no reason to be symmetrical with respect to  $\eta = 0$ , the side A and C of the detector are displayed separately. These profiles are shown both before and after the effective corrections applied to correct for the impact of short-circuits on the response of the calorimeter.

APPENDIX A. DISTRIBUTION OF THE RECONSTRUCTED  $Z^0$  BOSON MASS IN  
 $Z^0 \rightarrow ee$  EVENTS PROFILED ALONG  $\phi$  IN NARROW  $\eta$  BINS

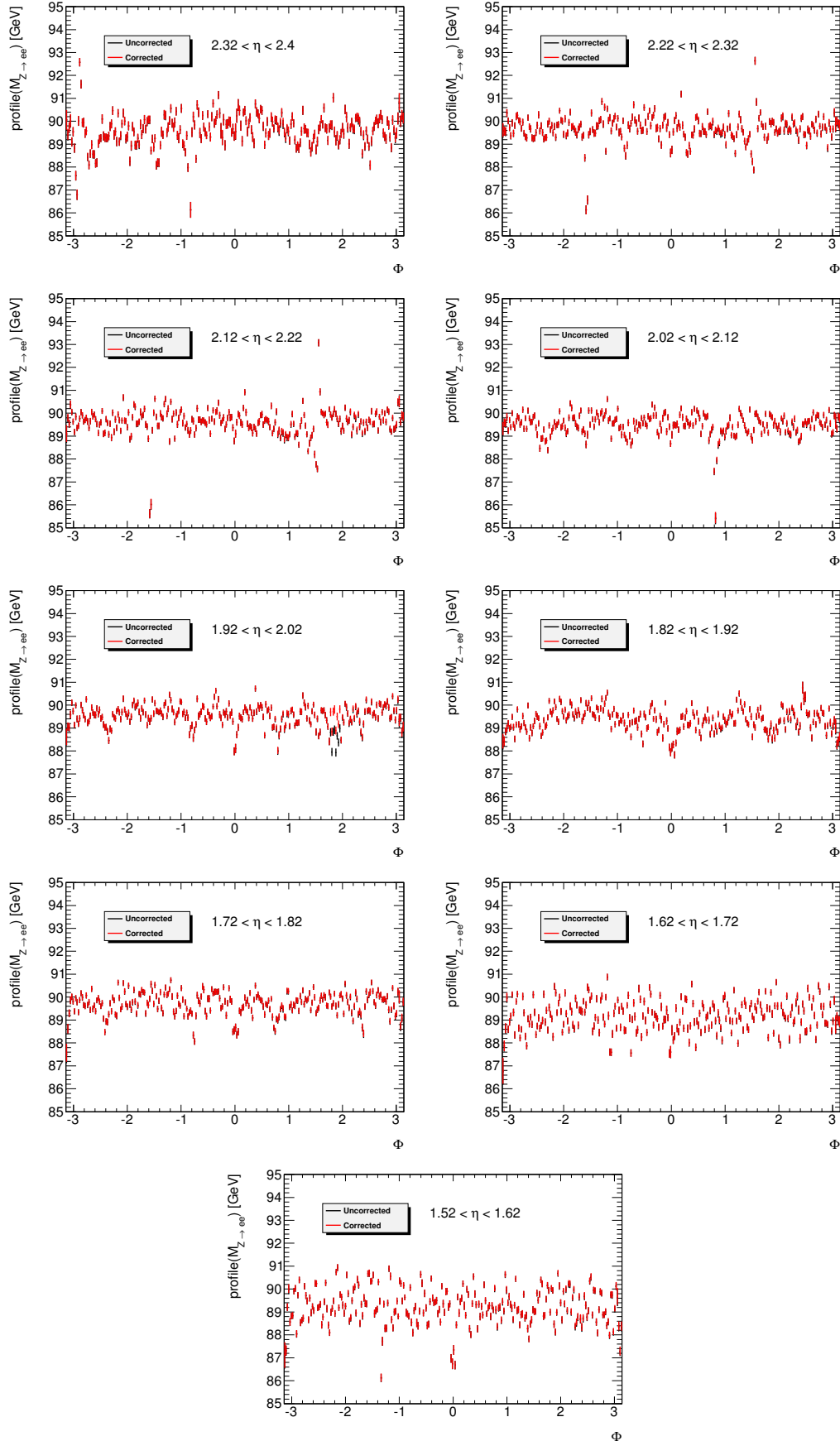


Figure A.1: Endcap C - Profile of  $M_{Z \rightarrow ee}$  along  $\phi$  by bins in  $\eta$ , before and after the HV correction  
 232

APPENDIX A. DISTRIBUTION OF THE RECONSTRUCTED  $Z^0$  BOSON MASS IN  $Z^0 \rightarrow ee$  EVENTS PROFILED ALONG  $\phi$  IN NARROW  $\eta$  BINS

---

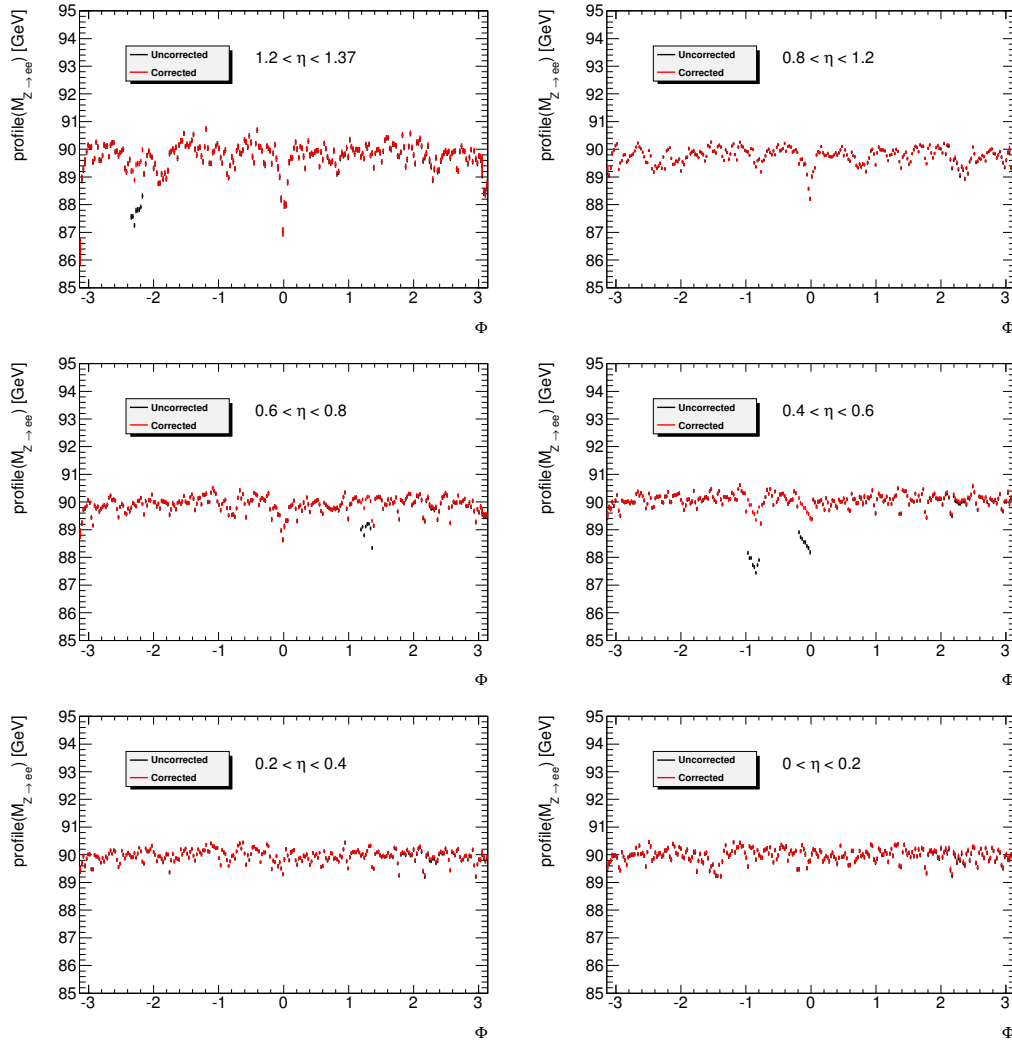


Figure A.2: Barrel C - Profile of  $M_{Z \rightarrow ee}$  along  $\phi$  by bins in  $\eta$ , before and after the HV correction

APPENDIX A. DISTRIBUTION OF THE RECONSTRUCTED  $Z^0$  BOSON MASS IN  
 $Z^0 \rightarrow EE$  EVENTS PROFILED ALONG  $\phi$  IN NARROW  $\eta$  BINS

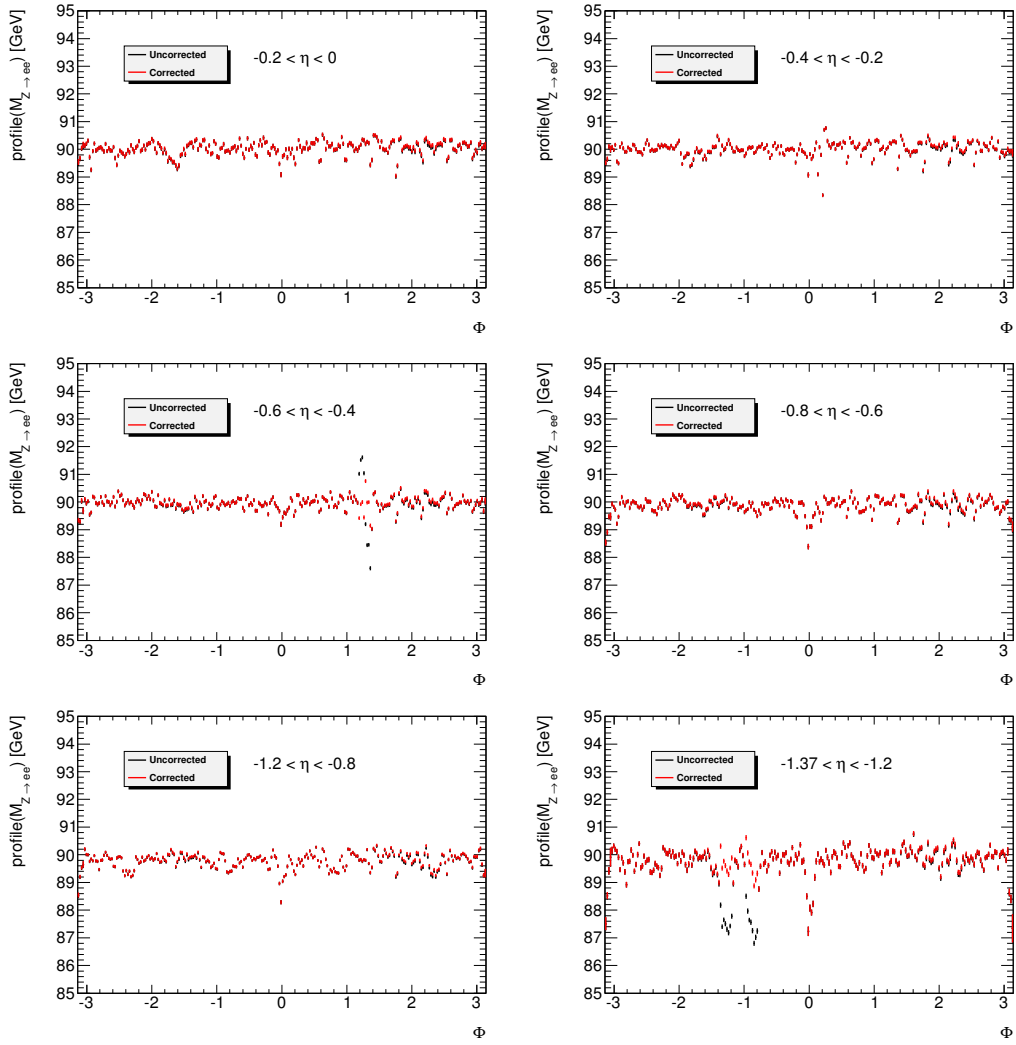


Figure A.3: Barrel A - Profile of  $M_{Z \rightarrow ee}$  along  $\phi$  by bins in  $\eta$ , before and after the HV correction

APPENDIX A. DISTRIBUTION OF THE RECONSTRUCTED  $Z^0$  BOSON MASS IN  $Z^0 \rightarrow ee$  EVENTS PROFILED ALONG  $\phi$  IN NARROW  $\eta$  BINS

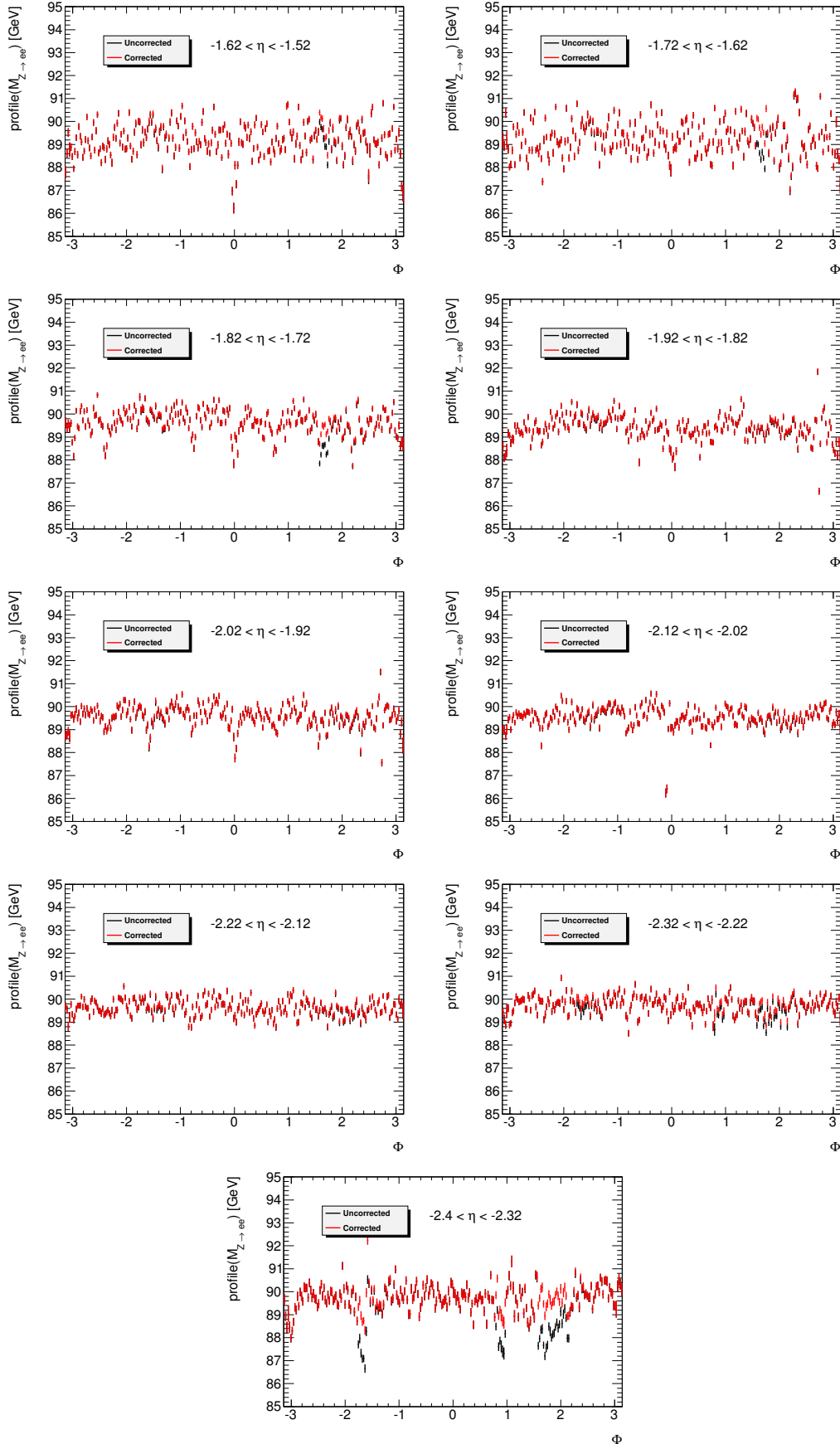


Figure A.4: Endcap A - Profile of  $M_{Z \rightarrow ee}$  along  $\phi$  by bins in  $\eta$ , before and after the HV correction

APPENDIX A. DISTRIBUTION OF THE RECONSTRUCTED  $Z^0$  BOSON MASS IN  
 $Z^0 \rightarrow EE$  EVENTS PROFILED ALONG  $\phi$  IN NARROW  $\eta$  BINS

---

## Appendix B

# Calculation of the error on the mass and of the upper limit on the width as a function of the resolution

**Error on  $m_h$**  The computation that is sketched below was initially done in [304], and shows the variation of the expected error on the mass  $\Delta$  as a function of the peak resolution  $\sigma$ . This error may be defined through  $\frac{1}{\Delta^2} = E(-\frac{\partial^2 \ln \mathcal{L}}{\partial m_h^2})$  where  $\mathcal{L}$  is the likelihood of the experiment and  $E()$  the expectation of a given parameter. This second-order derivative may be developed into :

$$\frac{\partial^2(-\ln \mathcal{L})}{\partial m_h^2} = \left(\frac{\partial \ln \mathcal{L}}{\partial m_h}\right)^2 - \frac{1}{\mathcal{L}} \frac{\partial^2 \mathcal{L}}{\partial m_h^2} \quad (\text{B.1})$$

Now by definition of the expectation we got  $E[\frac{1}{\mathcal{L}} \frac{\partial^2 \mathcal{L}}{\partial m_h^2}] = \int \frac{1}{\mathcal{L}} \frac{\partial^2 \mathcal{L}}{\partial m_h^2} \mathcal{L} dx$  where  $x$  corresponds to the observable, and  $m_h$  is the parameter of interest. The two  $\mathcal{L}$  are factorizing out and the derivative with respect to  $m_h$  may be inverted with the integral, which gives  $E[\frac{1}{\mathcal{L}} \frac{\partial^2 \mathcal{L}}{\partial m_h^2}] = \frac{\partial^2}{\partial m_h^2} (\int \mathcal{L} dx) = 0$  hence the error on the mass is only expressed as

$\frac{1}{\Delta^2} = E[(\frac{\partial \ln \mathcal{L}}{\partial m_h})^2]$  (see also [305] for a slightly different demonstration). For a signal plus background experiment the most general log-likelihood is written as  $\ln \mathcal{L} = -N_S - N_B + \sum_i \ln(N_S P_S + N_B P_B)$ , where  $P_{S,B}$  respectively corresponds to the signal and background PDFs, and if we assume a Gaussian signal the derivative may expressed as

$$E[(\frac{\partial}{\partial m_h} (\ln \mathcal{L}))^2] = \sum_i E[(\frac{N_S P_S}{N_S P_S + N_B P_B} \frac{m_i - m_h}{\sigma^2})^2] = \frac{1}{\Delta^2} \quad (\text{B.2})$$

where the expectation and the sum may be inverted because all the events are independent from each other, which implies that the cross-terms that are appearing in the development of the square are cancelling out in the expectation. So far the only assumption is that the signal peak is Gaussian, which is already an approximation although it is reasonable. It is not possible to go further without making stronger assumptions. Now we assume that the background is flat over the whole mass range that is being considered, and we approximate the mass peak by a square peak that has a non-zero value only in  $[m_h - \sigma; m_h + \sigma]$  where

$\sigma$  is the mass resolution. Then if we denote  $N_B^p$  the number of background events under the signal peak, eq. B.2 translates into :

$$\frac{1}{\Delta^2} = \left(\frac{N_S}{N_S + N_B^p}\right)^2 \sum_{m_i \in [m_h - \sigma; m_h + \sigma]} \left(\frac{m_i - m_h}{\sigma^2}\right)^2 \quad (\text{B.3})$$

If we assume that the background has a contribution to the total number of events under the peak that is much bigger than the signal contribution, this sum may be written as  $\frac{N_B^p}{3\sigma^2}$  which finally gives

$$\Delta = \sigma \frac{\sqrt{3N_B^p}}{N_S} = \sigma \times \sqrt{6}\sigma \times \frac{\sqrt{B/GeV}}{N_S} \quad (\text{B.4})$$

This formula is not perfect because it approximates a Gaussian peak to a square peak, and this is especially a bad approximation if the tails of the distribution are sizeable. But it is known to be a fairly good approximation for the mass measurement in the  $h \rightarrow \gamma\gamma$  channel where it qualitatively reproduces the results that are observed on pseudo-experiments.

**Upper limit on  $\Gamma_h$**  Instead of considering  $\Gamma_h$  itself we consider a measurement of the resolution of a Gaussian mass peak,  $\sigma$ , and the evolution of the limit on the width will then straightforwardly be estimated by considering a case where the convolution between the Breit-Wigner and the Gaussian can be approximated by a convolution between two Gaussian, which corresponds to another Gaussian of standard deviation  $\sigma_{eff} \approx \sqrt{\sigma^2 + \left(\frac{\Gamma}{2.35}\right)^2}$ . The biggest complication is the fact that the derivative involved in the definition of the uncertainty is not with respect to  $m_h$ , but with respect to  $\sigma$ . This gives, with the only assumption of a Gaussian signal :

$$\frac{1}{\Delta^2} = \sum_i E\left[\left(\frac{N_S P_S}{N_S P_S + N_B P_B} \left(\frac{(m_i - m_h)^2}{\sigma^3} - \frac{1}{\sigma}\right)\right)^2\right] \quad (\text{B.5})$$

Now if we apply the trick of approximating the signal peak to a square peak and consider only a flat background, this translates into :

$$\frac{1}{\Delta^2} = \left(\frac{N_S}{N_B^p + N_S}\right)^2 \frac{1}{\sigma^2} \sum_{m_i \in [m_h - \sigma; m_h + \sigma]} \left(\left(\frac{m_i - m_h}{\sigma}\right)^4 + 1 - 2\frac{(m_i - m_h)^2}{\sigma^2}\right) \quad (\text{B.6})$$

where the first part of the sum corresponds to the kurtosis of the distribution ( $\beta$ ), which is equal to 3 for a Gaussian and 1.8 for a square peak. As we only want to have a qualitative estimate of the evolution of the peak with respect to the resolution, the precise value of this multiplicative parameter is not important, as long as we can consider it to be constant, which we assume. Finally we have the following value for the uncertainty on  $\sigma$ , assuming  $N_S < N_B^p$  :

$$\Delta \approx \frac{\sigma \sqrt{N_B^p}}{N_S} \quad (\text{B.7})$$

This gives an uncertainty on the measurement of the resolution, which can also be interpreted as an uncertainty on the width, and we consider the 95% C.L. exclusion limit for the width to be at  $\approx 2\Delta$ . Since  $\sqrt{N_B^p}$  evolves as  $\sqrt{\sigma}$  the limit goes as  $\sigma^{3/2}$ , which corresponds to what is observed on pseudo-experiments in chapter 5 (fig. 5.29).

# Bibliography

- [1] ATLAS Collaboration, G. Aad et al., *The ATLAS Experiment at the CERN Large Hadron Collider*, **JINST** **3** (2008) S08003. 6, 59, 68, 69, 71, 76, 81, 84, 85, 86, 105
- [2] ATLAS Collaboration, *Photon identification efficiency measurements with the ATLAS detector using LHC Run 1 data*, Tech. Rep. To be published, CERN, Geneva. <https://cds.cern.ch/record/1747242>. 6, 60, 93, 94, 95
- [3] *Electron efficiency measurements with the ATLAS detector using the 2012 LHC proton-proton collision data*, Tech. Rep. ATLAS-CONF-2014-032, CERN, Geneva, Jun, 2014. <https://cds.cern.ch/record/1706245>. 6, 60, 96
- [4] N. Andari, *Observation of a BEH-like boson decaying into two photons with the ATLAS detector at the LHC*. PhD thesis, Orsay, LAL, Sep, 2012. <https://cds.cern.ch/record/1485052>. Presented 26 Sep 2012. 14, 89, 93, 157, 168
- [5] S. Weinberg, *The Making of the standard model*, **Eur.Phys.J.** **C34** (2004) 5–13, [arXiv:hep-ph/0401010](https://arxiv.org/abs/hep-ph/0401010) [hep-ph].
- [6] Royal Swedish Academy of Sciences Collaboration, *The BEH-mechanism, interactions with short range forces and scalar particles*, AAPPS Bulletin **23** no. 6, (2013) 3–19.
- [7] A. Borrelli, *The story of the Higgs boson: the origin of mass in early particle physics*, **Eur.Phys.J.** **H40** no. 1, (2015) 1–52.
- [8] J. C. Taylor, *Gauge Theories in the Twentieth Century*. World Scientific, Singapore, 2001. <https://cds.cern.ch/record/517302>.
- [9] V. Ezhela, *Particle Physics: One Hundred Years of Discoveries (An Annotated Chronological Bibliography)*. American Inst. of Physics, 1996. <https://books.google.fr/books?id=D-nANL1FkwYC>. 14
- [10] A. Pais, *Inward Bound: Of Matter and Forces in the Physical World*. Oxford paperbacks. Clarendon Press, 1988. <https://books.google.fr/books?id=mREnwpAqz-YC>. 14
- [11] J. Chadwick, *The intensity distribution in the magnetic spectrum of beta particles from radium (B + C)*, **Verh. Phys. Gesell.** **16** (1914) 383–391. 14

- [12] E. Fermi, *Tentativo di una Teoria Dei Raggi Beta*, *Il Nuovo Cimento* **11** no. 1, (1934) 1–19. <http://dx.doi.org/10.1007/BF02959820>. 14
- [13] T. D. Lee and C. N. Yang, *Question of Parity Conservation in Weak Interactions*, *Phys. Rev.* **104** (1956) 254–258. <http://link.aps.org/doi/10.1103/PhysRev.104.254>. 15
- [14] C. S. Wu, E. Ambler, R. W. Hayward, D. D. Hoppes, and R. P. Hudson, *Experimental Test of Parity Conservation in Beta Decay*, *Phys. Rev.* **105** (1957) 1413–1415. <http://link.aps.org/doi/10.1103/PhysRev.105.1413>. 15
- [15] R. L. Garwin, L. M. Lederman, and M. Weinrich, *Observations of the Failure of Conservation of Parity and Charge Conjugation in Meson Decays: the Magnetic Moment of the Free Muon*, *Phys. Rev.* **105** (1957) 1415–1417. <http://link.aps.org/doi/10.1103/PhysRev.105.1415>. 15
- [16] J. I. Friedman and V. L. Telegdi, *Nuclear Emulsion Evidence for Parity Nonconservation in the Decay Chain  $\pi^+ \rightarrow \mu^+ \rightarrow e^+$* , *Phys. Rev.* **106** (1957) 1290–1293. <http://link.aps.org/doi/10.1103/PhysRev.106.1290>. 15
- [17] J. Schwinger, *A theory of the fundamental interactions*, *Annals of Physics* **2** no. 5, (1957) 407 – 434. <http://www.sciencedirect.com/science/article/pii/0003491657900155>. 15
- [18] S. L. Glashow, *Partial Symmetries of Weak Interactions*, *Nucl. Phys.* **22** (1961) 579–588. 15, 22
- [19] Gargamelle Neutrino Collaboration, F. J. Hasert et al., *Observation of Neutrino Like Interactions Without Muon Or Electron in the Gargamelle Neutrino Experiment*, *Phys. Lett.* **B46** (1973) 138–140. 16
- [20] F. J. Hasert et al., *Search for elastic muon neutrino electron scattering*, *Phys. Lett.* **B46** (1973) 121–124.
- [21] Gargamelle Collaboration, F. J. Hasert et al., *Observation of neutrino like interactions without muon or electron in the Gargamelle neutrino experiment*, *Nucl. Phys.* **B73** (1974) 1. 16
- [22] UA1 Collaboration, G. Arnison et al., *Experimental Observation of Isolated Large Transverse Energy Electrons with Associated Missing Energy at  $s^{*(1/2)} = 540\text{-GeV}$* , *Phys. Lett.* **B122** (1983) 103–116. 16
- [23] UA2 Collaboration, M. Banner et al., *Observation of Single Isolated Electrons of High Transverse Momentum in Events with Missing Transverse Energy at the CERN anti-p p Collider*, *Phys. Lett.* **B122** (1983) 476–485. 16
- [24] UA1 Collaboration, G. Arnison et al., *Experimental Observation of Lepton Pairs of Invariant Mass Around  $95\text{-GeV}/c^{**2}$  at the CERN SPS Collider*, *Phys. Lett.* **B126** (1983) 398–410. 16

- [25] UA2 Collaboration, P. Bagnaia et al., *Evidence for  $Z^0 \rightarrow e^+ e^-$  at the CERN anti- $p$   $p$  Collider*, *Phys. Lett.* **B129** (1983) 130–140. [16](#)
- [26] V. L. Ginzburg and L. D. Landau, *On the Theory of superconductivity*, *Zh. Eksp. Teor. Fiz.* **20** (1950) 1064–1082. [16](#)
- [27] J. Bardeen, L. N. Cooper, and J. R. Schrieffer, *Theory of Superconductivity*, *Phys. Rev.* **108** (1957) 1175–1204.  
<http://link.aps.org/doi/10.1103/PhysRev.108.1175>. [16](#)
- [28] Y. Nambu and G. Jona-Lasinio, *Dynamical Model of Elementary Particles Based on an Analogy with Superconductivity. 1.*, *Phys. Rev.* **122** (1961) 345–358. [16](#)
- [29] Y. Nambu and G. Jona-Lasinio, *Dynamical model of elementary particles based on an analogy with superconductivity. II*, *Phys. Rev.* **124** (1961) 246–254.
- [30] Y. Nambu, *Axial Vector Current Conservation in Weak Interactions*, *Phys. Rev. Lett.* **4** (1960) 380–382.  
<http://link.aps.org/doi/10.1103/PhysRevLett.4.380>. [20](#)
- [31] Y. Nambu, *Quasi-Particles and Gauge Invariance in the Theory of Superconductivity*, *Phys. Rev.* **117** (1960) 648–663.  
<http://link.aps.org/doi/10.1103/PhysRev.117.648>. [16](#), [20](#)
- [32] J. Goldstone, A. Salam, and S. Weinberg, *Broken Symmetries*, *Phys. Rev.* **127** (1962) 965–970. [16](#), [20](#)
- [33] J. Goldstone, *Field Theories with Superconductor Solutions*, *Nuovo Cim.* **19** (1961) 154–164. [16](#), [20](#)
- [34] P. W. Anderson, *Plasmons, Gauge Invariance, and Mass*, *Phys. Rev.* **130** (1963) 439–442. <http://link.aps.org/doi/10.1103/PhysRev.130.439>. [16](#)
- [35] F. Englert and R. Brout, *Broken Symmetry and the Mass of Gauge Vector Mesons*, *Phys. Rev. Lett.* **13** (1964) 321–323.  
<http://link.aps.org/doi/10.1103/PhysRevLett.13.321>. [16](#), [20](#)
- [36] P. W. Higgs, *Broken symmetries, massless particles and gauge fields*, *Phys. Lett.* **12** (1964) 132–133. [16](#)
- [37] P. W. Higgs, *Broken Symmetries and the Masses of Gauge Bosons*, *Phys. Rev. Lett.* **13** (1964) 508–509. [16](#)
- [38] G. S. Guralnik, C. R. Hagen, and T. W. B. Kibble, *Global Conservation Laws and Massless Particles*, *Phys. Rev. Lett.* **13** (1964) 585–587.  
<http://link.aps.org/doi/10.1103/PhysRevLett.13.585>. [16](#), [20](#)
- [39] T. W. B. Kibble, *Symmetry Breaking in Non-Abelian Gauge Theories*, *Phys. Rev.* **155** (1967) 1554–1561. <http://link.aps.org/doi/10.1103/PhysRev.155.1554>. [16](#)

- [40] S. Weinberg, *A Model of Leptons*, *Phys. Rev. Lett.* **19** (1967) 1264–1266.  
<http://link.aps.org/doi/10.1103/PhysRevLett.19.1264>. 16, 22
- [41] A. Salam and J. Ward, *Electromagnetic and weak interactions*, *Physics Letters* **13** no. 2, (1964) 168 – 171.  
<http://www.sciencedirect.com/science/article/pii/0031916364907115>. 16, 22
- [42] ATLAS Collaboration, G. Aad et al., *Observation of a new particle in the search for the Standard Model Higgs boson with the ATLAS detector at the LHC*, *Phys. Lett.* **B716** (2012) 1–29, [arXiv:1207.7214](https://arxiv.org/abs/1207.7214) [hep-ex]. 16, 27
- [43] CMS Collaboration, S. Chatrchyan et al., *Observation of a new boson at a mass of 125 GeV with the CMS experiment at the LHC*, *Phys. Lett.* **B716** (2012) 30–61, [arXiv:1207.7235](https://arxiv.org/abs/1207.7235) [hep-ex]. 16, 27
- [44] S. L. Glashow, J. Iliopoulos, and L. Maiani, *Weak Interactions with Lepton-Hadron Symmetry*, *Phys. Rev. D* **2** (1970) 1285–1292.  
<http://link.aps.org/doi/10.1103/PhysRevD.2.1285>. 17, 22
- [45] E598 Collaboration, J. J. Aubert et al., *Experimental Observation of a Heavy Particle  $J$* , *Phys. Rev. Lett.* **33** (1974) 1404–1406. 17
- [46] J. E. Augustin, A. M. Boyarski, M. Breidenbach, F. Bulos, J. T. Dakin, G. J. Feldman, G. E. Fischer, D. Fryberger, G. Hanson, B. Jean-Marie, R. R. Larsen, V. Lüth, H. L. Lynch, D. Lyon, C. C. Morehouse, J. M. Paterson, M. L. Perl, B. Richter, P. Rapidis, R. F. Schwitters, W. M. Tanenbaum, F. Vannucci, G. S. Abrams, D. Briggs, W. Chinowsky, C. E. Friedberg, G. Goldhaber, R. J. Hollebeek, J. A. Kadyk, B. Lulu, F. Pierre, G. H. Trilling, J. S. Whitaker, J. Wiss, and J. E. Zipse, *Discovery of a Narrow Resonance in  $e^+e^-$  Annihilation*, *Phys. Rev. Lett.* **33** (1974) 1406–1408.  
<http://link.aps.org/doi/10.1103/PhysRevLett.33.1406>. 17
- [47] M. Kobayashi and T. Maskawa, *CP Violation in the Renormalizable Theory of Weak Interaction*, *Prog. Theor. Phys.* **49** (1973) 652–657. 17
- [48] J. H. Christenson, J. W. Cronin, V. L. Fitch, and R. Turlay, *Evidence for the  $2\pi$  Decay of the  $k(2)0$  Meson*, *Phys. Rev. Lett.* **13** (1964) 138–140. 17
- [49] V. C. Rubin, W. K. J. Ford, and N. . Thonnard, *Rotational properties of 21 SC galaxies with a large range of luminosities and radii, from NGC 4605  $/R = 4kpc/$  to UGC 2885  $/R = 122 kpc/$* , *apj* **238** (1980) 471–487. 17
- [50] B. Famaey and S. S. McGaugh, *Modified Newtonian Dynamics (MOND): Observational Phenomenology and Relativistic Extensions*, *Living Reviews in Relativity* **15** no. 10, (2012). <http://www.livingreviews.org/lrr-2012-10>. 17
- [51] R. Davis, D. S. Harmer, and K. C. Hoffman, *Search for Neutrinos from the Sun*, *Phys. Rev. Lett.* **20** (1968) 1205–1209.  
<http://link.aps.org/doi/10.1103/PhysRevLett.20.1205>. 17

- [52] Particle Data Group Collaboration, K. Olive et al., *Review of Particle Physics*, *Chin.Phys.* **C38** (2014) 090001. [17](#), [46](#), [49](#), [76](#), [77](#), [78](#), [104](#)
- [53] G. Marques Tavares, M. Schmaltz, and W. Skiba, *Higgs mass naturalness and scale invariance in the UV*, *Phys.Rev.* **D89** no. 1, (2014) 015009, [arXiv:1308.0025 \[hep-ph\]](#). [17](#)
- [54] D. Buttazzo, G. Degrassi, P. P. Giardino, G. F. Giudice, F. Sala, et al., *Investigating the near-criticality of the Higgs boson*, *JHEP* **1312** (2013) 089, [arXiv:1307.3536 \[hep-ph\]](#). [17](#)
- [55] E. Noether, *Invariant Variation Problems*, *Gott.Nachr.* **1918** (1918) 235–257, [arXiv:physics/0503066 \[physics\]](#). [18](#)
- [56] D. J. Gross, *The role of symmetry in fundamental physics*, Proceedings of the National Academy of Sciences **93** no. 25, (1996). <http://www.pnas.org/content/93/25/>. [18](#)
- [57] J. Iliopoulos, *Introduction to the Standard Model of the Electro-Weak Interactions*, [arXiv:1305.6779 \[hep-ph\]](#). [18](#)
- [58] W. Heisenberg, *Zur Theorie des Ferromagnetismus*, *Zeit.Phys.* **49** no. 9-10, (1928) 619–636. [18](#)
- [59] B. W. Lee, C. Quigg, and H. Thacker, *Weak Interactions at Very High-Energies: The Role of the Higgs Boson Mass*, *Phys.Rev.* **D16** (1977) 1519. [21](#)
- [60] J. M. Cornwall, D. N. Levin, and G. Tiktopoulos, *Derivation of Gauge Invariance from High-Energy Unitarity Bounds on the  $s$  Matrix*, *Phys.Rev.* **D10** (1974) 1145. [21](#)
- [61] A. Salam, *Weak and Electromagnetic Interactions*, Conf. Proc. **C680519** (1968) 367–377. [22](#)
- [62] C. Quigg, *Gauge Theories of the Strong, Weak, and Electromagnetic Interactions: Second Edition*. Princeton University Press, 2013. <https://books.google.fr/books?id=Lt6thfc1gAgC>. [22](#)
- [63] S. Elitzur, *Impossibility of spontaneously breaking local symmetries*, *Phys. Rev. D* **12** (1975) 3978–3982. <http://link.aps.org/doi/10.1103/PhysRevD.12.3978>. [23](#)
- [64] S. Friederich, *Gauge symmetry breaking in gauge theories—In search of clarification*, ArXiv e-prints (2011), [arXiv:1107.4664](#). [24](#)
- [65] V. Gribov and L. Lipatov, *Deep inelastic  $e p$  scattering in perturbation theory*, *Sov.J.Nucl.Phys.* **15** (1972) 438–450. [25](#), [215](#)
- [66] Y. L. Dokshitzer, *Calculation of the Structure Functions for Deep Inelastic Scattering and  $e+ e-$  Annihilation by Perturbation Theory in Quantum Chromodynamics.*, *Sov.Phys.JETP* **46** (1977) 641–653.

- [67] G. Altarelli and G. Parisi, *Asymptotic Freedom in Parton Language*, *Nucl.Phys.* **B126** (1977) 298. 25, 215
- [68] A. Vogt, S. Moch, and J. Vermaseren, *The Three-loop splitting functions in QCD: The Singlet case*, *Nucl.Phys.* **B691** (2004) 129–181, [arXiv:hep-ph/0404111](#) [[hep-ph](#)]. 25
- [69] S. Moch, J. Vermaseren, and A. Vogt, *The Three loop splitting functions in QCD: The Nonsinglet case*, *Nucl.Phys.* **B688** (2004) 101–134, [arXiv:hep-ph/0403192](#) [[hep-ph](#)]. 25
- [70] A. Martin, W. Stirling, R. Thorne, and G. Watt, *Parton distributions for the LHC*, *Eur.Phys.J.* **C63** (2009) 189–285, [arXiv:0901.0002](#) [[hep-ph](#)]. 25, 26, 43
- [71] S. Forte and G. Watt, *Progress in the Determination of the Partonic Structure of the Proton*, *Ann.Rev.Nucl.Part.Sci.* **63** (2013) 291–328, [arXiv:1301.6754](#) [[hep-ph](#)]. 25
- [72] J. Rojo et al., *The PDF4LHC report on PDFs and LHC data: Results from Run I and preparation for Run II*, [arXiv:1507.00556](#) [[hep-ph](#)]. 25, 27
- [73] S. Dulat, T. J. Hou, J. Gao, M. Guzzi, J. Huston, et al., *The CT14 Global Analysis of Quantum Chromodynamics*, [arXiv:1506.07443](#) [[hep-ph](#)]. 26
- [74] P. M. Nadolsky, H.-L. Lai, Q.-H. Cao, J. Huston, J. Pumplin, et al., *Implications of CTEQ global analysis for collider observables*, *Phys.Rev.* **D78** (2008) 013004, [arXiv:0802.0007](#) [[hep-ph](#)]. 26
- [75] NNPDF Collaboration, R. D. Ball et al., *Parton distributions for the LHC Run II*, *JHEP* **1504** (2015) 040, [arXiv:1410.8849](#) [[hep-ph](#)]. 26
- [76] M. Botje, J. Butterworth, A. Cooper-Sarkar, A. de Roeck, J. Feltesse, et al., *The PDF4LHC Working Group Interim Recommendations*, [arXiv:1101.0538](#) [[hep-ph](#)]. 26
- [77] J. Gao and P. Nadolsky, *A meta-analysis of parton distribution functions*, *JHEP* **1407** (2014) 035, [arXiv:1401.0013](#) [[hep-ph](#)]. 26
- [78] G. Watt, *Parton distribution function dependence of benchmark Standard Model total cross sections at the 7 TeV LHC*, *JHEP* **1109** (2011) 069, [arXiv:1106.5788](#) [[hep-ph](#)]. 27
- [79] R. D. Ball, *Global Parton Distributions for the LHC Run II*, in *29th Rencontres de Physique de La Vallée d’Aoste La Thuile, Aosta, Italy, March 1-7, 2015*. 2015. [arXiv:1507.07891](#) [[hep-ph](#)]. <http://inspirehep.net/record/1385320/files/arXiv:1507.07891.pdf>. 27
- [80] A. Djouadi, *Higgs Physics: Theory*, *Pramana* **79** (2012) 513–539, [arXiv:1203.4199](#) [[hep-ph](#)]. 28

- [81] LHC Higgs Cross Section Working Group Collaboration, S. Heinemeyer et al., *Handbook of LHC Higgs Cross Sections: 3. Higgs Properties*, [arXiv:1307.1347 \[hep-ph\]](#). 28, 29, 31, 175, 210, 221
- [82] M. Grazzini and H. Sargsyan, *Heavy-quark mass effects in Higgs boson production at the LHC*, *JHEP* **1309** (2013) 129, [arXiv:1306.4581 \[hep-ph\]](#). 29, 175, 215, 216, 217
- [83] D. de Florian, G. Ferrera, M. Grazzini, and D. Tommasini, *Higgs boson production at the LHC: transverse momentum resummation effects in the  $H \rightarrow 2\gamma$ ,  $H \rightarrow WW \rightarrow l\nu l\nu$  and  $H \rightarrow ZZ \rightarrow 4l$  decay modes*, *JHEP* **1206** (2012) 132, [arXiv:1203.6321 \[hep-ph\]](#). 29, 175, 216
- [84] D. de Florian and M. Grazzini, *Higgs production at the LHC: updated cross sections at  $\sqrt{s} = 8$  TeV*, *Phys. Lett.* **B718** (2012) 117–120, [arXiv:1206.4133 \[hep-ph\]](#). 29
- [85] C. Anastasiou, C. Duhr, F. Dulat, E. Furlan, T. Gehrmann, et al., *Higgs boson gluon–fusion production at threshold in  $N^3$ LO QCD*, *Phys.Lett.* **B737** (2014) 325–328, [arXiv:1403.4616 \[hep-ph\]](#). 29
- [86] S. Alioli, P. Nason, C. Oleari, and E. Re, *NLO Higgs boson production via gluon fusion matched with shower in POWHEG*, *JHEP* **0904** (2009) 002, [arXiv:0812.0578 \[hep-ph\]](#). 29, 212
- [87] E. Bagnaschi, G. Degrossi, P. Slavich, and A. Vicini, *Higgs production via gluon fusion in the POWHEG approach in the SM and in the MSSM*, *JHEP* **1202** (2012) 088, [arXiv:1111.2854 \[hep-ph\]](#). 29
- [88] T. Sjostrand, S. Mrenna, and P. Z. Skands, *A Brief Introduction to PYTHIA 8.1*, *Comput.Phys.Commun.* **178** (2008) 852–867, [arXiv:0710.3820 \[hep-ph\]](#). 29, 212
- [89] E. Scifo, *Measurement of the Brout-Englert-Higgs boson couplings in its diphoton decay channel with the ATLAS detector at the LHC. Mesure des couplages du boson de Brout-Englert-Higgs se désintégrant en deux photons par l'expérience ATLAS au LHC*. PhD thesis, U. Paris-Sud 11, Dept. Phys., Orsay, Jul, 2014. <https://cds.cern.ch/record/1756391>. Presented 11 Jul 2014. 29, 57, 93, 165, 168, 169, 175, 189, 216
- [90] A. Denner, S. Dittmaier, S. Kallweit, and A. Mück, *HAWK 2.0: A Monte Carlo program for Higgs production in vector-boson fusion and Higgs strahlung at hadron colliders*, *Comput.Phys.Commun.* **195** (2015) 161–171, [arXiv:1412.5390 \[hep-ph\]](#). 30
- [91] M. Garzelli, A. Kardos, C. Papadopoulos, and Z. Trocsanyi, *Standard Model Higgs boson production in association with a top anti-top pair at NLO with parton showering*, *Europhys.Lett.* **96** (2011) 11001, [arXiv:1108.0387 \[hep-ph\]](#). 30
- [92] LHC cross-section working group. 30

- [93] A. Djouadi, J. Kalinowski, and M. Spira, *HDECAY: A Program for Higgs boson decays in the standard model and its supersymmetric extension*, *Comput.Phys.Commun.* **108** (1998) 56–74, [arXiv:hep-ph/9704448 \[hep-ph\]](#). 30
- [94] A. Bredenstein, A. Denner, S. Dittmaier, and M. Weber, *Precision calculations for  $H \rightarrow WW/ZZ \rightarrow 4\text{fermions}$  with PROPHECY4f*, [arXiv:0708.4123 \[hep-ph\]](#). 30
- [95] *Calibration of the performance of b-tagging for c and light-flavour jets in the 2012 ATLAS data*, Tech. Rep. ATLAS-CONF-2014-046, CERN, Geneva, Jul, 2014. <http://cds.cern.ch/record/1741020>. 32
- [96] *Calibration of b-tagging using dileptonic top pair events in a combinatorial likelihood approach with the ATLAS experiment*, Tech. Rep. ATLAS-CONF-2014-004, CERN, Geneva, Feb, 2014. <http://cds.cern.ch/record/1664335>. 32
- [97] G. T. Bodwin, F. Petriello, S. Stoynev, and M. Velasco, *Higgs boson decays to quarkonia and the  $H\bar{c}c$  coupling*, *Phys. Rev.* **D88** no. 5, (2013) 053003, [arXiv:1306.5770 \[hep-ph\]](#). 32
- [98] ATLAS Collaboration, G. Aad et al., *Search for Higgs and Z Boson Decays to  $J/\Psi\gamma$  and  $\nu(nS)\gamma$  with the ATLAS Detector*, *Phys. Rev. Lett.* **114** no. 12, (2015) 121801, [arXiv:1501.03276 \[hep-ex\]](#). 32
- [99] *Measurements of the Higgs boson production and decay rates and coupling strengths using pp collision data at  $\sqrt{s} = 7$  and 8 TeV in the ATLAS experiment*, Tech. Rep. ATLAS-CONF-2015-007, CERN, Geneva, Mar, 2015. <http://cds.cern.ch/record/2002212>. 33, 43, 211
- [100] ECFA Higgs Working Group Collaboration, C. J. Seez, T. S. Virdee, L. Di Lella, R. H. Kleiss, Z. Kunszt, and W. J. Stirling, *Photon decay modes of the intermediate mass Higgs*,. <http://cds.cern.ch/record/220524>. 33
- [101] L. Fayard and G. Unal, *Search for Higgs decay into photons with EAGLE. Add. 1 Addendum on the Higgs search with photons. Add. 2 (final?) update on Higgs decay to photons*, Tech. Rep. ATL-PHYS-92-001. ATL-GE-PN-1, CERN, Geneva, Dec, 1992. <http://cds.cern.ch/record/682120>. 33
- [102] A. Djouadi, *The Anatomy of electro-weak symmetry breaking. I: The Higgs boson in the standard model*, *Phys.Rept.* **457** (2008) 1–216, [arXiv:hep-ph/0503172 \[hep-ph\]](#). 33, 209, 210
- [103] M. E. Peskin and D. V. Schroeder, *An introduction to quantum field theory*. Advanced book program. Westview Press Reading (Mass.), Boulder (Colo.), 1995. <http://opac.inria.fr/record=b1131978>. Autre tirage : 1997. 34, 35
- [104] D. Y. Bardin, S. M. Bilenky, W. Beenakker, F. A. Berends, W. L. van Neerven, S. C. Van der Marck, G. Burgers, W. F. L. Hollik, T. Riemann, and M. Sachwitz, *Z line shape*,. <https://cds.cern.ch/record/199969>. 34, 186

- [105] S. Goria, G. Passarino, and D. Rosco, *The Higgs Boson Lineshape*, *Nucl.Phys.* **B864** (2012) 530–579, [arXiv:1112.5517 \[hep-ph\]](#). 35, 186
- [106] ATLAS Collaboration, G. Aad et al., *Constraints on the off-shell Higgs boson signal strength in the high-mass ZZ and WW final states with the ATLAS detector*, [arXiv:1503.01060 \[hep-ex\]](#). 35, 41
- [107] CMS Collaboration, V. Khachatryan et al., *Constraints on the Higgs boson width from off-shell production and decay to Z-boson pairs*, *Phys. Lett.* **B736** (2014) 64, [arXiv:1405.3455 \[hep-ex\]](#). 35, 41
- [108] G. Breit and E. Wigner, *Capture of Slow Neutrons*, *Phys. Rev.* **49** (1936) 519–531. <http://link.aps.org/doi/10.1103/PhysRev.49.519>. 35
- [109] D. A. Dicus and S. S. Willenbrock, *Photon Pair Production and the Intermediate Mass Higgs Boson*, *Phys.Rev.* **D37** (1988) 1801. 36
- [110] L. J. Dixon and M. S. Siu, *Resonance continuum interference in the diphoton Higgs signal at the LHC*, *Phys.Rev.Lett.* **90** (2003) 252001, [arXiv:hep-ph/0302233 \[hep-ph\]](#). 36, 207
- [111] S. P. Martin, *Interference of Higgs diphoton signal and background in production with a jet at the LHC*, *Phys.Rev.* **D88** no. 1, (2013) 013004, [arXiv:1303.3342 \[hep-ph\]](#). 36, 38, 208
- [112] L. J. Dixon and Y. Li, *Bounding the Higgs Boson Width Through Interferometry*, *Phys.Rev.Lett.* **111** (2013) 111802, [arXiv:1305.3854 \[hep-ph\]](#). 36, 37, 38, 40, 208, 211, 219, 229
- [113] D. de Florian, N. Fidanza, R. Hernández-Pinto, J. Mazzitelli, Y. Rotstein Habarnau, et al., *A complete  $O(\alpha_S^2)$  calculation of the signal-background interference for the Higgs diphoton decay channel*, *Eur.Phys.J.* **C73** no. 4, (2013) 2387, [arXiv:1303.1397 \[hep-ph\]](#). 36, 208
- [114] Z. Bern, L. J. Dixon, and C. Schmidt, *Isolating a light Higgs boson from the diphoton background at the CERN LHC*, *Phys.Rev.* **D66** (2002) 074018, [arXiv:hep-ph/0206194 \[hep-ph\]](#). 38, 208, 221
- [115] D. de Florian, *Private Communication*,. 39
- [116] F. Coradeschi, D. de Florian, L. Dixon, N. Fidanza, S. Hoeche, et al., *Interference effects in the  $H(\rightarrow \gamma\gamma) + 2$  jets channel at the LHC*, [arXiv:1504.05215 \[hep-ph\]](#). 39, 40, 208, 228
- [117] J. R. Andersen and J. M. Smillie, *QCD and electroweak interference in Higgs production by gauge boson fusion*, *Phys. Rev.* **D75** (2007) 037301, [arXiv:hep-ph/0611281 \[hep-ph\]](#). 39
- [118] J. R. Andersen, T. Binoth, G. Heinrich, and J. M. Smillie, *Loop induced interference effects in Higgs Boson plus two jet production at the LHC*, *JHEP* **02** (2008) 057, [arXiv:0709.3513 \[hep-ph\]](#).

- [119] M. Ciccolini, A. Denner, and S. Dittmaier, *Electroweak and QCD corrections to Higgs production via vector-boson fusion at the LHC*, *Phys. Rev.* **D77** (2008) 013002, [arXiv:0710.4749 \[hep-ph\]](#).
- [120] A. Bredenstein, K. Hagiwara, and B. Jager, *Mixed QCD-electroweak contributions to Higgs-plus-dijet production at the LHC*, *Phys. Rev.* **D77** (2008) 073004, [arXiv:0801.4231 \[hep-ph\]](#). 39
- [121] J. Alwall, R. Frederix, S. Frixione, V. Hirschi, F. Maltoni, et al., *The automated computation of tree-level and next-to-leading order differential cross sections, and their matching to parton shower simulations*, *JHEP* **1407** (2014) 079, [arXiv:1405.0301 \[hep-ph\]](#). 40
- [122] E. Vryonidou, *MadGraph5\_aMC@NLO update*, <https://indico.cern.ch/event/400327/>. 40
- [123] CMS Collaboration, V. Khachatryan et al., *Limits on the Higgs boson lifetime and width from its decay to four charged leptons*, [arXiv:1507.06656 \[hep-ex\]](#). 41
- [124] F. Caola and K. Melnikov, *Constraining the Higgs boson width with ZZ production at the LHC*, *Phys.Rev.* **D88** (2013) 054024, [arXiv:1307.4935 \[hep-ph\]](#). 41
- [125] N. Kauer and G. Passarino, *Inadequacy of zero-width approximation for a light Higgs boson signal*, *JHEP* **08** (2012) 116, [arXiv:1206.4803 \[hep-ph\]](#). 42
- [126] C. Englert and M. Spannowsky, *Limitations and Opportunities of Off-Shell Coupling Measurements*, *Phys. Rev.* **D90** (2014) 053003, [arXiv:1405.0285 \[hep-ph\]](#). 43
- [127] H. E. Logan, *Hiding a Higgs width enhancement from off-shell  $gg (-> h^*) -> ZZ$  measurements*, [arXiv:1412.7577 \[hep-ph\]](#). 43
- [128] J. S. Gainer, J. Lykken, K. T. Matchev, S. Mrenna, and M. Park, *Beyond Geolocating: Constraining Higher Dimensional Operators in  $H \rightarrow 4\ell$  with Off-Shell Production and More*, *Phys. Rev.* **D91** no. 3, (2015) 035011, [arXiv:1403.4951 \[hep-ph\]](#). 43
- [129] ATLAS Collaboration, G. Aad et al., *Measurements of the Higgs boson production and decay rates and coupling strengths using pp collision data at  $\sqrt{s} = 7$  and 8 TeV in the ATLAS experiment*, [arXiv:1507.04548 \[hep-ex\]](#). 43, 44
- [130] CMS Collaboration, V. Khachatryan et al., *Precise determination of the mass of the Higgs boson and tests of compatibility of its couplings with the standard model predictions using proton collisions at 7 and 8 TeV*, *Eur. Phys. J.* **C75** no. 5, (2015) 212, [arXiv:1412.8662 \[hep-ex\]](#). 43, 228
- [131] LHC Higgs Cross Section Working Group Collaboration, A. David, A. Denner, M. Duehrssen, M. Grazzini, C. Grojean, G. Passarino, M. Schumacher, M. Spira, G. Weiglein, and M. Zanetti, *LHC HXSWG interim recommendations to explore the coupling structure of a Higgs-like particle*, [arXiv:1209.0040 \[hep-ph\]](#). 43

- [132] J. F. Gunion, H. E. Haber, and J. Wudka, *Sum rules for Higgs bosons*, *Phys. Rev. D* **43** (1991) 904–912. <http://link.aps.org/doi/10.1103/PhysRevD.43.904>. 43
- [133] B. A. Dobrescu and J. D. Lykken, *Coupling spans of the Higgs-like boson*, *JHEP* **02** (2013) 073, [arXiv:1210.3342](https://arxiv.org/abs/1210.3342) [hep-ph].
- [134] M. E. Peskin, *Comparison of LHC and ILC Capabilities for Higgs Boson Coupling Measurements*, [arXiv:1207.2516](https://arxiv.org/abs/1207.2516) [hep-ph].
- [135] M. Duhrssen, S. Heinemeyer, H. Logan, D. Rainwater, G. Weiglein, and D. Zeppenfeld, *Extracting Higgs boson couplings from CERN LHC data*, *Phys. Rev. D* **70** (2004) 113009, [arXiv:hep-ph/0406323](https://arxiv.org/abs/hep-ph/0406323) [hep-ph].
- [136] M. Duhrssen, S. Heinemeyer, H. Logan, D. Rainwater, G. Weiglein, and D. Zeppenfeld, *Determination of Higgs-boson couplings at the LHC*, 2004. [arXiv:hep-ph/0407190](https://arxiv.org/abs/hep-ph/0407190) [hep-ph]. [http://inspirehep.net/record/654651/files/arXiv:hep-ph\\_0407190.pdf](http://inspirehep.net/record/654651/files/arXiv:hep-ph_0407190.pdf). 43
- [137] H. E. Logan and M.-A. Roy, *Higgs couplings in a model with triplets*, *Phys. Rev. D* **82** (2010) 115011, [arXiv:1008.4869](https://arxiv.org/abs/1008.4869) [hep-ph]. 43
- [138] ALEPH, DELPHI, L3, OPAL, SLD, LEP Electroweak Working Group, SLD Electroweak Group, SLD Heavy Flavour Group Collaboration, S. Schael et al., *Precision electroweak measurements on the Z resonance*, *Phys.Rept.* **427** (2006) 257–454, [arXiv:hep-ex/0509008](https://arxiv.org/abs/hep-ex/0509008) [hep-ex]. 44, 104, 186
- [139] L. Arnaudon, B. Dehning, P. Grosse-Wiesmann, R. Jacobsen, M. Jonker, J. Koutchouk, J. Miles, R. Olsen, M. Placidi, R. Schmidt, J. Wenninger, R. Assmann, and A. Blondel, *Accurate determination of the LEP beam energy by resonant depolarization*, *Zeitschrift für Physik C Particles and Fields* **66** no. 1-2, (1995) 45–62. <http://dx.doi.org/10.1007/BF01496579>. 44
- [140] TLEP Design Study Working Group Collaboration, M. Bicer et al., *First Look at the Physics Case of TLEP*, *JHEP* **01** (2014) 164, [arXiv:1308.6176](https://arxiv.org/abs/1308.6176) [hep-ex]. 44
- [141] T. Behnke, J. E. Brau, B. Foster, J. Fuster, M. Harrison, et al., *The International Linear Collider Technical Design Report - Volume 1: Executive Summary*, [arXiv:1306.6327](https://arxiv.org/abs/1306.6327) [physics.acc-ph]. 44
- [142] T. Han and Z. Liu, *Potential precision of a direct measurement of the Higgs boson total width at a muon collider*, *Phys. Rev. D* **87** no. 3, (2013) 033007, [arXiv:1210.7803](https://arxiv.org/abs/1210.7803) [hep-ph]. 44
- [143] A. Conway and H. Wenzel, *Higgs Measurements at a Muon Collider*, [arXiv:1304.5270](https://arxiv.org/abs/1304.5270) [hep-ex]. 44
- [144] H. Li, *Higgs Recoil Mass and Cross-Section Analysis at ILC AND Calibration of the CALICE SiW ECAL Prototype*. Theses, Université Paris Sud - Paris XI, Oct., 2009. <https://tel.archives-ouvertes.fr/tel-00430432>. 44

- [145] K. Fujii et al., *Physics Case for the International Linear Collider*, [arXiv:1506.05992 \[hep-ex\]](#). 44
- [146] H. Baer, T. Barklow, K. Fujii, Y. Gao, A. Hoang, et al., *The International Linear Collider Technical Design Report - Volume 2: Physics*, [arXiv:1306.6352 \[hep-ph\]](#). 44
- [147] CLIC Detector and Physics Study Collaboration, H. Abramowicz et al., *Physics at the CLIC  $e+e-$  Linear Collider – Input to the Snowmass process 2013*, [arXiv:1307.5288 \[hep-ex\]](#). 44
- [148] A. Armbruster, *Discovery of a Higgs Boson with the ATLAS Detector*. PhD thesis, Michigan U., May, 2013. <https://cds.cern.ch/record/1553771>. Presented 02 May 2013. 47
- [149] J. Aldrich, *R.A. Fisher and the making of maximum likelihood 1912-1922*, *Statist. Sci.* **12** no. 3, (1997) 162–176. <http://dx.doi.org/10.1214/ss/1030037906>. 47
- [150] H. Cramer, *Mathematical methods of statistics*. Princeton Math. Princeton Univ. Press, Princeton, NJ, 1954. <https://cds.cern.ch/record/107581>. 47
- [151] K. Cranmer, *Practical Statistics for the LHC*, [arXiv:1503.07622 \[physics.data-an\]](#). 49, 50, 51
- [152] G. Cowan, *Statistical Data Analysis*. Oxford University Press, Oxford, 1998. 49
- [153] J. Neyman and E. S. Pearson, *On the Problem of the Most Efficient Tests of Statistical Hypotheses*, *Royal Society of London Philosophical Transactions Series A* **231** (1933) 289–337. 50
- [154] *Procedure for the LHC Higgs boson search combination in summer 2011*, Tech. Rep. ATL-PHYS-PUB-2011-011, CERN, Geneva, Aug, 2011. <https://cds.cern.ch/record/1375842>. 50, 55
- [155] J. Neyman, *Outline of a Theory of Statistical Estimation Based on the Classical Theory of Probability*, *Philosophical Transactions of the Royal Society of London A: Mathematical, Physical and Engineering Sciences* **236** no. 767, (1937) 333–380. 50
- [156] G. Cowan, K. Cranmer, E. Gross, and O. Vitells, *Asymptotic formulae for likelihood-based tests of new physics*, *Eur.Phys.J.* **C71** (2011) 1554, [arXiv:1007.1727 \[physics.data-an\]](#). 52, 53, 55, 56, 188
- [157] A. L. Read, *Presentation of search results: The  $CL(s)$  technique*, *J.Phys.* **G28** (2002) 2693–2704. 52, 192
- [158] G. J. Feldman and R. D. Cousins, *Unified approach to the classical statistical analysis of small signals*, *prd* **57** (1998) 3873–3889, [physics/9711021](#). 53, 188
- [159] G. Cowan, *Statistical Methods for Discovery and Limits in HEP Experiments*, [http://hacol13.physik.uni-freiburg.de/graduierntenkolleg/lectures/Cowan/cowan\\_freiburg\\_2011\\_3.pdf](http://hacol13.physik.uni-freiburg.de/graduierntenkolleg/lectures/Cowan/cowan_freiburg_2011_3.pdf). 54

- [160] G. Cowan, K. Cranmer, E. Gross, and O. Vitells, *Power-Constrained Limits*, ArXiv e-prints (2011), [arXiv:1105.3166 \[physics.data-an\]](#). 54
- [161] A. S. Forum, *Frequentist Limit Recommendation*, [https://twiki.cern.ch/twiki/pub/AtlasProtected/StatisticsTools/Frequentist\\_Limit\\_Recommendation.pdf](https://twiki.cern.ch/twiki/pub/AtlasProtected/StatisticsTools/Frequentist_Limit_Recommendation.pdf). 55
- [162] K. Cranmer, *Statistical Challenges for Searches for New Physics at the LHC*, p. , 112. 2006. [physics/0511028](#). 55
- [163] S. S. Wilks, *The Large-Sample Distribution of the Likelihood Ratio for Testing Composite Hypotheses*, *Ann. Math. Statist.* **9** no. 1, (1938) 60–62. <http://dx.doi.org/10.1214/aoms/1177732360>. 55
- [164] A. Wald, *Tests of statistical hypotheses concerning several parameters when the number of observations is large*, *Transactions of the American Mathematical Society* **54** no. 3, (1943) 426–482. 55
- [165] A. Newborough, M. Buzio, and R. Chritin, *Upgrade of the CERN Proton Synchrotron Booster Bending Magnets for 2 GeV Operation*, *IEEE Trans.Appl.Supercond.* **24** no. 3, (2014) 0500304. 61
- [166] J. Haffner, *The CERN accelerator complex. Complexe des accélérateurs du CERN*, General Photo. 61
- [167] LHC Magnets List at the LHC machine outreach. [https://lhc-machine-outreach.web.cern.ch/lhc-machine-outreach/components/magnets/types\\_of\\_magnets.htm](https://lhc-machine-outreach.web.cern.ch/lhc-machine-outreach/components/magnets/types_of_magnets.htm). 62
- [168] R. Bailey and P. Collier, *Standard Filling Schemes for Various LHC Operation Modes*, Tech. Rep. LHC-PROJECT-NOTE-323, CERN, Geneva, Sep, 2003. 63
- [169] M. Hostettler and G. Papotti, *Observations from LHC proton-proton physics operation*, [arXiv:1409.5216 \[physics.acc-ph\]](#). 64
- [170] S. van der Meer, *Calibration of the effective beam height in the ISR*, Tech. Rep. CERN-ISR-PO-68-31. ISR-PO-68-31, CERN, Geneva, 1968. 65
- [171] S. M. White, *Determination of the Absolute Luminosity at the LHC*. PhD thesis, Orsay, Université Paris-Sud 11, Orsay, 2010. <http://cds.cern.ch/record/1308187>. Presented on 11 Oct 2010. 65
- [172] P. Grafstrom and W. Kozanecki, *Luminosity determination at proton colliders*, *Prog.Part.Nucl.Phys.* **81** (2015) 97–148.
- [173] ATLAS Collaboration, G. Aad et al., *Luminosity Determination in pp Collisions at  $\sqrt{s} = 7$  TeV Using the ATLAS Detector at the LHC*, *Eur.Phys.J.* **C71** (2011) 1630, [arXiv:1101.2185 \[hep-ex\]](#).

- [174] ATLAS Collaboration, G. Aad et al., *Improved luminosity determination in pp collisions at  $\sqrt{s} = 7$  TeV using the ATLAS detector at the LHC*, *Eur.Phys.J. C* **73** no. 8, (2013) 2518, [arXiv:1302.4393 \[hep-ex\]](#). 65, 75
- [175] W.J.Stirling, *Private communication*,  
<http://www.hep.ph.ic.ac.uk/~wstirling/plots/plots.html>. 67
- [176] M. Escalier, L. Fayard, and J.-F. Marchand, *Reconstruction of the z vertex and direction of the photon*, Tech. Rep. ATL-COM-PHYS-2009-614, CERN, Geneva, Nov, 2009. <https://cds.cern.ch/record/1222687>. 69, 169
- [177] ATLAS Collaboration, *ATLAS central solenoid: Technical design report*,. 70
- [178] M. Aleksa, F. Bergsma, P. Giudici, A. Kehrli, M. Losasso, et al., *Measurement of the ATLAS solenoid magnetic field*, *JINST* **3** (2008) P04003. 70
- [179] ATLAS Collaboration, G. Aad et al., *Measurement of the muon reconstruction performance of the ATLAS detector using 2011 and 2012 LHC proton-proton collision data*, *Eur.Phys.J. C* **74** no. 11, (2014) 3130, [arXiv:1407.3935 \[hep-ex\]](#). 74
- [180] ATLAS Collaboration, *Expected performance of the ATLAS experiment: detector, trigger and physics*. CERN, Geneva, 2009.  
<https://cds.cern.ch/record/1125884>. 74
- [181] ATLAS Collaboration, G. Aad et al., *Commissioning of the ATLAS Muon Spectrometer with Cosmic Rays*, *Eur.Phys.J. C* **70** (2010) 875–916,  
[arXiv:1006.4384 \[physics.ins-det\]](#). 75
- [182] D. Fournier, *Liquid argon calorimetry*,. <https://cds.cern.ch/record/220648>. 76
- [183] V. N. Ivanchenko, *Geant4 toolkit for simulation of HEP experiments*, *Nucl. Instrum. Methods Phys. Res., A* **502** (2003) 666–668.  
<http://cds.cern.ch/record/624968>. 76
- [184] GEANT4 Collaboration, S. Agostinelli et al., *GEANT4: A Simulation toolkit*, *Nucl.Instrum.Meth. A* **506** (2003) 250–303. 76
- [185] L. Serin, *Cours de physique des detecteurs pour le NPAC*,  
<http://npac.lal.in2p3.fr/1st-semester-lectures/>. 79, 80
- [186] M. Hance, *Measurement of Inclusive Isolated Prompt Photon Production in Proton-Proton Collisions at  $\sqrt{s} = 7$  TeV with the ATLAS Detector*. PhD thesis, Pennsylvania U., Philadelphia, 2011. <http://cds.cern.ch/record/1367057>. Presented 11 Jul 2011. 80
- [187] RD3 Collaboration Collaboration, B. Aubert, A. Bazan, F. Cavanna, J. Colas, T. Le Flour, J. P. Vialle, H. A. Gordon, V. Polychronakos, V. Radeka, D. C. Rahm, D. Stephani, L. Baisin, J. C. Berset, C. W. Fabjan, D. Fournier, O. Gildemeister, P. Jenni, M. Lefebvre, C. P. Marin, M. Nessi, F. Nessi-Tedaldi,

- M. Pepé, G. Polesello, W. Richter, A. Sigrist, W. J. Willis, D. V. Camin, G. Costa, F. Gianotti, L. Mandelli, G. Pessina, L. Iconomidou-Fayard, B. Merkel, P. Pétrouff, and J. P. Repellin, *Performance of a liquid argon electromagnetic calorimeter with an "accordion" geometry*, Nucl. Instrum. Methods Phys. Res., A **309** no. CERN-PPE-91-73, (1991) 438–449. 28 p.  
<https://cds.cern.ch/record/220837>. 81
- [188] ATLAS Collaboration, *ATLAS liquid argon calorimeter: Technical design report*, 81, 88, 91
- [189] D. Fournier, L. Hervás, and S. Tisserant, *Burning shorts in ATLAS Liquid Argon Electromagnetic calorimeter modules*, Tech. Rep. ATL-COM-LARG-2006-001, CERN, Geneva, Feb, 2006. <https://cds.cern.ch/record/929929>. 82
- [190] L. Di Ciaccio, D. Fournier, and F. Hubaut, *High Voltage corrections for electromagnetic calorimeter*, Tech. Rep. ATL-COM-LARG-2005-003, CERN, Geneva, Apr, 2005. <https://cds.cern.ch/record/830849>. 82
- [191] J. Pequenaó, "Computer generated image of the ATLAS Liquid Argon." Mar, 2008. 83
- [192] F. Gianotti, G. Battistoni, D. Camin, D. Cavalli, G. Costa, et al., *Liquid argon calorimetry with LHC performance specifications*, Nucl.Instrum.Meth. **A315** (1992) 285–293. 83
- [193] ATLAS Electromagnetic Barrel Liquid Argon Calorimeter Group Collaboration, B. Aubert et al., *Construction, assembly and tests of the ATLAS electromagnetic barrel calorimeter*, Nucl. Instrum. Meth. **A558** (2006) 388–418. 84
- [194] N. Buchanan, L. Chen, D. Gingrich, S. Liu, H. Chen, et al., *ATLAS liquid argon calorimeter front end electronics*, JINST **3** (2008) P09003. 86, 87
- [195] N. Buchanan, L. Chen, D. Gingrich, S. Liu, H. Chen, et al., *Design and implementation of the Front End Board for the readout of the ATLAS liquid argon calorimeters*, JINST **3** (2008) P03004. 86
- [196] Liquid Argon Back End Electronics Collaboration, A. Bazan et al., *ATLAS liquid argon calorimeter back end electronics*, JINST **2** (2007) P06002. 87
- [197] P. O. Hansson Adrian, *The ATLAS b-Jet Trigger*, [arXiv:1111.4190](https://arxiv.org/abs/1111.4190) [hep-ex]. 88
- [198] ATLAS Collaboration, G. Aad et al., *Electron and photon energy calibration with the ATLAS detector using LHC Run 1 data*, Eur.Phys.J. **C74** no. 10, (2014) 3071, [arXiv:1407.5063](https://arxiv.org/abs/1407.5063) [hep-ex]. 89, 105, 107, 108, 110, 111, 112, 113, 114, 119, 121, 148, 149, 150, 151, 152, 153, 155, 157, 158
- [199] M. Aharrouche, C. Adam-Bourdarios, M. Aleksa, D. Banfi, D. Benckekroun, et al., *Measurement of the response of the ATLAS liquid argon barrel calorimeter to electrons at the 2004 combined test-beam*, Nucl.Instrum.Meth. **A614** (2010) 400–432. 89, 156

- [200] L. Courneyea, D. Dannheim, M. Delmastro, S. Elles, M. Gouighri, L. Iconomidou-Fayard, I. Koletsou, W. Lampl, Z. Liang, L. March, P. Strizenec, F. Tarrade, R. Ueno, M. Vincter, Z. Weng, and H. Zhang, *Computation and validation of the electronic calibration constants for the ATLAS Liquid Argon Calorimeters*, Tech. Rep. ATL-LARG-INT-2010-007, CERN, Geneva, Jul, 2010. <https://cds.cern.ch/record/1278462>. 89
- [201] W. Cleland and E. Stern, *Signal processing considerations for liquid ionization calorimeters in a high rate environment*, *Nucl.Instrum.Meth.* **A338** no. 2-3, (1994) 467–497. 89, 157
- [202] J. Colas, N. Dumont-Dayot, J. Marchand, N. Massol, P. Perrodo, et al., *Electronics calibration board for the ATLAS liquid argon calorimeters*, *Nucl.Instrum.Meth.* **A593** (2008) 269–291. 90, 118
- [203] J. Labbe and R. Ishmukhametov, *Crosstalk Measurements in the Electromagnetic Calorimeter during ATLAS Final Installation*, Tech. Rep. ATL-LARG-INT-2009-004. ATL-COM-LARG-2008-012, CERN, Geneva, Dec, 2008. <https://cds.cern.ch/record/1143373>. 90
- [204] W. Lampl, S. Laplace, D. Lelas, P. Loch, H. Ma, S. Menke, S. Rajagopalan, D. Rousseau, S. Snyder, and G. Unal, *Calorimeter Clustering Algorithms: Description and Performance*, Tech. Rep. ATL-LARG-PUB-2008-002. ATL-COM-LARG-2008-003, CERN, Geneva, Apr, 2008. <https://cds.cern.ch/record/1099735>. 92, 169
- [205] J. Marchand, *Etude de la recherche du boson de higgs en deux photons dans l'expérience atlas au lhc et calibration du calorimetre a argon liquide*. PhD thesis, Annecy, LAPP, Annecy-le-Vieux, 2009. <https://cds.cern.ch/record/1221859>. Presented on 03 Jun 2009. 92
- [206] *Expected photon performance in the ATLAS experiment*, Tech. Rep. ATL-PHYS-PUB-2011-007, CERN, Geneva, Apr, 2011. <https://cds.cern.ch/record/1345329>.
- [207] ATLAS Collaboration, *Photon Conversions at  $\sqrt{s} = 900\text{GeV}$  measured with the ATLAS Detector*, Tech. Rep. ATLAS-CONF-2010-007, CERN, Geneva, Jun, 2010. <http://cds.cern.ch/record/1274001>. 106
- [208] J.-F. Marchand, *Photon reconstruction overview, talk at the 2013 e/gamma workshop*,. <https://indico.cern.ch/event/219420/session/11/contribution/35/material/slides/1.pdf>. 92
- [209] H. Abreu, *Measurement of the inclusive prompt photon cross section and preparation of the search of the Higgs boson decaying into two photons with the ATLAS detector at the LHC*. PhD thesis, Orsay, LAL, 2011. <https://inspirehep.net/record/1088024/files/CERN-THESIS-2011-157.pdf>. 93

- [210] B. W. Jamie Saxon, *Neural Net Photon Identification*,. <https://indico.cern.ch/event/153698/session/1/contribution/26/material/2/0.pdf>. Presented 24 november 2011. 93
- [211] ATLAS Collaboration, *Electron and photon reconstruction and identification in ATLAS: expected performance at high energy and results at 900 GeV*, Tech. Rep. ATLAS-CONF-2010-005, CERN, Geneva, Jun, 2010. <http://cds.cern.ch/record/1273197>. 93, 106
- [212] L. Carminati, M. Delmastro, M. Hance, M. Jimenez Belenguer, R. Ishmukhametov, Z. Liang, G. Marchiori, V. Perez Reale, D. Malinsky, M. Tripijana, and G. Unal, *Reconstruction and Identification Efficiency of Inclusive Isolated Photons*, Tech. Rep. ATL-PHYS-INT-2011-014, CERN, Geneva, Mar, 2011. <https://cds.cern.ch/record/1333390>. 93, 106
- [213] *Measurements of the photon identification efficiencies using 20.3 fb<sup>-1</sup> of pp collisions collected by ATLAS at  $\sqrt{s} = 8$  TeV in 2012*, Tech. Rep. ATL-COM-PHYS-2014-542, CERN, Geneva, June, 2014. <https://atlas.web.cern.ch/Atlas/GROUPS/PHYSICS/EGAMMA/PublicPlots/20140611/ATL-COM-PHYS-2014-542/index.html>. 95, 97
- [214] L. Devroye, *Non-uniform random variate generation*. Springer-Verlag, 1986. [https://books.google.fr/books?id=mEw\\_AQAAIAAJ](https://books.google.fr/books?id=mEw_AQAAIAAJ). 95
- [215] M. Kuna, K. Liu, Y. Liu, G. Marchiori, and M. Pitt, *Measurement of the identification efficiency of isolated prompt photons with the “matrix method” in pp collisions at  $\sqrt{s} = 8$  TeV using 21.0fb<sup>-1</sup> of ATLAS data*, Tech. Rep. ATL-COM-PHYS-2013-1628, CERN, Geneva, Dec, 2013. <https://cds.cern.ch/record/1635964>. 96
- [216] K. Liu, Y. Liu, and G. Marchiori, *Measurement of the identification efficiency of isolated prompt photons using the matrix method and 4.9 fb<sup>-1</sup> of ATLAS data*, Tech. Rep. ATL-COM-PHYS-2012-242, CERN, Geneva, Mar, 2012. <https://cds.cern.ch/record/1428909>. 96
- [217] CMS Collaboration, S. Chatrchyan et al., *The CMS experiment at the CERN LHC*, *JINST* **3** (2008) S08004. 98
- [218] D. Froidevaux and P. Sphicas, *General-Purpose Detectors for the Large Hadron Collider*, Annual Review of Nuclear and Particle Science **56** no. 1, (2006) 375–440. <http://dx.doi.org/10.1146/annurev.nucl.54.070103.181209>. 98
- [219] CMS Collaboration, F. Beaudette, *The CMS Particle Flow Algorithm*, [arXiv:1401.8155](https://arxiv.org/abs/1401.8155) [hep-ex]. 98
- [220] T. Sakuma and T. McCauley, *Detector and event visualization with SketchUp at the CMS experiment*, Tech. Rep. CMS-CR-2013-379. arXiv:1311.4942, CERN, Geneva, Oct, 2013. <https://cds.cern.ch/record/1626816>. Comments: 5 pages, 6 figures, Proceedings for CHEP 2013, 20th International Conference on Computing in High Energy and Nuclear Physics. 99

- [221] CMS Collaboration, V. Khachatryan et al., *Performance of photon reconstruction and identification with the CMS detector in proton-proton collisions at  $\sqrt{s} = 8$  TeV*, [arXiv:1502.02702](https://arxiv.org/abs/1502.02702) [[physics.ins-det](#)]. 98, 101, 160, 162, 163, 164, 165
- [222] M. Anfreville, D. Bailleux, J. P. Bard, A. Bornheim, C. Bouchand, E. Bougamont, M. Boyer, R. Chipaux, V. Daponte-Puill, M. Dejardin, J.-L. Faure, P. Gras, P. Jarry, C. Jeanney, A. Joudon, J.-P. Pansart, Y. Penichot, J. Rander, J. Rolquin, J.-M. Reymond, J. Tartas, P. Venault, P. Verrecchia, L. Zhang, K. Zhu, and R.-Y. Zhu, *Laser monitoring system for the CMS lead tungstate crystal calorimeter*, Tech. Rep. CMS-NOTE-2007-028, CERN, Geneva, Nov, 2007. <https://cds.cern.ch/record/1073694>. 98
- [223] CMS Collaboration, *Image of all ECAL*, 2008. [http://cms-project-ecal-p5.web.cern.ch/cms-project-ECAL-P5/images/ecal\\_all.jpeg](http://cms-project-ecal-p5.web.cern.ch/cms-project-ECAL-P5/images/ecal_all.jpeg). 100
- [224] CMS Collaboration, V. Khachatryan et al., *Performance of electron reconstruction and selection with the CMS detector in proton-proton collisions at  $\sqrt{s} = 8$  TeV*, *JINST* **10** no. 06, (2015) P06005, [arXiv:1502.02701](https://arxiv.org/abs/1502.02701) [[physics.ins-det](#)]. 100
- [225] D. Banfi, L. Carminati, and L. Mandelli, *Calibration of the ATLAS electromagnetic calorimeter using calibration hits*,. 105, 161
- [226] B. Lenzi and R. Turra, *Monte Carlo calibration update for electrons and photons using multivariate techniques*, Tech. Rep. ATL-COM-PHYS-2013-1426, CERN, Geneva, Oct, 2013. <https://cds.cern.ch/record/1609589>. 105, 108, 212
- [227] N. Lorenzo Martinez, *Observation of a Higgs boson and measurement of its mass in the diphoton decay channel with the ATLAS detector at the LHC*. PhD thesis, Orsay, 2013. <https://cds.cern.ch/record/1640199>. Presented 10 Sep 2013. 106, 111, 207
- [228] ATLAS Collaboration, *Study of the Material Budget in the ATLAS Inner Detector with K0S decays in collision data at  $\sqrt{s}=900$  GeV*, Tech. Rep. ATLAS-CONF-2010-019, CERN, Geneva, Jul, 2010. <http://cds.cern.ch/record/1277651>. 106
- [229] ATLAS Collaboration, *Photon conversion plots for Summer conferences 2011* , Tech. Rep. ATL-COM-PHYS-2011-120, CERN, Geneva, 2011. <http://cds.cern.ch/record/1274001>. 106
- [230] ATLAS Collaboration, G. Aad et al., *A study of the material in the ATLAS inner detector using secondary hadronic interactions*, *JINST* **7** (2012) P01013, [arXiv:1110.6191](https://arxiv.org/abs/1110.6191) [[hep-ex](#)]. 106
- [231] M. Kuna, C. Gabaldon, F. Hubaut, and P. Pralavorio, *Study of material in front of the EM calorimeter with high  $pT$  electron shower shapes and tracks*, Tech. Rep. ATL-PHYS-INT-2008-026. ATL-COM-PHYS-2008-081, CERN, Geneva, Jun, 2008. <https://cds.cern.ch/record/1107811>. 106

- [232] M. Boonekamp, O. Fedin, D. Froidevaux, and G. Unal, *Passive material determination using electrons and photons*, Tech. Rep. ATL-COM-PHYS-2013-1644, CERN, Geneva, Dec, 2013. <https://cds.cern.ch/record/1636887>. 106, 119
- [233] A. Hoecker, P. Speckmayer, J. Stelzer, J. Therhaag, E. von Toerne, and H. Voss, *TMVA: Toolkit for Multivariate Data Analysis*, PoS **ACAT** (2007) 040, [arXiv:physics/0703039](https://arxiv.org/abs/physics/0703039). 108
- [234] M. Aleksa, C. Becot, B. Laforge, N. Lorenzo Martinez, F. Teischinger, and G. Unal, *Calibration stability and uniformity measurements of electrons and photons*, Tech. Rep. ATL-COM-PHYS-2013-1421, CERN, Geneva, Oct, 2013. <https://cds.cern.ch/record/1608607>. 111, 112, 145, 150
- [235] M. Boonekamp, B. Lenzi, N. Lorenzo Martinez, P. Schwemling, F. Teischinger, G. Unal, and L. Yao, *Electromagnetic calorimeter layers energy scales determination*, Tech. Rep. ATL-COM-PHYS-2013-1423, CERN, Geneva, Oct, 2013. <https://cds.cern.ch/record/1609068>. 111, 118, 120, 157
- [236] H. Abreu, M. Aharrouche, M. Aleksa, L. Aperio Bella, J. Archambault, et al., *Performance of the electronic readout of the ATLAS liquid argon calorimeters*, **JINST** **5** (2010) P09003. 118
- [237] ATLAS Collaboration, *Readiness of the ATLAS Liquid Argon Calorimeter for LHC Collisions*, Eur. Phys. J. C **70** no. arXiv:0912.2642. CERN-PH-EP-2010-041, (2010) 723–753. 31 p. <https://cds.cern.ch/record/1228823>. Comments: 31 pages, 34 figures, accepted in EPJC. 118
- [238] M. Aharrouche, C. Adam-Bourdarios, M. Aleksa, D. Banfi, D. Bencheekroun, et al., *Measurement of the response of the ATLAS liquid argon barrel calorimeter to electrons at the 2004 combined test-beam*, **Nucl.Instrum.Meth.** **A614** (2010) 400–432. 118
- [239] ATLAS Collaboration, *Observation and study of the Higgs boson candidate in the two photon decay channel with the ATLAS detector at the LHC*, Tech. Rep. ATLAS-CONF-2012-168, CERN, Geneva, Dec, 2012. <http://cds.cern.ch/record/1499625>. 122
- [240] C. Becot, N. Andari, L. Fayard, and G. Unal, *Difference of energy response between the high and medium gain of the ATLAS electromagnetic calorimeter*, Tech. Rep. ATL-PHYS-INT-2015-001, CERN, Geneva, Jan, 2015. <https://cds.cern.ch/record/1981535>. 123, 130, 131, 132, 136, 137
- [241] J. Collot, C. de La Taille, D. Dzahini, F. Lugiez, J. Pascual, J. Richer, and J. Teiger, *The LAr Tri-Gain Shaper*, Tech. Rep. ATL-LARG-98-092. ATL-A-PN-92, CERN, Geneva, Mar, 1998. <http://cds.cern.ch/record/682111>. 128

- [242] K. Grevtsov, M. Delmastro, and I. Wingerter, *Gain and LAr cell non-linearity ; egamma workshop 2014*,. <https://indico.cern.ch/event/310874/session/2/contribution/32/material/slides/0.pdf>. 136
- [243] ATLAS Collaboration, *Data/MC Comparison for Calorimeter Shower Shapes of High Et Electrons*,. <https://atlas.web.cern.ch/Atlas/GROUPS/PHYSICS/EGAMMA/PublicPlots/20111005/ATL-COM-PHYS-2011-1299/index.html>. 138, 164
- [244] G. Unal, *Private communication*, 2012. [https://indico.cern.ch/event/116188/contribution/5/attachments/52646/75750/eg\\_calib.pdf](https://indico.cern.ch/event/116188/contribution/5/attachments/52646/75750/eg_calib.pdf). 138
- [245] N. Andari, *Checks of out-of-cluster leakage for photons. Talk at the 2012 HSG1 Workshop*,. <https://indico.cern.ch/event/214002/session/4/contribution/15/material/slides/0.pdf>. 138
- [246] G. Unal, *Correcting cell energies for BX-dependent pile-up and impact on egamma*, Feb, 2012. <https://indico.cern.ch/event/163454/>. 139
- [247] R. Hanna, *Lateral leakage in the strips*, Feb, 2013. <https://indico.cern.ch/event/299124/contribution/2/material/slides/0.pdf>. 144
- [248] C. Becot, *Cluster leakage data/MC difference vs. conversion reconstruction mismodeling*,. <https://indico.cern.ch/event/303622/>. 145
- [249] F. Djama, *Using  $Z^0 \rightarrow e^+e^-$  for Electromagnetic Calorimeter Calibration*, Tech. Rep. ATL-LARG-2004-008, Aix-Marseille 2. Cent. Phys. Part., Marseille, Jun, 2004. <https://cds.cern.ch/record/745592>. 146
- [250] J.-B. Blanchard, J.-B. de Vivie, and P. Mastrandrea, *In situ scales and smearings from Z and  $J/\Psi$  events*, Tech. Rep. ATL-COM-PHYS-2013-1653, CERN, Geneva, Dec, 2013. <https://cds.cern.ch/record/1637533>. 146, 152, 156
- [251] ATLAS Collaboration, G. Aad et al., *Electron performance measurements with the ATLAS detector using the 2010 LHC proton-proton collision data*, *Eur.Phys.J. C72* (2012) 1909, [arXiv:1110.3174](https://arxiv.org/abs/1110.3174) [hep-ex]. 148
- [252] ATLAS Collaboration, A. Airapetian et al., *ATLAS calorimeter performance Technical Design Report*,. 150
- [253] G. Unal, *Pedestal shifts, at the LAr general meeting*,. <https://indico.cern.ch/event/301145/contribution/7/material/slides/0.pdf>. 152
- [254] G. Unal, *LAr issues for egamma calibration, at the 2014 egamma workshop*,. <https://indico.cern.ch/event/310874/session/2/contribution/31/material/slides/0.pdf>. 152

- [255] B. Lenzi, *Fraction of converted photons in data and MC, at the 2014 egamma workshop*, <https://indico.cern.ch/event/310874/session/6/contribution/52/material/slides/0.pdf>. 153
- [256] C. Rangel-Smith, B. Lopez Paredes, and Y. Yamaguchi, *In-situ photon scales from radiative Z decays*, Tech. Rep. ATL-COM-PHYS-2013-1634, CERN, Geneva, Dec, 2013. <https://cds.cern.ch/record/1636233>. First complete version: changes might occur. 154
- [257] G. Unal, *Electron and Photon energy resolutions and their uncertainties for run-1 calibration*, Tech. Rep. ATL-COM-PHYS-2013-1651, CERN, Geneva, Dec, 2013. <https://cds.cern.ch/record/1637528>. 157
- [258] T. T. de Fatis, *Searches of the Higgs boson in the diphoton decay mode in CMS*, 2014, Dec. <https://indico.lal.in2p3.fr/event/2561/>. 160
- [259] CMS Collaboration, S. Chatrchyan et al., *Energy Calibration and Resolution of the CMS Electromagnetic Calorimeter in pp Collisions at  $\sqrt{s} = 7$  TeV*, *JINST* **8** (2013) P09009, [arXiv:1306.2016](https://arxiv.org/abs/1306.2016) [[hep-ex](#)]. 160
- [260] G. Unal, *CMS vs ATLAS mass measurement in  $h \rightarrow \gamma\gamma$* , <https://indico.cern.ch/event/329356/contribution/1/attachments/640465/881356/atlas-cms-escale-10july2014.pdf>. 161, 166
- [261] CMS Collaboration, V. Khachatryan et al., *Observation of the diphoton decay of the Higgs boson and measurement of its properties*, *Eur.Phys.J.* **C74** no. 10, (2014) 3076, [arXiv:1407.0558](https://arxiv.org/abs/1407.0558) [[hep-ex](#)]. <https://twiki.cern.ch/twiki/bin/view/CMSPublic/Hig13001PubTWiki>. 165, 188, 205, 206
- [262] ATLAS Collaboration, G. Aad et al., *Measurement of Higgs boson production in the diphoton decay channel in pp collisions at center-of-mass energies of 7 and 8 TeV with the ATLAS detector*, *Phys.Rev.* **D90** no. 11, (2014) 112015, [arXiv:1408.7084](https://arxiv.org/abs/1408.7084) [[hep-ex](#)]. 165, 168, 170, 213
- [263] ATLAS, CMS Collaboration, G. Aad et al., *Combined Measurement of the Higgs Boson Mass in pp Collisions at  $\sqrt{s} = 7$  and 8 TeV with the ATLAS and CMS Experiments*, *Phys. Rev. Lett.* **114** (2015) 191803, [arXiv:1503.07589](https://arxiv.org/abs/1503.07589) [[hep-ex](#)]. 166, 182, 183, 228
- [264] ATLAS Collaboration, G. Aad et al., *Measurement of the Higgs boson mass from the  $H \rightarrow \gamma\gamma$  and  $H \rightarrow ZZ^* \rightarrow 4\ell$  channels with the ATLAS detector using 25 fb<sup>-1</sup> of pp collision data*, *Phys.Rev.* **D90** no. 5, (2014) 052004, [arXiv:1406.3827](https://arxiv.org/abs/1406.3827) [[hep-ex](#)]. <https://atlas.web.cern.ch/Atlas/GROUPS/PHYSICS/PAPERS/HIGG-2013-12/>. 168, 172, 176, 177, 178, 179, 180, 181, 182, 183, 184, 185, 190, 192, 201, 205, 206, 213, 224, 228, 229

- [265] I. Koletsou, *Recherche du boson de Higgs dans le canal diphoton au LHC avec le détecteur ATLAS*. PhD thesis, Orsay, Paris 11, Orsay, 2008.  
<https://cds.cern.ch/record/1109597>. Presented on 02 Apr 2008. 169
- [266] J. Marchand and E. Scifo, *Oscillation of calorimeter pointing  $z$  position as a function of pseudo-rapidity in the end-cap*, Tech. Rep. ATL-COM-CAL-2012-003, CERN, Geneva, Apr, 2012. <https://cds.cern.ch/record/1438738>. 169
- [267] ATLAS Collaboration Collaboration, *Observation of an excess of events in the search for the Standard Model Higgs boson in the gamma-gamma channel with the ATLAS detector*, Tech. Rep. ATLAS-CONF-2012-091, CERN, Geneva, Jul, 2012.  
<https://cds.cern.ch/record/1460410>. 169
- [268] D. Delgove, *An update on the selection of the diphoton vertex, HSG1 meeting*,  
<https://indico.cern.ch/event/166261/contribution/1/material/slides/0.pdf>. 169
- [269] S. Laplace and J. de Vivie, *Calorimeter isolation and pile-up*, Tech. Rep. ATL-COM-PHYS-2012-467, CERN, Geneva, May, 2012.  
<https://cds.cern.ch/record/1444890>. 171
- [270] C. Rangel-Smith, *Photon performance studies with Radiative  $Z$  decays, and the search for the Higgs boson in the  $H \rightarrow \gamma\gamma$  and  $H \rightarrow Z\gamma$  channels with the ATLAS detector of the LHC*. PhD thesis, Paris U., VI-VII, Jan, 2014.  
<https://cds.cern.ch/record/1642824>. Presented 27 Sep 2013. 171
- [271] ATLAS Collaboration, G. Aad et al., *Search for the Standard Model Higgs boson in the two photon decay channel with the ATLAS detector at the LHC*, *Phys.Lett. B* **705** (2011) 452–470, [arXiv:1108.5895 \[hep-ex\]](https://arxiv.org/abs/1108.5895). 173, 205
- [272] N. Lorenzo Martinez and R. Turra, *Mass measurement in the  $H \rightarrow \gamma\gamma$  channel: Supporting documentation for the Mass Paper*, Tech. Rep. ATL-COM-PHYS-2014-018, CERN, Geneva, Jan, 2014.  
<https://cds.cern.ch/record/1642851>. 174, 182
- [273] ATLAS Collaboration, *Combined measurements of the mass and signal strength of the Higgs-like boson with the ATLAS detector using up to  $25 \text{ fb}^{-1}$  of proton-proton collision data*, Tech. Rep. ATLAS-CONF-2013-014, CERN, Geneva, Mar, 2013.  
<https://cds.cern.ch/record/1523727>. 183
- [274] ATLAS Collaboration, *Measurements of the properties of the Higgs-like boson in the two photon decay channel with the ATLAS detector using  $25 \text{ fb}^{-1}$  of proton-proton collision data*,. 183, 229
- [275] G. Unal and N. Andari, *Expected mass difference - HSG1 Meeting*,  
<https://indico.cern.ch/event/293748/contribution/7/attachments/550363/758380/HmassDiff.pdf>. 183

- [276] Wikipedia, *Voigt profile*, 2015.  
[https://en.wikipedia.org/wiki/Voigt\\_profile](https://en.wikipedia.org/wiki/Voigt_profile). 185, 203
- [277] ATLAS Collaboration, *Mass and signal strength measurement of the Higgs particle in the four leptons decay channel with the ATLAS detector*, Tech. Rep. ATL-COM-PHYS-2014-007, CERN, Geneva, Jan, 2014.  
<https://cds.cern.ch/record/1641921>. 185
- [278] CMS Collaboration Collaboration, *Properties of the observed Higgs-like resonance using the diphoton channel*, Tech. Rep. CMS-PAS-HIG-13-016, CERN, Geneva, 2013. <https://cds.cern.ch/record/1558930>. 188
- [279] K. Cranmer, A. Read, and W. Verkerke, *Extensions to the Frequentist Recommendation*,. <https://twiki.cern.ch/twiki/pub/AtlasProtected/StatisticsTools/ExtendedStatForumRecommendations.pdf>. 192
- [280] *Constraints on New Phenomena via Higgs Coupling Measurements with the ATLAS Detector*, Tech. Rep. ATLAS-CONF-2014-010, CERN, Geneva, Mar, 2014.  
<https://cds.cern.ch/record/1670531>. 192
- [281] N. Andari, Y. Fang, L. Fayard, M. Kado, Y. Pan, F. Polci, H. Wang, and S. Wu, *Exclusion limits and Systematics*, Tech. Rep. ATL-COM-PHYS-2010-844, CERN, Geneva, Sep, 2010. <https://cds.cern.ch/record/1299070>. 198
- [282] ATLAS Collaboration, G. Aad et al., *Measurements of Higgs boson production and couplings in the four-lepton channel in pp collisions at center-of-mass energies of 7 and 8 TeV with the ATLAS detector*, *Phys.Rev.* **D91** no. 1, (2015) 012006, [arXiv:1408.5191](https://arxiv.org/abs/1408.5191) [hep-ex]. 201
- [283] S. Sun and R. Di Nardo, *Private communication*,. 202
- [284] O. Vitells, *Energy scale systematics at high significance*,. 202
- [285] O. Vitells, *Estimating the look elsewhere effect when searching for a signal*, Apr, 2012. <https://indico.lal.in2p3.fr/event/1819/>. 202
- [286] E. Gross and O. Vitells, *Trial factors for the look elsewhere effect in high energy physics*, *European Physical Journal C* **70** (2010) 525–530, [arXiv:1005.1891](https://arxiv.org/abs/1005.1891) [physics.data-an]. 202
- [287] M. R. Leadbetter, *On Crossings of Levels and Curves by a Wide Class of Stochastic Processes*, *Ann. Math. Statist.* **37** no. 1, (1966) 260–267.  
<http://dx.doi.org/10.1214/aoms/1177699615>. 202
- [288] Sherpa Team, *Sherpa 2.0.0 Manual*,.  
<http://sherpa.hepforge.org/doc/SHERPA-MC-2.0.0.html>. 208
- [289] *Projections for measurements of Higgs boson cross sections, branching ratios and coupling parameters with the ATLAS detector at a HL-LHC*, Tech. Rep. ATL-PHYS-PUB-2013-014, CERN, Geneva, Oct, 2013.  
<http://cds.cern.ch/record/1611186>. 208, 219

- [290] S. Catani and M. Grazzini, *An NNLO subtraction formalism in hadron collisions and its application to Higgs boson production at the LHC*, *Phys.Rev.Lett.* **98** (2007) 222002, [arXiv:hep-ph/0703012 \[hep-ph\]](#). 210
- [291] Andrew Hard, Yanping Huang, Fuquan Wang, Haichen Wang, Hongtao Yang and Sau Lan Wu, *Smearred simulation sample*, 2012. <https://indico.cern.ch/event/214002/session/11/contribution/42/material/slides/0.pdf>. 212
- [292] ATLAS Collaboration, G. Aad et al., *Measurements of fiducial and differential cross sections for Higgs boson production in the diphoton decay channel at  $\sqrt{s} = 8$  TeV with ATLAS*, *JHEP* **1409** (2014) 112, [arXiv:1407.4222 \[hep-ex\]](#). 213, 214
- [293] S. Schumann and F. Krauss, *A Parton shower algorithm based on Catani-Seymour dipole factorisation*, *JHEP* **0803** (2008) 038, [arXiv:0709.1027 \[hep-ph\]](#). 215
- [294] R. Ellis, W. Stirling, and B. Webber, *QCD and Collider Physics*. Cambridge Monographs on Particle Physics, Nuclear Physics and Cosmology. Cambridge University Press, 2003. <https://books.google.fr/books?id=TqrPVoS6s0UC>. 215
- [295] J. M. Campbell, J. Huston, and W. Stirling, *Hard Interactions of Quarks and Gluons: A Primer for LHC Physics*, *Rept.Prog.Phys.* **70** (2007) 89, [arXiv:hep-ph/0611148 \[hep-ph\]](#). 215
- [296] S. Moch, *Expectations at LHC from hard QCD*, *J.Phys.* **G35** (2008) 073001, [arXiv:0803.0457 \[hep-ph\]](#). 216
- [297] S. Yuen,  *$h \rightarrow \gamma\gamma$  Width analysis: Status Report ; presentation at the HGam meeting of February,3 , 2015.* <https://indico.cern.ch/event/370434/>. 219
- [298] L. Dixon, *Private communication.*. 221
- [299] M. Escalier, *Private communication.*. 222
- [300] K. Melnikov, *Private communication.*. 222
- [301] T. Adye and H. Yang, *minutes of ATLAS Higgs approval meeting 5 February 2015*, Feb, 2015. <https://indico.cern.ch/event/366179/contribution/7/attachments/728013/998987/150205-higgs.pdf>. 225
- [302] S. Hoeche, F. Krauss, M. Schonherr, and F. Siegert, *A critical appraisal of NLO+PS matching methods*, *JHEP* **09** (2012) 049, [arXiv:1111.1220 \[hep-ph\]](#). 226
- [303] S. Höche and S. Prestel, *The midpoint between dipole and parton showers*, *Eur. Phys. J.* **C75** no. 9, (2015) 461, [arXiv:1506.05057 \[hep-ph\]](#). 226
- [304] N. Berger, *Backup slides, HSG1 Meeting.* [https://indico.cern.ch/event/321222/contribution/3/attachments/620318/853564/StatError\\_28052014.pdf](https://indico.cern.ch/event/321222/contribution/3/attachments/620318/853564/StatError_28052014.pdf). 237
- [305] M. G. Kendall, A. Stuart, and J. K. Ord, eds., *Kendall's Advanced Theory of Statistics*. Oxford University Press, Inc., New York, NY, USA, 1987. 237

# Remerciements

Pour commencer je tiens à remercier Louis Fayard pour son encadrement exceptionnel au cours des dernières années. Je te remercie de m'avoir permis de découvrir la physique des particules, d'abord avec Henso puis Jean-François. Je te remercie aussi d'avoir su, au cours des trois dernières années, trouver des réponses à toutes mes questions, aussi tordues soient-elles, depuis les fondements du modèle standard jusqu'aux détails du détecteur. Je te remercie de m'avoir fait profiter de ta disponibilité, ta patience et ton sens du détail, ainsi que d'avoir essayé de me transmettre ta rigueur. Je suis infiniment reconnaissant de la confiance que tu m'as accordé, et de la liberté que tu m'as laissé dans mon travail.

De même, je tiens à remercier Guillaume Unal et Nancy Andari pour le rôle central qu'ils ont eu dans le travail présenté ici. Guillaume, ton humilité et ta capacité à apporter des solutions à tous les problèmes, quel que soit le sujet, m'impressionneront toujours, et je te remercie de m'en avoir fait profiter. Je ne suis pas sûr que j'aurais pu atteindre le même niveau de compréhension sur l'ensemble des sujets présentés ici sans ton aide. Nancy, le soutien que tu m'as apporté, qu'il soit technique ou moral, a été d'une importance inestimable. Je te remercie pour ta persévérance à chercher les bugs les plus fins, générosité sans fin, ton altruisme et ta capacité à continuer à te pré-occuper de mon travail et de la direction qu'il prend, même plus d'un an après avoir changé de sujet.

I warmly thank all the members of my thesis jury : M. Boonekamp, M. Cacciari, L. Fayard, K. Melnikov, M. Pieri, P. Savard, A. Stocchi, G. Unal. I am grateful to Marco Pieri and Pierre Savard to have spent a part of their otherwise busy summers reading this document and reporting on it. Je remercie également Achille de m'avoir accueilli dans son laboratoire et de m'avoir permis d'y faire ma thèse. Je remercie Maarten pour tout le travail accompli sur la calibration, et l'aide qu'il m'a apporté lorsque j'y travaillais. I thank Kirill Melnikov as well as Matteo Cacciari for accepting to be part of this jury too.

Je suis profondément reconnaissant à l'ensemble des physiciens du LAL impliqués dans l'analyse  $h \rightarrow \gamma\gamma$  et l'étalonnage du calorimètre EM pour tout ce qu'ils m'ont apporté. D'abord Daniel pour l'ensemble des discussions sur le calorimètre, ta précision et la relecture de ce manuscrit, ainsi que Stefan pour tes (patientes) explications sur l'électronique du calo. Je dois également beaucoup à Jean-Baptiste, en particulier pour tes connaissances encyclopédiques sur la stat. et les Monte-Carlo (entre autres). Je remercie aussi Marumi pour ton enthousiasme constant et en particulier pour avoir poussé l'étude des interférences au cours de ces derniers mois. Je remercie aussi Marc Escalier pour l'intérêt porté à mon travail et les conseils fournis.

Au delà du groupe  $h \rightarrow \gamma\gamma$ , je tiens aussi à remercier le reste du groupe ATLAS-LAL, en particulier Luc pour sa bonne humeur et ses vannes, Lydia pour ses conseils, Laurent Dufflot pour son aide, et Reisaburo pour les discussions sur les interférences ou la

phénoménologie du Higgs en général.

Je tiens aussi à remercier l'ensemble du personnel du laboratoire sans qui rien ne marcherait, en particulier Genevieve pour veiller sur notre couloir et t'assurer que tout fonctionne idéalement. Je remercie aussi l'équipe du CC-IN2P3, et en particulier Suzanne et Nadia pour le support sans faille, et ce malgré les spécificités de mes jobs...

I warmly thank Lance Dixon and Ye Li for all their patient and precise explanations of the interference effect, as well as (and especially) Stefan Hoeche for all the in-depth discussions on interferences, parton shower and his help with Sherpa. This project would most likely not exist without your advices.

I am grateful to all the statistics experts with whom we could discuss our study of the upper limit of the width : Alex Read, Kyle Cranmer and especially Marumi and Glen Cowan, whose numerous explanations and suggestions definitely gave us a strong insight about the issue we were dealing with, and about statistics in general.

I deeply appreciated the support and trust shown by the successive HGamma conveners (Nicolas Berger, Sandrine Laplace, Dag Gillberg and Elisabeth Petit) while I was working within this subgroup, and I hope we will be able to work together again. I also thank the whole HGamma community, especially Hongtao Yang, James Saxon and Narei Lorenzo, for the discussions, help and comments.

The help provided by the e/gamma calibration group has been invaluable. I am grateful to Maarten and Leonardo Carminati, first for all the work done as calibration conveners, but also for all the insightful comments and incredible help provided throughout the various calibration projects I've been involved in. Within the calibration group I also acknowledge Mike Hance for all his work on the PhotonD3PDMaker (this cell-dumping story would probably never have worked without your help) as well as Bruno Lenzi and especially Jean-François Marchand for all the technical help they provided, as well as Remie Hanna for the work we shared on the leakage. I also thank the successive e/gamma conveners that followed this work (Andrea Bocci, Marco Delmastro and Kerstin Tackmann).

Au delà du cercle d'ATLAS de nombreuses personnes ont facilité la réalisation de cette thèse, à commencer par les autres étudiants. Je remercie l'ensemble des étudiants rencontrés durant 3 ans que ce soit pour l'aide technique (en particulier Estelle, pour avoir continué à en fournir cette année aussi), la cohésion et la bonne ambiance générale (qui semblent être entre des mains capables : Baptiste, Christophe, Steven ou Charles), et l'ensemble des discussions, indépendamment du sujet (particulièrement avec mon co-bureau, David, dont les conversations m'ont aidé à éclaircir plusieurs problèmes). Je porte une attention particulière pour le "groupe rédaction", qu'ils soient du LAL ou non : Camille et ta passion pour la gouache et baywatch, François et tes vidéos de petits poneys hallucinés, Choppy (même si un premier année en rédaction...), Laura, Alexis, Marija, Marta pour le concept de Marta Spinelli, et aussi ce traître de Philippe (en espérant qu'il vienne ici qu'on en finisse !). Je ne suis pas sûr que ça ait amélioré la productivité de la rédaction, mais ça l'a rendu largement plus supportable ! Plus largement je remercie l'ensemble des étudiants déjà rencontrés avant, en particulier Anais et Alexis (H.).

Pour finir je remercie ma famille et les amis de plus longue date que je n'ai pas cité, c'est à dire toutes les personnes qui m'ont poussé à aiguiser ma curiosité ou apprendre de nouvelles choses, et m'ont aidé à approfondir celles qui m'intéressaient le plus. Sans vous je ne ferais sûrement pas un travail de ce genre aujourd'hui.